Diss. ETH No 17466

Large Eddy Simulation of Turbulent Channel and Jet Flows using the Approximate Deconvolution Model

A dissertation submitted to the
Swiss Federal Institute of Technology Zürich

for the degree of
Doctor of Technical Sciences

presented by
Marco Küng
Dipl. Masch.-Ing. ETH

born 4 January 1972
citizen of Switzerland

Accepted on the recommendation of

Prof. Dr. K. Boulouchos, examiner
Prof. Dr. L. Kleiser, co-examiner
Prof. Dr. A. G. Tomboulides, co-examiner
Dr. C. E. Frouzakis, co-examiner

2007

Zwei Dinge erfüllen das Gemüth mit immer neuer Bewunderung und Ehrfurcht, je öfter und anhaltender sich das Nachdenken damit beschäftigt: Der bestirnte Himmel über mir und das moralische Gesetz in mir.

—*Immanuel Kant*

Preface

The present work was performed at the Aerochemistry and Combustion System Laboratory (LAV) at the Swiss Federal Institute of Technology (ETH) in Zürich from 2001 to 2005.
I would like to thank all the people who have helped me with my work in preparing and completing this dissertation. In particular, I want to express my thank to: Prof. Konstantinos Boulouchos: for supervising my research and for providing the best possible support for my work; Prof. Ananias Tomboulides: for his excellent academic guidance, sustained interest in my work and his friendship. His keen insight and vast knowledge together with his dedication to teaching students were an invaluable source of motivation; Dr. Christos Frouzakis: for all the insightful discussions and for his generous advice and support. He had always an open eye for me and my problems and helped me so much to bring the thesis in a readable form; Prof. Leonard Kleiser: for his interest, fruitful discussions and valuable comments, as well as for his support; Dr. Steffen Stolz: for his excellent support in implementing ADM, fruitful discussions and friendship; Dr. Markus Klein from Cambridge University for the advise of implementing his inflow generator in my numerical code; my good friend Luzi Valär: for many excellent discussions and helpful comments to improve the thesis as well for his friendship; Pat Kirchen for correcting the English language of the thesis; Philip Morris for the fruitful support in giving me a better life, especially at hard times; Matthias Essig und Tillman Koschnik: for their excellent support of the Intel Xeon computer-cluster and the Silicon Graphics workstation *ismene*.
I am grateful to my colleagues Dr. Christian Lämmle, Dr. Gabriel Barroso, Dr. Yuri Wright, Pascal Wilhelm, Dr. Andreas Escher, Gian-Marco Pizza and Dr. Benjamin Rembold for many professional discussions and for the good time we had together.
I can not find words to express my most heartfelt gratitude and ap-

preciation to my wife Heidi and my children Jill, Elena and Sina for their loving support and patience during all these years. They always looked to give me a balanced and relaxing life. Of course, my love and deepest thanks go to my parents for their continuous encouragement and emotional support. I want to thank the Küng Logistik-Center AG, for giving me the time and the possibility to finish this dissertation in 2007.

This work was financially supported by ETH Zürich and the Swiss Federal Office of Energy (BFE).

Oberuzwil — Marco Küng
25. 10. 2007

Abstract

In the frame of the present work, Large Eddy Simulations (LES) of turbulent low-Mach number flows were performed. The work is part of an extended project with the goal of establishing LES for turbulent reacting flows.
The goal of the present work was the combination of a spectral element code, which in the past was used for Direct-Numerical Simulations (DNS), and the Approximate Deconvolution Model (ADM) as a subgrid model for LES. The spectral element method combines high accuracy with the flexibility for handling complex geometries.

ADM was first implemented for incompressible, turbulent flows and validated for a turbulent channel flow at Reynolds numbers $Re = 2,800$ and $Re = 10,935$. The flow in the doubly periodic (stream- and spanwise directions) channel was forced at the inflow, maintaining a constant mass flux. Good agreement was obtained between the LES and the DNS results of Moser et al. (R. D. Moser, J. Kim, and N. N. Mansour, Direct numerical simulation of turbulent channel flow up to $Re_\tau = 590$, *Phys. Fluids*, 11(4):943-945, 1999) with respect to the friction Reynolds number and the Reynolds and shear stresses and the logarithmic law of the wall. The spatial resolution especially at the wall is comparable with the LES of Stolz et al. (S. Stolz, N. A. Adams, and L. Kleiser, An Approximate Deconvolution Model for Large Eddy Simulations of compressible flows and its application to incompressible wall-bounded flows, *Phys. Fluids*, 13(4):997-1015, 2001).
In the original version of the model, the relaxation term of ADM is used to account for the interaction between the large and the small scales of the turbulent flow and is based on low-order statistics. An alternative formulation, based on higher-order statistics was proposed by Yakhot (private communication, 2002). He proposed a relaxation term based on

low-order statistics and a correction based on the local value of the rate of strain. This model was implemented in a global spectral-LES code. It was found that with this modification the logarithmic wall law and the friction Reynolds number (Re_τ) were almost insensitive to the spatial resolution in stream- and spanwise directions and the spatial resolution in wall-normal direction could be significantly reduced with respect to that of the standard ADM.

The incompressible LES code was then used for turbulent jet flows for $Re = 2,000$. The setup is that of a jet issued from a nozzle of diameter d_j into a co-flowing stream in a domain of diameter $11d_j$ and length $40d_j$. The domain is bounded moving with the velocity of the co-flowing stream. The jet flow is perturbed with correlated velocity fluctuations and the goal was the investigation of the scale-similarity region ($x/d_j > 20$). The LES results were compared with DNS simulation results performed for this project. The investigation shows an overestimation of the centerline turbulent velocity intensity in the transition region ($x/d_j < 20$), whereas a good agreement was obtained in the scale-similarity region. Two different LES filters were investigated. The first filter (Boyd filter) filters the spectral element excluding the elemental boundaries and the second filter (Legendre filter) filters it including the elemental boundaries. The agreement of the turbulent velocity intensity in the scale-similarity region with the DNS result was only obtained with the second filter. Further, a variation of Re, different mean velocity profiles at the exit, different correlation of the inflow perturbations, different values of the relaxation parameter of ADM, different filter types for the explicit LES filtering and an alternative formulation of the filtered conservation equations could not eliminate the overestimation of the turbulent intensities. Summarizing, the combination of the spectral element code and ADM shows satisfying results in the scale-similarity region whereas the turbulent intensities are overestimated in the transition region ($x/d_j < 20$).

The LES code was then extended for variable-density, low-Mach number flows and was validated against DNS results computed for a non-isothermal, single-species jet. The same setup was used as for the isothermal jet with $Re = 2,000$ and the length of the domain was set to $20d_j$. The Boyd and the Legendre filter were investigated and the LES with the Legendre filter were unstable whereas the Boyd filter stabilized the simulation. Overall the turbulent intensities for velocity

and temperature and the decrease of the mean quantities along the centerline were overestimated by the LES.

Zusammenfassung

Die vorliegende Arbeit handelt von der Grobstruktursimulation (LES) von turbulenten Strömungen unter der Annahme von kleinen Mach-Zahlen. Sie ist Teil einer Entwicklung mit dem Ziel, reaktive Strömungen mit Hilfe der Grobstruktursimulation zu berechnen.
Ziel der Arbeit war es, einen spektralen Elemente Code, welcher bisher für Direkte Numerische Simulationen (DNS) verwendet wurde, mit dem LES-Feinstruktur-Modell *Approximate Deconvolution Model* (ADM) für Grobstruktursimulationen zu kombinieren. Spektrale Elemente Codes kombinieren die Genauigkeit von spektralen Methoden mit der Flexibilität für komplexe Simulationsgeometrien.

ADM wurde zunächst für inkompressible, turbulente Strömungen in den Code implementiert und am Fall der inkompressiblen, turbulenten Kanalströmung für $Re = 2,800$ und für $Re = 10,935$ untersucht. Die Simulationen nehmen in Strömungs- und Spannweitenrichtung periodische Randbedingungen an. Die Strömung wurde mit einem zusätzlichen Kraft-Term in der Impulsgleichung versehen, um den Massenfluss während der Simulation konstant zu halten. Dabei zeigte sich eine sehr gute Übereinstimmung zwischen den LES-Resultaten, im Speziellen dem logarithmische Wandgesetz, den Reynolds-Zahlen Re_τ sowie den Reynolds-Spannungen, mit den DNS-Daten von Moser et al. (R. D. Moser, J. Kim, and N. N. Mansour, Direct numerical simulation of turbulent channel flow up to $Re_\tau = 590$, *Phys. Fluids*, 11(4):943-945, 1999). Die räumliche Auflösung entspricht derjenigen der LES von Stolz et al. (S. Stolz, N. A. Adams, and L. Kleiser, An Approximate Deconvolution Model for Large Eddy Simulations of compressible flows and its application to incompressible wall-bounded flows. *Phys. Fluids*, 13(4):997-1015, 2001).
Die originale Version von ADM wird ein Relaxationsterm verwendet,

um die Interaktion zwischen den grossen und den kleinen Skalen zu berechnen. Der Relaxationsterm basiert dabei auf Statistiken tiefer Ordnung. Eine alternative Formulierung wurde von Yakhot (private Kommunikation, 2002) vorgeschlagen, indem der originale Relaxationsterm korrigiert wird mit der lokalen Scherrate der Strömung und in einen globalen, spektralen LES-Code implementiert wurde. Die LES zeigte, dass das logarithmische Wandgesetz der Wandströmung und in diesem Zusammenhang die Reynolds-Zahl an der Wand Re_τ nur noch gering von der räumlichen Auflösung abhängen.

Die Kombination von ADM und dem spektralen Elemente Code wurde weiter für LES von inkompressiblen, turbulenten Freistrahl-Strömungen verwendet. Das Rechengebiet entspricht einem Rohr mit einem Durchmesser von $11d_j$ und einer Düse mit Durchmesser d_j. Einer Mantelströmung wird die turbulente Freistrahl-Strömung überlagert und der Freistrahl wird mit Hilfe eines Einström-Generators an der Düse verrauscht. Die Länge des Rechengebietes entspricht $40d_j$ und die LES-Resultate werden mit eigens für diese Arbeit berechneten DNS-Daten verglichen. Die Untersuchungen zeigten, dass insbesondere die turbulenten Geschwindigkeits-Intensitäten in Strömungsrichtung entlang der Freistrahl-Achse im Bereich der Transition ein Überschwingen zeigen und im Ähnlichkeitsbereich ($x/d_j > 20$) mit der DNS Lösung exakt übereinstimmen. Zwei unterschiedliche LES Filter wurden untersucht. Der erste Filter (Boyd Filter) filtert das Element ausschliesslich dem Rand. Hingegen filtert der zweite Filter (Legendre Filter) den Rand auch mit. Die gute Übereinstimmung im Ähnlichkeitsbereich der Fluktuation mit der DNS konnte nur mit dem Legendre Filter erreicht werden. Im weiteren, wurde eine Variation der Reynolds-Zahl, des mittleren Geschwindigkeits-Einströmprofils, der räumlichen und zeitlichen Korrelation der dem mittleren Geschwindigkeits-Einströmprofil überlagerten Fluktuationen, des Relaxations-Parameters von ADM, der Filter-Arten und eine alternative Formulierung der Impulsgleichung untersucht und konnten das Überschwingen nicht eliminieren. Zusammenfassend kann gesagt werden, dass die LES im Bereich $x/d_j > 20$ eine gute Übereinstimmung mit den DNS Resultaten zeigen und die Statistiken im transienten Bereich des Freistrahls ($x/d_j < 20$) überschätzt werden.

Der Code wurde anschliessend weiterentwickelt für die Grobstruktursimulation von nicht-isothermen, turbulenten Freistrahl-Strömungen. Dabei wurde das Rechengebiet des isothermen Freistrahls auf eine Länge

von $20d_j$ verkürzt und die LES-Resultate wurden mit ebenfalls eigens für diese Arbeit berechneten DNS-Resultaten verglichen. Wiederum wurden der Boyd und der Legendre Filter untersucht und es zeigte sich, dass der Legendre Filter zu instabilen Grobstruktursimulationen führte, was der Boyd Filter nicht tat. Die LES mit dem (stabilen) Boyd Filter überschätzen die Geschwindigkeits- und Temperaturfluktuationen als auch den Abfall der mittleren Grössen entlang der Strömungsachse.

Nomenclature

Symbol	Description	Unit
c_p	heat capacity	[J/(kgK)]
c_p^a	average heat capacity	[J/(kgK)]
C_S	Smagorinsky constant	[-]
Ct	Craya-Curtet number	[-]
d	diameter of the nozzle	[m]
dt	timestep	[s]
$E(k)$	energy spectrum	[Ws]
$\underline{e}_g$	gravitation unity vector	[-]
Fr	Froude number	[-]
G	LES-filter function	[-]
g	gravity constant	$[m/s^2]$
h	specific enthalpy	[J/kg]
h_c	channel-half width	[m]
$\underline{\underline{I}}$	unity tensor	[-]
$\overline{\overline{J}}$	momentum flux	$[N/m^2]$
k	wavenumber	[-]
KC	von-Karman constant	[-]
L	reference length scale	[m]
l_k	Kolmogorov length scale	[m]
L_i	Legendre polyomial of order i	[-]
m	mass	[kg]
$\hat{Ma}$	Mach number	[-]
M_x, M_y	spatial, equidistant resolution inflow generator	[-]
M	mean molecular weight	[kg/kmol]
N_d	deconvolution order	[-]
N_s	maximal polynomial order	[-]

Symbol	Description	Unit
N_e	number of element in one spatial direction	[-]
N_t	number of timesteps	[-]
N_x	number of spectral points in the x-direction	[-]
p	thermodynamic pressure	[Pa]
p_2	hydrodynamic pressure	[Pa]
Pr	Prandtl number	[-]
Q	mass flux	[kg/s]
q	entrainment	[kg/s]
Q_N	inverse filter operator	[-]
Q_T	thermal divergence	[1/s]
r	radius	[m]
Re	Reynolds number	[-]
Re_τ	friction Reynolds number	[-]
R_{vv}	correlation function	[-]
$r_{1/2}$	velocity half width	[m]
$\underline{\underline{S}}$	stress tensor	$[kg/(m^3 s)]$
t	time	[s]
T	temperature	[K]
t_k	Kolmogorov time scale	[s]
t_u	time scale	[s]
$\underline{u}$	velocity vector $(u, v, w)^T$	[m/s]
u	axial velocity	[m/s]
u_τ	friction velocity	[m/s]
v	radial velocity	[m/s]
w	azimuthal velocity	[m/s]
$\underline{x}$	space vector $(x, y, z)^T$	[m]
x	x-direction	[m]
y	y-direction	[m]
y^+	wall unit	[m]
Y	mass fraction	[-]
z	z-direction	[m]

Greek

Symbol	Description	Unit
Δ	difference	[-]
Δ_d	inversion error	[-]
δ_v	viscous scale	[m]
ϵ	dissipation rate	[W]
κ	polynomial order	[-]
κ_{ct}	cutoff of the filter	[-]
λ_e	velocity excess	[m/s]
Γ	mesh-filter operator	[-]
λ	thermal diffusivity	$[kg/(ms)]$
μ	dynamic viscosity	$[m^2/s]$
ν	kinematic viscosity	$[kg/(ms)]$
ξ	Boyd functions	[-]
Φ	arbitrary quantity	[-]
σ	correlation scale	[-]
τ	time scale	[s]
τ_w	wall-shear stress	$[kg/(m^3s)]$
Ω	mesh ratio	[-]
ρ	density	$[kg/m^3]$

Subscripts and Special Symbols

Symbol	Description
0	bulk quantity at the orifice
c	quantity along the jet axis
D	diameter
e	external, refers to the co-flow
i	species
j	on the jet axis, at the nozzle exit
L	spectral-resolved solution
nrp	non-representative scales
r	rectangular
s	spatial
S	spectral-non resolved solution
rep	for representative scales
t	temporal
$()'$	fluctuation
$()^*$	dimensional quantity
$()^\star$	deconvoluted quantity
$\grave{}$	Lagrange polynomial coefficients
$\acute{}$	Legendre polynomial coefficients
$\bar{}$	filtered quantity
$\tilde{}$	Favre-filtered quantity
$\breve{}$	dimensional quantity
$\breve{}$	Boyd coefficients
∞	farfield or stagnation conditions

Abbreviations

Symbol	**Description**
ADM	Approximate Deconvolution Model
HIST	homogenous, isotropic turbulence
LES	Large Eddy Simulation
DNS	Direct numerical simulation
RANS	Reynolds averaged Navier-Stokes equations
SE-filter	spectral element filter

Contents

Chapter 1

Introduction

Computational fluid dynamics (CFD) is the study of fluid flows with the help of numerical simulations. In most cases, CFD deals with the numerical simulation of turbulent flows by solving the equations with appropriate algorithms.
Numerical simulations are used for two kinds of problems:

1. They are used in fundamental research to first study in detail fluid dynamics phenomena and then to model and control them. Fundamental investigations require that all spatial and temporal scales must be resolved to perform numerical simulations with high accuracy. If turbulent flows are considered, a large range of physical scales must to be resolved and the associated computational cost is very high.

2. Numerical simulations are also used as an engineering tool to decrease the time to the market. Here, the primary interest is not to understand the fluid-mechanical effects in detail, but to obtain information about global quantities, such as frictional resistance on a surface of a plane, noise production of a gas turbine or the mixing of chemical species in a chemical reactor. In addition, the sensitivity of the system behavior to changes in the operating conditions can be investigated.

The turbulence is one of the most fascinating phenomena of fluid mechanics. The mathematical description of this phenomena were independently developed 150 years ago by the French engineer Claude Louis M.

H. Navier (1785-1836) and the Irish mathematician George Gabriel Stokes (1819-1903). The numerical algorithms to solve the equations are known and have been improved during the last years and supercomputers with more than 10^{13} floating-point operations per second are available at the begin of the new millennium. Yet, turbulence is still one of the unsolved problems of classical physics.
There are different definitions for *turbulence* and one can find different explanations in the literature. There is no unique definition of turbulence; instead, it is easier to characterize turbulent flows by their properties. These flows are always three-dimensional, non-stationary, contain eddies, are diffusive and dissipative. It is well known that turbulent flows are present only for high enough Reynolds numbers Re, defined as

$$Re = \frac{ul}{\nu} \ , \tag{1.1}$$

where u, l and ν are a characteristic velocity, a length scale and the kinematic viscosity, respectively. The flow is laminar below some critical value of Re. The flow becomes turbulent as the Reynolds number is increased and the energy spectrum become broader.
Almost all technical flows are turbulent. All bodies of modern means of transportation are surrounded by turbulent flows, which increases their frictional resistance and therefore the energy consumption and noise production. Turbulent flows have also advantages. They are used for example to enhance mixing between fuel and air in a combustion chamber of a gas turbine, leading to a more efficient and cleaner combustion.

Extensive efforts are made to gain a deeper physical understanding of turbulent flows, leading to a large demand for accurate calculations, especially for engineering applications. Until the middle of the previous century, the investigations were based on experimental studies and empirical correlations. The conservation equations, being a nonlinear system of coupled partial differential equations, except in idealized cases. Numerical solutions of the Navier-Stokes equations were first made possible with the development of fast computers. Today, the Navier-Stokes equations can be solved numerically for laminar flows at an appropriate accuracy. The situation for turbulent flows looks different. Direct-Numerical Simulations (DNS) of unsteady, three dimensional turbulent flows with fast supercomputers and efficient numerical algorithms are limited to relatively small Re of the order of 10^4. DNS is free of models and assumptions, gives almost exact results when using an

appropriate numerical scheme in combination with an appropriate mesh, and is an invaluable tool for the research of turbulent flows.
The limitation to low Re for DNS is explained by the model of turbulent flows developed by Kolmogorov in 1941 [70]. Kolmogorov described the chaotic behavior of local homogenous and isotropic turbulent flow by a superposition of eddies of different sizes. The largest eddies have the dimension of the flow geometry whereas the smallest elements of the turbulent flow depend on the Reynolds number. It is assumed that the energy is provided by the large eddies and is transferred by a cascade process to the smaller eddies. The end of the energy cascade is reached when the supplied energy of the smallest eddies is dissipated into heat through viscous effects. The smallest characteristic length of the turbulent elements is called Kolmogorov length l_k. Using dimensional arguments, it can be expressed as a function of the kinematic viscosity ν and the dissipation rate ε as $l_k = (\nu^3/\varepsilon)^{1/4}$, while the Kolmogorov time is defined as $t_k = (\nu/\varepsilon)^{1/2}$.
The distribution of the turbulent kinetic energy as a function of different length scales or associated wavenumbers k, is described by the energy spectrum $E(k)$, shown schematically in Fig. 1.1 in a doubly logarithmic presentation. L^{-1} is the wavenumber of the large eddies and l_k^{-1} the wavenumber of the smallest eddies. The energy cascade is present in the so-called inertial range. This means that the energy transfer from large to small eddies is achieved only by inertial forces. The energy spectra $E(k)$ in the inertial range are proportional to $k^{-5/3}$. The supplied energy is dissipated into heat at the wavenumber l_k^{-1}. The ratio of the largest to the smallest length scales can be estimated as $L/l_k \sim Re^{3/4}$ from these considerations. It is obvious that the range of scales increases with increasing Reynolds number Re. Based on this, it is possible to

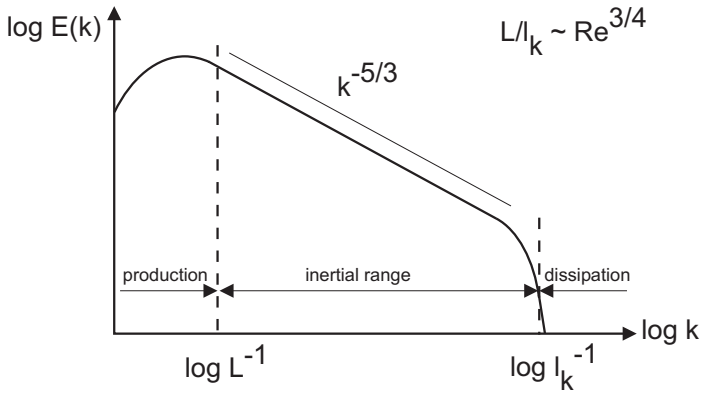

Figure 1.1: Energy spectrum $E(k)$ of a local homogenous and isotropic, fully developed turbulent flow.

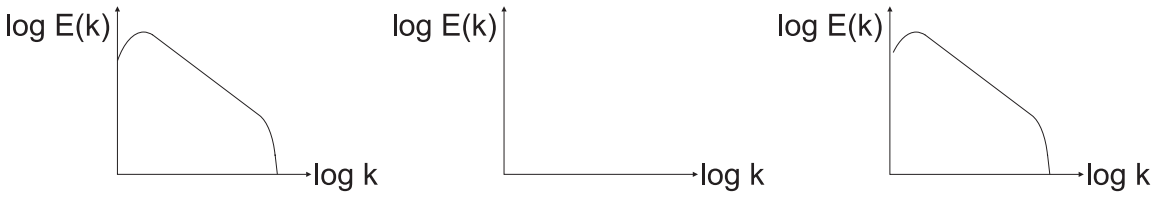

(a) total = (b) resolved + (c) modeled

Figure 1.2: Decomposition of the energy spectrum by Reynolds-Averaged Numerical Simulation (RANS).

estimate the costs for a DNS of a turbulent flow. The mesh size required for the spatial approximation increases with $\left(Re^{(3/4)}\right)^3$ due to the fact that a turbulent flow is always three-dimensional. Furthermore, the characteristic time scale decreases with increasing Re and the total cost for the simulation are actually proportional to $Re^{11/4}$. Current computers allow DNS for Re of the order of 10^4 which limits the range of possible applications. The limitation of DNS are obvious if one considers that most technical problems have Reynolds numbers several orders of magnitude larger than 10^4.

In most cases, the detailed information provided by DNS is not needed. Rather, the technically more relevant data such as mean velocities and temperature profiles, buoyancy and friction coefficients, and heat transfer are of interest; they can be more efficiently obtained by resorting to a statistical describtion. The theoretical basis for this description was laid by Osborne Reynolds in the 19th century. He proposed to decompose a turbulent quantity into a temporally averaged (ensemble averaged) and a fluctuating quantity which leads, when applied to the Navier-Stokes equations, to the Reynolds-Averaged Navier Stokes (RANS) formulation. Ensemble averaging introduces additional terms which must be closed with appropriate models. The advantage of solving for ensemble-averaged quantities are the relatively low computational costs of the simulation because small structures has not to be resolved. The splitting into an ensemble averaged and a fluctuating quantity is illustrated in Fig. 1.2. It is obvious that the whole energy spectrum has to be modelled.

The Large Eddy Simulation (LES) is an alternative to RANS where it is assumed that large turbulent scales are sensitive to large changes in the flow conditions (the nozzle geometry, for example), while the smaller scales have a more universal character independent of geometry. In LES, the large scales are explicitly computed while the small one are modelled. This decomposition is illustrated in Fig. 1.3. The large structures of

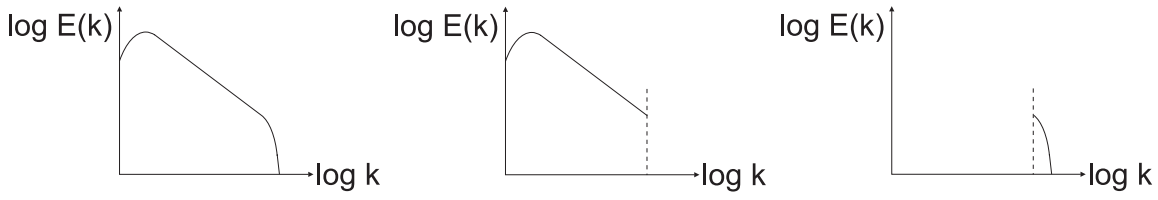

(a) total = (b) resolved + (c) modeled

Figure 1.3: Decomposition of the energy spectrum in the solution associated with the Large Eddy Simulation (LES).

the turbulent flow are resolved by the simulation while the residual fluctuation is supposed to represent the random part of turbulence by a turbulence model. The set of filtered Navier-Stokes equations include new additional terms, which have to be modelled by subgrid scale (SGS) models (see Section 2.3). The decomposition is supported by experimental evidence that shows that small-scale turbulence is often isotropic (Kraichnan [71]), but development of these notions into a numerical procedure entails many subtleties, not all of which have been fully resolved yet. A major difficulty is the lack of a rigorous separation between the large and small scales. Instead, the nonlinearities in the flow equations couple all scales, which makes modelling difficult. Often, LES is called the *happy medium* between DNS and RANS because of the computational time and the storage requirements. The interest in LES has increased significantly during the last years mainly due to the large increase of computational power. An overview of recent activities in LES can be found in [134, 26, 135, 49, 75, 78, 112].

The present works aims at developing a numerical tool for the LES of turbulent flows. A DNS code based on the spectral element method is coupled with the Approximate Deconvolution Model (ADM), presented in Section 2.3. The developed LES code was first tested with an incompressible, turbulent channel flow and mean velocity profiles, Reynolds stresses and the friction Reynolds numbers are investigated for $Re = 2,800$ and $Re = 10,935$ (Chapter 3). Further an incompressible, isothermal and turbulent jet flow for $Re = 2,000$ was simulated with the focus on mean and turbulent quantities in the scale-similarity range (Chapter 4). To extend the LES code for the simulation of variable density flows, a non-isothermal, turbulent jet flow for $Re = 2,000$ was investigated with LES. The focus also was the quantities in the scale-similarity range (Chapter 5).

Chapter 2

Basic Equations

The present work constitutes a first step towards the development of an LES code for turbulent, low speed, variable density and reactive flows. To this end the capabilities of a spectral element DNS code for low-Mach number compressible flows (Tomboulides et al. [128]) is extended for LES. In this Chapter, the equations for turbulent, single phase, single species and variable density LES are introduced; whereas their derivations are partially presented in Appendix A.
In Section 2.1, the basic equations for low-Mach number flows are discussed, and further modified to Favre-filtered equations for LES in Section 2.2. The Favre-filtered equations contain unclosed terms, which must be modeled using an SGS model. The Approximate Devonvolution Model (ADM), which is the SGS model used in this work, is introduced in Section 2.4, together with the set of equations used in the spectral element code.

2.1 Low-Mach Number Flows

The physical state of a single species, single phase and non-isothermal flow is described mathematically with the velocity $\underline{u}(\underline{x}, t)$ and two arbitrary thermodynamic quantities, (e.g. pressure $p(\underline{x}, t)$ and temperature $T(\underline{x}, t)$). For variable density flows, the Navier-Stokes equations, the mass conservation, the internal energy and the equation of state must be solved. In the numerical solution of low speed, compressible and reacting flows involved in combustion problems, the existence of high frequency acoustic waves places a severe restriction on the time step. Perturbation methods

(see Rehm and Baum [107]) are used to derive approximations, suitable for low-Mach number flows, where the thermodynamic pressure p is no longer a function of space and, as a consequence, acoustic waves are eliminated. Instead of the thermodynamic pressure, the hydrodynamic pressure $p_2(t)$ appears in the momentum equation (see Appendix B). The equations are formulated for an open system, where the thermodynamic pressure will be constant and the normalized pressure therefore becomes unity. The energy equation consists of only the sensible enthalpy (see Appendix A) and the system of non-dimensional equations for low-Mach number, non-reactive, open flows can be written as

$$\frac{\partial \rho}{\partial t} + \nabla \cdot (\rho \underline{u}) = 0 \tag{2.1}$$

$$\begin{aligned} \rho\Big[\frac{\partial \underline{u}}{\partial t} + (\underline{u} \cdot \nabla)\underline{u}\Big] &= \left[\frac{\partial \rho \underline{u}}{\partial t} + \nabla \cdot (\rho \underline{u}\ \underline{u})\right] \\ &= -\nabla p_2 + \frac{1}{Re}\nabla \cdot (\mu \underline{\underline{S}}) + \frac{1}{Fr^2}\rho \underline{e}_g \end{aligned} \tag{2.2}$$

$$\rho c_p^a \frac{DT}{Dt} = \frac{1}{RePr}\nabla \cdot \Big[\lambda(\nabla T)\Big] \tag{2.3}$$

$$1 = \rho T\ , \tag{2.4}$$

where $\underline{u} = \underline{u}(\underline{x}, t)$, $p_2 = p_2(\underline{x})$, $T(\underline{x}, t)$ and $\rho = \rho(T)$ are the mass-averaged velocity vector, the hydrodynamic pressure, the temperature and the density, respectively. The quantities $\mu(T)$, $c_p^a(T)$ and $\lambda(T)$ denote the dynamic viscosity, the average heat capacity at constant pressure and the thermal diffusivity, respectively, and $\underline{e}_g$ is a unit vector in the direction of gravity. The non-dimensional numbers Re, Fr and Pr are the Reynolds, Froude and Prandtl number, respectively, $\underline{\underline{S}}$ is the stress tensor and D/Dt the material derivative, defined as

$$Re = \frac{u_\infty L_\infty \rho_\infty}{\mu_\infty} = \frac{u_\infty L_\infty}{\nu_\infty} \tag{2.5}$$

$$Fr = \frac{u_\infty}{\sqrt{g L_\infty}} \tag{2.6}$$

$$Pr = \frac{c_{p\infty}\mu_\infty}{\lambda_\infty} \tag{2.7}$$

$$\underline{\underline{S}} = \nabla \underline{u} + (\nabla \underline{u})^T - \frac{2}{3}(\nabla \cdot \underline{u})\underline{\underline{I}}\ , \tag{2.8}$$

with $\underline{\underline{I}}$ being the unit tensor and g the gravitational acceleration. The quantities subscribed by ∞ (e.g., the farfield or stagnation conditions

and a characteristic length scale L_∞) are used for non-dimensionalization.

The continuity, momentum and energy equations are coupled by the velocity and the density. Decoupling the velocity and the density simplifies the algorithm for their numerical solution (Tomboulides et al. [128]). The continuity equation can be rewritten as

$$\nabla \cdot \underline{u} = -\frac{1}{\rho}\left(\frac{\partial \rho}{\partial t} + \underline{u} \cdot (\nabla \rho)\right) = \frac{-1}{\rho}\frac{D\rho}{Dt} \ . \tag{2.9}$$

For variable-density flows the divergence of the velocity field is $\nabla \cdot \underline{u} \neq 0$ which is in contrast to incompressible flows. The right-hand side of the continuity equation for variable-density flows contains temporal derivatives which will be substituted through spatial derivatives with the help of the equation of state and the energy equation. The substitution starts by taking the logarithm of the equation of state Eq. (2.4)

$$ln(1) = ln(\rho) + ln(T) \ . \tag{2.10}$$

The substantial derivative then becomes

$$0 = \frac{D[ln(\rho)]}{Dt} + \frac{D[ln(T)]}{Dt} \tag{2.11}$$

so that

$$-\frac{1}{\rho}\frac{D\rho}{Dt} = \frac{1}{T}\frac{DT}{Dt} \tag{2.12}$$

and

$$\frac{-1}{\rho}\frac{D\rho}{Dt} = \frac{1}{T}\frac{DT}{Dt} = \frac{1}{T}\Big(\frac{\partial T}{\partial t} + \underline{u} \cdot \nabla T\Big) \ . \tag{2.13}$$

Eqs. (2.13) and (2.3) can be substituted in the continuity equation (Eq. (2.9)) resulting in

$$\nabla \cdot \underline{u} \quad = \quad \frac{1}{T\rho c_p^a}\left\{\frac{1}{RePr}\nabla \cdot [\lambda(\nabla T)]\right\} \ . \tag{2.14}$$

The expression on the right-hand side of Eq. (2.14) allows the calculation of the divergence of the velocity field by only spatial derivatives.
The set of equations, derived above, is implemented in the spectral element code and used for the DNS in this work. They can be summarized as

$$\rho c_p^a \frac{DT}{Dt} \quad = \quad \frac{1}{RePr}\nabla \cdot \Big[\lambda(\nabla T)\Big] \tag{2.15}$$

$$\nabla \cdot \underline{u} = \frac{1}{T\rho c_p^a}\left\{\frac{1}{RePr}\nabla\cdot[\lambda(\nabla T)]\right\} \tag{2.16}$$

$$\rho\Big[\frac{\partial \underline{u}}{\partial t} + (\underline{u}\cdot\nabla)\underline{u}\Big] = \left[\frac{\partial \rho\underline{u}}{\partial t} + \nabla\cdot(\rho\underline{u}\ \underline{u})\right]$$

$$= -\nabla p_2 + \frac{1}{Re}\nabla\cdot(\mu\underline{\underline{S}}) + \frac{1}{Fr^2}\rho\underline{e}_g \tag{2.17}$$

$$1 = \rho T\ , \tag{2.18}$$

where only a single species fluid is considered.

2.2 Favre-Filtered Equations

Turbulent motion is a random and irregular process containing a broad range of length scales. For the solution of three-dimensional, time-dependent problems, a tremendous amount of computational recourses is necessary at high Re. The Large Eddy Simulation method (LES) with filtered quantities can reduce this high computational costs. Instead of solving for the whole range of turbulent scales, LES solves for the large scales, and models the subgrid scales. The filtered conservation equations can be obtained by applying a spatial filtering procedure to Eqs. (2.15) - (2.18). However, most experimental results for variable density flows are based on mass-weighted quantities rather than filtered quantities. Applying filtering in combination with mass weighting to Eqs. (2.15) to (2.18), the resulting equations are of simpler form (Favre-filtered equations). For variable-density flows, Favre-filtered values have the advantage of providing equations in a form similar to that known in an unfiltered situation. The mass-weighted (or Favre-filtered) quantity is defined as

$$\widetilde{\Phi} \equiv \frac{\overline{\Phi\rho}}{\overline{\rho}}\ , \tag{2.19}$$

where Φ is any variable of interest, and the overbar and tilde denote spatial filtering and Favre-filtering, respectively. Favre-filtering of Eqs. (2.15) to (2.18) is performed in combination with the decoupling of the velocity and the temperature, which results in a set of Favre-filtered equations. The temperature field is solved first and then used for the determination of the velocity divergence of the continuity equation. The equation of state, Eq. (2.18), can be written in Favre-filtered form in combination with Eq. (2.19) as

$$1 = \overline{\rho}\widetilde{T}\ . \tag{2.20}$$

Similarly, the energy equation, Eq. (2.15), becomes

$$c_p^a\overline{\rho}\left(\frac{\partial\widetilde{T}}{\partial t}+\underline{u}\cdot\widetilde{(\nabla T)}\right) = \frac{1}{RePr}\nabla\cdot\left[\widetilde{\lambda}(\nabla\widetilde{T})\right]+ + \frac{1}{RePr}\nabla\cdot\left[\overline{\lambda(\nabla T)}-\widetilde{\lambda}(\nabla\widetilde{T})\right]. \quad (2.21)$$

Often the term $\overline{\lambda(\nabla T)}-\widetilde{\lambda}(\nabla\widetilde{T})$ is neglected as it is expected to be smaller than other SGS-terms (see Vreman [137]), resulting in the Favre-filtered energy equation

$$c_p^a\overline{\rho}\left(\frac{\partial\widetilde{T}}{\partial t}+\underline{u}\cdot\widetilde{(\nabla T)}\right)=\frac{1}{RePr}\nabla\cdot\left[\widetilde{\lambda}(\nabla\widetilde{T})\right]. \quad (2.22)$$

The procedure for decoupling the momentum from the energy equation starts with Favre-filtering of the continuity equation, Eq. (2.9),

$$\nabla\cdot\widetilde{\underline{u}}=-\frac{1}{\overline{\rho}}\left(\frac{\partial\overline{\rho}}{\partial t}+\widetilde{\underline{u}}\cdot(\nabla\overline{\rho})\right)=\frac{-1}{\overline{\rho}}\frac{\widetilde{D}\overline{\rho}}{Dt}, \quad (2.23)$$

where $\widetilde{D}/Dt$ is the material derivative using the Favre-filtered velocity for the convective term. Taking the logarithm of Eq. (2.20),

$$ln(1)=ln(\overline{\rho})+ln(\widetilde{T}) \quad (2.24)$$

whose substantial derivative is

$$0=\frac{D[ln(\overline{\rho})]}{Dt}+\frac{D[ln(\widetilde{T})]}{Dt} \quad (2.25)$$

so that

$$-\frac{1}{\overline{\rho}}\frac{D\overline{\rho}}{Dt}=\frac{1}{\widetilde{T}}\frac{D\widetilde{T}}{Dt} \quad (2.26)$$

and

$$\frac{-1}{\widetilde{\rho}}\frac{\widetilde{D}\overline{\rho}}{Dt}=\frac{1}{\widetilde{T}}\frac{\widetilde{D}\widetilde{T}}{Dt}=\frac{1}{\widetilde{T}}\left(\frac{\partial\widetilde{T}}{\partial t}+\widetilde{\underline{u}}\cdot\nabla\widetilde{T}\right). \quad (2.27)$$

Eqs. (2.23), (2.27) and (2.22) are substituted into the Favre-filtered continuity equation to obtain

$$\nabla\cdot\widetilde{\underline{u}} = \frac{1}{\widetilde{T}\overline{\rho}c_p^a}\left\{\frac{1}{RePr}\nabla\cdot[\widetilde{\lambda}(\nabla\widetilde{T})]+\overline{\rho}c_p^a\left(\widetilde{\underline{u}}\cdot\nabla\widetilde{T}-\widetilde{\underline{u}\cdot\nabla T}\right)\right\} \quad (2.28)$$

The expression on the right-hand side of Eq. (2.28) allows the calculation of the velocity divergence by only spatial derivatives. The momentum equation, Eq. (2.17), can be written in Favre-filtered form as

$$\overline{\rho}\left[\frac{\partial\widetilde{\underline{u}}}{\partial t}+\widetilde{(\underline{u}\cdot\nabla)\underline{u}}\right]+\nabla\overline{p}_2=\frac{1}{Re}\nabla\cdot(\tilde{\mu}\tilde{\underline{\underline{S}}})+\frac{1}{Re}\nabla\cdot(\overline{\mu\underline{\underline{S}}}-\tilde{\mu}\tilde{\underline{\underline{S}}})+\frac{1}{Fr^2}\overline{\rho}\underline{e}_g\ . \quad (2.29)$$

The term $\nabla\cdot(\overline{\mu\underline{\underline{S}}}-\tilde{\mu}\tilde{\underline{\underline{S}}})$ is neglected according to [137], leading to the Favre-filtered momentum equation

$$\overline{\rho}\left[\frac{\partial\widetilde{\underline{u}}}{\partial t}+\widetilde{(\underline{u}\cdot\nabla)\underline{u}}\right]+\nabla\overline{p}_2=\frac{1}{Re}\nabla\cdot(\tilde{\mu}\tilde{\underline{\underline{S}}})+\frac{1}{Fr^2}\overline{\rho}\underline{e}_g \quad (2.30)$$

with

$$\widetilde{\underline{\underline{S}}}=\nabla\widetilde{\underline{u}}+(\nabla\widetilde{\underline{u}})^T-\frac{2}{3}(\nabla\cdot\widetilde{\underline{u}})\underline{\underline{I}}\ . \quad (2.31)$$

The set of Favre-filtered equations are then

$$c_p^a\overline{\rho}\left(\frac{\partial\widetilde{T}}{\partial t}+\underline{u}\cdot\widetilde{(\nabla T)}\right)=\frac{1}{RePr}\nabla\cdot\left[\widetilde{\lambda}(\nabla\widetilde{T})\right] \quad (2.32)$$

$$\nabla\cdot\widetilde{\underline{u}} \;=\; \frac{1}{\widetilde{T}\overline{\rho}c_p^a}\left\{\frac{1}{RePr}\nabla\cdot[\widetilde{\lambda}(\nabla\widetilde{T})]+\overline{\rho}c_p^a\left(\widetilde{\underline{u}}\cdot\nabla\widetilde{T}-\widetilde{\underline{u}\cdot\nabla T}\right)\right\} \quad (2.33)$$

$$\overline{\rho}\left[\frac{\partial\widetilde{\underline{u}}}{\partial t}+\widetilde{(\underline{u}\cdot\nabla)\underline{u}}\right]+\nabla\overline{p}_2=\frac{1}{Re}\nabla\cdot(\tilde{\mu}\tilde{\underline{\underline{S}}})+\frac{1}{Fr^2}\overline{\rho}\underline{e}_g \quad (2.34)$$

$$1=\overline{\rho}\widetilde{T}\ . \quad (2.35)$$

There is no equation for the hydrodynamic pressure p_2 in the momentum equation. This pressure p_2 is used in the numerical algorithm as a Lagrange parameter to satisfy the continuity equation. The convective terms in Eqs. (2.32) to (2.34) are unclosed and are modelled by using an SGS model. An overview of the most important subgrid models is given in Section 2.3 whereas the subgrid model employed in this work, the Approximative Deconvolution Model (ADM), is introduced in Section 2.4.

2.3 Subgrid-Scale Models for LES

Subgrid-scale models for LES of turbulent flows fall into two general categories: The eddy-viscosity concept and the inverse concept models. The two categories are discussed in the following.

2.3.1 Eddy-Viscosity Concept

Since the first days of LES, the Samagorinsky model (Smagorinsky [117], Rogallo and Moin [111]) is the most popular SGS model for LES. For the turbulent momentum transport, proportionality, expressed by the eddy viscosity, between the SGS and the strain-rate tensor is assumed. From the point of dimensional analysis, the eddy viscosity can be written as a product of a characteristic length and a characteristic velocity scale. The main problem reduces then to the determination of these characteristic quantities. The classical Smagorinsky model prescribes them as the mesh size and the filtered rate of strain $\underline{\underline{S}}$, and introduces the Smagorinsky constant C_S as a tuning parameter. Eddy-viscosity concepts are very popular because of their robustness and the simple implementation in numerical codes. However, eddy-viscosity concepts have some serious drawbacks: The eddy viscosity is drastically underestimated in flows with steep velocity gradients which have a non-negligible influence on the transition to turbulence (Vreman [136]). Wall-bounded shear flows need special treatment near the walls (Van Driest [131] Horiuti [63]). Furthermore, turbulent structures are not reproduced properly which is reflected in poor correlations between the results of the Smagorinsky model and the actual turbulent stress (Liu et al. [80], Domaradzki and Yee [39]). Chollet [25] formulated an eddy-viscosity model in spectral space based on homogeneous isotropic turbulence. The method is well suited for use in spectral space but must be transformed to physical space for consideration in practical problems with complex geometries. The model in physical space is called structure-function model and shows good results for isotropic turbulence and shear flows (Metais and Lesieur [86]). However, for wall-bounded flows the structure-function model, in contrast to the Smagorinsky model (Ducros et al. [42]), is too dissipative leading to incorrect asymptotic near-wall behavior. These deficiencies of the model can be improved by different modifications (Lesieur and Metais [78], Ducros et al. [42]).
The correct determination of the flow-regime-dependent constant C_S is one of the most significant problems of the classical Smagorinsky model. Dynamic models [52, 79, 56, 85] offer the option for a time- and space dependent identification of C_S. These models determine C_S by applying dif-

ferent filtering operations and leads to two problems: An over-determined system of equations which is contracted by a least-square approach of Lilly [79] to minimize the residual of resolved and modelled SGS stresses, as well as a strong fluctuation of C_S which must be damped by averaging in homogeneous directions. The assignment of a dynamic model leads to significant improvements of the near-wall description (Germano et al. [52]). To avoid averaging in homogeneous directions, a localized-dynamic model (Ghosal et al. [56], Piomelli and Liu [100]) or the Lagrangian-dynamic model of Meneveau et al. [85], which was successfully used for turbulent flow simulations in an inhomogeneous, spark ignition cylinder (Haworth and Jansen [61]) can be used.

2.3.2 Inverse Model Concepts

The other class of models are based on inverse or deconvolution concepts. The idea behind the deconvolution model is shown on the right side of Fig. 2.1, while that of a *perfect* LES is shown on the left side. A perfect LES would require the DNS solution in the perfect model M and the definition of the specific filter L for the exact evaluation of the nonlinear terms. An approximate reconstruction of u, called the deconvolved solution $u^\star$, can be recovered to some degree from the filtered solution $\overline{u}$ through an approximate inversion of the filter operation G^{-1} (see Eq. (2.37)) and an appropriate model $M^\star$. This approach explicitly involves the specific filter and leads to generalized inverse-modelling concepts. A model which follows this idea is the subgrid-estimation model of Domaradzki and Siki [38] which has been adopted for turbulent channel flow simulations. Although the approach is theoretically appealing, the

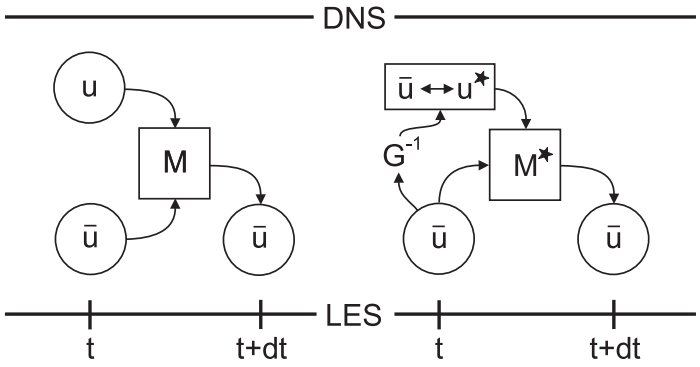

Figure 2.1: Definition of a perfect LES (left) and of the concept of inverse modelling (right) [54]. The reconstructed approximation $u^\star$ and the filtered solution are combined to yield a generalized scale similarity model $M^\star$.

implementation includes some ad hoc steps and parameters and the resolution must be fine enough, requiring a considerable computational effort and memory usage.
The filter inversion is the central part of inverse-model concepts: The polynomial expansion (Geurts [53]) and geometric series approximations (Adams and Stolz [2]) are the most appropriate approaches for any filter function. General inverse models are, in contrast to eddy-viscosity models, free of physical assumptions and the SGS tensor tends asymptotically to the exact solution as the filter length goes to zero (Domaradzki and Adams [40]). Recovering the unfiltered field can be performed accurately for length scales approximately equal to the filter length. Contributions from smaller scales cannot be recovered and additional physical information is required for modelling the full SGS tensor (Geurts [54]).
The most prominent member of this class is Bardina's scale-similarity model [12] using polynomial inversion (Geurts [53]). The more physical interpretation of the Bardina model is the SGS-tensor by neglecting the cross- and Reynolds stresses and using the Leonard stress only [103]. Bardina's model [12] applies the filter with only one filter length in contrast to Meneveau [84] which use two different filter lengths. The advantage, compared to the eddy-viscosity model, is the possibility of backscatter energy from the small to the large turbulent structures. A-priori tests of Meneveau [84] and Vreman [136] identified a better correlation for scale-similarity models than for eddy-viscosity models. However, scale similarity models underestimate the magnitude of the turbulent stress tensor contributions (Meneveau [84]). Further disadvantages are the inadequate energy transfer from the resolved to the unresolved scales, as well as the computational costs of implementing several explicit filtering operations, all of which make the Bardina model unattractive. An alternative approach, which avoids the computationally costly explicit filtering, is Clark's model [28] which expresses the SGS tensor as a Taylor expansion of derivatives keeping only the leading order term. The Clark model computes derivatives, which are numerically cheaper than explicit filtering operations. The inadequate energy transport of Bardina's model is an example of the challenge to recover subgrid information from the filtered field so that it can be combined with eddy viscosity concepts to compensate for the deficit of scant energy transport. The combinations of inverse and eddy-viscosity concepts are called dynamic mixed models, and were introduced by Zang et al. [146] and modified by Vreman et al. [138]. Dynamic mixed models are considered to be the best classical

models today [1].
Newer approaches are based on the high-order approximation of the inverse filter kernel [116, 53]. The Approximate Deconvolution Model (ADM) (Stolz and Adams [120]) expands the inverse filter in a power series of the filter operation and models the interaction between the resolved and unresolved scales using a high-pass filter. ADM is investigated by a-posteriori tests simulating incompressible, turbulent channel flows, compressible turbulent wall-bounded and jet flows [120, 122, 121, 108] and the agreement with DNS data is good, but has increased computational costs compared to standard inverse model concepts.

LES of passive scalars has relied largely on a simple gradient approximation to the subgrid scalar flux that introduces a turbulent Prandtl number. The value of the Prandtl number is either a specified model parameter (Horiuti [62]), or obtained via a dynamic procedure (Moin et al. [90]). The dynamic Prandtl number model has been used, for example by Askelvoll and Moin [9], as part of the simulation of two co-axial jets with fast combustion and by Vreman et al. [139] for the closure of the energy equation for the simulation of a temporally evolving compressible mixing layer. An alternative procedure for obtaining the subgrid scalar flux, a tensor-eddy diffusivity, given by modelled stretched-vortex dynamics, was introduced by Pullin [105]. LES of non-premixed turbulent reacting flows often requires models for the subgrid scalar variance in addition of the filtered scalar. Proposals for the modeling of subgrid scalar variance include a scalar-similarity model (Cook and Riley [30]), a gradient model [30] and a moment-based reconstruction of the scalar field (Pierce and Moin [98]). ADM has been used for the SGS tensor of the energy equation, and is considered as a universal model for the SGS tensors of all involved conservation equations.

2.4 The Approximate Deconvolution Model

In physical terms, subgrid scale models try to model the energy transfer from resolved to unresolved scales by providing expressions for the unclosed convection terms of Eqs. (2.32) to (2.34). ADM belongs to the class of scale similarity models, as discussed in Section 2.3, and starts with the definition of the filtering operation of a physical quantity Φ

$$\overline{\Phi}(x) = G * \Phi = \int_{x_2}^{x_1} G(x - x')\Phi(x')dx' \ , \tag{2.36}$$

where $G(\underline{x})$ is the filter function. In the context of the spectral element method, filtering is performed in polynomial space as described in Section 2.5.1. The approximate inverse-filter operator Q_{N_d} is defined as

$$Q_{N_d} = \sum_{\nu=0}^{N_d} (I - G)^{\nu} \approx G^{-1} \ , \tag{2.37}$$

where N_d and I denote the deconvolution order and the identity operator, respectively. The approximate inverse filter operator of Eq. (2.37) is used to approximate the subgrid scale field by

$$\Phi^{\star} = Q_{N_d} * \overline{\Phi} \approx \Phi \ , \tag{2.38}$$

where $\Phi^{\star}$ is the deconvolved field and is used to compute the unfiltered quantities in the unclosed convective terms of Eqs. (2.32) to (2.34).
In LES, the numerical resolution used to represent the filtered vector field $\overline{\underline{\Phi}}$ is much lower than required to represent the equivalent Navier-Stokes solution $\underline{\Phi}$. To show the influence of the mesh size on the SGS tensor, the velocity, as an example, is split into two terms

$$\underline{u} = \underline{u}^L + \underline{u}^S \ , \tag{2.39}$$

where $\underline{u}^L$ and $\underline{u}^S$ denote the resolved part and its complement, respectively. Expressing all variables in this form, the momentum equation, Eq. (2.34), as a representative equation, can then be rewritten according to Domaradzki and Adams [40] and neglecting the buoyancy term as

$$\overline{\rho}\left[\frac{\partial \widetilde{\underline{u}}^L}{\partial t} + (\widetilde{\underline{u}}^L \cdot \nabla)\widetilde{\underline{u}}^L\right] + \nabla \overline{p}_2^L = \frac{1}{Re}\nabla \cdot (\tilde{\mu}\tilde{\underline{\underline{S}}}^L) - \nabla \cdot \left(\underline{\underline{\tau}}^{rep} + \underline{\underline{\tau}}^{nrp}\right) \ , \tag{2.40}$$

where

$$\underline{\underline{\tau}}^{rep} = \tau_{ij}^{rep} = \widetilde{(u_i^L u_j^L)}^L - (\widetilde{u_i}^L \widetilde{u_j}^L)^L \ , \tag{2.41}$$

$$\underline{\underline{\tau}}^{nrp} = \tau_{ij}^{nrp} = \widetilde{(u_j^L u_j^S + u_i^S u_j^L + u_i^S u_j^S)}^L \ . \tag{2.42}$$

The SGS tensor consists of two terms: τ_{ij}^{rep} and τ_{ij}^{nrp}. The represented term τ_{ij}^{rep} has the form of a generalized similarity model and results from the nonlinear interaction among scales represented on a numerical grid. The non-represented term τ_{ij}^{nrp} accounts for the effects of nonlinear interaction involving scales which cannot be represented on a grid. With ADM (Stolz et al. [122]), the term τ_{ij}^{rep} is approximated with Eq. (2.38) and the non-represented term is modelled by the relaxation term

$$\underline{\underline{\tau}}_{ij}^{nrp} = -\chi(I - Q_N * G) * \widetilde{\underline{u}} \ . \tag{2.43}$$

The relaxation parameter χ has the dimension of inverse time and represents the timescale with which energy is annihilated by driving the Favre-filtered solution $\widetilde{\underline{u}}$ to the somewhat smoother solution $Q_N * G * \widetilde{\underline{u}}$, where $Q_N * G$ is a secondary filter with significantly larger cutoff scale than the primary filter G. Stolz et al. [122] use a dynamic procedure for the determination of χ based on the calculation of a structure function. In the present work, χ is considered to be constant in time and space.

The Favre-filtered version of Eqs. (2.32) to (2.35), in combination with ADM and the assumptions, that $\check{\lambda} = \lambda_\infty$, $\check{\nu} = \nu_\infty$ and $\check{c}_p^a = c_{p\infty}^a$ ($\check{\phi}$ are non-dimensional quantities and ϕ_∞ the farfield conditions) lead to

$$\begin{aligned} \overline{\rho}\left[\frac{\partial \widetilde{T}}{\partial t} + \underline{u}^\star \cdot \widetilde{(\nabla T^\star)}\right] &= \frac{1}{RePr}\nabla^2 \widetilde{T} - \\ &- \overline{\rho}\chi_T (I - Q_N * G) * \widetilde{T} \ , \end{aligned} \tag{2.44}$$

$$\begin{aligned} \nabla \cdot \widetilde{\underline{u}} &= \frac{1}{\overline{\rho}\widetilde{T}}\left\{ \frac{1}{RePr}\nabla^2 \cdot \widetilde{T} - \overline{\rho}\chi_T (I - Q_N * G) * \widetilde{T} + \right. \\ &+ \left. \overline{\rho} c_p^a \left[\widetilde{\underline{u}} \cdot (\nabla \widetilde{T}) - \underline{u}^\star \cdot \widetilde{(\nabla T^\star)}\right] \right\} , \end{aligned} \tag{2.45}$$

$$\begin{aligned} \overline{\rho}\Big[\frac{\partial \widetilde{\underline{u}}}{\partial t} + (\underline{u}^\star \cdot \widetilde{\nabla})\underline{u}^\star)\Big] + \nabla \overline{p}_2 &= \frac{1}{Re}\nabla \cdot \tilde{\underline{\underline{S}}} - \\ &- \overline{\rho}\chi_u (I - Q_N * G) * \widetilde{\underline{u}} \end{aligned} \tag{2.46}$$

with

$$\widetilde{\underline{\underline{S}}} = \nabla \widetilde{\underline{u}} + (\nabla \widetilde{\underline{u}})^T - \frac{2}{3}(\nabla \cdot \widetilde{\underline{u}})\underline{\underline{I}} \tag{2.47}$$

$$1 = \overline{\rho}\widetilde{T} \ , \tag{2.48}$$

which is implemented in the spectral element code and used in this work for the LES of turbulent flows. Depending on the system under consideration, additional assumptions are made and discussed separately in Chapter 3 for the incompressible turbulent channel flow, Chapter 4 for the isothermal turbulent jet and Chapter 5 for the non-isothermal turbulent jet.

2.5 ADM and the Spectral Element Code

The numerical code, used in this work employs as a basis the spectral element approach. The code was originally developed by Paul Fischer for DNS [45]. The DNS code was later extended by Illiescu et al. [65] for LES in combination with the classical Smagorinsky model for the simulation of turbulent channel flows. This work presents the first implementation of ADM in a spectral element code. Further Bouffanais et al. [17] proposed an LES of a lid-driven cubic cavity flow, using the dynamic Smagorinsky model.
The implementation of ADM in the DNS code is explained in the following.

2.5.1 Temporal Discretization

The temporal discretization is based on a second-order, operator-splitting formulation for low speed, variable density flows. The code uses scalable, domain-decomposition based iterative solvers with efficient preconditioners. The parallel implementation is based on the standard message passing Single Program Multiple Data (SPMD) mode, where contiguous groups of elements are distributed to processors and the computation proceeds in a loosely synchronous manner; communication is based on the message-passing interface (MPI) standard [44, 128, 36]. The code exhibits very good parallel efficiency and scalability properties on distributed-memory platforms.
A Spectral Element filter (SE-filter) can be used for the stabilization of turbulent flow simulations (Fischer and Mullen [46], Boyd [18]). The SE-filter is a low-pass filter and is applied on each field to eliminate high-order fluctuations. The filter function in the polynomial space show in Fig. 2.2, is almost rectangular and affects only the highest polynomial order N_s by a magnitude of 5%. Fischer et al. [46] showed that filtering the highest polynomial order stabilizes the computation of turbulent flows and flows containing high gradients (for example steep velocity profiles).

2.5.2 Spatial Discretization

Equations (2.44) - (2.48) are discretized in space using spectral elements. The computational domain is broken into general hexahedrals, which are mapped to unit squares cubes in 2- and 3-D, respectively. The data are then expressed in terms of Lagrangian polynomials of order N_s and evaluated at the nodes x_j. The approximation of a one-dimensional function

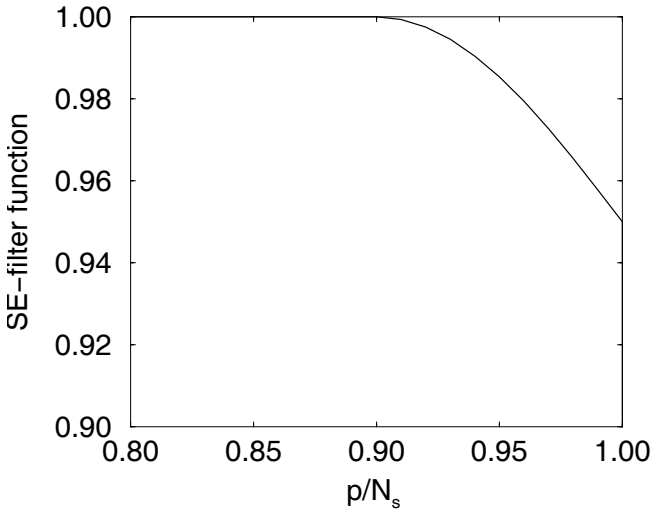

Figure 2.2: The almost rectangular filter function of the SE-filter . The filter modifies only the highest polynomial order N_s by 5%.

$\Phi(x)$ is

$$\Phi(x) = \sum_{j=0}^{N_s} \phi_j h_j(x) \tag{2.49}$$

with

$$h_j(x) = \prod_{k=0,k\neq j}^{N_s+1} \frac{x - x_k}{x_j - x_k} \ , \tag{2.50}$$

evaluated at the nodes x_j, defined as the roots of the derivatives of the Legendre polynomial L_n $(0 \leq n \leq N_s)$

$$\frac{dL_n(x_j)}{dx} = 0 \ . \tag{2.51}$$

The Legendre polynomials can be defined recursively as

$$L_n(x) \begin{cases} 1 & \text{if } n = 0 \\ x & \text{if } n = 1 \\ \frac{1}{n}\Big[(2n)xL_{n-1}(x) - (n-1)L_{n-2}(x)\Big] & \text{if } n > 2 \end{cases}$$

for $j = 0, ..., N_s$ (see for example Schwarz [115]).
In a fully implicit solution of the nonlinear system all variables have to be evaluated at the new time level t^{n+1}. The fully implicit approach is quite expensive and a combined implicit/explicit formulation is preferable for temporal discretization. All terms in equations (2.44) and (2.45) are

advanced in time explicitly except for the viscous and the pressure terms. Therefore the integration can be performed with a semi-implicit splitting method, where the updated temperature field is used to compute density, from Eq. (2.48), and divergence of the velocity field from Eq. (2.45). The integration then proceeds in the following way. First the energy equation is integrated with a J^{th} order scheme for fixed velocity fields

$$\frac{\overline{\rho}^n}{\Delta t}\Big(\sum_{q=0}^{J}\alpha_q\widetilde{T}^{n+1-q}\Big) = \frac{1}{RePr}\nabla^2\widetilde{T}^{n+1} - \\ -\overline{\rho}^n\sum_{q=0}^{J}\beta_q\Big[\chi_T(I-Q_N*G)*\widetilde{T} + \underline{u}^\star\cdot\widetilde{(\nabla T^\star)}\Big]^{n-q} \tag{2.52}$$

Then, density $1=\overline{\rho}^{n+1}\widetilde{T}^{n+1}$ and *thermal* divergence, Q_T, are computed

$$Q_T^{n+1} = \frac{1}{[\overline{\rho}\widetilde{T}]^{n+1}}\Bigg\{\frac{1}{RePr}\nabla^2\cdot\widetilde{T}^{n+1} - \overline{\rho}^{n+1}\chi_T(I-Q_N*G)*\widetilde{T}^{n+1} + \\ + \overline{\rho}^{n+1}\Big[\widetilde{\underline{u}}^n\cdot(\nabla\widetilde{T}^{n+1}) - [\underline{u}^\star]^n\cdot\widetilde{(\nabla[T^\star]^{n+1})}\Big]\Bigg\}. \tag{2.53}$$

Finally, using the updated density field and Q_T,

$$\frac{\overline{\rho}^{n+1}}{\Delta t}\Big(\sum_{q=0}^{J}\alpha_q\widetilde{\underline{u}}^{n+1-q}\Big) = \frac{1}{Re}\nabla\widetilde{\underline{\underline{S}}}^{n+1} - \nabla\overline{p}_2^{n+1} - \\ -\overline{\rho}^n\sum_{q=0}^{J}\beta_q\Big[\chi_u(I-Q_N*G)*\widetilde{\underline{u}} + \widetilde{(\underline{u}^\star\cdot\nabla)}\underline{u}^\star\Big]^{n-q}. \tag{2.54}$$

Here, Q_T^{n+1} is the *thermal* divergence of the velocity field, and α_q, β_q are the coefficients of the implicit and explicit, respectively, part of the Jth order integration scheme (Orszag et al. [94], Karniadakis et al. [66], Tomboulides et al. [127]).

After determining the temperature $\widetilde{T}^{n+1}$ at the new time level t^{n+1} the density ρ, which is only a function of $\widetilde{T}^{n+1}$ can be computed. The integration of Eqs. (2.53), and (2.54) is therefore performed using a mixed explicte-implicit splitting approach which results in an overall high-order scheme in time, minimal errors in mass conservation, and a partially decoupled solution procedure (see Tomboulides et al. [128]).

The central part of ADM is the explicit filtering. It characterizes the

cutoff-polynomial order κ_{ct}, the inversion of the filter function, and the inverse filtering. In the following Section, the implementation of ADM in the code is explained, the inverse filtering is investigated and the LES-filter function is determined.

2.5.3 Implementation of the ADM

The explicit spatial filtering process plays a central role in ADM and is in this work performed in polynomial space as a low pass-filter. The LES filter is a one-dimensional operator similar to the one used by Stolz et al. [122] defined as

$$G\Big(\frac{\kappa}{N_s},\kappa_{ct}\Big)=\begin{cases}1 & \text{if } \frac{\kappa}{N_s}\leq 2\kappa_{ct}-1\\ \frac{1}{2}\left[1+\cos\left(\frac{\pi\left(\frac{\kappa}{N_s}-1\right)}{2(1-\kappa_{ct})}+\pi\right)\right] & \text{otherwise}\\ 0 & \text{if } \frac{\kappa}{N_s}>1\end{cases} \tag{2.55}$$

where κ is the polynomial order, N_s its maximum of the spatial discretization (see Section 2.5.1) and $0<\kappa_{ct}<1$ the cutoff-polynomial order, respectively. For a three-dimensional flow, filtering is applied in each spatial direction. The filter function for $\kappa_{ct}=0.7$ is shown in Fig. 2.3. The cutoff scale κ_{ct} is defined as

$$G(\kappa/N_s=\kappa_{ct})=\frac{1}{2}\ . \tag{2.56}$$

The determination of the cutoff scale κ_{ct} for the LES is discussed in Section 3.2.1. The main issues of filtering in spectral space are related to the global and elemental boundary conditions. Spectral element codes split the global domain into a number of spectral elements. Each spectral element is filtered separately, which changes each element's boundary values independently from the other elements. After filtering, it is necessary to ensure that the global boundary conditions are fulfilled and that the values at the elemental boundaries of adjacent elements are identical. These constraints can be satisfied either by first filtering and then correcting the boundary conditions by a direct-stiffness summation, where the different values at the same discrete points of neighboring elements are smoothed (defined in this work as filtering in Legendre space), or by filtering each spectral element without modifying the values at the boundaries (defined in this work as filtering in Boyd space). Both filters are presented in Section 2.5.4.

Besides the filtering process, a further crucial point is the filter-function inversion which is performed as by Stolz and Adams [120]

$$\begin{aligned} \underline{u}^{\star} = Q_N * \underline{\bar{u}} &= \underline{\bar{u}} + (\underline{\bar{u}} - \underline{\bar{\bar{u}}}) + (\underline{\bar{u}} - 2\underline{\bar{\bar{u}}} + \underline{\bar{\bar{\bar{u}}}}) + ... \\ &= 3\underline{\bar{u}} - 3\underline{\bar{\bar{u}}} + \underline{\bar{\bar{\bar{u}}}} + ... \ . \end{aligned} \tag{2.57}$$

The explicit filtering procedure allows the subdivision of length scales in three parts: the resolved region, where the length scales are fully resolved; the represented region, where the computational grid has the ability to represent the length scales; and the subgrid scale. The interaction between represented and subgrid scales has to be modelled by a subgrid model. The resolved, the represented and the subgrid scales are separated by the cutoff scale κ_{ct} and the minimum grid spacing $\kappa/N_s = 1.0$, respectively. The

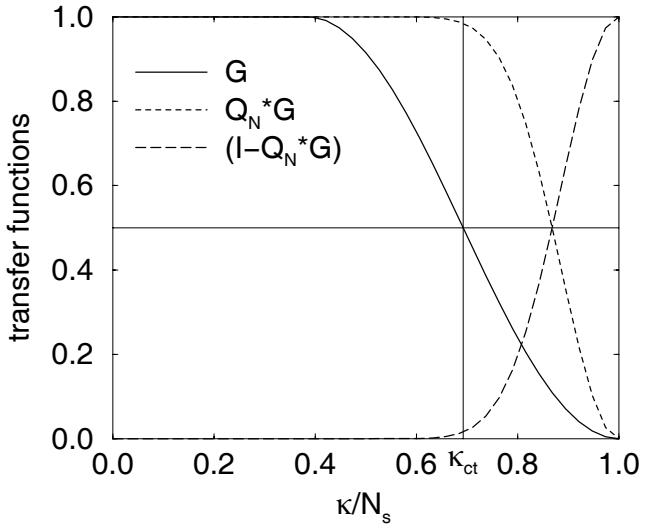

Figure 2.3: Transfer functions of the filter (G), the imperfect identity ($Q_N * G$) and the high-pass filter for the relaxation term ($I - (Q_N * G)$) for $\kappa_{ct} = 0.7$.

idea of the ADM-based LES is to accurately capture the resolved region up to the cutoff scale κ_{ct}. As a consequence, Q_{N_d} with an appropriate deconvolution order N_d should reproduce perfectly the deconvolved field from the filtered field up to the cutoff scale κ_{ct} (or the filter inversion Q_{N_d} should be perfect up to κ_{ct}). The effect of N_d on the deconvolved field in spectral space is qualitatively illustrated in Fig. 2.4 (a). As N_d is increased, the deconvolved transfer function ($Q_{N_d} * (G * u)$) reduces the inversion error Δ_d, defined in Fig. 2.4 (a) as the difference between the function of $Q_N * G$ and one at $\kappa/N_s = \kappa_{ct}$. According to Fig. 2.4 (b), the error Δ_d for different N_d decreases as 2^{1-N_d} and depends weakly on the cutoff scale κ_{ct}. A deconvolution order of $N_d = 5$ will be used for the

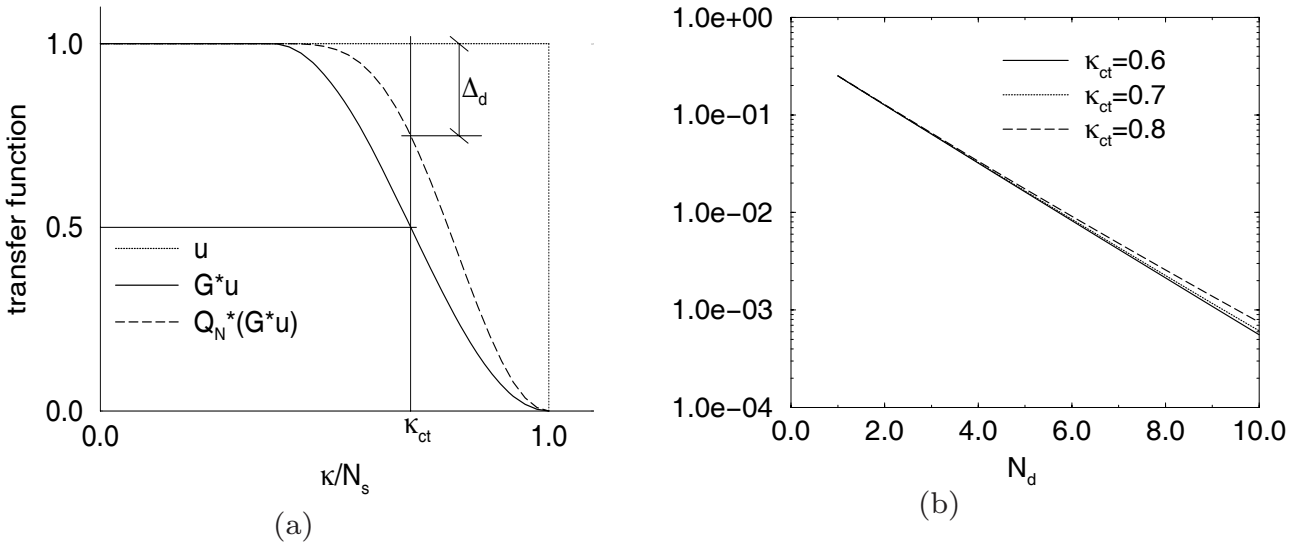

Figure 2.4: Definition of the inversion error Δ_d. (a) The deconvolution order N_d on the inversion error Δ_d and (b) Influence of the inversion error Δ_d as a function of N_d and κ_{ct}.

simulations in the present work, which has an inversion error of the order of 1% .

2.5.4 Filtering Procedure

The Legendre and Boyd filters, two different filtering approaches for spectral element codes, were briefly introduced in the previous Section. The topic of this Section is the detailed description and the investigation of the two filtering approaches. In contrast to global spectral codes, where the whole domain is filtered by one filtering procedure, in spectral element codes each element is filtered separately. This means that the filter width is not constant in physical space but adapted to the dimension of each spectral element.
With the Legendre filter the spectral element including the elemental boundary is filtered as well whereas the Boyd filter does not affect elemental boundaries. Direct-stiffness summation is needed to smooth the values at the elemental boundaries when the Legendre filter is used, while the Boyd filter does not require any special treatment.

Legendre filter

In the spectral element code the value of a function $u(x)$ at the collocation point x_i in terms of the Legendre-Lagrangian interpolants $h_j(x)$ are

written as

$$u(x_i) = \sum_{j=0}^{N_s} \grave{u}_j h_j(x_i) = u_i \ , \tag{2.58}$$

where $\grave{u}_j$, h_j and x_i are the j^{th} coefficient of the expansion, the Lagrangian polynomial of order j (see for example Schwarz [115]) and the Gauss-Lobatto collocation points (see for example Canuto et al. [21]), respectively. It is unfavorable to filter Eq. (2.58) directly because the values of the coefficients $\grave{u}_j$ do not decrease with increasing order j (an inherent property of Lagrangian polynomials). This can be achieved by using Legendre polynomials instead of Lagrange polynomials:

$$u(x_i) = \underline{u} = \sum_{j=0}^{N_s} \acute{u}_j L_j(x_i) = \underline{\underline{L}}\ \underline{\acute{u}} \ , \tag{2.59}$$

where L_j is defined as the j^{th} Legendre polynomial defined in Section 2.5.2 and $\acute{u}_j$ are the corresponding coefficients. The filter operation is defined by a diagonal matrix $\underline{\underline{D}}_F$ which acts on all coefficients $\acute{u}_j$ during filtering and therefor also modifies the solution at the elemental boundaries. The filtered vector $\underline{\acute{u}}$ can then be written as

$$\bar{\underline{\acute{u}}} = \underline{\underline{D}}_F \underline{\acute{u}} \ . \tag{2.60}$$

Filtering Eq. (2.59) leads to

$$\bar{u}(x_i) = \bar{\underline{u}} = \underline{\underline{L}}\ \bar{\underline{\acute{u}}} \tag{2.61}$$

which can be combined with Eq. (2.60) to

$$\bar{\underline{u}} = \underline{\underline{L}}\ \underline{\underline{D}}_F \underline{\acute{u}} \tag{2.62}$$

and with Eq. (2.59) to

$$\bar{\underline{u}} = \underline{\underline{L}}\ \underline{\underline{D}}_F \underline{\underline{L}}^{-1} \underline{u} \ . \tag{2.63}$$

Eq. (2.63) is the filtering operation implemented in the code. The diagonal elements of $\underline{\underline{D}}_F$ correspond to the discrete values of $G(\kappa/N_s)$, defined in Eq. (2.55). After filtering, the elemental boundaries are smoothed using a direct-stiffness summation, such that the values at the common boundaries of neighboring elements become equal (see Deville et al. [36]).

Boyd Filter

Another option is to perform filtering in a space where the element boundaries are not influenced, thus avoiding the direct-stiffness summation. Such a space is, for example, the Boyd space (see Boyd [18]), where $u(x_i)$ can be written in terms of new basis functions $\xi_j(x)$, which individually satisfy homogenous boundary conditions.
Consider for example, Dirichlet boundary conditions,

$$\begin{aligned} u(-1) &= \alpha \\ u(1) &= \beta \ . \end{aligned} \tag{2.64}$$

If the (new) basis functions $\xi_j(x)$ are choosen to satisfy homogenous Dirichlet-boundrary conditions, i.e. $\xi_j(\pm 1) = 0$, then

$$u(x) = \frac{\alpha+\beta}{2} + \frac{\beta-\alpha}{2}x + \sum_{j=2}^{N_s} \breve{u}_j \xi_j(x) \ . \tag{2.65}$$

The Boyd basis-functions $\xi_j(x)$ are defined as

$$\xi_j(x) = \begin{cases} L_0(x) & \text{if } j = 0 \\ L_1(x) & \text{if } j = 1 \\ L_j(x) - L_{j-2}(x) & \text{if } j > 1 \end{cases} , \tag{2.66}$$

where L_j is the Legendre polynomial of order j, defined in Section 2.5.2. At each node x_i, Eq. (2.65) can be written as

$$\begin{aligned} u(x_i) &= \frac{\alpha+\beta}{2} + \frac{\beta-\alpha}{2}x_i + \sum_{j=2}^{N_s} \breve{u}_j \xi_j(x_i) \\ &= \frac{\alpha+\beta}{2} + \frac{\beta-\alpha}{2}x_i + \sum_{j=2}^{N_s} \breve{u}_j \xi_{ij} \\ &= \frac{\alpha+\beta}{2} + \frac{\beta-\alpha}{2}x_i + \underline{\underline{\Xi}}\ \underline{\breve{u}} \ , \end{aligned} \tag{2.67}$$

with the transformation matrix $\underline{\underline{\Xi}} = \xi_{ij} = \xi_j(x_i)$. Filtering in the Boyd space is then performed by

$$\underline{\bar{u}} = \frac{\alpha+\beta}{2} + \frac{\beta-\alpha}{2}x + \underline{\underline{\Xi}}\ \underline{\underline{D}}_F \underline{\underline{\Xi}}^{-1} \underline{u} \ , \tag{2.68}$$

which results in the elemental boundary points remaining unaffected.

Chapter 3

Turbulent Channel Flow

In contrast to the free shear flows considered in Chapter 4 and 5, most technical, turbulent flows are bounded (at least partly) by one or more solid surfaces. Examples include internal flows such as the flow through pipes and ducts; external flows such as the flow around aircraft and ships' hulls; and flows in the environment such as the atmospheric boundary layer, and the flow of rivers.
In this chapter, Large Eddy Simulations of fully developed, incompressible turbulent channel flows, one of the simplest bounded flow configurations, are considered. This simple flow is of practical importance and played a prominent role in the historical development of the study of turbulent flows. The determination of the correct wall law and the corresponding Reynolds and shear stresses (see Pope [103]) are the challenges that any numerical simulation of turbulent channel flows face.

The primary goal of this Chapter is to simulate turbulent channel flows with ADM in combination with the spectral element code. The Chapter is organized in two parts. The first part deals with ADM in combination with a spectral element code and the goal is to implement ADM and to validate it for incompressible flows: Section 3.2 discusses the setup and the wall law and the Reynolds and shear stresses are investigated for Large Eddy Simulations (LES) of $Re = 2,800$ (corresponding to a friction Reynolds number, $Re_\tau \approx 180$) in Section 3.2.1. An LES of $Re = 10,935$ ($Re_\tau \approx 575$) is performed to eliminate viscous effects and the results are presented in Section 3.2.2.
The second part deals with ADM in combination with a global spectral code and the goal is to investigate a new intermittency correction

proposed by Yakhot [144], aiming at obtaining good results even at low resolution in the wall-normal direction. The intermittency correction is introduced in Sections 3.3.1, 3.3.2 and 3.3.3. In Section 3.3.4 and 3.3.5 the results of the low and high Reynolds number LES are presented and discussed.

3.1 Turbulent Channel Flows

The turbulent channel flow is a prototype for the class of wall-bounded shear flows. The essential problems of hydrodynamic instability and the resulting turbulent flow were recognized and formulated in the nineteenth century, notably by Reynolds in the year of 1883 who investigated the instability of a flow in a pipe by injecting dye to the turbulent flow. Reynolds went on to show that the laminar flow breaks down when the non-dimensional Reynolds number, defined as $Re = (ur)/\nu$, exceeds a certain critical value, u being the maximum velocity of the water in the pipe, r the radius of the pipe, and ν the kinematic viscosity of water at an appropriate temperature. The series of experiments gave the critical value of Re as nearly $13,000$. Below a critical value of the Reynolds number there was a Poiseuille pipe flow with a parabolic velocity profile. As the velocity increased above the critical value, Reynolds found that the flow became turbulent, with a chaotic three-dimensional motion that strongly diffused the dye throughout the water in the pipe. However, the critical value was found to be very sensitive to disturbances in the water before entering the pipe. Just above the critical flow another phenomenon was the intermittent character of the disturbance. The disturbance would suddenly appear through a certain length of the tube, die out and then reappear, giving the appearance of flashes. Such flashes are now called turbulent spots or turbulent bursts.
Later experimentalists introduced disturbances of finite amplitude at the intake or used pipes with rough walls to find Re as low as $2,000$, and have used such regular flows and such smooth-wall pipes that Re was 10^5 or even more (see Breuer [19]). Today, the benchmark results for turbulent channel flows are from the DNS of Moser et al. [91], which will be also used for the comparison of the present LES.

The first result of LES of turbulent, incompressible channel flows were published by Deardorff [34] in 1970. The eddy-viscosity model was used, as proposed by Smagorinsky [117] to model the subgrid-scale terms. The problems of the near-wall behavior of the Smagorinsky model were

subsequently investigated. Moin et al. [89] coupled the model constant of the Smagorinsky model to the mixing length, proportional to the distance to the wall and Moin et Kim [88] used a Van Driest damping function proposed by Van Driest [131].
The work of Germano et al. [52] improved the near-wall behavior of the eddy-viscosity SGS significantly by using a procedure to dynamically compute the eddy-viscosity coefficient. In contrast to earlier works, this so-called dynamic subgrid-scale eddy viscosity model does not require a special near-wall treatment.
Stolz et al. [122] used the Approximate Deconvolution Model (ADM), which can be considered as a generalization of the scale similarity model for the LES of incompressible, turbulent channel flows. Illescu and Fischer [65] used a spectral element code for the simulation of turbulent channel flow.

3.2 Channel Setup

As sketched in Fig. 3.1, the domain is a rectangular duct with a height of $L_z = 2h_c$. The mean flow is predominantly in the axial (x) direction, with the mean velocity varying mainly in wall-normal (z) direction. The

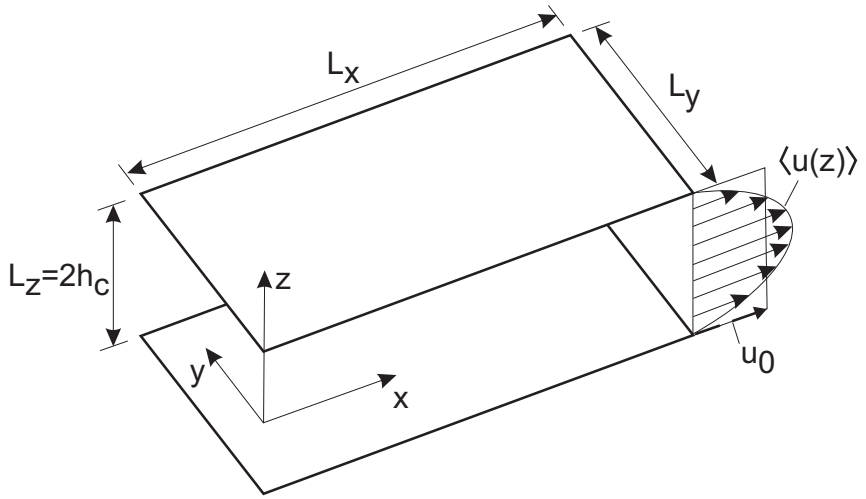

Figure 3.1: Sketch of channel flow with the cartesian coordinate system spanning the streamwise (x), spanwise (y) and wall-normal directions (z).

bottom and the top walls are located at $z = -h_c$ and $z = h_c$, respectively, with the mid-plane being at $z = 0$. The centerline is defined by $z = 0$ and $y = 0$. The velocities in the three directions (x, y, z) are (u, v, w) and the fluctuations are defined as (u', v', w'). The reference length and the

timescales of the turbulent channel flow are defined as h_c and $t_u = h_c/u_0$ with u_0 the bulk velocity and t_u the time scale, respectively. The statistics presented later in this Chapter are ensemble (time) averaged results, denoted as $\langle\ \rangle$, which are based on results obtained over a simulation time of $400 \cdot t_u$. The flow has periodic boundary conditions in the stream- and spanwise directions and has no-slip walls in wall-normal direction at $z = \pm h_c$. The attention is to the fully developed region in which velocity statistics no longer vary with x. The fully developed channel flow being considered is statistically stationary and statistically one-dimensional, with velocity statistics depending only on z.
The Reynolds number used to characterize the flow is defined as

$$Re = \frac{u_0 h_c}{\nu} \ , \tag{3.1}$$

where the inflow-bulk velocity for incompressible fluids is

$$u_0 = \frac{1}{2h_c L_x L_y} \int_{-h_c}^{h_c} \int_0^{L_y} \int_0^{L_x} u(x,y,z)\ dx\ dy\ dz \ . \tag{3.2}$$

Simulations are performed for the friction Reynolds number

$$Re_\tau = \frac{u_\tau h_c}{\nu} \ . \tag{3.3}$$

In Eq. 3.3, the friction velocity u_τ and wall shear stress, τ_w, are defined as,

$$u_\tau = \sqrt{\frac{\tau_w}{\rho}} \tag{3.4}$$

$$\tau_w = \rho\nu \Big(\frac{\partial \langle \overline{u} \rangle}{\partial z} \Big)_{z=|h_c|} \ , \tag{3.5}$$

where $\langle\ \rangle$ is the operator for ensemble averaging. Close to the wall, the viscosity ν and the wall shear stress are important parameters. From these quantities (and ρ), we define viscous scales that are the appropriate velocity and length scales in the near-wall region. These are the friction velocity u_τ and the viscous length scale

$$\delta_v = \nu \sqrt{\frac{\rho}{\tau_w}} = \frac{\nu}{u_\tau} \ . \tag{3.6}$$

The distance from the wall measured in viscous lengths - or wall units - is denoted by

$$y^+ = \frac{y}{\delta_v} = \frac{u_\tau y}{\nu} \ . \tag{3.7}$$

Notice that y^+ is similar to a local Reynolds number, so its magnitude can be expected to determine the relative importance of viscous and turbulent processes.
The Reynolds number Re is fixed and Re_τ is obtained from the simulation. The simulation is forced (see, for example Gilbert [57]) in the x-direction for a constant mass flux.
The set of Eqs. (2.44) to (2.48) for the incompressible channel flow without buoyancy reduces to

$$\nabla \cdot \underline{\overline{u}} = 0 \tag{3.8}$$

$$\frac{\partial \underline{\overline{u}}}{\partial t} + \overline{(\underline{u}^\star \cdot \nabla)\underline{u}^\star} - \nabla \overline{P} = \frac{1}{Re}\nabla^2 \underline{\overline{u}} - \chi_u (I - Q_N * G) * \underline{\overline{u}} \ , \tag{3.9}$$

where $P = p_2/\rho$. Relevant scales for the validation of an LES simulation are the resolved ones. Thus, the comparison between LES and DNS results must involve these scales only. In other words, DNS simulation should be filtered. Many authors proceed in this way (see, for example Ribault et al. [76], Vreman et al. [140] and Stolz et al. [122]). In this work the LES results are directly compared with the DNS results as proposed by Gago et al. [43] and because of a simpler post processing. The mean velocity and the Reynolds stresses are ensemble averaged, averaged on the x-y plane, plotted in wall-normal direction and compared with the unfiltered DNS-data of Moser et al. [91].
The LES filtering is performed with the Boyd filter (presented in Chapter 2) and flows for $Re = 2,800$ and $Re = 10,935$ are investigated. For high Reynolds numbers, viscous effects can be neglected whereas for the low Reynolds number viscous effects are still important.

3.2.1 LES for Re=2,800

Large Eddy Simulations are first performed for $Re = 2,800$. The geometry of the computational domain is shown in Fig. 3.1 with $L_x \times L_y \times L_z = 4\pi \times 4\pi/3 \times 2$. The results will be compared against the DNS data of Moser et al. [91]. The comparison between the spatial resolutions of the LES, the LES of Stolz et al. [122] and the DNS of Moser et al. [91] are compared in Table 3.1.

Spatial Resolution Study

The resolution study is performed for two meshes C1 and C2. Mesh C1 contains 4 elements in each direction (resulting in a total number of

elements $N_e = 64$) whereas mesh C2 is based on 6 elements in each direction ($N_e = 216$). The spectral elements are distributed uniformly in the streamwise and spanwise direction and nonuniformly in the wall normal direction, where the element distribution is transformed with $sin(2z\pi)$ to increase the resolution close to the walls. The resolution in the wall-normal direction is very important because the flow close to the wall has to be resolved correctly. The wall law (logarithmic velocity profile at the wall), the friction Reynolds number Re_τ and the Reynolds stresses depend sensitively on the correct description of the flow close to the wall. Stolz et al. [122] recommend to have the first three mesh points in the range of $z^+ \leq 10$ and the fourth and the fifth points in the range of $10 < z^+ < 20$. The spatial resolution in the spanwise and streamwise direction are defined according to Stolz et al. [122] and the three investigated resolutions based on mesh C1, C2 and $C2^s$ are summarized in Table 3.1. The spatial resolution in the wall-normal direction, presented in z^+ units, are given in Table 3.2. It is evident from Table 3.2 that the recommendation of Stolz

Case	N_e $(x \times y \times z)$	N_s	Mesh points $(x \times y \times z)$
C1	$4 \times 4 \times 4 = 64$	10	$41 \times 41 \times 41$
C2	$6 \times 6 \times 6 = 216$	8	$49 \times 49 \times 49$
$C2^s$	$6 \times 6 \times 6 = 216$	10	$61 \times 61 \times 61$
LES [122]	$(Re = 2800)$		$48 \times 48 \times 49$
DNS [91]	$(Re = 2800)$		$128 \times 129 \times 128$

Table 3.1: Channel-flow cases for the spatial resolution study in comparison with the DNS of Moser et al. [91] and the LES of Stolz et al. [122]. (N_e: number of elements, N_s: order of the polynomial order in each spatial direction)

	C1 $[z^+]$	C2 $[z^+]$	$C2^s$ $[z^+]$
1. point	0.0	0.0	0.0
2. point	1.7	1.8	1.2
3. point	5.4	5.9	4.0
4. point	10.9	11.6	8.1
5. point	17.6	18.2	13.0

Table 3.2: Mesh points for the investigated resolutions at the wall, given in wall units.

et al. [122] concerning the spatial resolution close to the wall is satisfied for the three cases. For the LES, a timestep of $0.01 \cdot t_u$ is used.
The influence of the spatial resolution is investigated by considering the friction Reynolds number Re_τ as a function of the relaxation term χ_u. The results using the SE-filter of 5% (see Fig. 2.2) for different resolutions are shown in Fig. 3.2, whereas for grid C2 ($N_s = 8$) the results without the SE-filter are also presented. The insensitive behavior of Re_τ for $\chi_u > 20$ is clearly seen for all cases and the three resolutions show only marginal differences in Re_τ. In the range $\chi_u < 20$ the stabilizing effect

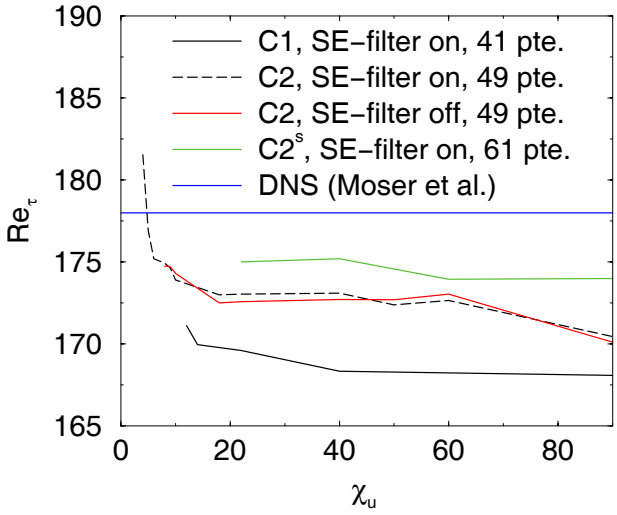

Figure 3.2: Sensitivity investigation of Re_τ for different spatial resolutions of the turbulent channel flow. The value of $Re_\tau = 178$ corresponds to the DNS of Moser et al. [91].

of the SE-filter is obvious if χ_u is decreased to zero, the LES will become unstable. The effect of the SE-filter can be demonstrated with mesh C2 where the LES with SE-filter allows a reduction of χ_u to smaller values. The SE-filter influences neither the Re_τ nor the radial profiles of the mean velocity and Reynolds stresses shown in Figs. 3.3 and 3.4. The resolution study with the meshes C1, C2 and $C2^s$showed for all investigated resolutions an insensitive behavior of Re_τ for $\chi_u > 20$ and their magnitudes (between $Re_\tau = 168$ and $Re_\tau = 175$) are close to the DNS result of Moser et al. [91] with $Re_\tau = 178$. As a consequence the mesh C2 with $N_s = 8$ in combination with the SE-filter of 5% and $\chi_u = 40$ will be used for the further LES of $Re = 2,800$.

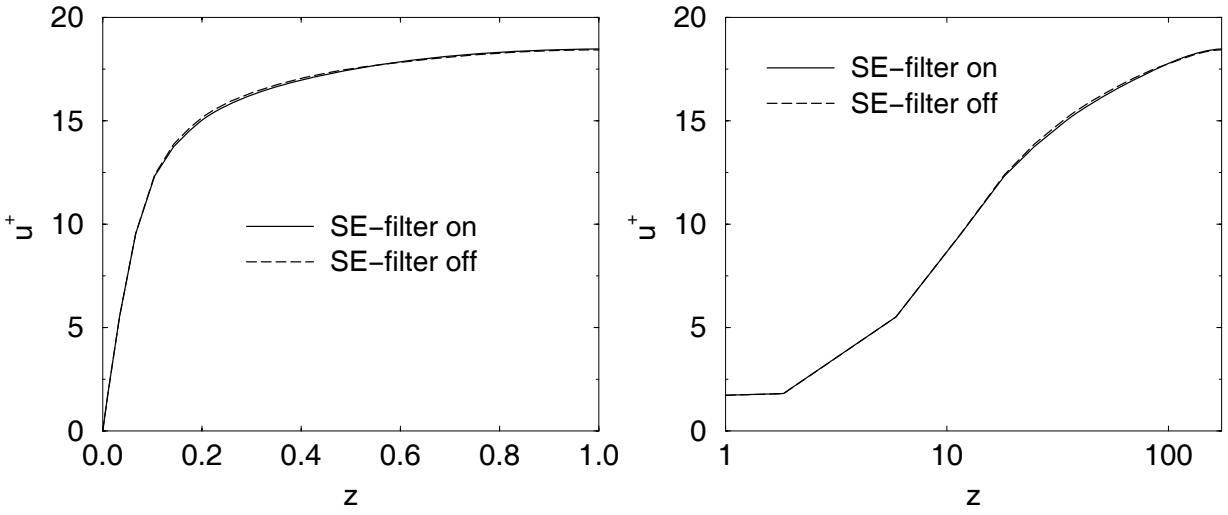

(a) (b)

Figure 3.3: Velocity profile scaled with u_τ for $Re_\tau \approx 180$ and mesh C2, (a) linear plot, (b) logarithmic plot. Solid line is for *SE-filter on* and dashed line is for *SE-filter off*.

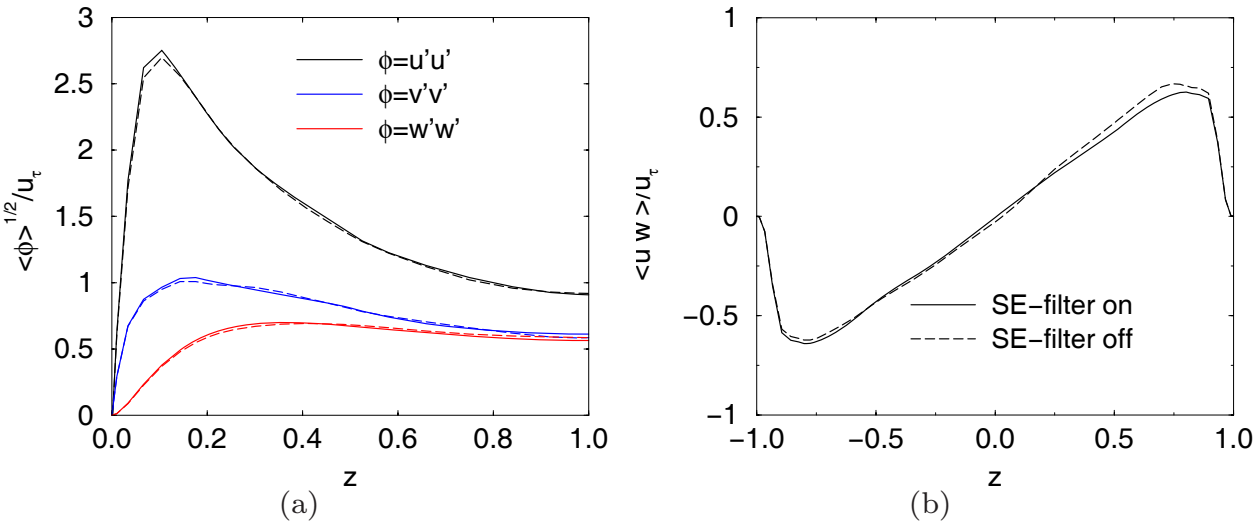

(a) (b)

Figure 3.4: Velocity fluctuations and Reynolds stresses for $Re_\tau \approx 180$ and mesh C2, (a) Reyonlds-stresses in axial (u), spanwise (v) and wall-normal directions (w), (b) shear stress. Solid line is with the *SE-filter on* and dashed line is with the *SE-filter off*.

Determination of the Filter Function

The definition of the low-pass filter function G (see Eq. (2.55)) contains two free parameters: the cutoff scale κ_{ct} and the maximal polynomial order N_s. The influence of κ_{ct} and N_s are investigated in the following. The velocity profile of a laminar channel flow is a parabolic profile. Thus, the low-pass filter formulated in the polynomial space should not affect second-order polynomials. To fulfill this constraint either N_s should be high enough for low κ_{ct}, or κ_{ct} should be high enough for small N_s. This is explained in Fig. 3.5 where the line marks the κ_{ct}-N_s region where the LES filter modifies the 2nd order polynomial of the unfiltered field. In this work $\kappa_{ct} = 0.7$ is used, based on the work of Stolz et al. [122] and Rembold [108] which used $\kappa_{ct} \approx 0.63$. According to Fig. 3.5 a polynomial order of $N_s > 5$ has to be used for $\kappa_{ct} = 0.7$.

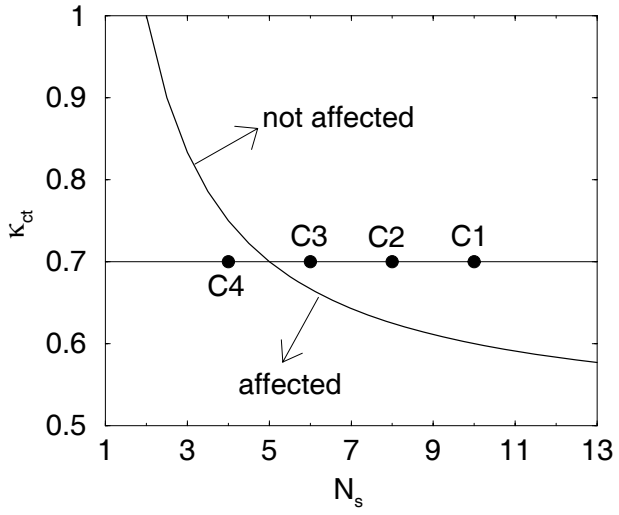

Figure 3.5: Region of κ_{ct} as a function of N_s (maximal polynomial order), where the filter does not affect the second polynomial order.

To test the influence of this constraint, different spatial resolutions are used which are presented in Table 3.3 and plotted in Fig. 3.5. Cases C1, C2 and C3 are representative of the *not-affected* region, whereas case C4 is representative for the *affected* region. The influence of different $N_e(x)/N_s$-combinations (C1 to C4) are investigated by considering the friction Reynolds number Re_τ of the turbulent channel flow as a function of the relaxation parameter χ_u of ADM and the results are plotted in Fig. 3.6. The friction Reynolds number Re_τ is insensitive to χ_u for the cases C1, C2 and C3, but not for C4. The reason for this is the modification of the 2nd order polynomial by the LES filter of the mesh C4 (see Fig. 3.5). As a consequence, for $\kappa_{ct} = 0.7$ a polynomial order of $N_s > 5$ should be

case	N_e (x=wall normal)	N_s	$N_e(x) \cdot N_s + 1$
C1	4	10	41
C2	6	8	49
C3	8	6	49
C4	12	4	49

Table 3.3: Overview of the investigated channel cases with N_s, N_e and the total number of collocation points in wall normal-direction.

used.

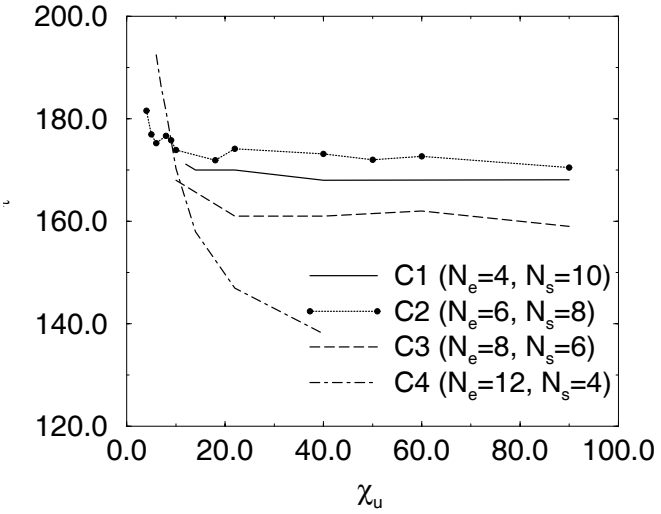

Figure 3.6: Friction Reynolds number Re_τ as a function of the relaxation parameter χ_u of ADM for the meshes C1 to C4.

Results and Discussion

The low Reynolds number LES is performed for $Re = 2,800$, according to the setup of Stolz et al. [122], with a corresponding $Re_\tau = 178$, computed by Moser et al. [91]. The following results are based on the mesh C2 ($N_e = 216$, $N_s = 8$) and a relaxation parameter of $\chi_u = 40$. The spatial resolution is compared with the DNS of Moser et al. [91] and the LES of Stolz et al. [122] in Table 3.1. The mean velocity profiles, scaled with z in outer units and in wall units, are displayed together with the DNS data from Moser et al. [91] in Fig. 3.7. The good agreement between LES and the DNS is evident.
The root-mean-square of the velocity fluctuations $\underline{\phi}' = \underline{\phi} - \langle \underline{\phi} \rangle$, where ϕ

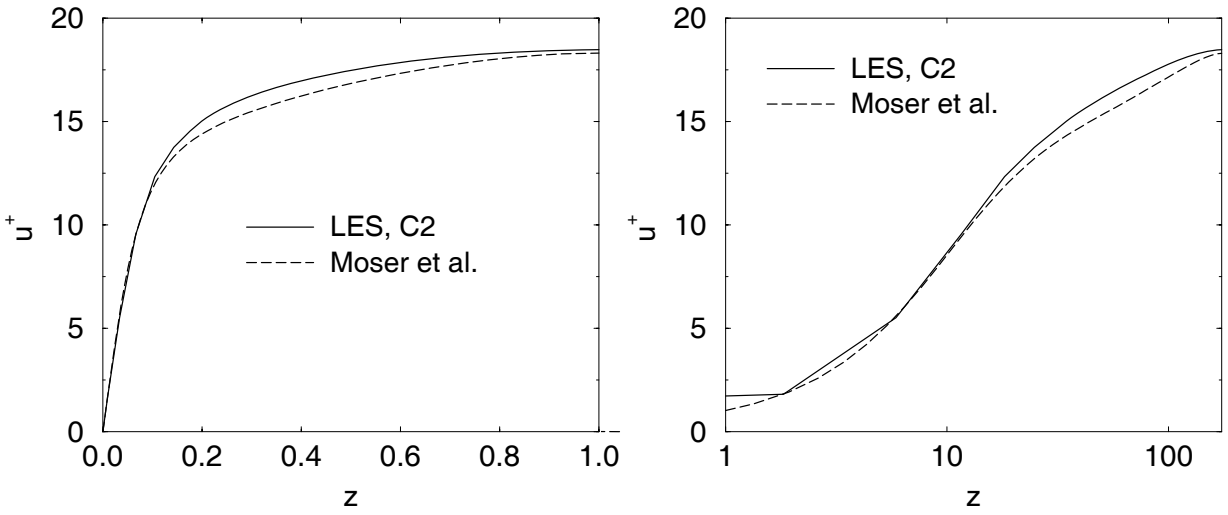

(a) (b)

Figure 3.7: Mean velocity profile scaled with u_τ for $Re_\tau \approx 180$ and mesh C2, (a) linear plot, (b) logarithmic plot. Solid line is for the LES with $\chi_u = 40$ and dashed line is for the DNS of Moser et al. [91].

is the velocity in one direction, is shown in Fig. 3.8 (a). The velocity fluctuations of the LES are plotted with solid lines, those of the unfiltered DNS with dashed lines. The overall agreement between LES and unfiltered DNS is good. However, the LES underpredicts the unfiltered DNS except in the range of the maximum streamwise value, where the LES overshoots the unfiltered DNS data. It should be noted that the root-mean-square of the velocity fluctuations are expected to be smaller for the LES due to the spatial filtering. The Reynolds shear stress, presented in Fig. 3.8 (b) shows the same trends as the normal Reynolds stresses.

3.2.2 LES for Re=10,935

Since Reynolds experiment in 1883, it is known that depending on their entrance and the roughness of the walls channel flows become turbulent in the range of $2,300 \leq Re \leq 40,000$ according to Thomann [125]. The low-Re simulation from the previous Section with $Re = 2,800$ is close to the lower limit and viscous effects still influence the turbulent flow. To reduce the influence of viscous effects an LES for $Re = 10,935$ was performed. The corresponding reference friction Reynolds number is $Re_\tau = 586$ obtained from the DNS of Moser et al. [91]. The geometry of Fig. 3.1 has the dimensions of $L_x \times L_y \times L_z = 2\pi \times \pi \times 2$ for the case of $Re = 10,935$ and is discretized with 9 elements in the streamwise

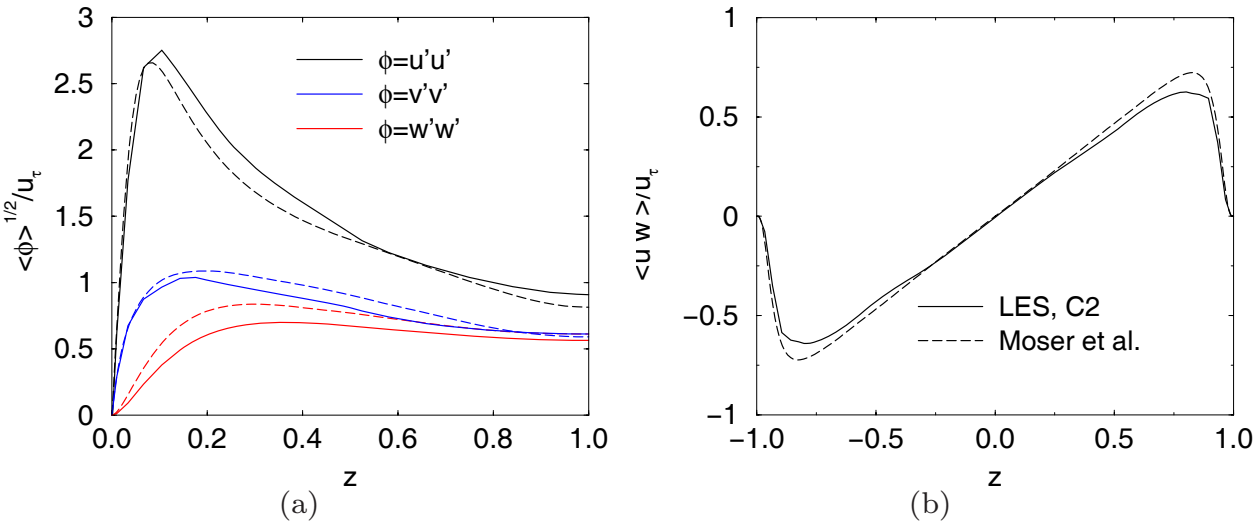

Figure 3.8: Velocity fluctuations and Reynolds stresses for $Re_\tau \approx 180$ and mesh C2, (a) Reynolds stresses in axial (u), spanwise (v) and wall-normal directions (w), (b) shear stress. Solid lines are for the LES with $\chi_u = 40$ and dashed lines are for the DNS of Moser et al. [91].

direction and 12 elements in the spanwise and wall-normal directions ($N_e(x) = 9, N_e(y) = 12, N_e(z) = 12$). The maximal polynomial order is chosen as $N_s = 8$ resulting in a spatial resolution of $73 \times 97 \times 97$ points. The spectral elements are distributed as described in the previous Section and the timestep is set equal $0.005 \cdot t_u$. This is two times smaller than for the LES of $Re = 2,800$ and can be justified by the ratio of the viscous-length scales. The spatial resolution is comparable with that of Stolz et al. [122] (Table 3.4) while the DNS of Moser et al. [91] used a spatial resolution of $384 \times 257 \times 384$.

	present LES $[z^+]$	Stolz et al. [122] $[z^+]$
1. point	0.0	0.0
2. point	1.0	0.7
3. point	3.2	4.9
4. point	6.3	8
5. point	9.9	11

Table 3.4: Comparison of the distribution of mesh points close the wall in the LES with that of Stolz et al. [122] in z^+-units.

The LES is performed with $\chi_u = 80$ and results in $Re_\tau = 575$. The mean velocity profiles plotted in linear and logarithmic scales are showed

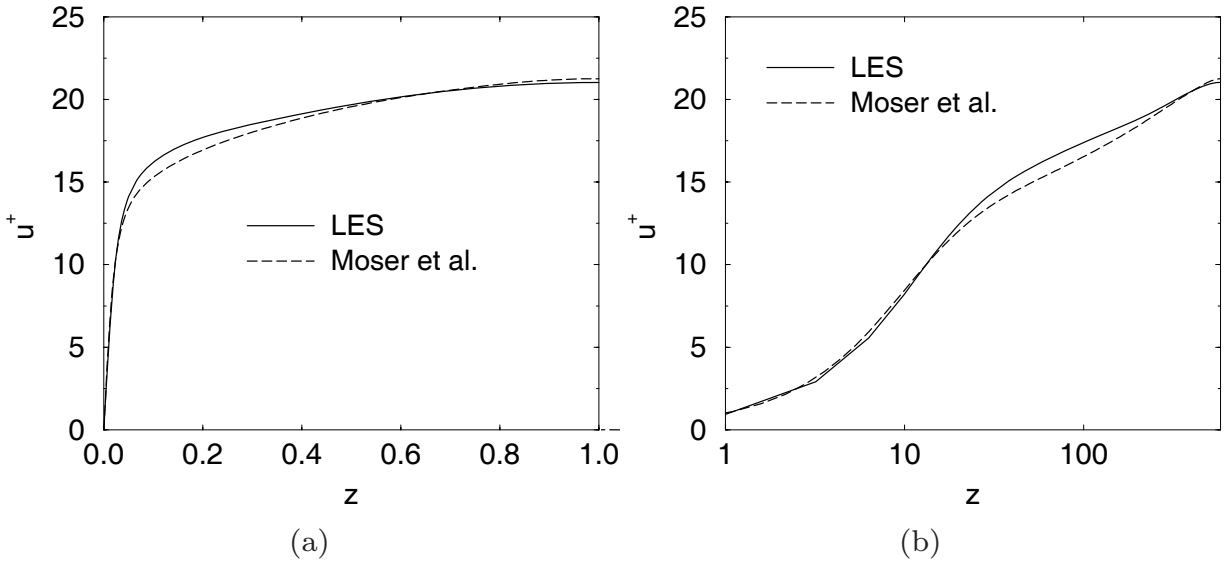

Figure 3.9: Mean velocity profile scaled with u_τ for $Re_\tau = 575$, (a) linear plot, (b) logarithmic plot. Solid line is from the LES with $\chi_u = 80$ and the dashed line is for the DNS of Moser et al. [91].

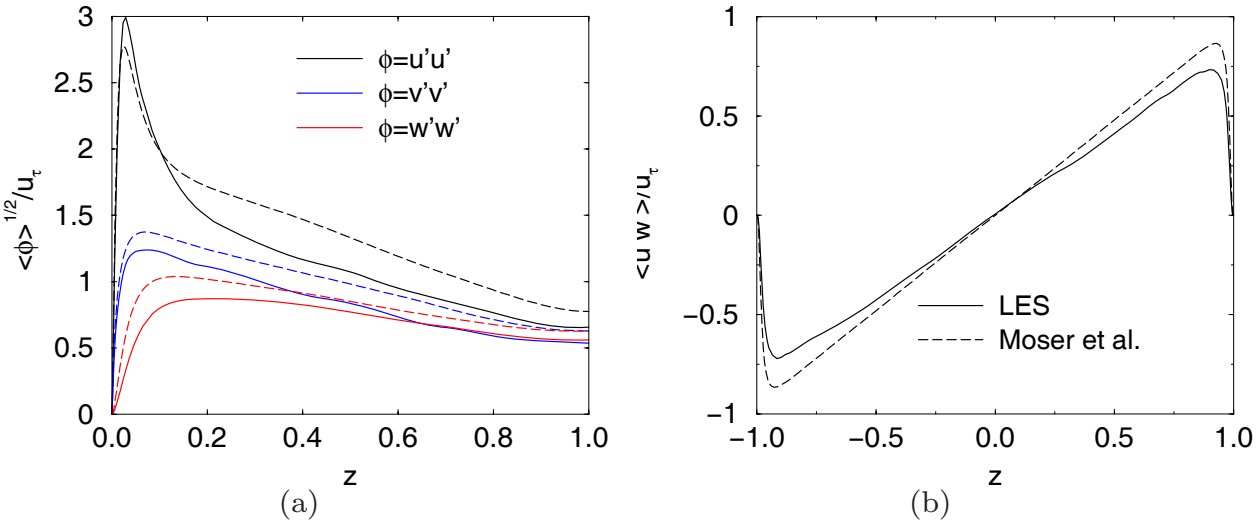

Figure 3.10: Velocity fluctuations and Reynolds stresses for $Re_\tau = 575$, (a) Reyonlds stresses in axial (u), spanwise (v) and wall-normal directions (w), (b) shear stress. Solid lines are for the LES with $\chi_u = 80$ and the dashed lines are from the DNS of Moser et al. [91].

together with the DNS-profiles of Moser et al. [91] in Fig. 3.9 (a) and (b); the good agreement is obvious and the law of the wall is satisfied. The mean-velocity overestimation in the outer layer can be attributed to the Re_τ-underestimation of the LES. The Reynolds normal stresses of the LES are compared with unfiltered DNS in Fig. 3.10 (a). The agreement

between LES and unfiltered DNS is good and the Reynolds stresses are expected to be smaller for the LES because of spatial filtering. The same trend is valid for the Reynolds shear stresses, which are plotted in Fig. 3.10 (b).

The LES for $Re = 2,800$ and $Re = 10,935$ show a good agreement with the DNS data. In contrast to the LES of Stolz [120], who used a dynamic procedure for the calculation of the relaxation parameter χ_u as a function of time and space, the combination of ADM and the spectral element code gives satisfactory results for constant χ_u.

3.3 Reynolds number Scaling of LES

One of the first LES of turbulent channel flows computing the log-distribution near the wall successfully was performed by Moin et al. [88] using the Smagorinsky model. They simulated the channel flow at $Re_\tau = 180$. However, similar success could be achieved for higher Re-number flows only with substantial increase of the spatial resolution.
The problem of the breakdown of the Smagorinsky-like approaches was addressed in the work of Yakhot et al. [143]. Channel flow Large Eddy Simulations conducted for different Reynolds numbers on the same grid showed that the breakdown of the approach (loss of the log profile and poor prediction of the friction coefficient) happens together with substantial deterioration of prediction of the normalized turbulence intensities. Investigation of the near-wall dynamics revealed extremely strong intermittency, i.e. bursting, very spotty distribution of turbulent viscosity and rate of strain.
A new idea of Yakhot [144] to modify ADM is investigated. The motivation of the modification is to reduce the wall-normal resolution dependence of Re. For this investigation ADM was implemented into the global spectral LES code of Gilbert [58, 57] and Stolz et al. [122] for incompressible channel flows. The global spectral code was used for better comparison with the results of Stolz et al. [122], obtained with the same code using the standard ADM formulation. The incompressible Navier-Stokes equations are discretized by Fourier expansions in the stream- and the spanwise directions and by Chebyshev polynomials in the wall-normal direction. The mesh is equidistant in the wall-parallel directions (x and y) and for the wall-normal direction z the non-equidistant Gauss-Lobatto collocation points are used (see for example Canuto et al. [21])

$$z_i = cos(i\pi/N_z),\ 0 \leq i \leq N_z\ . \tag{3.10}$$

The divergence-free condition is enforced exactly by an influence-matrix technique (see Kleiser and Schumann [69]). Time advancement is done by a semi-implicit Runge-Kutta / Crank-Nicolson scheme (see Sandman et al. [113]). The nonlinear terms are computed pseudospectrally and full dealiasing is achieved by applying the 3/2 rule (see Canuto et al. [21]). For the LES a filter in physical space with $k_c = \frac{2}{3}N_s$ (see Fig. 2.3) is used and the series of the inverse filter function (Eq. 2.57) is truncated at $N_d = 5$.

3.3.1 Breakdown of Smagorinsky-Like Approaches

To illustrate the mechanism responsible for the failure of Smagorinsky-like approaches, let us first recall the reasoning behind it. According to Kolmogorov's picture of isotropic and homogeneous turbulence, the turbulent viscosity, generated by the small-scale velocity fluctuations, felt by the inertial-range modes at the scale Δ_i is given by

$$\nu \approx \varepsilon^{1/3}\Delta_i^{4/3} \ , \tag{3.11}$$

where ε is the mean dissipation rate of the turbulent kinetic energy, equal to the energy flux in the wavenumber space. At this point, Smagorinsky made a drastic assumption,

$$\varepsilon \approx \nu S_{ij}^2 \tag{3.12}$$

with S_{ij} denoting the local, fluctuating value of the resolved rate of strain. Substituting this into the previous expression we obtain the Smagorinsky model

$$\nu \approx \mid S_{ij} \mid \Delta_i^2 \ . \tag{3.13}$$

The dimensional considerations leading to this expression, are correct only when all ingredients are weakly fluctuating quantities. In general the expansion of turbulent viscosity (see Yakhot and Orszag [145]) gives

$$\nu \approx \langle \frac{u^2}{\sigma} \rangle + O\Big(\langle \frac{u^2 S_{ij}^2}{\sigma^3} \rangle + ... \Big) \ , \tag{3.14}$$

where $u(x,t)$ is the sub-grid velocity field and $1/\sigma = \tau$ is the local value of the characteristic turbulent time scale τ which, being a dynamic variable, is a functional of the entire field. The rate of strain, S_{ij}, is computed from the resolved velocity field. Consider the first-order contribution to this expression. If, as in the Kolmogorov theory, $\sigma \approx \varepsilon^{1/3}\Delta^{-2/3}$, and Eq. (3.12) is used for the dissipation rate, the Smagorinsky model is readily derived. This is possible only if the fluctuations are weak. Near

the wall or any other even instantaneously strongly sheared region, where the Kolmogorov picture of the energy cascade from large-to-small scales is incorrect, the above expression for the characteristic time breaks down and one shouold instead use $1/\sigma = \tau \approx 1/\mid S_{ij} \mid$. Substituting this into the first term of Eq. (3.14) we can approximately split the averaging in expression Eq. (3.14) to derive

$$\nu \approx \langle u^2 \rangle \langle \frac{1}{\mid S_{ij} \mid} \rangle \ . \tag{3.15}$$

In general, the expression for a physically plausible model must involve the combination of the Kolmogorov relaxation time and the one determined by the local value of the rate of strain $1/\mid S_{ij} \mid$. Equation (3.14) illustrates the physical reason of the failure of all Smagorinsky-like approaches: due to strong intermittency in near-wall regions or in the inertial range of any high Reynolds number flow, the Smagorinsky viscosity Eq. (3.13), strongly overestimates the relaxation time of the bursting, most violent events, leading to an incorrect description of the turbulence production process.

This problem exists in all approaches based on low-order statistics. For example, it is customary to use second-order structure functions to estimate the characteristic velocity fluctuation at scale Δ

$$u_2(\Delta) = \sqrt{\langle [u(x) - u(x+\Delta)]^2 \rangle} \ . \tag{3.16}$$

This is correct in the case of Kolmogorov (intermittency-free) turbulence. However, due to intermittency, in high Re flows, we can define

$$u_n(\Delta) = S_n^{1/2} = \langle [u(x) - u(x-\Delta)]^n \rangle^{1/n} \tag{3.17}$$

which for large values of n is much larger than $u_2(\Delta)$. Indeed, due to corrections to the Kolmogorov scaling exponents ($\xi_n > 0$), the structure functions are

$$S_n \approx \varepsilon^{n/3} \Delta^{n/3} \Big(\frac{\Delta}{L} \Big)^{-\xi_n} \ , \tag{3.18}$$

when $\Delta \ll L$. Since the resolved strain rate $S_{ij} \approx [u(x+\Delta) - u(x)]/\Delta$, we see that according to Eq. (3.14), to accurately describe the transport coefficients for the resolved velocity fluctuations one has to sum up the entire expansion in powers of the dimensionless parameter

$$\eta_{ij}^2 = [u^4 S_{ij}^2]/\varepsilon^2 \tag{3.19}$$

or

$$\eta_{ij}^2 = S_{ij}/\sigma^2 \ . \tag{3.20}$$

This is not easy, since in the strongly sheared regions of the flow the local values of $\eta_{ij} \gg 1$. As a result, we do not have an *a priori* way to determine the order of the correlation functions contributing to the model for the effective equation (LES model) and truncate expansion Eq. (3.14).
The approximate (semi-qualitative) model, including an infinite series in powers of η_{ij}^2 will be presented below and used for the LES of turbulent channel flow.

3.3.2 The Modified ADM

In wall-bounded flows, where turbulence is mainly generated in the vicinity of the walls and later diffuses into the bulk, the definitions based on the local values of the dissipation rate, velocity field, rate of strain etc, cannot be correct: The information characterizing the wall dynamics must be included in the model even far from the wall. This resembles the problem of diffusion of a contaminant from a constant in time and space source: the spatial distribution of the contaminant concentration contains the source input as a factor. The importance of this fact for LES will be demonstrated below.
The results of the simulations reported in Stolz et al. [122] are summarized in Table 3.3.2. The LES of a channel flow $Re = 2,800$ ($Re_\tau = 178$),

Method	Re	resolution	domain	Re_τ
DNS	$2,800$	$128 \times 128 \times 129$	$4\pi \times 4\pi/3 \times 2$	178
LES	$2,800$	$32 \times 32 \times 33$	$4\pi \times 4\pi/3 \times 2$	173
LES	$2,800$	$48 \times 48 \times 49$	$4\pi \times 4\pi/3 \times 2$	178
DNS	$10,935$	$384 \times 384 \times 257$	$2\pi \times \pi \times 2$	586
LES	$10,935$	$48 \times 64 \times 65$	$2\pi \times \pi \times 2$	574
LES	$10,935$	$72 \times 96 \times 97$	$2\pi \times \pi \times 2$	587

Table 3.5: Overview about the DNS and LES of the turbulent channel flow of different Re.

defined on a domain $4\pi \times 4\pi/3 \times 2$ were conducted on two meshes with $32 \times 32 \times 33$ and $48 \times 48 \times 49$ points, respectively, compared with the high resolution ($128 \times 128 \times 129$) DNS of the same flow by Moser et al. [91]. The results for the higher resolution were excellent, while the friction Reynolds number of the $32 \times 32 \times 33$ simulation was by some $2\% - 3\%$ smaller than the one obtained in the DNS.
The DNS of the flow at $Re = 10,935$ ($Re_\tau = 586$) were performed by

Moser et al. [91] on a $384\times384\times257$ grid spread over the $2\pi\times\pi\times2$ domain. As can be observed, the rescaling of the domain reduces the number of mesh points needed for accurate DNS of the high Re flow. For the same domain size, however, the number of points increases approximately by a factor 50. The accurate LES of the flow at $Re_\tau = 586$ was achieved on a $72 \times 96 \times 97$ mesh by Yakhot et al. [145]. Interestingly, for the LES simulations, the ratio of the number of points is $N(590)/N(180) = 15.8$ which is close to $\Big(590/180\Big)^{9/4} \approx 14.5$. Therefore, the computational work involved in the LES, though giving substantial computational savings compared to the DNS, still scales as $W \sim Re_\tau^3$.

3.3.3 Intermittency-corrected LES

To account for the strong fluctuations of the rate of strain in the sub-grid scale dynamics the resummation of the entire perturbation expansion Eq. (3.14) has to be performed. Unable to rigorously perform this task, a model giving correct asymptotics in the limit of both small and large values of S_{ij} can be introduced

$$\frac{1}{\tau_r} = \frac{\chi}{\left[1 + \Big(S_{ij}\frac{L}{u_0}\Big)^2\right]^{1/2}} \ , \tag{3.21}$$

where L is the reference length scale and u_0 is the reference velocity scale, and use Eq. (3.21) in Eq. (2.43) with relaxation time τ_r instead of $\tau = 1/\chi$. The model Eq. (2.43) must conserve momentum. This means that the operator in the right side of Eq. (2.43), acting on the velocity field u must be at least $O(\partial_j^2)$ and the relaxation parameter χ is, up to a factor, turbulent viscosity or hyper-viscosity. We see that the effect of the rate of strain is to reduce this viscosity in regions of strong fluctuations of S_{ij}. Since the relaxation time is a functional of the entire field, the term viscosity used here, is to be taken loosely. The simulations presented below, which use Eq. (3.21) with $L = const$ and $u_0 = const$, serve only to illustrate the basic ideas and qualitative features of the approach. Equation (3.21) can be generalized to account for the local features of the mean Reynolds stress,

$$\frac{1}{\tau} = \frac{\chi}{\left[1 + (\nu\frac{S_{ij}}{\langle u_i u_j\rangle})^2\right]^{1/2}} \approx \frac{\chi}{\left[1 + (\frac{S_{ij}}{\langle S_{ij}(y)\rangle})^2\right]^{1/2}} \ . \tag{3.22}$$

To understand the physics behind Eq. (3.21), let us recall that in a sheared flow the Kolmogorov inertial range interval stress is

$$S_{ij} < \varepsilon^{1/3} k^{2/3} < \varepsilon^{1/3} k_d^{2/3} \approx \varepsilon^{1/3} \Delta^{-2/3} \ . \tag{3.23}$$

Here Δ stands for the mesh size in the well-resolved viscous sub-layer, and k is the wavenumber. We can see that in the viscous sub-layer this interval shrinks to zero. This means that the energy flux toward small scales tends to zero, sometimes, being negative, even leading to the energy production instead of dissipation. The model expression Eq. (3.21) accounts for the reduction of the energy flux and turbulent viscosity or hyper-viscosity in strongly sheared parts of the flow, thus reducing the impact of the short-lived structures, overestimated by approaches based on low-order statistics.

3.3.4 Low Reynolds number LES

First, the effect of the intermittency correction Eq. (3.21) (denoted by (YKT)) is investigated on the performance of the model used by Stolz et al. [122] (denoted as (SAK)). Both LES results are compared with the DNS results of Moser et al. [91] The simulations were conducted on the $24 \times 36 \times 49$ mesh spread over the $2\pi \times \pi \times 2$-domain. The results are summarized in Table 3.6 and compare the computed friction Reynolds number Re_τ and the von-Karman constant KC (corresponds to the linear slope in the outer layer: $u^+ \sim KCln(y^+)$). The results are presented in

model	Re	Re_τ (DNS)	N_x	Re_τ (calc)	KC(calc)	KC(DNS)
SAK	2,800	178	49	180	2.5	2.5
YKT	2,800	178	49	186	2.4	2.5
SAK	6,874	395	49	361	2.17	2.5
YKT	6,874	395	49	395	2.5	2.5
SAK	10,935	586	49	517	2.15	2.5
YKT	10,935	586	49	549	2.5	2.5
YKT	10,935	586	97	592	2.5	2.5

Table 3.6: Overview of YKT- and SAK-simulations in combination with the Re_τ from the DNS of Moser et al. [91] and for a spatial resolution of $24 \times 36 \times N_x$.

Fig. 3.11 for $Re = 2,800$, Fig. 3.12 for $Re = 6,874$ and Fig. 3.13 for

$Re = 10,935$. As we see in Fig. 3.11 (a), the results of the SAK model for $Re = 2,800$, giving $Re_\tau = 180$ agree with the DNS data very well. The results on a flow at $Re = 6,874$ (Fig. 3.12 (b)) demonstrate some deviation from the DNS and yield a low value for Re_τ. The disagreement with the DNS becomes more pronounced in the case of $Re = 10,935$ (Fig. 3.13 (a)), investigated earlier by the well-resolved DNS of Moser et al. [91] who obtained a well-developed logarithmic layer and $Re_\tau = 586$. For this low resolution ($24 \times 36 \times 49$) the SAK model gives $Re_\tau = 517$ leading to a 25% error in the computed friction coefficient.
The results obtained with the YKT model, based on Eq. (3.21), are presented on Figs. 3.11 (b), 3.12 (b) and 3.13 (b). In the low Reynolds number ($Re = 2,800$) case (Fig. 3.12 (b)), the obtained $Re_\tau = 186$ deviated from the DNS only by 2.7%, while the outcome of the simulation ($Re = 6,874$) agreed with DNS velocity profile (Fig. 3.12 (b)). In the case $Re = 10,935$ (Fig. 3.13 (b)), a logarithmic velocity profile with the correct value of the von Karman constant was obtained. To understand the reasons for this discrepancy, $Re = 10,935$-simulation is repeated on a finer ($24 \times 36 \times 97$) grid. The result is shown on Fig. 3.13 (b). The velocity profile is close to the wall law with $Re_\tau = 592$. It is interesting to note that the results did not improve upon further increasing the resolution to $24 \times 36 \times 193$. The fact that the original ADM-model gave results of comparable accuracy only on a $72 \times 96 \times 97$ grid, demonstrates the potential of the intermittency correction Eq. (3.21) to an order-of-magnitude savings in computational cost.

3.3.5 High Reynolds number LES

The DNS conducted by Moser et al. [91] at $Re_\tau = 586$ correspond to the highest Re_τ available in the literature. To compare the results of the LES at higher Reynolds numbers we must develop the criteria to assess the quality of the results. Below we compare results of our simulations with the DNS results from Moser et al. [91]. Wherever possible, to determine the correct value of Re_τ, we will use the Blasius relation

$$8\left(\frac{Re_\tau}{Re_D}\right)^2 = 0.316 Re^{-1/4} , \tag{3.24}$$

valid for turbulent pipe flows when $Re_D < 10^5$. Here, Re_D is a Reynolds number based on the pipe diameter and $Re_D = 4Re_{h_c}$, where Re_{h_c} is the Reynolds number of a channel flow based on its half-width h_c, and Moody diagrams (see Pope [103]) for the friction coefficient for turbulent

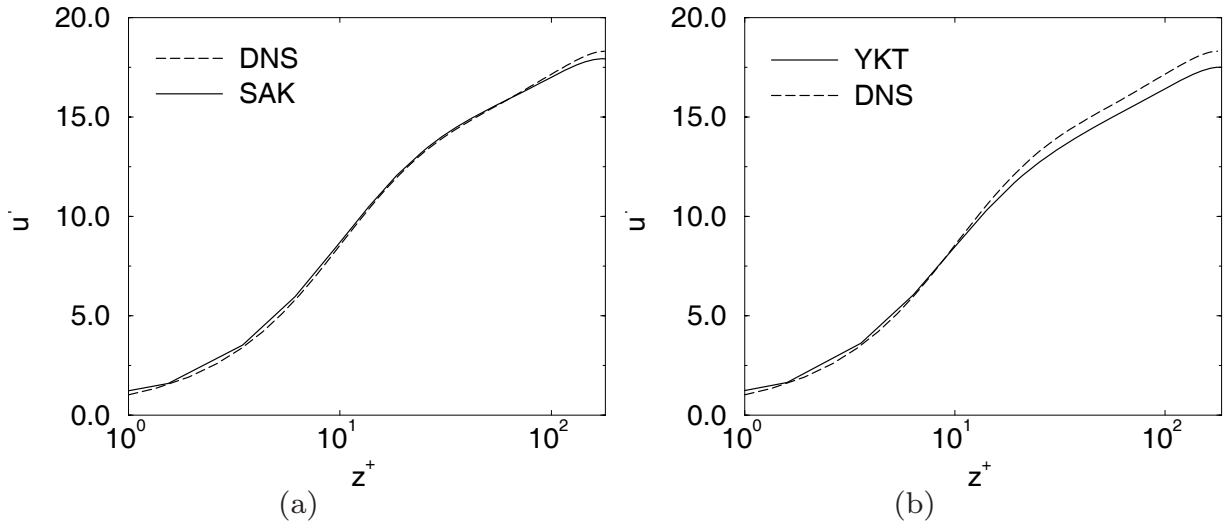

Figure 3.11: Logarithmic wall profiles for a spatial resolution of $24\times36\times49$ (a) $Re = 2,800$, SAK, $Re_\tau = 180$, $z_1^+ = 0.3854$, (b) $Re = 2,800$, YKT, $Re_\tau = 186$, $z_1^+ = 0.3982$.

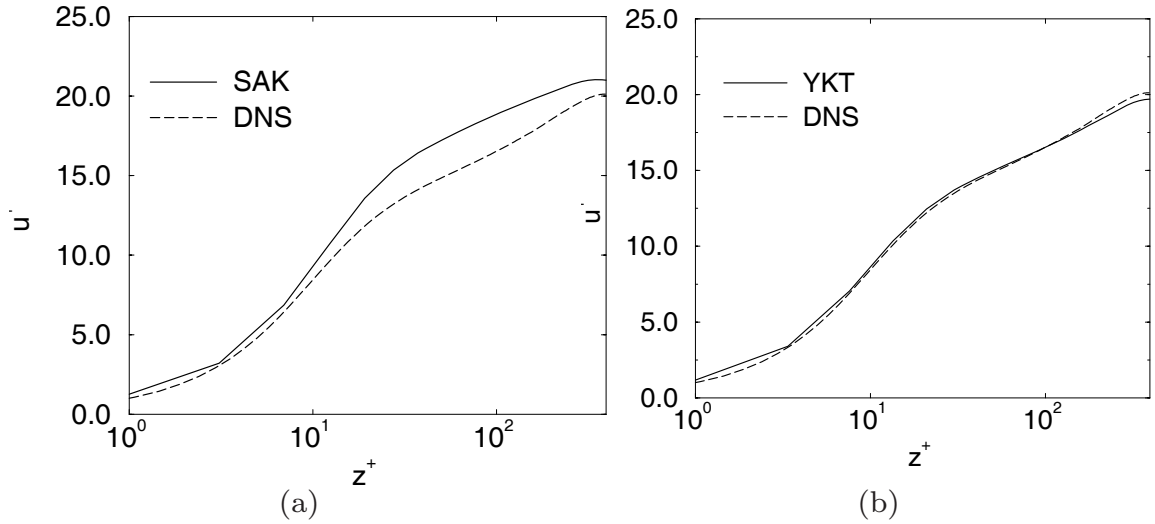

Figure 3.12: Logarithmic wall profiles for a spatial resolution of $24\times36\times49$ (a) $Re = 6,874$, SAK, $Re_\tau = 361$, $z_1^+ = 0.7729$, (b) $Re = 6,874$, YKT, $Re_\tau = 395$, $z_1^+ = 0.8457$.

flow in smooth-pipes. The symbol b.f. will refer to Re_τ evaluated from the Blasius relation. In addition, the existence of a close to logarithmic velocity profile with a correct value of the von-Karman constant KC will be used to assess the outcome of the LES. The results are summarized in Table 3.7. For $Re = 21,869$, the results obtained from a simulation on a $24 \times 36 \times 97$ mesh are presented in Fig. 3.14 (a). Close to logarithmic velocity profile with correct von-Karman constant was obtained. The

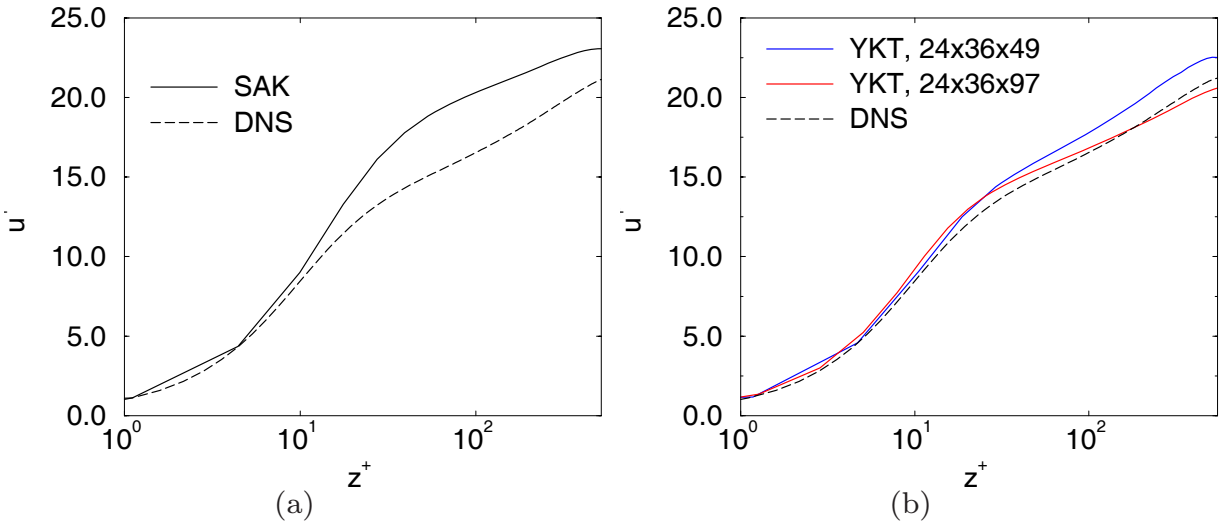

Figure 3.13: Logarithmic wall profiles for a spatial resolution of $24\times36\times49$ a) $Re = 10,935$, SAK, $Re_\tau = 517$, $z_1^+ = 1.1$, b) $Re = 10,934$, YKT, $Re_\tau = 549$; $z_1^+ = 1.2$ (solid line), $Re_\tau = 592$ $(24 \times 36 \times 97)$, $z_1^+ = 0.3$ (long dashed line).

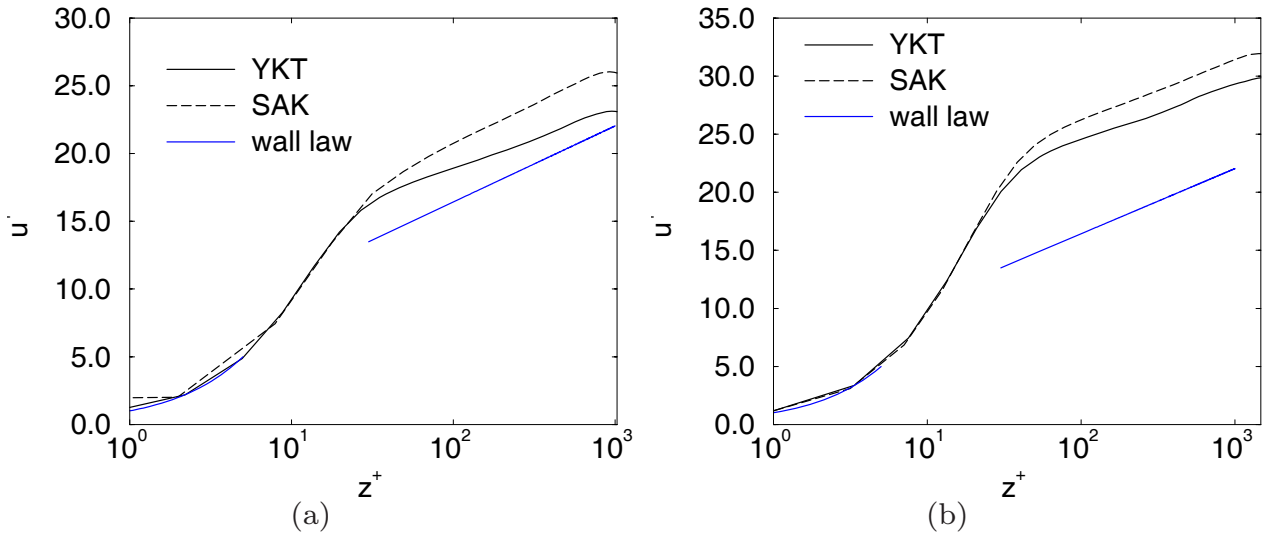

Figure 3.14: Logarithmic wall profiles for a spatial resolution of $24\times36\times97$ (a) $Re = 21,869$, YKT: $Re_\tau = 1,027$: SAK: $Re_\tau = 905$, $z_1^+ = 0.48$; (b)$Re = 43,739$, YKT: $Re_\tau = 1,566$: SAK: $Re_\tau = 1468$, $z_1^+ = 0.78$.

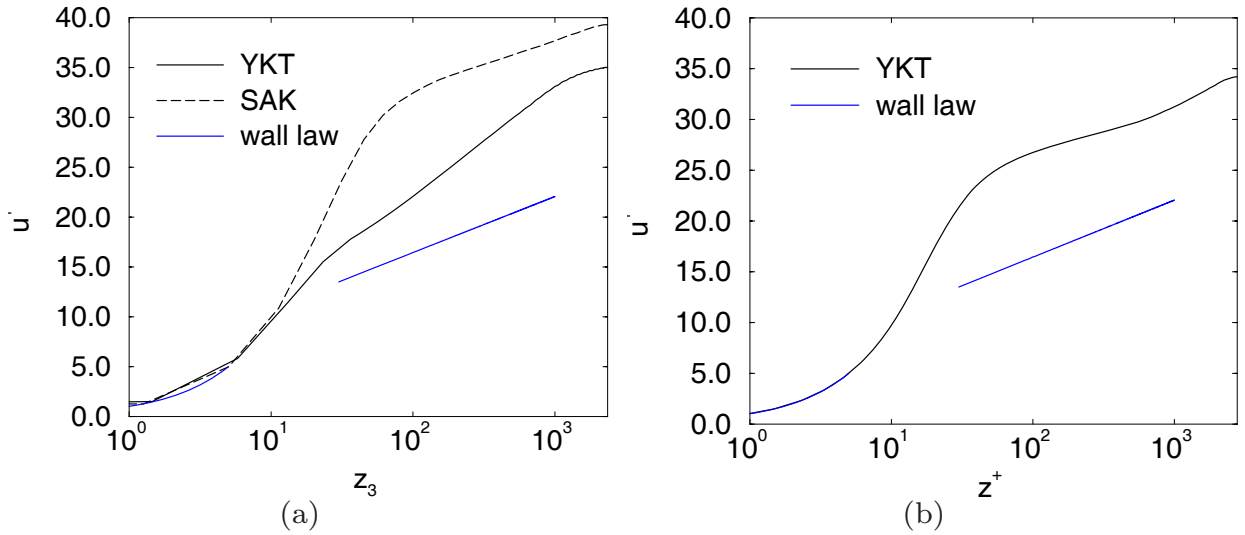

Figure 3.15: Logarithmic wall profiles for a spatial resolution of (a) $Re = 87,478$, $24 \times 96 \times 97$, YKT: $Re_\tau = 2,712$, $z_1^+ = 1.45$, SAK: $Re_\tau = 2,355$, $z_1^+ = 1.26$; (b)$Re = 87,478$, $24 \times 96 \times 385$, $Re_\tau = 27,78$, $z_1^+ = 0.093$.

Re	res	Re_τ (calc)	Re_τ (lit.)	KC (calc)
$6,874$	$24 \times 36 \times 49$	408	395 (DNS)	2.5
$6,874$	$24 \times 36 \times 97$	408	395 (DNS)	2.5
$10,934$	$24 \times 36 \times 49$	586	586 (DNS)	2.5
$10,934$	$24 \times 36 \times 97$	590	586 (DNS)	2.5
$21,869$	$24 \times 36 \times 97$	$1,027$	$1,072$ (b.f.)	2.5
$43,739$	$24 \times 36 \times 97$	$1,566$	$1,980 - 2,100$ (e, b.f.)	2.5
$43,739$	$24 \times 36 \times 193$	$1,687$	$1,980 - 2,100$ (e, b.f.)	2.5
$87,478$	$24 \times 36 \times 97$	$2,715$	$3,600$ (e)	4.3
$87,478$	$24 \times 36 \times 385$	$2,800$	$3,600$ (e)	2.5

Table 3.7: Overview of high-Re simulations in comparison with DNS-results. e: experiment, b.f.: Blasius-relation.

calculated $Re_\tau = 1,027$ was quite close to $Re_\tau = 1,072$ corresponding to the friction Reynolds number evaluated using the Blasius relation, valid in this range of Re.

At this point we would like to discuss the physical conditions corresponding to our simulations. The most prominent flow structures, observed in wall flows, are streaks, having approximate dimensions $1,000 \times 100 \times (10 - 20)$ in wall units. Due to the weak variation of

the velocity field in the streamwise direction, numerical resolution in this direction does not seem to be very important. In the wall-normal direction, all simulations were conducted using Chebyshev polynomials, which ensure good resolution of the structures in the normal direction, especially close to walls.
The results of the calculation for $Re = 43,739$ on a $24 \times 36 \times 97$ mesh are presented on Fig. 3.14 (b). As we see, a logarithmic velocity profile with correct von-Karman constant is obtained here as well. However, the computed value $Re_\tau = 1,566$ was significantly lower than $Re_\tau = 1,980 - 2,100$ extracted from the experimental data on the pipe flow and from the Blasius expression for the friction coefficient. A reason for this disagreement could be found directly from Fig. 3.14 (b) where the poor resolution of the viscous sub-layer is evident. Repeating this calculation on a $24 \times 36 \times 192$-grid led to somewhat improved results: $Re_\tau \approx 1,687$ and the velocity distribution, which was closer to the law of the wall. Since at this low resolution we have only one point per two streaks, the remaining disagreement of the LES results with the experimental data may be attributed to the inadequate streak resolution. Another possibility is that the friction velocity given by the filtered equations may differ from the correct one. To address this problem, the simulations at $Re = 87,478$ were conducted on a $24 \times 96 \times 97$ grid, with more points in the spanwise direction, thus with improved streak resolution. The results, presented on Fig. 3.15 (a), show a grossly incorrect prediction of the von Karman constant and a value of $Re_\tau = 2,717$, which is approximately 40% smaller than the experimentally observed value. On the other hand, a $24 \times 36 \times 385$-simulation (Fig. 3.15 (b)) revealed a much improved value of the von Karman constant; the magnitude of the friction velocity remained too low.

Concluding, if the computational mesh is fine enough to provide at least one point per streak, the LES based on model Eq. (3.21) gives an accurate description of the turbulent channel flow. If this resolution requirement is not satisfied, the low-resolution LES of a high Reynolds number flow produces a mean velocity distribution which is in reasonable agreement with the experimentally observed one in the outer part of the flow (i.e. an accurate value of the von Karman constant). However, due to insufficient resolution in the spanwise direction, the calculated friction velocity and wall-stress are somewhat smaller than the ones observed in both physical and numerical experiments.

3.4 Conclusions

The Approximate Deconvolution Model (ADM) was investigated in spectral and spectral element codes for incompressible, turbulent channel flows. Two main points are considered:

ADM is implemented in a spectral element code for LES of incompressible, turbulent channel flows and the filtering is performed in spectral space for $Re = 2,800$ and $Re = 10,935$. The wall law for the mean streamwise velocity and the Reynolds and the shear stresses are considered.
The filtering was performed in spectral space based on Legendre and Boyd polynomials. Where filtering in the Legendre space does filter the boundary conditions, filtering in the Boyd space does not. The cutoff of the filter function is at $\kappa/N_s = 0.7$. According to this the characteristics of the filter as a function only of κ depends on N_s. The investigation showed that for $N_s \leq 4$ the mean velocity profile $\langle \underline{u} \rangle$ is affected by the filter and the friction Reynolds number Re_τ becomes very sensitive to the relaxation parameter χ_u.
The LES results for $Re = 2,800$ using ADM and the spectral element code were compared with the DNS results of Moser et al. [91]. The LES and DNS agree well, especially with respect to the wall law for the mean spanwise velocity. However, the maxima of the Reynolds stresses in the spanwise and wall-normal direction as well the shear stress in the range of $0.1 < |x_3| < 0.3$ are slightly underestimated by the LES, whereas the maxima of the Reynolds stress in the streamwise direction is slightly overestimated.
An LES for $Re = 10,935$ was performed to reduce the importance of the viscous effects compared to the LES of $Re = 2,800$. The agreement between the DNS and the LES for $Re = 10,935$ is good. Especially the wall law of the mean velocity, the Reynolds and shear stresses of the LES agree well the DNS results of Moser et al. [91].

The relaxation time of ADM (ADM was already implemented in the work of Stolz et al. [122]) of a spectral code was corrected by a local time determined from the rate of strain. This intermittency correction of Yakhot [144] suggest, that a relaxation term for shear flows based on Kolmogorov's theory should be corrected by the influence of the intermittency. The reason for using a global spectral code was the comparison of the present LES with the incompressible, turbulent channel LES results of Stolz et al. [122] who also used ADM in the same code.

The spatial resolution in wall-normal direction could be drastically reduced by the intermittency correction. LES results of $Re = 6,874$ and $Re = 10,935$ agreed well with the wall law and the friction Reynolds number Re_τ of the DNS with a spatial resolution of an LES of $Re = 2,800$.

Chapter 4

Isothermal Turbulent Jet

In contrast to turbulent channel flows, where the entire flow is stabilized by a confinement, turbulent jet flows are not stabilized by walls or similar conditions when entering an open region. Turbulent jets are widely used as benchmark cases for experimental and numerical investigations. The transition of a turbulent jet flow is a more challenging test for an SGS model than for a statistically stationary turbulent channel LES.
The Chapter is organized as follows: In Section 4.1 an introduction of the physics of isothermal, turbulent jets is given and in Section 4.2 an overview of related experiment and numerical work is presented. Section 4.3 defines the setup and Section 4.4 discusses the inflow treatment, especially the inflow generator used to perturb the mean inflow velocity profile. A preliminary LES is compared with experiment results in Section 4.5, and Section 4.6 presents the performed DNS. The final LES results are compared with the DNS in Section 4.7.

4.1 The Physics of Turbulent Jets

An axisymmetric jet is obtained when a fluid flows through a round orifice into a free space. The jet is considered as a *free jet* if it flows in an infinitely extended, quiescent and open space, or a *co-flowing jet*, if it is surrounded by a fluid flowing with velocity u_e in the streamwise direction. In Fig. 4.1 the unstable behavior of a variable density free jet is shown (the picture is from Van Dyke [132]). The flow is laminar as it leaves the nozzle and about one nozzle diameter, d_j, downstream instability, formation of vortex rings, and transition to turbulence can be observed. The

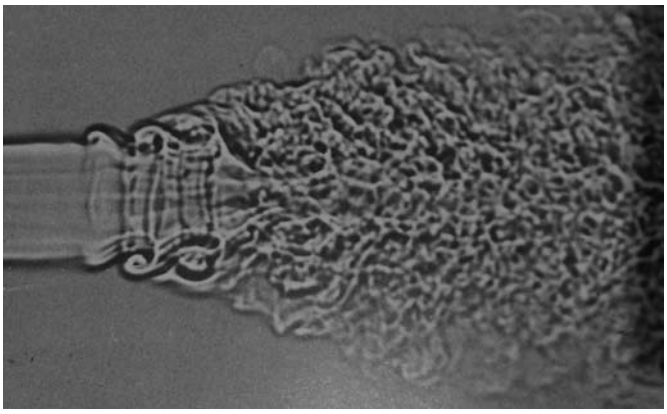

Figure 4.1: A shadowgraph of a round jet of carbon dioxide issuing into air at a Reynolds number of $Re = 30,000$.

jet behavior depends on parameters such as the ambient noise level, mean inflow velocity profile, and characteristics of the inflow perturbations at the orifice, and is further influenced by the entrainment of the surrounding fluid. The defining parameter is the Reynolds number Re,

$$Re = \frac{d_j(u_0 - u_e)}{\nu} \ , \tag{4.1}$$

where u_0, u_e and ν are the bulk velocity at the nozzle exit, the co-flow velocity and the kinematic viscosity, respectively. In addition to the velocity excess $\lambda = (u(0, r, \varphi) - u_e)/u_e$, defined at the jet exit, the jet velocity in the axial direction at the inflow is of interest for a co-flowing jet. Small differences in ambient-noise levels, different mean inflow velocity profiles and different levels of inflow perturbations as well the Reynolds number and the differences in the velocity excess can influence strongly the statistics of velocity. Therefore, direct comparison of the numerical results with experimental data is often difficult because not all mentioned parameters are available from the experiment.
The Reynolds number divides the jet in different flow regimes. The following definitions are based on experimental work and axisymmetric jets and the values are to be interpreted with some generosity. A laminar jet is present for Reynolds numbers $Re < 10$ (Pourquie [104]) and develops to a turbulent jet for Reynolds numbers between $10 < Re < 30$ (Pourquie [104]). A smooth, almost rectilinear, slightly diverging shape which moves to a chaotic, mushroom-shaped flow was the motivation of Viilu [133] to assume a turbulent jet for $Re > 10$. The rectilinear region increases, axisymmetric roll-ups are generated for Reynolds numbers between $30 < Re < 150$ and then breaks into a kind of droplets in

combination with the generation of paddel structures for Reynolds numbers of $150 < Re < 300$. Between $300 < Re < 1,000$ the length of the rectilinear region decreases with increasing Re and disappears for $Re > 2000$. The turbulent flow structures are not significantly affected by increasing Re (Pourquie [104]).
For $Re > 2,000$, which is the topic of the present work, the flow in the streamwise direction can be divided into three regions, shown schematically in Fig. 4.2. The *near-field* region is characterized by the transition to a turbulent flow field and is dominated by the potential core. It starts at the pipe exit with a fully developed turbulent profile with bulk velocity equal to u_0. Close to the orifice, the potential core is surrounded by a growing shear-layer which reaches the centerline after a distance of about 10 to 15 times the nozzle diameter downstream, where the potential core disappears (Olsson and Fuchs [93]). The mixing layer surface contains ripples, which scale with the initial boundary layer of the nozzle, initiate roll-ups and lead to vortex rings which become unstable and once again initiate helical structures (Petersen [97]). All turbulent quantities are fully developed in the *far field*, where all mean and fluctuating quantities become scale similar. Scale similarity implies that with an appropriate normalization the profile of a physical quantity, for example the velocity, becomes independent of the location. The *developing region* lies between the near and the far field, and is located between $5d_j$ and approximately $80d_j$. The mean axial velocity will become scale similar at $10d_j$, whereas the scale similarity of the velocity fluctuations is not reached until $40d_j$ in the axial direction, and $70d_j$ (Wygnanski and Fiedler [142]) for the radial and azimuthal components. If passive scalars are involved, their concentration fluctuations do not reach scale similarity until $80d_j$ (Dowling and Dimotakis [41]).
One can summarize as follows: after the merging of the shear-layers, asymmetric structures appear in the fully developed (far field) region of the jet. The self-preserving region is characterized by a linear increase in thickness, inversely proportional decay of the mean centerline velocity, and constant values of the centerline turbulence intensities (when normalized by the centerline velocity) with the axial distance from the jet exit. The far field is characterized by the fact that, by definition, turbulence is fully developed and therefore all physical quantities reach scale similarity, which is generally accepted for free jets but is not necessarily the case for co-flowing jets (see Rodi [110] and Antonia and Bilger [5]).

An important feature of all turbulent shear flows is entrainment,

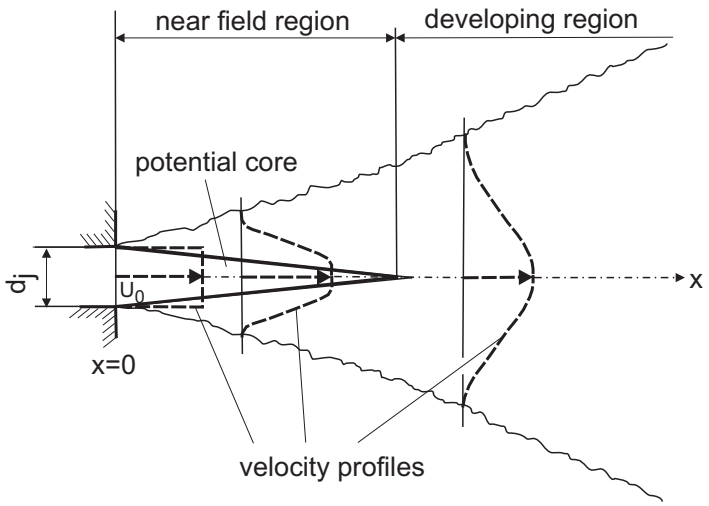

Figure 4.2: A free jet from the side view with its near region, which is potential-core dominated and its developing region in which the turbulent quantities are developed.

which is the process of moving the co-flowing fluid into the jet fluid, influencing the motion of both fluids. The jet behavior is very sensitive to the entrainment and its influence was investigated for example by Babu and Krishnan [10]. The potential core is seen to close earlier in the presence of entrainment and as a result the near-field turbulent intensities on the jet centerline are noticeably affected, while the far field with and without entrainment agree well with each other and with experiments.

A co-flowing jet (decrease of the mean centerline velocity, spread of the jet, entrainement) shows a strong dependence on the velocity excess $\lambda_e = u_e/(u_0 - u_e)$ and the jet development is similar to that of the free jet if λ_e is not too small and the considered flow region is not too far from the orifice. The co-flowing jet behaves significantly differently from the free jet far downstream if $\lambda_e < 10^{-1}$ and the jet no longer spreads linearly in the far field, but slowly in the axial direction (see Nickels and Perry [92] and Antonia and Bilger [5]). Two types of development are present in the developing region of a co-flowing jet: The development of the turbulent quantities (spreading rate, mean centerline velocity-decay, turbulence intensity) and the development of the variable velocity excess $\lambda_e(x)$ in the axial direction. Thus, the developing-region length can be completely different for different λ_e. Antonia and Bilger [5] report that for a co-flowing jet with $\lambda_e = 2$ self-similarity is reached for the axial velocity fluctuations at $x/d_j = 100$, but with $\lambda_e = 3.5$ it is still growing at $x/d_j = 250$.

4.1.1 Influence of the Confinement

Confined jets are jets with lateral walls and have the advantage of well-defined lateral boundary conditions. Confined jet flows are of interest for many practical applications. The configuration shown in Fig. 4.3, in which an axisymmetric jet discharges into a co-flow is relevant in particular to ejector systems and combustion chambers. Of particular relevance are the pioneering experimental and theoretical analysis of Craya and Curtet [31] and Curtet [32], which addressed the emergence of regions of reverse flow near the confining wall when a sufficiently weak co-flow is present. A dimensionless parameter based on similarity considerations is proposed to characterize the resulting flow, similar to that proposed by Thring and Newby [126] in their study of turbulent, co-flow diffusion flames, for which the recirculation flow provides a key stabilizing mechanism. For the case of uniform co-flow investigated by Craya and Curtet [31], the parameter reduces to the Craya-Curtet number $Ct = (J_c/J_j)^{1/2}$, where J_c and J_j represent the momentum fluxes of the co-flow and the jet, respectively. It has been observed by Barchilon and Curtet [11] that recirculation occurs in cylindrical ducts for $Ct \leq 0.9$.

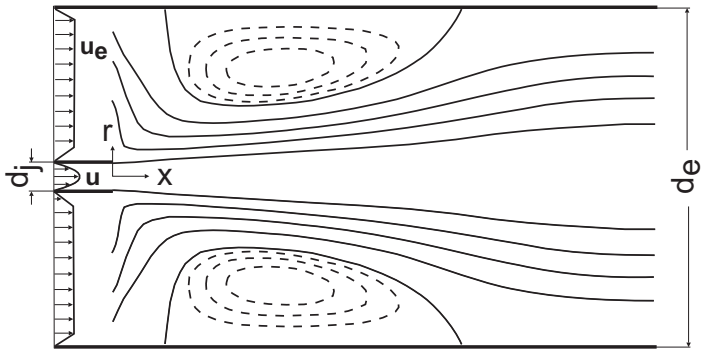

Figure 4.3: Streamlines of typical configuration with reverse flow for $Ct = 0.3$ (Revuelta et al. [109]).

4.2 Literature Review of Isothermal Jets

Turbulent jets have been studied in the past for different reasons, for example for aeroacoustics, for mixing or for self-similarity. Most work on turbulent jets is experimental, but also numerical results of DNS and LES are available in the literature. Most is focused on compressible, high-Mach number jet flows [83, 82, 50, 24, 147, 14, 15, 29, 35, 16, 129, 130], containing aeroacoustics effects, which are not part of this work. The

review here is mainly focused on the investigation of the scale-similarity behavior of turbulent jets.

Direct Numerical Simulations (DNS) of spatial evolving turbulent jets is relatively recent. Boersma et al. [13] used DNS to study the dependence of the far-field self-similarity of inflow conditions. More recently the work was extended for the study of mixing of a passive scalar by Lubbers et al. [81]. The works of Boersma et al. [13] and Lubbers et al. [81] were performed for $Re = 2,000$, without co-flow in a conical domain with a length of $40d_j$.

One of the earliest LES of a spatially developing, circular and low-Mach number turbulent jet is performed by Olsson and Fuchs [93]. The work is based on a dynamic Smagorinsky model, the mean inflow is perturbed by random noise to trigger the unstable modes and the investigation focused on the proximal region until $x/d_j = 12$. For different Reynolds numbers, the faster decay of the mean streamwise centerline velocity at lower Reynolds number was found to coincide with higher levels of turbulent velocity intensity. The investigation of inflow boundary conditions of co-flowing jets is the motivation of Glaze and Frankel [59] to perform an LES of $Re = 21,000$ for the experimental setup of Amielh et al. [3]. The work of Glaze and Frankel [59] used an inflow-velocity profile according to the 1/7-law and to investigate the difference of correlated and non-correlated perturbations. It was shown that correlated perturbations lead to a faster transition process of the turbulent jet. It was also demonstrated that it is difficult to get scale similarity results with synthetic generated perturbations.
Ribault et al. [76] performed LES of a planar jet for $Re = 3,000$ and $Re = 30,000$ in a domain with a length $x/d_j = 15$, comparing the Smagorinsky, the dynamic Smagorinsky and the dynamic-mixed models. For the perturbation of the mean inflow velocity correlated, synthetic fluctuations were used. The axial turbulent velocity intensity overshoot in the near-field region was not observed, but the results were surprising in giving overall better results with the dynamic Smagorinsy model than with the mixed model, contrary to what can be found in the literature (see Zang et al. [146] and Germano et al. [52]). In the work of Suto et al. [123], the Smagorinsky and the dynamic Smagorinsky in a round jet with scalar transport are compared and the results of the dynamic Smagorinsky are generally in better agreement with the experimental results than the standard Smagorinsky model. The dynamic Smagorinsky model is

almost exclusively used in the literature, with the exception of Rembold [108], where the Approximate Deconvolution Model was employed for the simulation of the transition of a rectancular, compressible jet.

4.3 Isothermal Jet Setup

Isothermal, confined, axisymmetric, turbulent jets in cylindrical coordinates for $Re = 2,000$ are considered in this Chapter. The cylindrical coordinate system and the setup are shown schematically in Fig. 4.4. Although the spectral element code works in a cartesian coordinate system, the results are transformed into the cylindrical one. In general, the advantage of a confined jet is that the boundary conditions on the lateral boundaries are well defined. The setup considered is based on the ex-

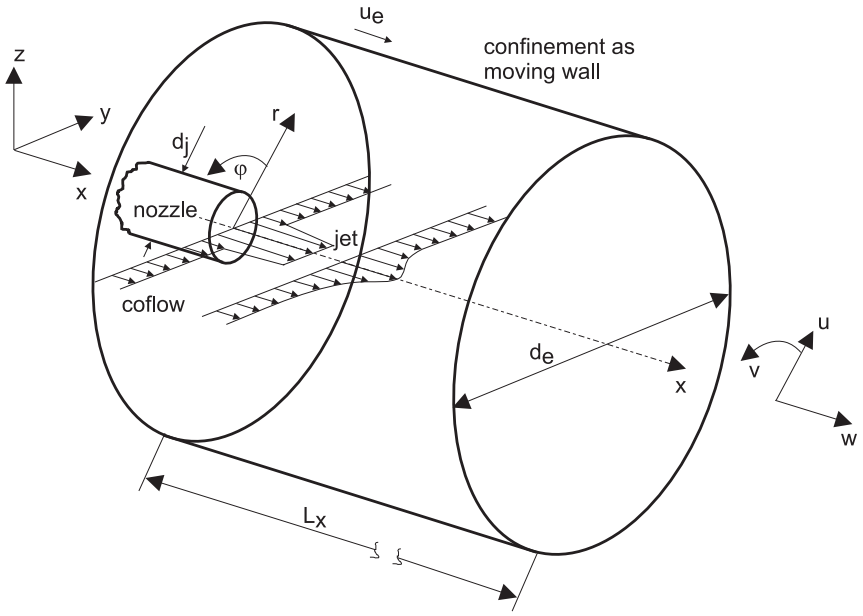

Figure 4.4: Setup for the isothermal turbulent jet with co-flow. The mean flow enters the domain through the nozzle, where it is be perturbed by the inflow generator. A moving-wall confinement is used as the lateral boundary for the velocity.

perimental setup of Amielh et al. [3] of a confined jet. In this work, wall moving with the velocity of the co-flowing stream is used to circumvent the near-wall refinement of the numerical grid and reduce the computational cost in comparison to the stationary walls of Amielh et al. [3]. Preliminary investigations showed no influence of the moving-wall confinement on the statistics of the turbulent jet. An axisymmetric round jet issues from a circular nozzle of diameter d_j and enters in a moving-wall confined

domain of diameter d_e in which a co-flow with streamwise velocity u_e is present. Dirichlet boundary conditions are used for the velocity on the inflow boundary according to Fig. 4.5, and for the jet velocity profile in the axial direction a fully-developed turbulent 1/7-law pipe flow profile according to Laufer [74] is used; the radial and azimuthal velocities at the inflow are set to zero $v(x/d_j = 0) = w(x/d_j = 0) = 0$. The mass flux of the 1/7-law velocity profile shown in Fig. 4.5 has the same mass flux as a top-hat profile with bulk velocity u_0

$$u_0 = \frac{8}{d_j^2} \int_0^{d_e/2} u(0, r, \varphi) dr \ . \tag{4.2}$$

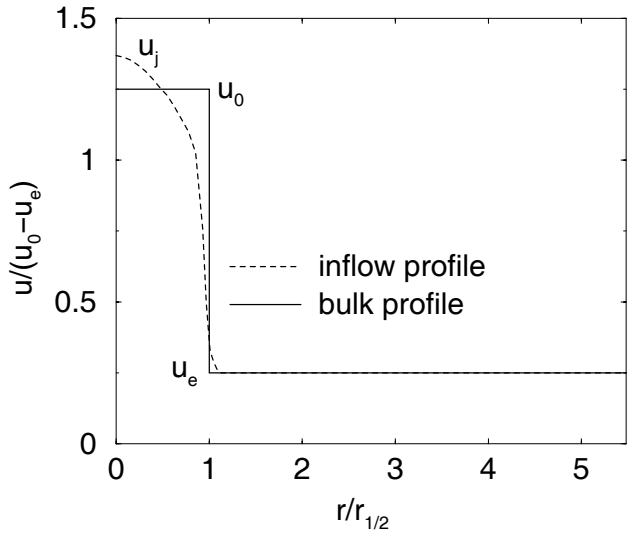

Figure 4.5: Mean axial velocity profile at the inflow in combination with the bulk velocity u_0. The maximum inflow velocity at the centerline is $u_j(0) = 1.369$.

The Reynolds number used in the following discussion is defined as

$$Re = \frac{(u_0 - u_e) d_j}{\nu} \tag{4.3}$$

and is in this Chapter set equal to $Re = 2,000$. The reference length, velocity and time scales are d_j, the velocity difference $(u_0 - u_e)$, and $d_j/(u_0 - u_e)$, respectively. The co-flow velocity of $u_e = \frac{1}{5} u_0$ is employed in order to prevent negative axial velocities at the outflow, which could lead to numerical instabilities, and Neumann velocity boundary conditions are imposed at the outflow (outflow boundary conditions). The velocity excess is $\lambda_e = \frac{u_0 - u_e}{u_e} = 4$ and should result, according to Antonia et

al. [5] in a linear inverse centerline decay of the axial mean velocity. The Craya-Curtet number for the isothermal jet is $C_t = 2.4 > 0.9$ and therefore does not lead to strong recirculation zones of the confined jet (see Section 4.1.1).
The computational domain has a length of $L_x = 40d_j$ and a diameter of $d_e = 10.96d_j$ and is discretized with a mesh of 1144 spectral elements. The spectral element skeleton of half of the domain is shown in Fig. 4.6.

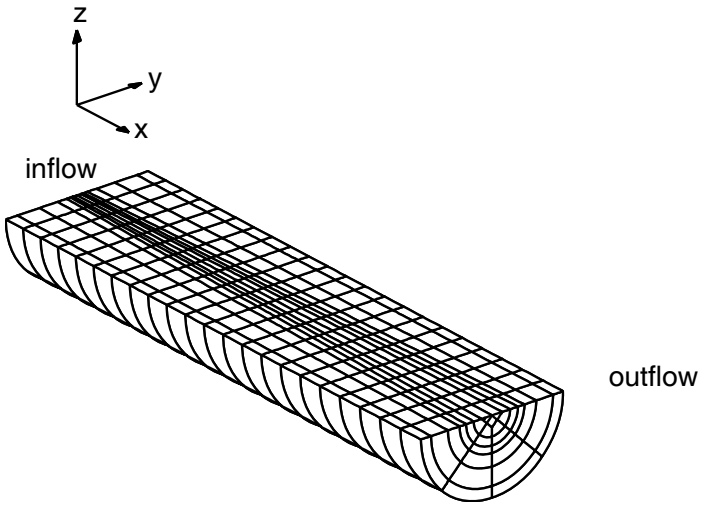

Figure 4.6: The geometry of half of the domain of the confined jet showing the spectral element skeleton that was used in the simulations presented in this Chapter.

The statistics presented in this Chapter are obtained by first simulating 200 time units to obtain a statistically-stationary solution that is used to initialize the final DNS or LES over 400 time units. The initial condition for the velocity of the very first simulation was a quite domain with velocity initial conditions at $x/d_j = 0$ shown in Fig. 4.5. The presented statistics are ensemble-averaged mean and correlations and are determined by computing the following summations during the simulation

$$\langle \phi \rangle = \frac{1}{N_t} \sum_{i=1}^{N_t} \phi(\underline{x}, t_i) \ , \tag{4.4}$$

where ϕ and N_t are physical quantities (velocities in streamwise and radial directions) and the number of timesteps, respectively. Turbulent intensities are then computed as

$$\langle \phi' \phi' \rangle^{1/2} = \langle \phi \phi \rangle - \langle \phi \rangle \langle \phi \rangle \tag{4.5}$$

(a) (b)

Figure 4.7: The vorticity of an LES of a jet at $Re = 2,000$ (a) with and (b) without disturbances of the mean velocity flow at the inlet.

$$\langle \phi' \xi' \rangle = \langle \phi \xi \rangle - \langle \phi \rangle \langle \xi \rangle \ . \tag{4.6}$$

4.4 Inflow Velocity Forcing

The transition from laminar to turbulent jet flows is initiated by perturbing the base flow. In experiments, such disturbances are omni present and could have their origin in rough nozzle walls or pump-pressure fluctuations. Well-resolved numerical simulations do not show such disturbances and resulted in laminar flows. Figure 4.7 shows the vorticity as a result of an LES with and without disturbances of the mean inflow velocity profiles. While the LES with disturbances shows a turbulent field, the LES without disturbances shows only convective Kelvin Helmholz instabilites. The generation of disturbances is a challenging task because they have to be correlated in space and time for correct break-up lengths of the jet.

In RANS simulations, depending on the closure model it may only be necessary to define parameters such as turbulent kinetic energy and its dissipation rate. Although this is not without its challenges, it is certainly easier to specify characteristics of a turbulent flow than it is to generate the turbulence itself. The latter is, unfortunately, necessary for time-resolved simulation techniques such as LES and DNS. Because both experimental and numerical results of jets indicate a strong sensitivity to inlet conditions (see Stanley and Sarkar [119], Mi et al. [87] and Glaze and Frankel [59]), their specification is critical. Considerable effort has been and still is investigated to develop generators of physical disturbances for realistic transition processes. The simplest way is the use of random noise. However, random-noise fluctuations will be damped to zero after a short streamwise distance due to the lack of energy in the low wavenumber range (the corresponding energy spectrum is constant) [68]. Alternatively, a turbulent pipe flow direct numerical simulation coupled to the inflow of

the jet domain would provide the best, physical inflow condition for the turbulent jet simulation, but is associated with high computational costs and is not practical as an engineering tool. An overview of so-called inflow generators is given by Klein et al. [68], where, among others, the inflow generator used in this work is proposed.
The inflow generator used in this work correlates random noise in space and time using a digital filter. Inflow of spatially and temporally correlated disturbances are generated for a number of timesteps N_t in a pre-processing step, stored in files and read in during the simulations. Following this, the experimental Reynolds stresses of a pipe flow from Moser et al. [91] are adapted to the generated disturbances and simultaneously superimposed to the mean velocity profiles.
The correlation in space and time of the fluctuated field is obtained with a digital filter from Klein et al. [68], leading to an approximate energy spectrum according to the Gaussian distribution of the correlation function in space

$$R_{uu}(\Delta_y, \Delta_z) = \exp\Big(- \frac{\pi \Delta_y^2}{4\sigma_y} - \frac{\pi \Delta_z^2}{4\sigma_z} \Big) \ , \tag{4.7}$$

and time

$$R_{uu}(\Delta_t) = \exp(-\frac{\pi \Delta_t^2}{4\sigma_t}) \ , \tag{4.8}$$

where σ is the desired Taylor microscale (see Fig. 4.8) and conforms to the correlation scale either in time, (σ_t), or in space, $\sigma_s = \sigma_y = \sigma_z$. From an engineering point of view, the Gaussian distribution of Eqs. (4.7) and (4.8) with the Taylor microscales as the only parameters is desirable. Perturbations for $\sigma = \sigma_t = \sigma_s = 0.1$ are generated by the inflow generator and the correlation functions of the target Eqs. (4.7) and (4.8) are compared with the correlation functions of the generated signal, as shown in Fig. 4.8. The generated signal shows a larger correlation scale but the agreement between the target and generated signals is acceptable. In Fig. 4.9, a random and a correlated instantaneous disturbation field for the velocity in the axial direction is shown. The humps of the correlated field change their height and spatial extend at a rate that depends on the temporal correlation σ_t.
The disadvantage of the digital filter based generation of inflow data (Klein et al. [68]) is the restriction to equidistant grids, which prohibits the direct application to the grid used in this work, or engineering problem grids in general, where non-equidistant grids are commonly used. To overcome this restriction, the inflow data, generated on an equidistant mesh, are interpolated to the non-equidistant mesh at the inflow boundary. The process

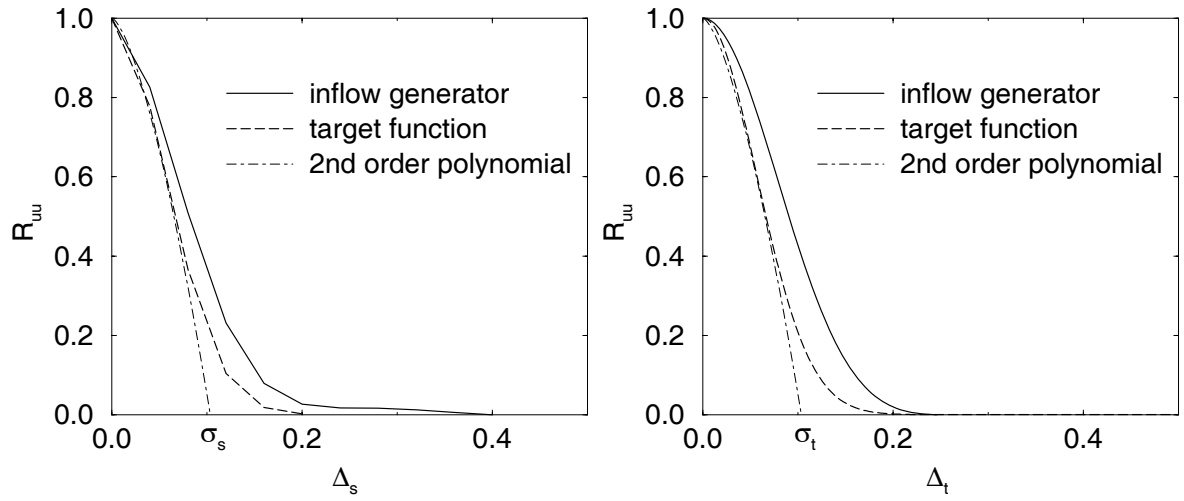

(a) (b)

Figure 4.8: Correlation functions for (a) space and (b) time. The correlation function of the generated field by the inflow generator is compared with its target function (Eqs. (4.7) and (4.8)). The intersection between the 2nd order polynomial curve and the abscissa defines the correlation length scale.

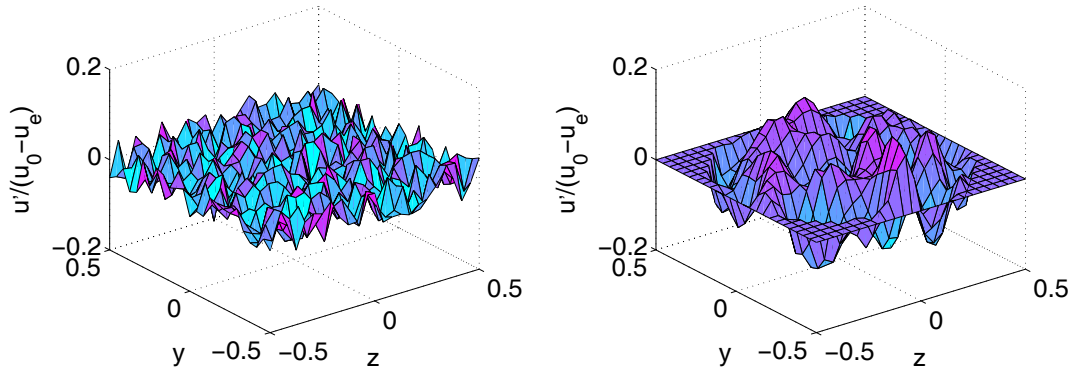

(a) (b)

Figure 4.9: Fields for perturbing the mean velocity field at the inlet (a) with random noise, (b) with correlation corresponding the inflow generator.

is schematically shown in Fig. 4.10 where the generated disturbances on a square mesh are interpolated to the computational mesh employed in the simulation.
At each timestep, the inflow generator provides a 2D field on an equidistant mesh with an edge of length d_j and a spatial resolution of $M_y \times M_z$, where $M_y = M_z = M$ are the number of points in the cartesian directions y and z. The generated field is then linearly interpolated to the grid points of the circular non-equidistant inflow boundary of the mesh. The

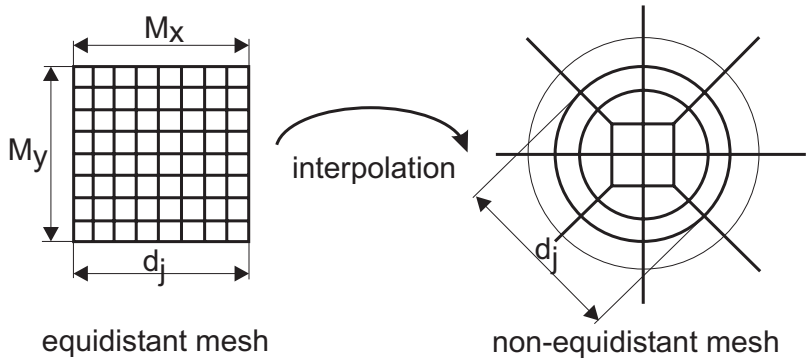

Figure 4.10: Interpolation from an equidistant mesh, on which the disturbances are generated, to the non-equidistant mesh used in the simulations. For the non-equidistant computational mesh only the spectral element skeleton is shown.

resolution M influences the quality of the interpolation and is investigated for the four different values given in Table 4.1. Further, the ratio of total number of the collocation points (number of elements times number of collocation points in each element) in the equidistant to the non-equidistant mesh Ω, based on an inflow boundary of diameter d_j, is also shown in Table 4.1. The influence of M on the performance of the interpolated

Case	$M_y \times M_z$	Ω
vlow	11×11	0.05
low	25×25	0.3
std	47×47	1.0
high	61×61	1.7

Table 4.1: Inflow generator resolution cases

field (i.e. after interpolation from the equidistant to the non-equidistant mesh for *vlow*, *low*, *std* and *high* case), with respect to the normal and

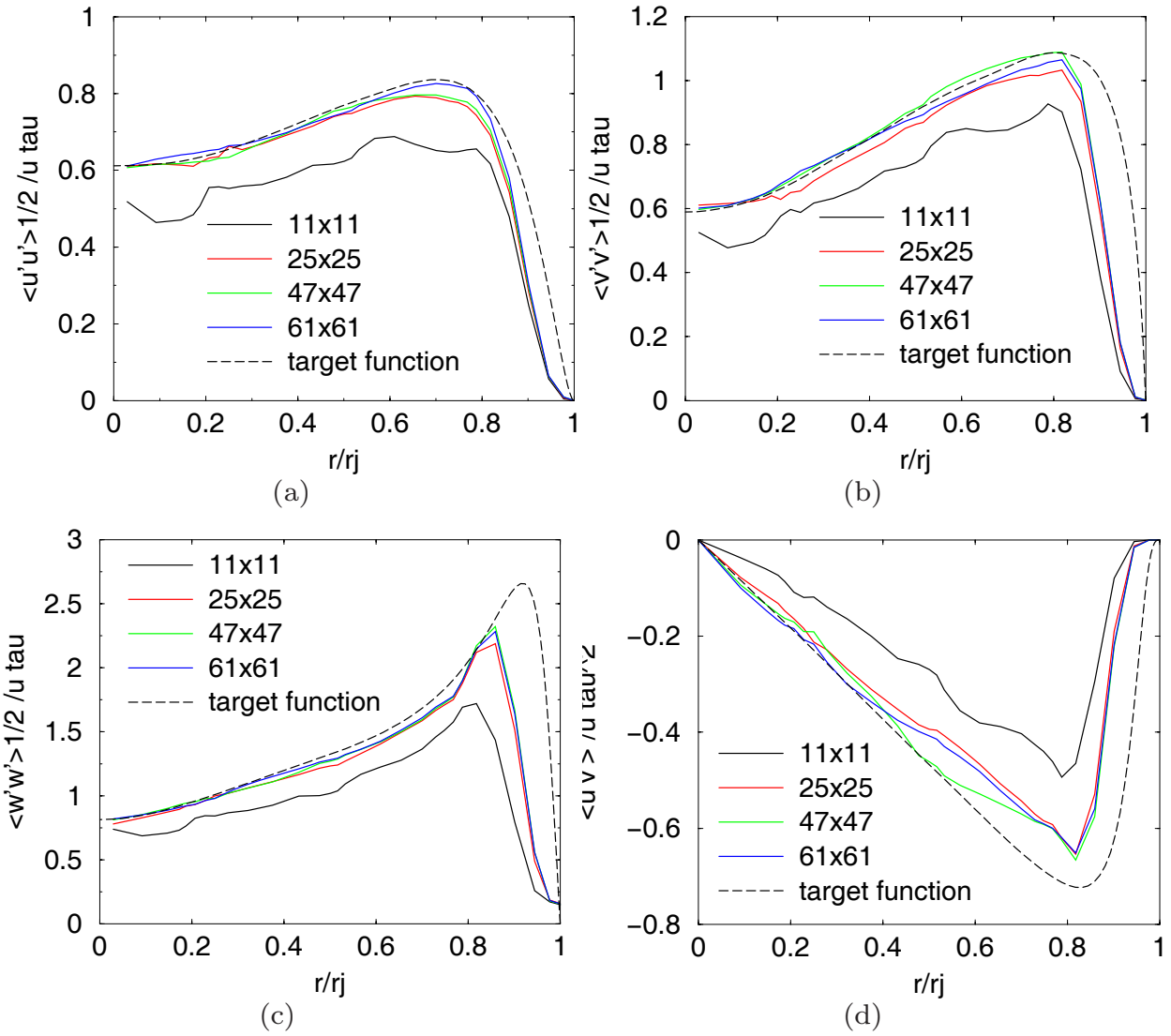

Figure 4.11: Validation of the inflow generator: Reynolds normal stresses in (a) circumferential, (b) radial and (c) axial direction, and (d) Reynolds shear stress compared with the target functions of [91]

shear stresses of the synthetic flow field, is shown in Fig. 4.11, where the target results are from Moser et al. [91]. The equidistant mesh data are based on $\sigma_s = \sigma_t = 0.1$ and the non-equidistant mesh corresponds to the mesh of Fig. 4.6. The results after interpolation for *low*, *std* and *high* are almost identical and therefore, for all further simulations an equidistant resolution of $M = M_y = M_z = 25$ will be used.

The generation of the synthetic, correlated inflow fields is done in a pre-processing step. The CPU-time for the generation of N_t correlated fields (N_t is the number of timesteps for the jet simulation) depends on the correlation scales σ_t and σ_s and the spatial resolution. The generation of

49,000 correlated fields with a resolution of $M_y = M_z = 25$ and correlation scales of $\sigma_t = \sigma_x = 0.1$ requires around 100 hours of CPU-time on a single processor machine and generates data of about 1.4 GB.

4.5 Preliminary LES

The aim of this Chapter is the comparison between the LES of the isothermal, turbulent jet and experimental results from Amielh et al. [3].
The setup is identical to the one described in Section 4.3, and the LES is performed with the mesh of Fig. 4.6 using 8th order interpolating polynomials ($N_s = 8$). The coupled set of Favre filtered differential equations Eqs. (2.44) to (2.48) reduces to

$$\nabla \cdot \underline{\overline{u}} = 0 \tag{4.9}$$

$$\frac{\partial \underline{\overline{u}}}{\partial t} + \overline{\underline{u}^{\star}(\nabla \cdot \underline{u}^{\star})} + \nabla \overline{p}_2 = \frac{1}{Re}\nabla^2 \underline{\overline{u}} - \chi_u (I - Q_N * G) * \underline{\overline{u}} \,, \tag{4.10}$$

where the equations are based on the assumption of constant dynamic viscosity μ_∞ and the absence of buoyancy and $Re = 2,000$. The Boyd filter is used for ADM (see Section 2.5.4) with cutoff $\kappa_{ct} = 0.7$, the relaxation parameter is set to $\chi_u = 100$, the inflow generator on $\sigma_s = \sigma_t = \sigma = 0.1$ is used to perturb the mean inflow velocity profiles, and a timestep of $dt = 0.001$ is used. The top-hat profile (smoothed via tanh) is used as the mean inflow profile.

The velocity statistics from the LES along the centerline are shown in Fig. 4.12 and compared with the experimental data from Amielh et al. [3]. Four observations can be made:

- The mean axial velocity on the centerline of the preliminary LES decays faster than in the experiments (Fig. 4.12 (a)).
- The axial turbulent velocity intensity overshoots the experimental profile in the region of $10 < x/d_j < 20$ (Fig. 4.12 (b)).
- The axial turbulent velocity intensity increases much faster than the experiment (Fig. 4.12 (b) and (c)).
- The axial and radial turbulent velocity intensity is overestimated by the preliminary LES compared to the experiment (Fig. 4.12 (b) and (c)).

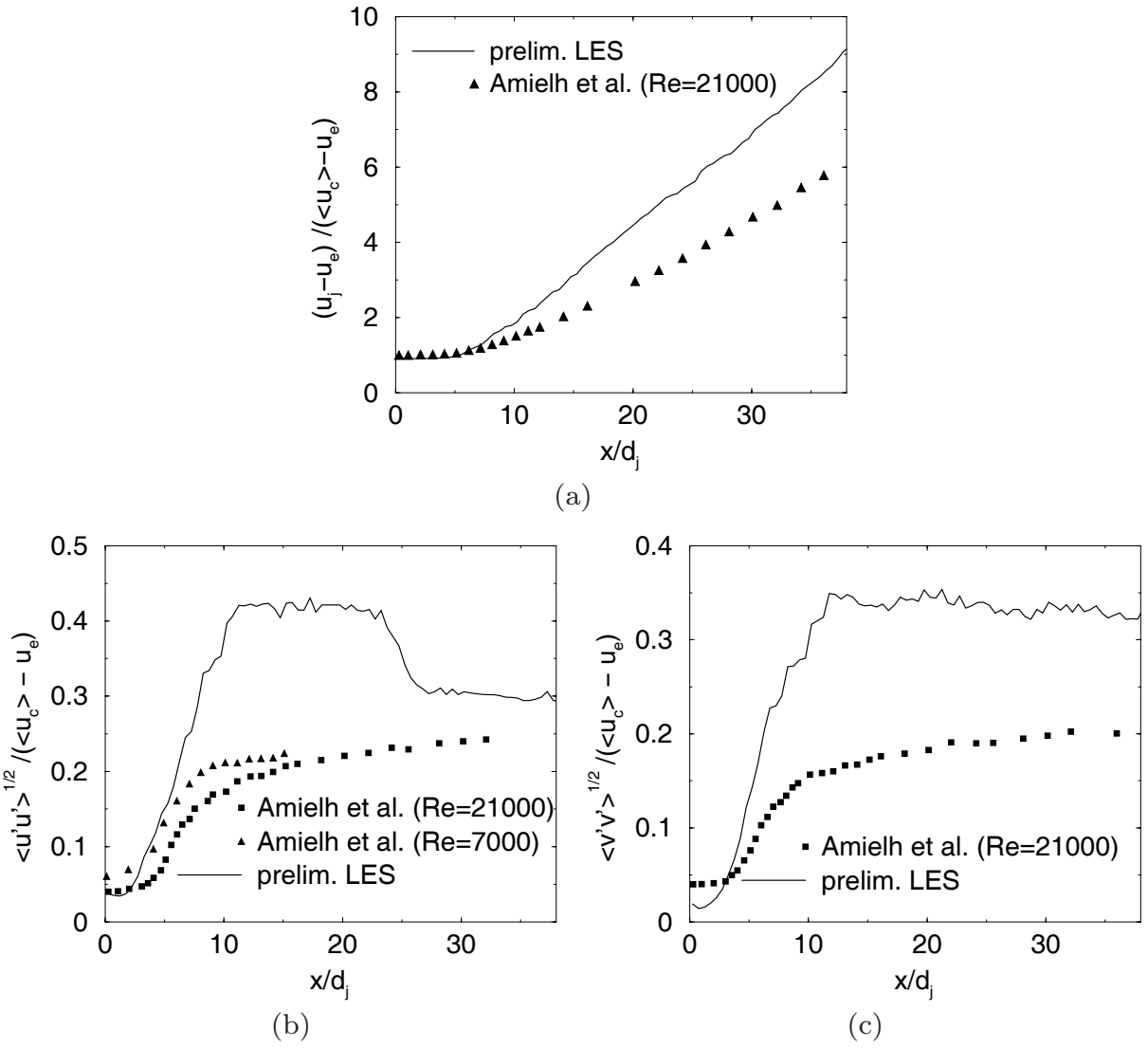

Figure 4.12: Preliminary LES with the top-hat velocity profile and using the Boyd filter compared with experimental data form Amielh et al.[3]: (a) mean, axial velocity decay, (b) turbulent velocity intensity in axial direction and (c) turbulent velocity intensity in radial direction along the centerline.

The experimental data of Amielh et al. [3] are based on $Re = 21,000$ and on $Re = 7,000$. It is evident from Fig. 4.12 (b) that the slope of the axial turbulent velocity intensity in the experiment is increasing by reducing the Reynolds number from $Re = 21,000$ to $Re = 7,000$. The preliminary LES is performed for $Re = 2,000$ and therefore, the faster increase of the preliminary LES can be partially attributed to the low Reynolds number of the LES. The next question was the overshoot, especially of the axial turbulent velocity intensity of Fig. 4.12 (b). It is not clear whether the overshoot has its origin in the subgrid model of ADM or results from the

boundary conditions of the numerical simulation.
The detailed boundary conditions on which the experimental results are based is unknown. Therefore the comparison between experimental and numerical results is difficult because small changes of boundary conditions (i.e. pressure fluctuations, level and correlation of velocity inflow perturbations, mean inflow velocity profiles) have a strong effect on the behavior and the statistics of the turbulent jet. To explain the overshoot of the axial turbulent velocity intensity several parameters of the LES code were investigated: inflow profile (smoothed top-hat and 1/7-law profile; different levels of inflow perturbation ($\sigma = 0.1$ and $\sigma = 0.15$); the turbulent flow of the nozzle was simulated instead of using the inflow generator; ADM relaxation parameter χ_u, the LES filter function κ_{ct} and the filter-type (Boyd- and Legendre filter); and instead of a moving-wall confinement a real walls were simulated at d_e.
The investigations showed some partially improvement in some cases, but the overshoot could not be eliminated. There is still the uncertainty of identical boundary conditions between the experiment and the simulations. Therefore it is not possible to dedicate the overshoot of the LES because of boundary conditions or because of ADM.
Therefore, it was decided to perform a DNS with exactly the same boundary and initial conditions as for the LES and to use the DNS data for further comparisons.

4.6 Direct Numerical Simulation

The set of differential equations Eqs. (2.1) to (2.4) for the DNS of the isothermal, incompressible, turbulent jet reduces to

$$\nabla \cdot \underline{u} = 0 \tag{4.11}$$

$$\frac{\partial \underline{u}}{\partial t} + \underline{u}(\nabla \cdot \underline{u}) + \nabla p_2 = \frac{1}{Re} \nabla \cdot \underline{\underline{S}} \,, \tag{4.12}$$

assuming constant dynamic viscosity μ_∞ in the absence of buoyancy. The inflow generator with $\sigma_s = \sigma_t = \sigma = 0.1$ is used to perturb the mean inflow velocity profiles based on the 1/7-law profile according to Laufer [74]. The DNS is performed for $Re = 2,000$ with the spectral element mesh of Fig. 4.6, with a polynomial order of $N_s = 12$ and a timestep of $dt = 0.001$.
The DNS results will be compared with the experimental results of Amielh et al. [3] which were obtained for $Re = 7,000$ and for $Re = 21,000$. The

comparison of results based on different Re is in principle allowed only if the results are normalized and are compared in the scale-similarity region of the jet ($x/d_j > 10$). The experimental data of $Re = 7,000$ and $Re = 21,000$ are used to verify the plausibility of the DNS results in the scale-similarity region.

Two DNS of isothermal, turbulent jets are of interest in the literature (already discussed in Section 4.2).
The first DNS is the work of Boersma et al.[13] of a round turbulent jet with $Re = 2,400$ without co-flow. The goal was the investigation of the effect of the inflow conditions on the self-similarity region of a round jet. Boersma et al. [13] use a conical mesh with a diameter of $4d_j$ at the inflow, a diameter of $10.3dj$ at the outflow and a length in streamwise direction of $45d_j$. A mean axial top-hat was used without forcing. Walls, which allow entrainement are set as lateral boundary conditions and at the outflow outflow-boundary conditions are used. The governing equations are discretized on a three-dimensional grid with a second-order finite volume method and integrated with a second-order Adams-Bashforth scheme in time. The discretization of the grid is done by $450 \times 80 \times 64$ cells (axial, radial, azimuthal directions, respectively).
The second DNS is the work of Rembold [108] of a rectancular turbulent jet with $Re = 2,000$ without co-flow. The ratio of the domain height L_3 to the width of the rectangular nozzle is equal to five and the Reynolds number is based on the size of the nozzle L_3. The aim of the work was the investigation of the transition of the jet. Rembold [108] used a rectangular mesh with a domain height of $8.75L_3$, a width of $8.75L_3$ and a length of $18.75L_3$. A top-hat mean axial velocity profile perturbed by the inflow generator of Klein et al. [68] was used. The governing equations are discretized on a three-dimensional grid with a fifth-order compact upwind scheme and integrated with a third-order Runge-Kutta scheme in time. The discretization of the grid is done by $229 \times 229 \times 337$ cells (domain height, width, length).
The spatial resolution of the studies of Boersma et al. [13] and Rembold [108] are used in the next Section for comparison with the DNS resolution of the isothermal, turbulent round jet of this work.

4.6.1 Spatial Resolution Study

The governing equations are discretized in space using the spectral element skeleton shown in Fig. 4.6 (the half of the domain is shown) with $1,144$ spectral elements. Three different polynomial orders N_s, defined in

Table 4.6.1, are used for the DNS and the resolutions are compared with the resolutions reported above. The resolution in the axial and radial direction (Δx and Δr) is normalized with the nozzle diameter d_j in Table 4.6.1.

The spatial resolution of the DNS with $N_s = 12$ in the axial direction is higher than the axisymmetric DNS of Boersma et al. [13] but lower than for the rectangular DNS of Rembold [108]. The comparison of the spatial resolution in the radial direction (measured at the outflow diameter of $10.96d_j$) of the present DNS with $N_s = 12$ is comparable with the DNS of Boersma et al. [13] and Rembold [108]. Summarizing, the spatial resolution of the present DNS with $N_s = 12$ is comparable with the literature but the DNS with $N_s = 8$ and $N_s = 10$ are under-resolved. Numerical instabilities were observed for $N_s = 8$ and 10 and the simula-

Sim.	**flow**	Re	Δx	Δr	
DNS	axis. 3D jet	$2,000$	$0.226d_j$	$0.0961d_j$	$N_s = 8$
DNS	axis. 3D jet	$2,000$	$0.181d_j$	$0.0772d_j$	$N_s = 10$
DNS	axis. 3D jet	$2,000$	$0.151d_j$	$0.0647d_j$	$N_s = 12$
DNS	axis. 3D jet	$2,400$	$0.5d_j$	$0.023d_j$	[13]
DNS	rect. 3D jet	$2,000$	$0.0556L_3$	$0.0382L_3$	[108]
-	HIST	$2,000$	$0.0033d_j$	$0.0033d_j$	[70]

Table 4.2: Comparison of spatial resolutions of DNS, literature and Kolmogorov's theory. The Δ values (x: axial, r: radial) are normalized on the nozzle diameter d_j. axis jet: axisymmetric jet; rect. jet with nozzle height of L_3 : rectangular jet; HIST: homogeneous, isotropic turbulence

tion could not be performed. The statistics for the DNS with $N_s = 12$ are shown in Fig. 4.13 for the centerline profiles and in Fig. 4.14 for the radial profiles. The results are compared with the experimental data of Amielh et al. [3]. The decay in the DNS starts earlier, but the slopes after $x/d_j = 20$ of the experiment and the DNS are identical. The earlier begin of the DNS decay can be explained by the lower Reynolds number used ($Re = 2,000$ for the DNS and $Re = 21,000$ for the experiment). The influence of the Re is shown in Fig. 4.13 (b) where the axial turbulent velocity intensity along the centerline is plotted. The experimental data show that the breakup begins earlier for lower Reynolds numbers than for higher Re. The turbulent velocity intensity in the axial and radial directions show a faster increase of the intensity after breakup than the

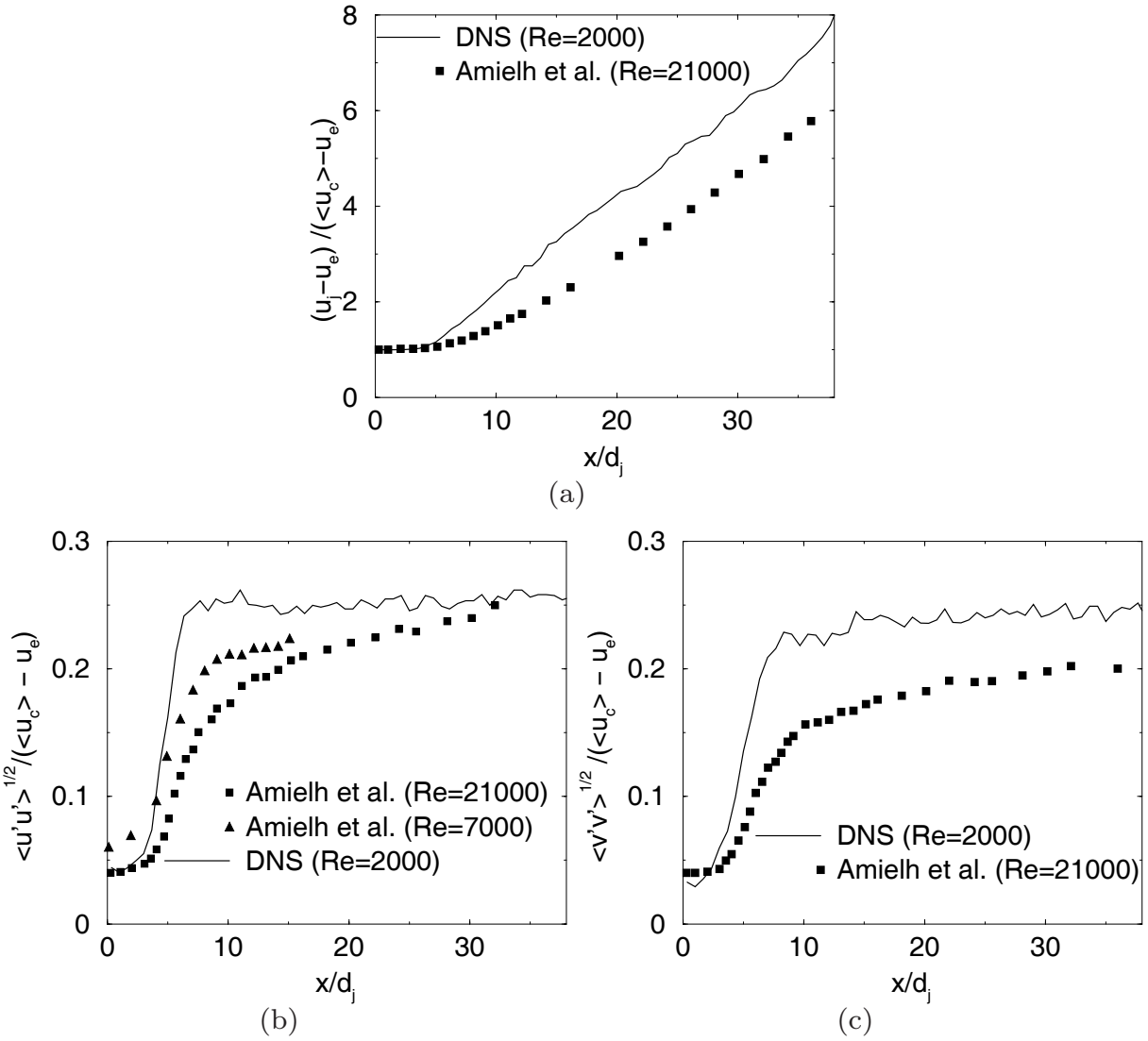

Figure 4.13: Comparison between DNS using the 1/7-law velocity inflow profile with $N_s = 12$ and experiment results of Amielh et al. [3]: (a) mean axial velocity, (b) turbulent velocity intensity in the axial and (c) in the radial direction.

experimental one and reach a plateau with a constant level of 25% and 24%, respectively, at approximately $x/d_j = 10$, while the experiment increases slower and reaches the plateau further downstream. After $x/d_j = 30$, the centerline axial velocity intensity of the DNS reaches the same value of intensity as the experiment, where the radial DNS intensity overestimates the experiment by 25%.

The radial distributions are shown in Fig. 4.14 for $x/d_j = 15$ and 20, respectively. The good agreement of the mean axial velocity between DNS and experimental results over the radius of the jet is evident, as illustrated in the profile of Fig. 4.14 (a), whereas the DNS normal

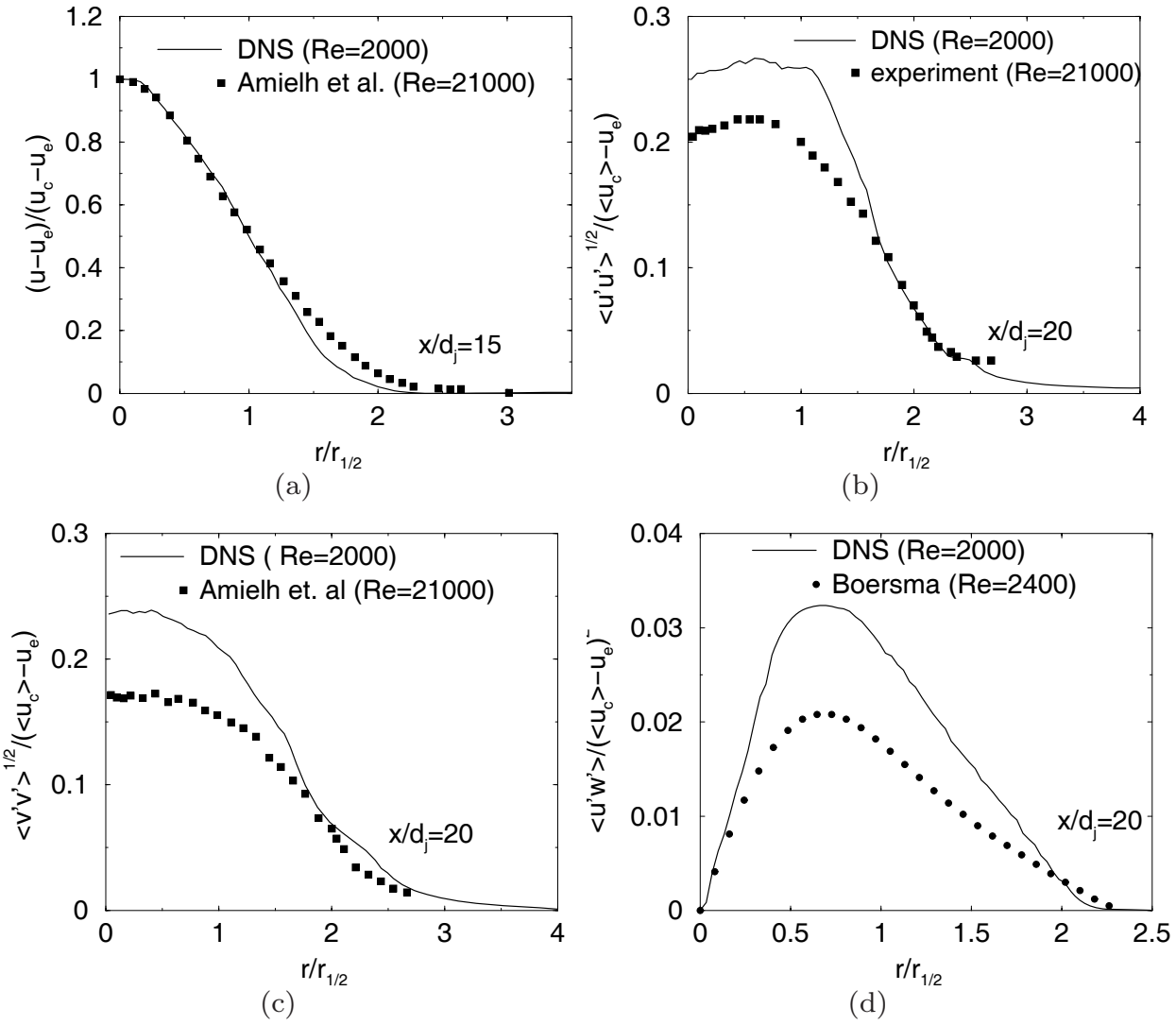

Figure 4.14: Comparison between DNS data of Boersma et al. [13] and experimental data of Amielh et al. [3]: (a) mean axial velocity at $x/d_j = 15$, (b) normal stress in axial direction at $x/d_j = 20$, (c) normal stress in radial direction $x/d_j = 20$ and (d) shear stress at $x/d_j = 20$ across the radius of the jet.

stresses in the axial and radial directions (see Fig. 4.14 (b)and (c)) agree qualitatively but overestimate the experimental results (the DNS shows a 30% higher axial turbulent velocity intensity at $x/d_j = 20$). The overestimation can be explained by the slower increase of the experimental velocity turbulent intensities in the axial direction (Fig. 4.13 (b)). The shear stress in Fig. 4.14 (d) is qualitatively correct but overestimates the experimental results, a consequence of the overestimation of the axial and radial stresses.

Given the significant difference in Re and the uncertainties in the bound-

ary conditions, the agreement between the DNS and the experimental results of Amielh et al. [3] and the DNS shear stress of Boersma et al. [13] is considered to be acceptable, and the DNS data will be used for validation of the LES.

4.7 Large Eddy Simulations

Large Eddy Simulations of isothermal, turbulent jets for $Re = 2,000$ will be compared with the DNS data of the previous Section. The LES is performed for the setup proposed in Section 4.5.

4.7.1 Spatial Resolution Study

The effect of spatial resolution on the LES results using the Legendre filter is investigated by varying the polynomial order N_s. The spatial resolution is compared with LES from the literature and is summarized in Table 4.7.1. The polynomial order for the present LES is varied between $N_s = 6$, 8 and 12. It should be noted that contrary to the unstable DNS for $N_s = 8$ LES is stable for all resolutions considered. In Table 4.7.1 estimates of the smallest length scale of the flow according to Kolmogorov's theory are given. Preliminary tests in Section 4.5 with the setup showed the most sensitive effects on the turbulent velocity intensity on the centerline when the spatial resolution in radial direction was changed. In this work the highest spatial resolution was used in the radial direction which is evident in Table 4.7.1.

Sim.	**flow**	Re	Δx	Δr	
LES	axis. 3D jet	$2,000$	$0.301d_j$	$0.127d_j$	$N_s = 6$
LES	axis. 3D jet	$2,000$	$0.226d_j$	$0.0961d_j$	$N_s = 8$
LES	axis. 3D jet	$2,000$	$0.151d_j$	$0.0647d_j$	$N_s = 12$
LES	axis. 3D jet	$10,000$	$0.1d_j$	$0.1d_j$	[93]
LES	rect. 3D jet	$2,000$	$0.166L_3$	$0.114L_3$	[108]
-	HIST	$2,000$	$0.0033d_j$	$0.0033d_j$	[70]

Table 4.3: Spatial resolutions for the present LES compared with the literature and Kolmogorov's theory. (axis jet: axisymmetric jet; rect: rectangular jet with nozzle height of L_3; HIST: homogeneous, isotropic turbulence)

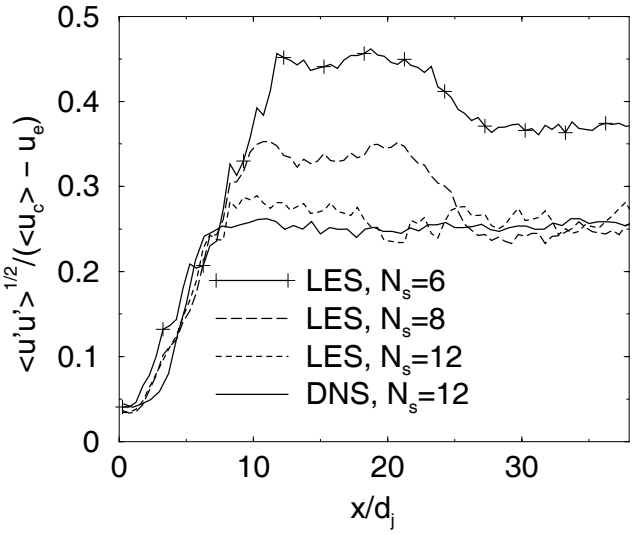

Figure 4.15: Turbulent velocity intensity on the centerline in axial direction of the resolution study with the mesh of Fig. 4.6 and for $Re = 2000$. The comparisons are done with results from LES (with the Legendre filter) and DNS using top-hat inflow profile.

The LES spatial results are compared with the DNS results obtained with $N_s = 12$; LES and the DNS are performed with the top-hat mean axial velocity profile (see Fig. 4.32). The axial turbulent velocity intensities along the centerline from the LES with $N_s = 6$, 8 and 12 are compared with the DNS result for $N_s = 12$ in Fig. 4.6. All three LES show an overshoot in the region of $10 < x/d_j < 20$. The overshoot is investigated in the next Sections and, in the context of spatial resolution, only the quantitative results will be considered. As expected, for the same resolution LES and DNS give very similar results. The centerline turbulent velocity intensity stabilizes at 28% and almost no LES-overshooting is seen in the near field. If the LES resolution is reduced to $N_s = 8$ and 6, the overshoot at approximately $x/d_j = 10$ increases with lower N_s, whereas for $N_s = 8$ the turbulent velocity intensity reduces to the DNS value of 28% at $x/d_j = 25$. The overshoot for $N_s = 6$ increases to 40% and does not decrease to the DNS value. The mesh of Fig. 4.6 with $N_s = 8$ will be employed for the turbulent-jet LES with $Re = 2,000$.

Figure 4.16 shows the CPU time for the LES with $N_s = 6$, 8 and 12 in comparison with the CPU time for the DNS with $N_s = 12$ after $50,000$ timesteps. The CPU time for the simulations increases almost linearly with increasing the resolution.

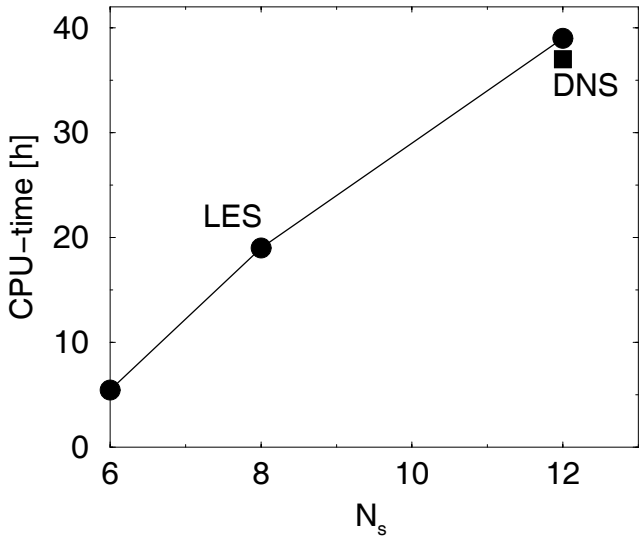

Figure 4.16: CPU-time, based on 64 parallel processors and 50 time-units simulation (50,000 timesteps) for the LES with different resolutions and the DNS.

A Priori Investigations

The basis of the *a priori* investigations are the results of the DNS with $N_s = 12$, described in Section 4.6. The axial velocity-field of the DNS is filtered and the deconvolved field, $(Q_N * G)\underline{\overline{u}}$, and the field of the relaxation term, $\chi_u(I - Q_N * G)\underline{\overline{u}}$ with $\chi_u = 1.0$, are computed using the Boyd and the Legendre filter for different deconvolution orders N_d. These Section contains two parts: first, the filtered centerline axial velocity and the relaxation term are investigated and the behaviour at the elemental boundaries for the Boyd- and the Legendre filter are considered. Then the DNS fields are interpolated onto the LES grid and compared for both filters for different deconvolution orders and cutoff scales.

The influence of the filter on the subgrid model ADM is analyzed in the following. ADM is based on a inverse-model approach (see Chapter 1) and uses a relaxation term $(I - Q_N * G) * \underline{\overline{u}}$ to increase the dissipation. The relaxation term can be rewritten as

$$(I - Q_N G) * \underline{\overline{u}} = \underline{\overline{u}} - (Q_N G) * \underline{\overline{u}} \ , \tag{4.13}$$

acts as a high-pass filter (see Fig. 2.3) and depends on the filter function as well as on the filter type (Legendre or Boyd). As discussed before, the filtering with the Legendre filter affects differently the points on the elemental boundaries between two neighboring elements. The direct-stiffness summation operator is applied to smooth out the differences. The effect

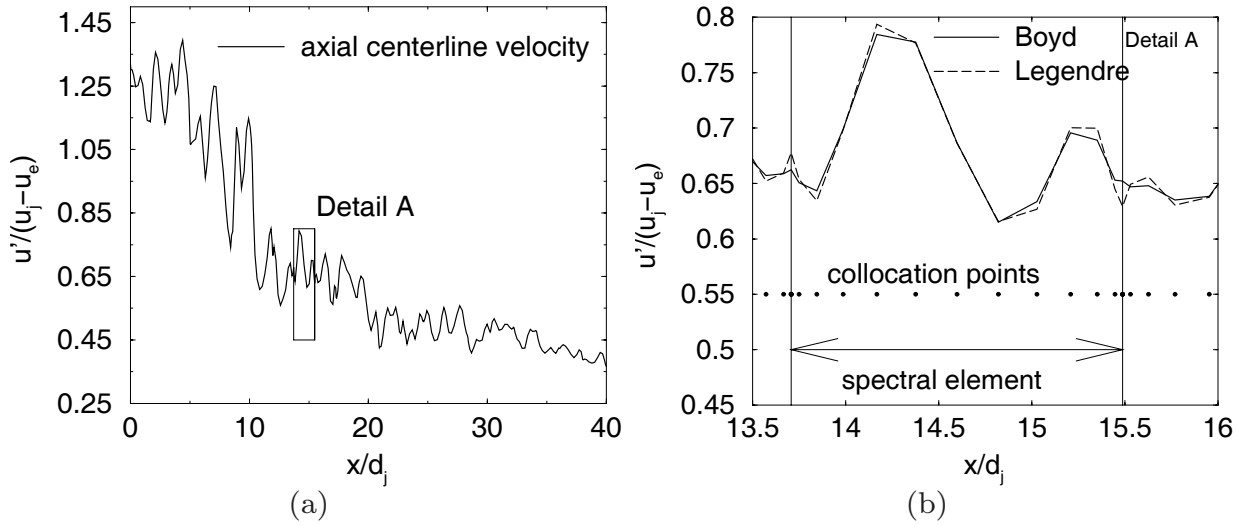

Figure 4.17: (a) Centerline axial velocity of an isothermal jet is used to show the effect between the Boyd and Legendre filter at the elemental boundaries: (b) Boyd- and the Legendre filter (Detail A). The horizontal points mark the collocation points of the spectral element.

of this unnatural process can be seen in Fig. 4.17 which (a) shows the axial velocity of the filtered field along the centerline of the jet. In Fig. 4.17 (b) the filtered solutions with the Boyd and the Legendre filter for the region marked as *Detail A* are shown. The influence of the Legendre filter is obvious, with the solution showing peaks at the elemental boundaries, which are not present when the Boyd filter is used.
The right hand-side of Eq. (4.13), which corresponds to the relaxation term, contains only filtering operations. With the Boyd filter the solution at the elemental boundaries will be unaffected and the application of the operator of Eq. (4.13) leads to a solution at the elemental boundaries which is zero.

The results for both filters are shown in Fig. 4.18, where the values of the relaxation term along the centerline for the spectral elements of *Detail A* are shown. It is obvious, that the solutions for the Legendre filter at the elemental boundaries are zero. This leads in general to a lower relaxation term for the Legendre filter.

In order to compare the LES and the DNS results, the DNS field (denoted as unfiltered field) of the axial velocity u is first interpolated from DNS grid $N_s = 12$ to the LES grid ($N_s = 8$, same spectral element skeleton). This operation can be considered as a mesh filter and is denoted by the operator Γ. Thus, the filtered field $\overline{\Gamma(u)}$, the

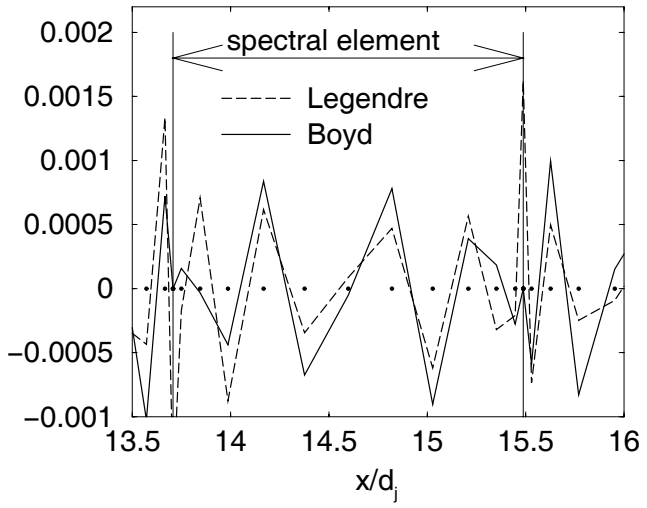

Figure 4.18: Centerline values of the relaxation term in axial direction for Detail A (see Fig. 4.17) and the Boyd and the Legendre filter.

deconvoluted field $\Big(\Gamma(u)\Big)^{\star}$, the QNG-term $(Q_N * G)\overline{\Gamma(u)}$, and the relaxation term $(I - Q_N * G)\overline{\Gamma(u)}$ are determined. Figs. 4.19 to 4.26 show the instantaneous fields for the Boyd and the Legendre-filter, for deconvolution orders $N_d = 3, 5, 7, 9$ and for two different filter functions ($\kappa_{ct} = 0.7$ and $\kappa_{ct} = 0.6$). The following observations can be made:

1. As expected, the mesh- and LES-filtered field (denoted as filtered field in the figures) are smoother than the original, unfiltered field.

2. The lower the cutoff scale κ_{ct} for both filters, the higher are the values of the relaxation term;

3. The Legendre filter shows a higher magnitude of the relaxation term, compared to the Boyd filter, containing larger structures.

The filter-function inversion (Eq. (2.57)) is performed as an infinite series which is truncated at some order N_d. In the ideal case, the filter-function inversion converges to a perfect inversion as N_d is increased. The consequences are seen in Figs. 4.19 - 4.26 where with increasing N_d the relaxation term becomes disappearing.
The deconvolved field is perfectly inverted from the filtered field up to κ_{ct}. The cutoff scale κ_{ct} is the location on the κ/N_s-axis where the high-pass filter function $(I - Q_N * G) * \overline{u}$ starts to increase with increasing κ/N_s (see Fig. 2.3). It is obvious from this point of view that the relaxation term for $\kappa_{ct} = 0.6$ contains more higher-mode information than it does for $\kappa_{ct} = 0.7$. This is the reason why a higher value of N_d (for example,

$N_d = 9$) shows lower values of the term than a lower one (for example, $N_d = 3$).
One can infer from the theory of ADM that the better the inverse filter Q_N is the less information contains the relaxation term $(I - Q_N * G)$ (this is the case for high N_d or a large κ_{ct}). The relaxation term is needed for stabilizing the LES and it is necessary to have high-mode information in it. The relaxation terms of both filters, Boyd and Legendre, contains high-mode information whereas the relaxation term of the Legendre filter shows a more intens behavior with larger structures.

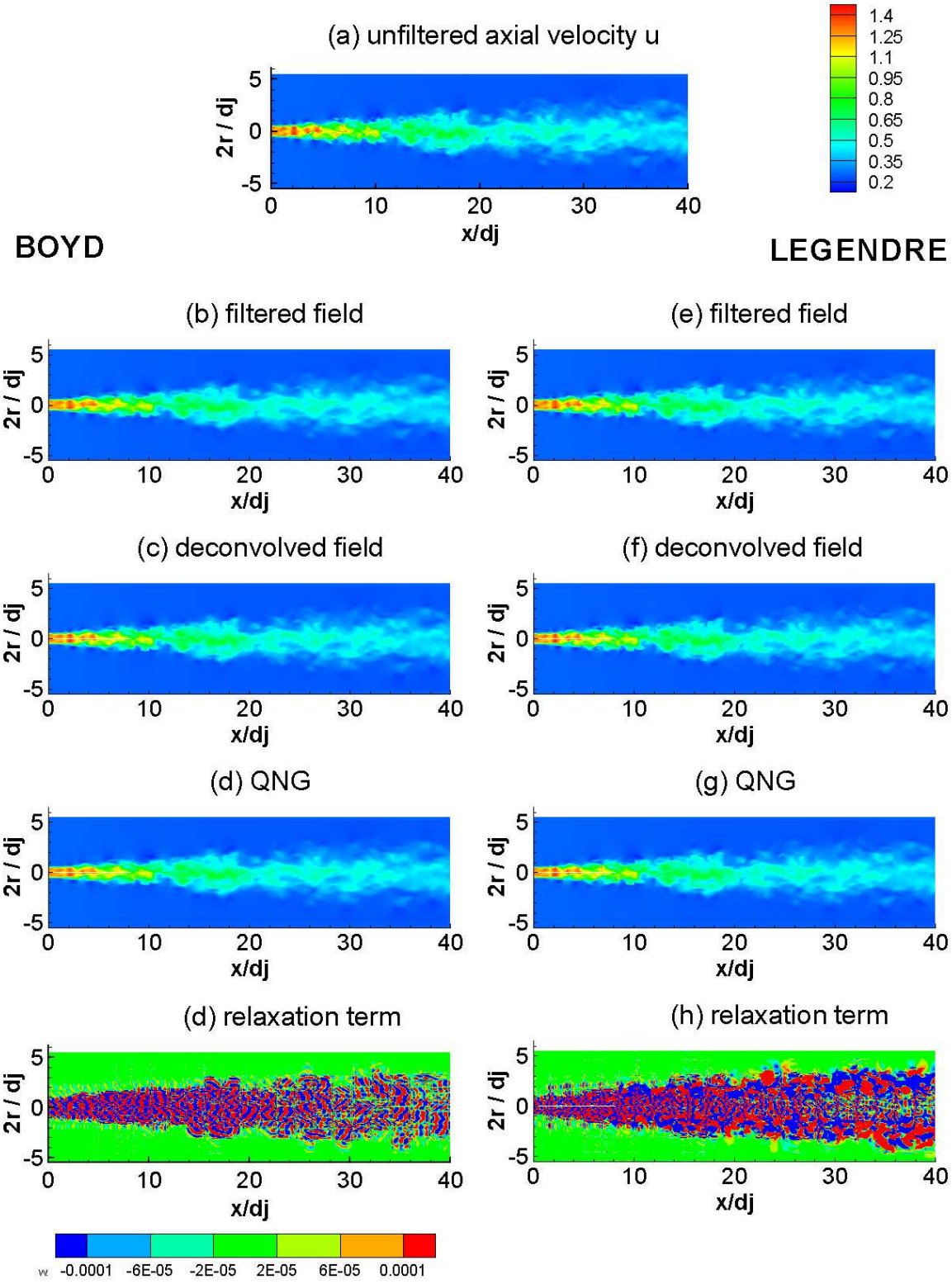

Figure 4.19: Comparison of the Boyd (b) - (d) and the Legendre filter (e) - (h) for an LES filter of $\kappa_c = 0.7$ and a deconvolution order of $N_d = 3$. The a priori tests start with the unfiltered axial velocity field u and after mesh filtering (Γ), the filtered field $\overline{\Gamma(u)}$, the decovolved field $\Big(\Gamma(u)\Big)^{\star}$, the QNG field $(Q_N * G)\overline{\Gamma(u)}$ and the relaxation term $(I - Q_N * G)\overline{\Gamma(u)}$ are compared.

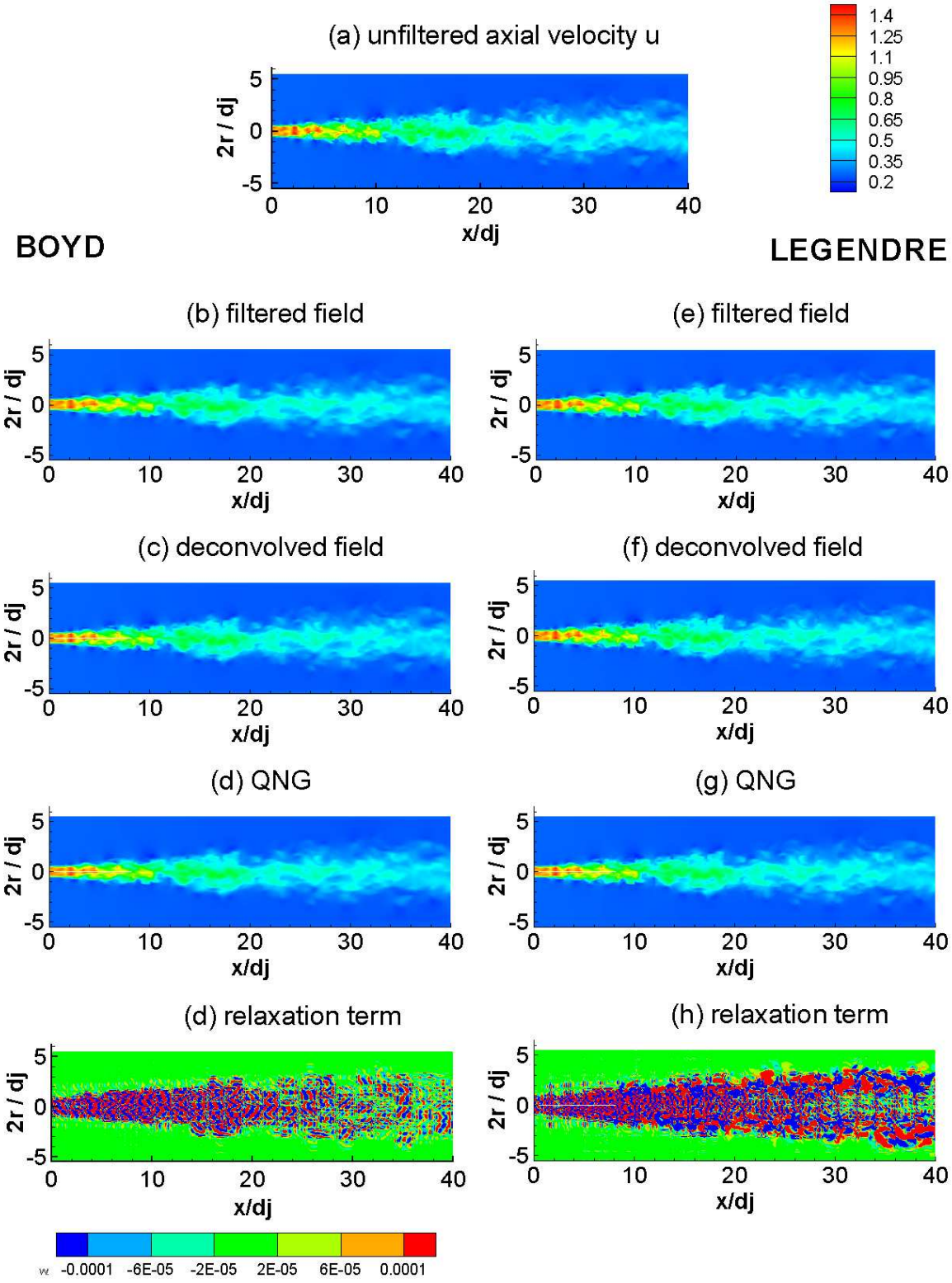

Figure 4.20: Comparison of the Boyd (b) - (d) and the Legendre filter (e) - (h) for an LES filter of $\kappa_c = 0.7$ and a deconvolution order of $N_d = 5$. The a priori tests start with the unfiltered axial velocity field u and after mesh filtering (Γ), the filtered field $\overline{\Gamma(u)}$, the decovolved field $\left(\Gamma(u)\right)^{\star}$, the QNG field $(Q_N * G)\overline{\Gamma(u)}$ and the relaxation term $(I - Q_N * G)\overline{\Gamma(u)}$ are compared.

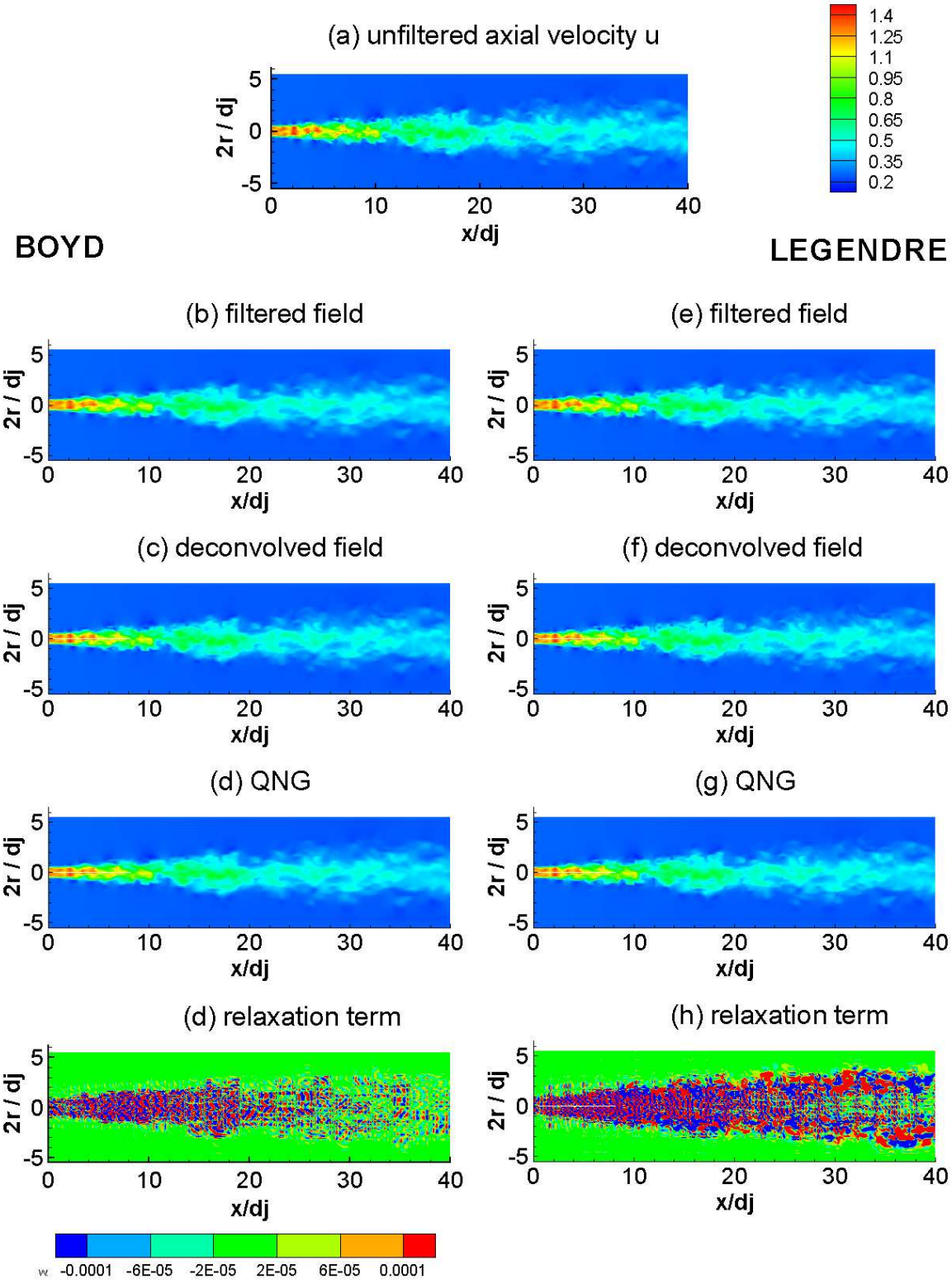

Figure 4.21: Comparison of the Boyd (b) - (d) and the Legendre filter (e) - (h) for an LES filter of $\kappa_c = 0.7$ and a deconvolution order of $N_d = 7$. The a priori tests start with the unfiltered axial velocity field u and after mesh filtering (Γ), the filtered field $\overline{\Gamma(u)}$, the decovolved field $\Big(\Gamma(u)\Big)^{\star}$, the QNG field $(Q_N * G)\overline{\Gamma(u)}$ and the relaxation term $(I - Q_N * G)\overline{\Gamma(u)}$ are compared.

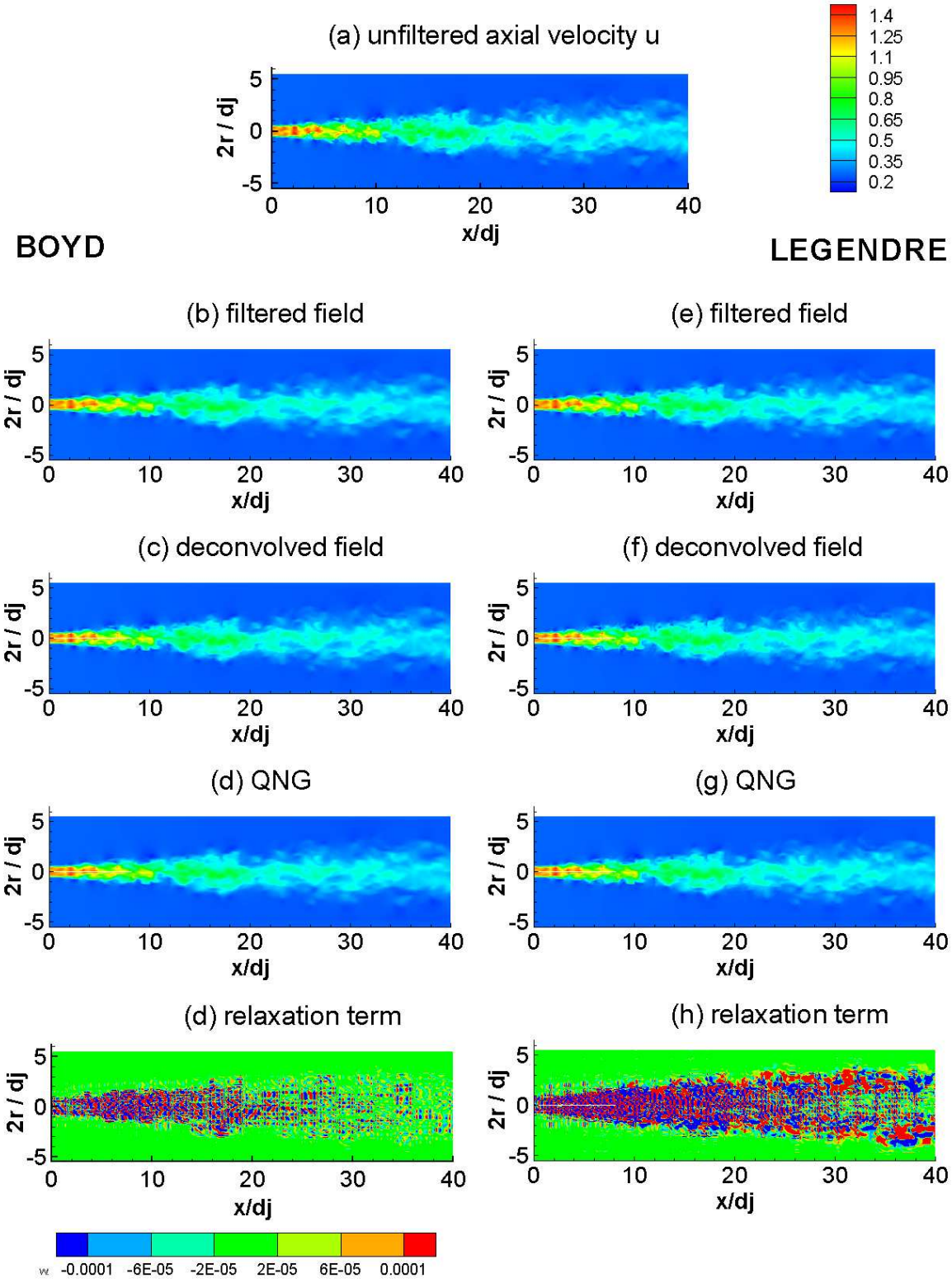

Figure 4.22: Comparison of the Boyd (b) - (d) and the Legendre filter (e) - (h) for an LES filter of $\kappa_c = 0.7$ and a deconvolution order of $N_d = 9$. The a priori tests start with the unfiltered axial velocity field u and after mesh filtering (Γ), the filtered field $\overline{\Gamma(u)}$, the decovolved field $\left(\Gamma(u)\right)^{\star}$, the QNG field $(Q_N * G)\overline{\Gamma(u)}$ and the relaxation term $(I - Q_N * G)\overline{\Gamma(u)}$ are compared.

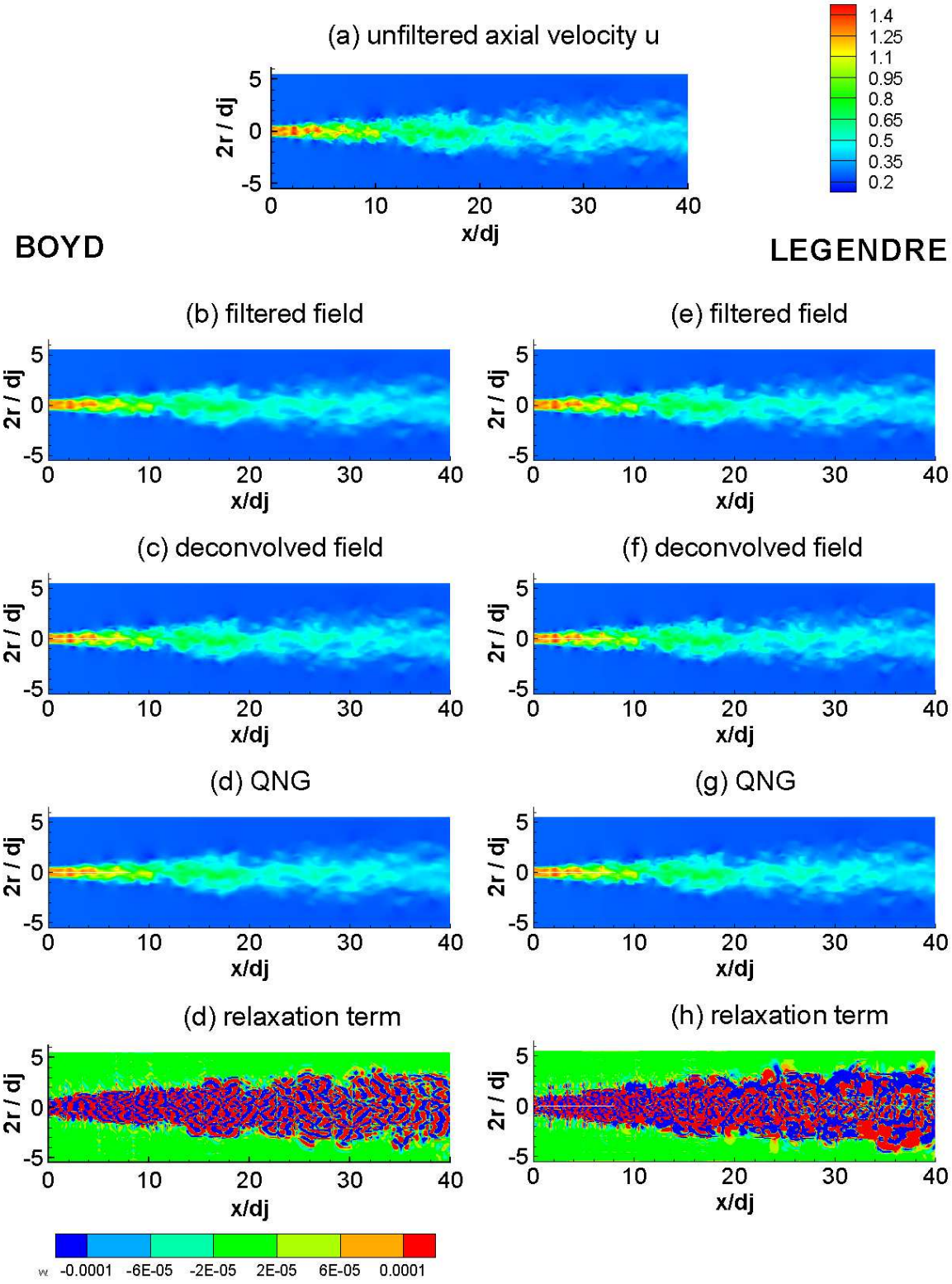

Figure 4.23: Comparison of the Boyd (b) - (d) and the Legendre filter (e) - (h) for an LES filter of $\kappa_c = 0.6$ and a deconvolution order of $N_d = 3$. The a priori tests start with the unfiltered axial velocity field u and after mesh filtering (Γ), the filtered field $\overline{\Gamma(u)}$, the decovolved field $\Big(\Gamma(u)\Big)^{\star}$, the QNG field $(Q_N * G)\overline{\Gamma(u)}$ and the relaxation term $(I - Q_N * G)\overline{\Gamma(u)}$ are compared.

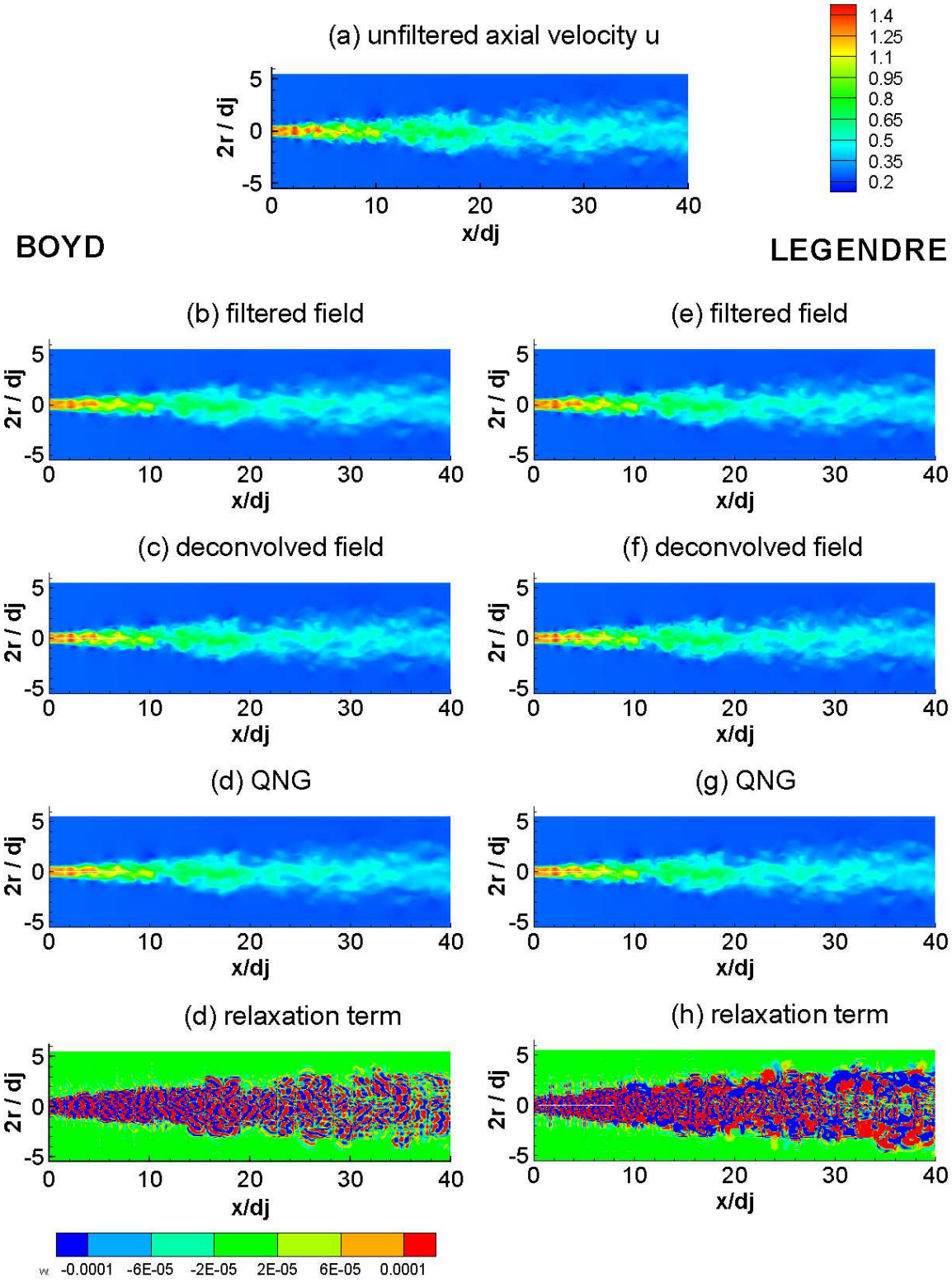

Figure 4.24: Comparison of the Boyd (b) - (d) and the Legendre filter (e) - (h) for an LES filter of $\kappa_c = 0.6$ and a deconvolution order of $N_d = 5$. The a priori tests start with the unfiltered axial velocity field u and after mesh filtering (Γ), the filtered field $\overline{\Gamma(u)}$, the decovolved field $\left(\Gamma(u)\right)^{\star}$, the QNG field $(Q_N * G)\overline{\Gamma(u)}$ and the relaxation term $(I - Q_N * G)\overline{\Gamma(u)}$ are compared.

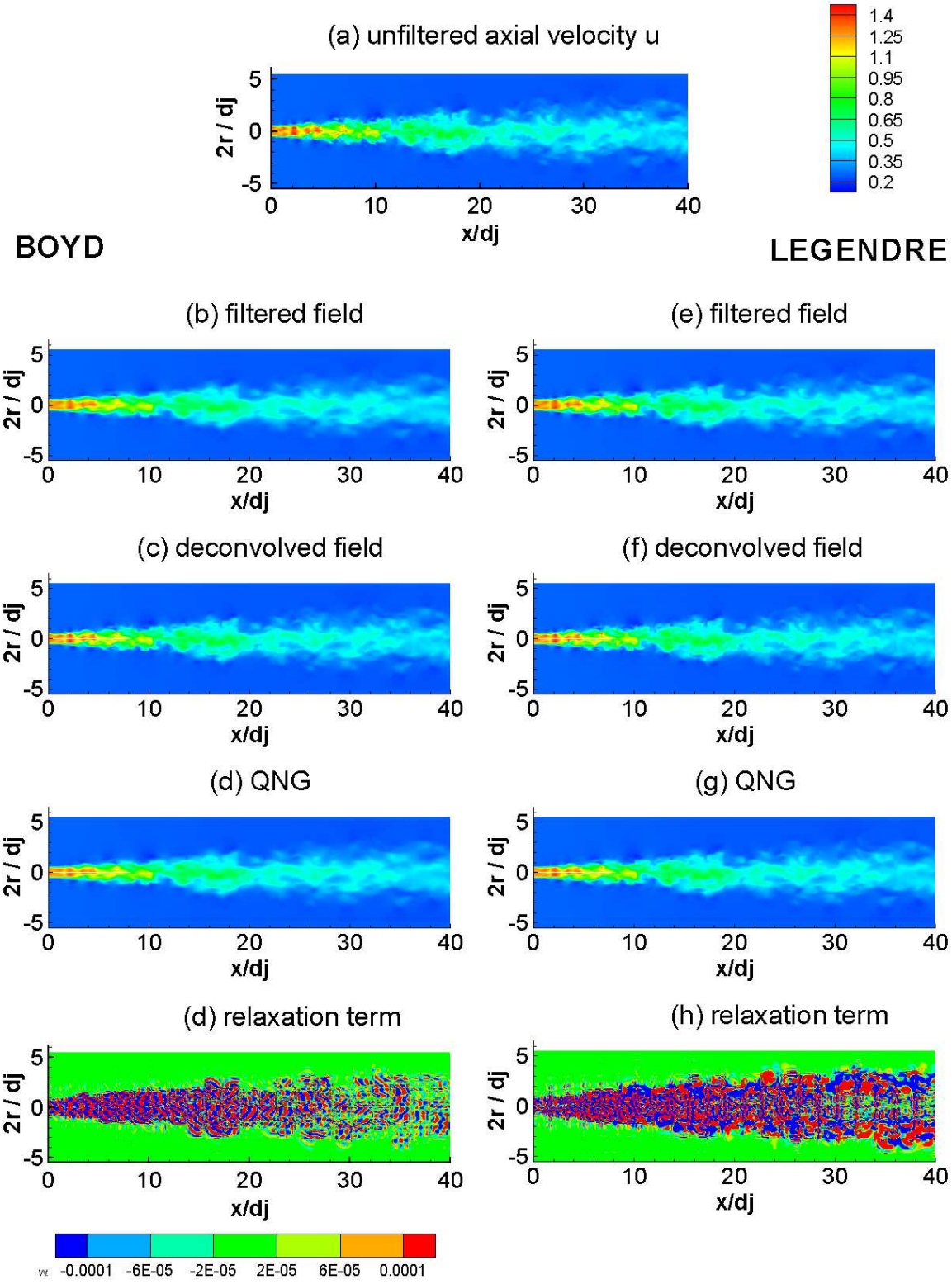

Figure 4.25: Comparison of the Boyd (b) - (d) and the Legendre filter (e) - (h) for an LES filter of $\kappa_c = 0.6$ and a deconvolution order of $N_d = 7$. The a priori tests start with the unfiltered axial velocity field u and after mesh filtering (Γ), the filtered field $\overline{\Gamma(u)}$, the decovolved field $\Big(\Gamma(u)\Big)^{\star}$, the QNG field $(Q_N * G)\overline{\Gamma(u)}$ and the relaxation term $(I - Q_N * G)\overline{\Gamma(u)}$ are compared.

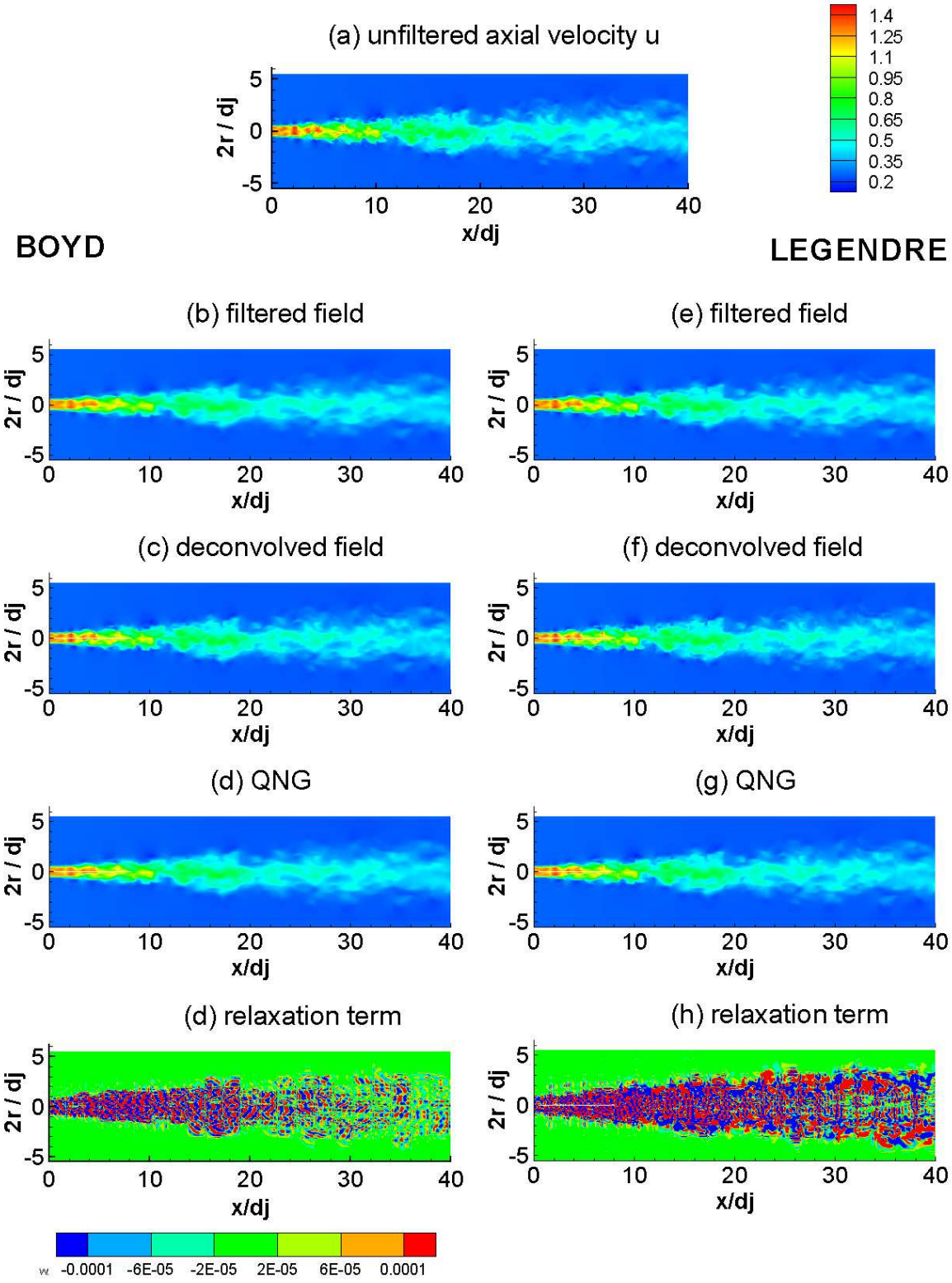

Figure 4.26: Comparison of the Boyd (b) - (d) and the Legendre filter (e) - (h) for an LES filter of $\kappa_c = 0.6$ and a deconvolution order of $N_d = 9$. The a priori tests start with the unfiltered axial velocity field u and after mesh filtering (Γ), the filtered field $\overline{\Gamma(u)}$, the decovolved field $\left(\Gamma(u)\right)^{\star}$, the QNG field $(Q_N * G)\overline{\Gamma(u)}$ and the relaxation term $(I - Q_N * G)\overline{\Gamma(u)}$ are compared.

A Posteriori Investigations

To test the conclusions in the previous Section, LES are performed with $N_s = 8$ and $\chi_u = 100$ using the top-hat inflow velocity profile. Fig. 4.27 shows the centerline axial velocity fluctuations and compares the results with the DNS. Fig. 4.28 compares instantaneous distributions of the axial velocity obtained with the Boyd and the Legendre filter. Both filters overestimate the turbulent velocity intensity along the centerline in Fig. 4.27 in the near field $5 < x/d_j < 25$, with the Boyd-filter overestimation being larger. Further downstream, the intensity with the Legendre filter reduces to the DNS level of 25%, while the results with the Boyd filter reach a level of 30%. The result is interesting because the overestimation of the fluctuations with the Boyd filter compared with the DNS results are more drastic than the fluctuations with the Legendre filter, especially after the transition to a turbulent flow in the far field ($x/d_j > 25$). We assume that the higher magnitude of the relaxation term acts as a dissipation of the turbulent fluctuations.
It seems that the larger structures of the relaxation term, shown in the *a priori* investigations of the Legendre filter create more dissipation and we assume this will be the reason for a better stabilization of the turbulent velocity intensity along the centerline. The Legendre filter was chosen for the following LES.

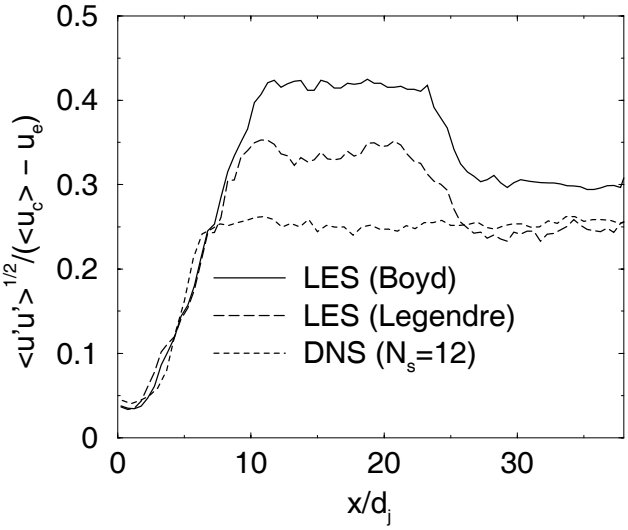

Figure 4.27: Comparison between the Boyd- and the Legendre filter of the turbulence intensities in axial direction along the centerline using the top-hat velocity inflow profile (see Fig. 4.32).

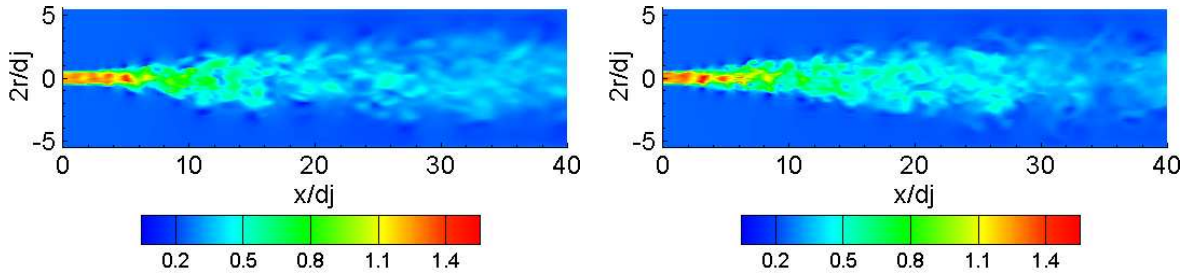

(a) (b)

Figure 4.28: Comparison of the axial velocity between (a) the Boyd- and (b) the Legendre filter.

4.7.2 Results and Discussions

In this Section, the LES results for the reference case (Legendre filter, 1/7-law inflow profile, inflow correlation length of $\sigma_s = \sigma_t = \sigma = 0.1$, $N_s = 8$ and $\chi = 100$) are presented.
The instantaneous axial velocity distribution is shown in Fig. 4.29. An almost laminar flow field can be seen close to the jet exit and then the flow becomes turbulent.

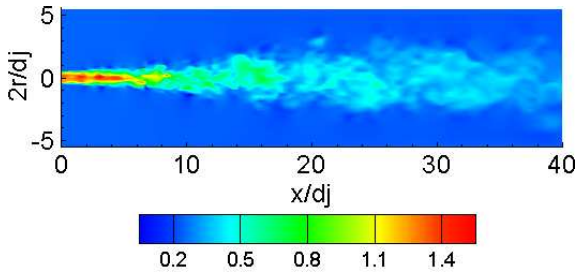

Figure 4.29: Isocontours of the axial velocity obtained with LES using the Legendre filter and the 1/7-law inflow profile.

The following results are obtained by averaging over several data fields and over the self-similarity coordinate $r/r_{1/2}$, where r is the radial distance from the centerline and $r_{1/2}$ denotes the velocity half width, i.e. the radial distance where the local mean axial velocity is equal to half the value of the mean centerline velocity, $\langle\overline{u}\rangle(r_{1/2}) = \langle\overline{u}_c\rangle/2$.

Centerline Profiles

Velocity half widths at each axial location and shown in Fig. 4.30 (a). In agreement with the requirement for self-similarity, confined turbulent

jets are expected to spread linearly if the co-flow velocity u_e is small compared to the jet velocity u_j and the jet considered is not in the far field ($x/d_j < 70$) according to Antonia and Bilger [5]. However Fig. 4.30 shows a non-linear behavior which can be attributed to the confinement. The co-flow in combination with the confinement creates a backflow showed in the work of Barchilon and Burchet [11] and constricts the mean axial velocity profile, because, in contrast to experiments , for example Amielh et al. [3], the inflow boundary condition do not allow for entrainment.

It has been shown that the mean centerline velocity profile in a turbulent jet decays linearly with increasing distance from the virtual origin of the jet (see for instance, Tennekes and Lumley [124]). The location of the virtual origin and to a lesser extend the decay constant, depend on the jet inflow conditions, shown in Boersma et al. [13]. The inverse of the centerline velocity $(u_0 - u_e)/(u_c - u_e)$ of Fig. 4.30 (b) shows a slightly overprediction of the LES for the velocity decay compared to the DNS.

The evolution of the centerline turbulent velocity intensity is presented in Fig. 4.30 (c) and (d): Experiments show that the increase of $u'/(u_c - u_e)$ is much more rapid for low Reynolds numbers than for higher Reynolds flows in the near-field region (see Amielh et al. [3]). In the present LES, a turbulent intensity of around 27% is reached at $x/d_j = 20$. This value is in good agreement with the DNS and the experimental results of Amielh et al. [3]. Different values for the final value of the turbulent velocity intensity can be found in the literature, ranging from 22% for the experiment of Panchapakesan and Lumley [95] to 28% for the DNS of Boersma et al. [13]. However, the LES results show an overshoot of the turbulent intensity in the region of $8 < x/d_j < 20$. The overshoot is not seen in experiments of Hussein et al. [64] and Panchapakesan and Lumley [95] but it has been reported in the literature for numerical investigations (see Glaze and Frankel [59], Boersma et al. [13] and Gharbi et al. [55]).

We assume that the transition of the jet flow close to the jet exit is the reason for the overshoot of the turbulent velocity intensity. This assumption is based on the facts, that the turbulent intensity reduces to the expected value from the DNS for $x/d_j > 20$ and that the LES of turbulent channel flow of Chapter 3, which is a steady state flow, gave

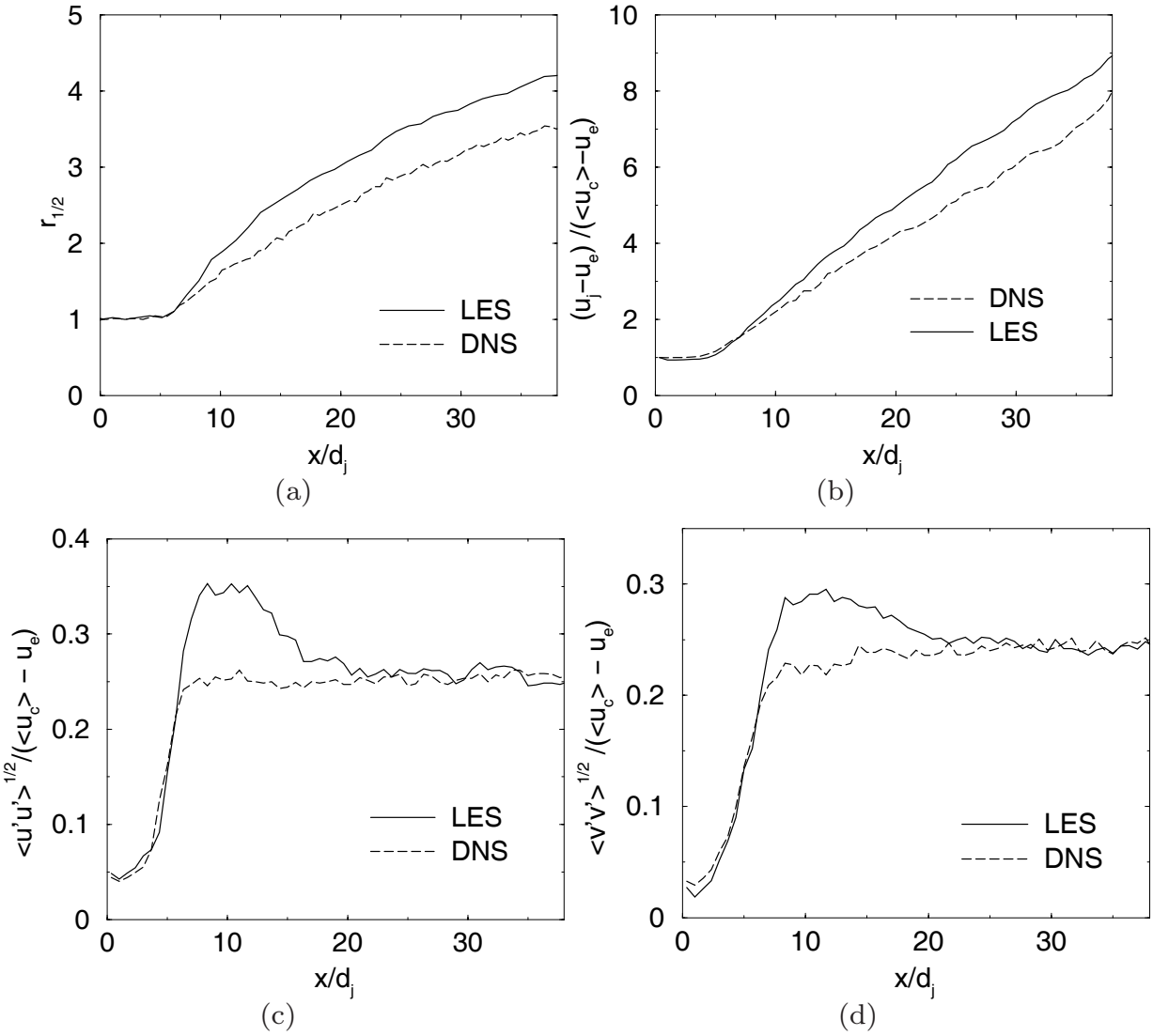

Figure 4.30: Evolution of (a) the mean longitudinal velocity half-width, (b) the inverse mean axial velocity and the turbulent velocity intensity in (c) axial and d) radial direction on the centerline between the reference LES and the DNS

good results.

The transition is a complex process and its main characteristic is the generation of smaller scales through the non-linear advection terms. SGS models are in general based on the assumption of an developed inertial range. According to Kolmogorov's theory, turbulent kinetic energy is only transported in the inertial range, whereas the energy is transported and dissipated in the dissipation range of small modes. Fully developed flows in general have a developed inertial range whereas flows in transition are building their inertial range. Therefore, transitional flows are a challange for SGS models in general. Several conditions such

as the co-flow, entrainment, Reynolds number, inflow conditions (mean and perturbations) and the SGS model could influence the transition. The fact that the overshoot is not present in the DNS suggest that the overshoot results from the ADM/spectral element code. In this context, it should be noted that both the DNS and the LES use the same spectral element mesh, but not the same polynomial order ($N_s = 12$ for the DNS and $N_s = 8$ for the LES). In order to clarify the reason for the overshoot, the influence of the following parameter are investigated and discussed:

- the Reynolds number: $Re = 2,000$ and $Re = 21,000$
- the mean velocity inflow profile: top-hat and 1/7-law inflow profile
- the correlation length of the inflow generator: $\sigma = 0.1$ and $\sigma = 0.15$
- the relaxation parameter: $\chi_u = 100$ and $\chi_u = 900$
- an alternative, mathematically equivalent formulation for the Favre-filtered momentum equation in combination with ADM.

Effect of the Reynolds number: A Reynolds number of $Re = 2,000$ was chosen to reduce the computational costs. To reduce the effect of the viscous term, an LES at $Re = 21,000$ is performed and the results are compared to the experimental data of Amielh et al. [3]. The spatial and temporal resolutions are the same as for the $Re = 2,000$ case, as the primary interest is on the qualitative trends. Fig. 4.31 (a) and (b) show the turbulent intensity in the axial and radial directions for both Re; the overshoot between $8 < x/d_j < 15$ is obvious for the $Re = 21,000$ as well. Moreover, the asymptotic value is overestimated by the high-Re LES due to the low spatial resolution. The influence of low spatial resolution on the turbulent intensity is known from the study of Section 4.7.1 and is seen in Fig. 4.15 for $N_s = 6$.

Effect of the inflow profile: The sensitivity of the jet behavior on the mean inflow velocity profile is also reported by George [51]. The influence of a top-hat shaped inflow profile and a profile according to the 1/7-law (both profiles are shown in Fig. 4.32) are investigated and the results are presented in Fig. 4.33. Both inflow profiles are based on the same mass flux and therefore on the same bulk velocity u_0, used in the definition of Re (Eq. 4.1)

$$\dot{m} = u_0 \frac{d_j^2 \pi}{4} = \int_0^{r_e} \int_0^{2\pi} r u(0, r, \varphi) d\varphi dr \ , \tag{4.14}$$

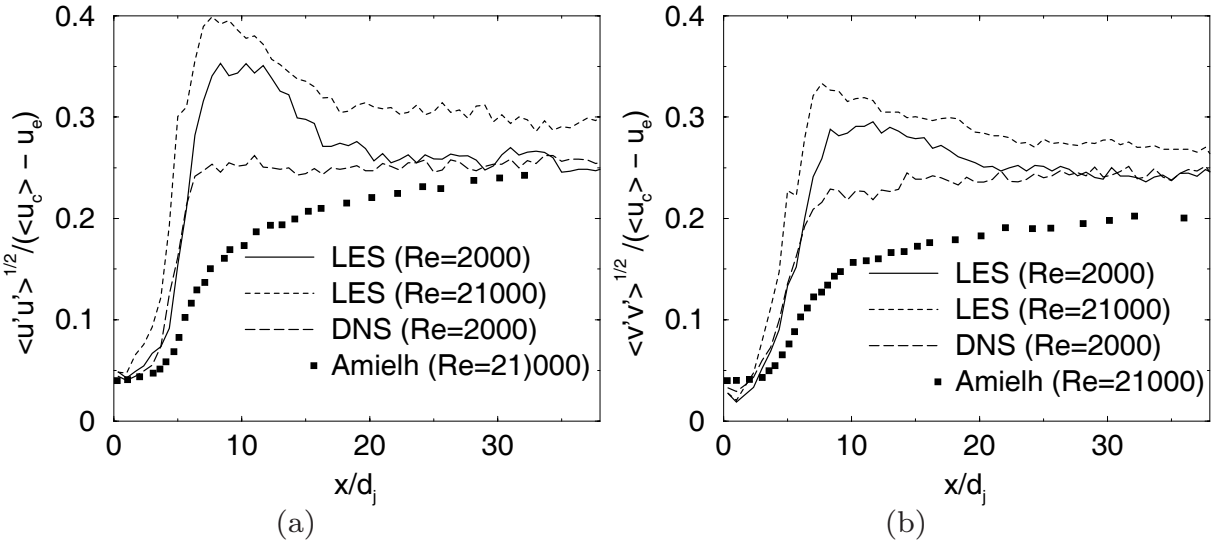

(a) (b)

Figure 4.31: The influence of different Re on the centerline turbulent velocity intensity in (a) the axial and (b) the radial direction. The figure also shows the experimental results from Amielh et al. [3] for $Re = 21,000$.

where r_e is the radius of the lateral co-flow confinement of the moving wall. The two profiles differ on one hand by their shapes, where the

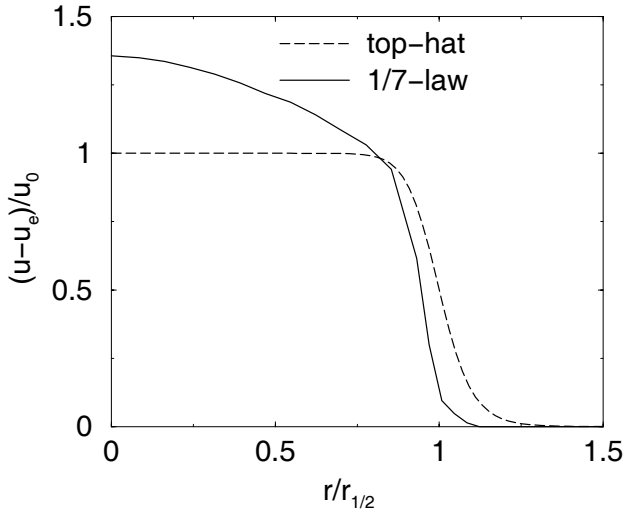

Figure 4.32: Mean axial velocity at the inflow: The reference 1/7-law and the top-hat profiles.

1/7-law profile is closer to the realistic turbulent-pipe profile, and on the other hand by the shear-layer thickness, which influences the jet stability. Rais [106] has investigated the influence of the shear-layer thickness on the jet stability and shown that the thinner the shear-layer, the shorter the potential core of the jet in the near field. Fig. 4.33 shows the

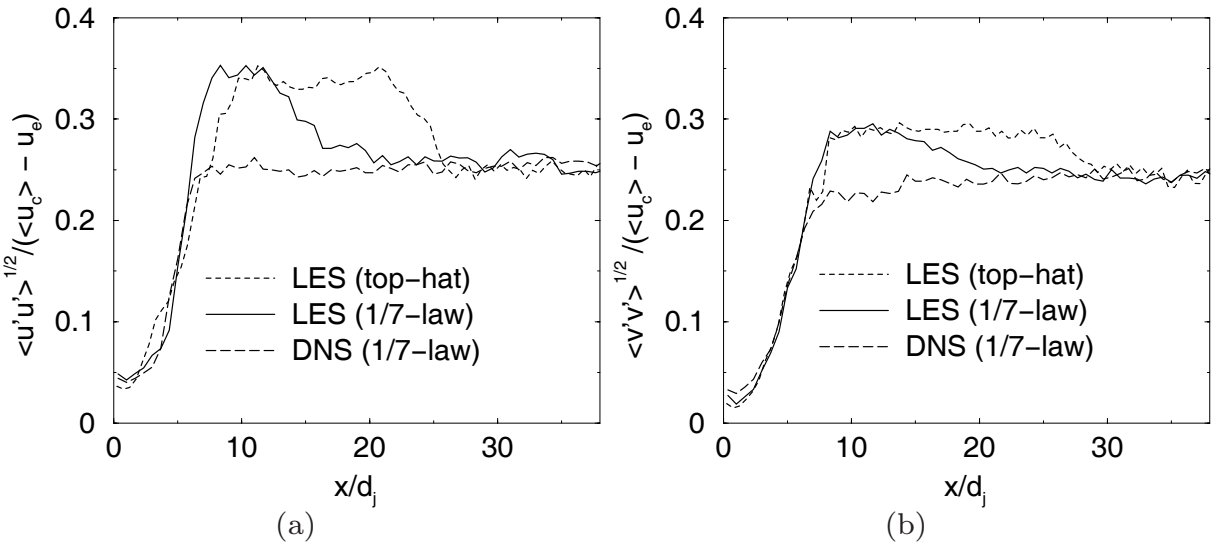

Figure 4.33: Comparison of the turbulent velocity intensity in (a) the axial and (b) the radial directions for both the standard 1/7-law and the top-hat profile.

centerline turbulent velocity intensity in the axial and radial direction for both inflow profiles. A faster breakup is obvious for the top-hat profile, but the overshoot remains for the top-hat profile. However, in contrast to the reference 1/7-law profile, the maximum turbulent velocity intensity extends further in streamwise direction before it falls down to an asymptotic value of 27%. Therefore the length for the transition from the top-hat profile to a developed, turbulent flow becomes longer.

Effect of the correlation length: Inflow-velocity profiles must be perturbed for turbulent flow simulations, as discussed in Section 4.4. In this work the inflow generator of Klein [68] is used, based on a Gaussian autocorrelation function. The Fourier transform of the autocorrelation function, is by definition, the energy spectrum in wavenumber space. It is evident that a Gaussian energy spectrum is not representative of a realistic turbulent spectrum and that the transition to the real energy spectra in the far field can lead to processes possibly causing an overshoot. The correlation scale σ is the only available parameter of the Gaussian autocorrelation function defining the width of the Gaussian. For large values of σ, the focal point of the energy distribution is located at large, unstable scales leading to an earlier breakup, whereas for smaller σ, the focal point is shifted to smaller scales. In Fig. 4.34 the centerline turbulent velocity intensity in the axial and radial direction is shown for $\sigma_s = \sigma_t = \sigma = 0.1$ (reference case) and $\sigma = 0.15$. As expected, an earlier

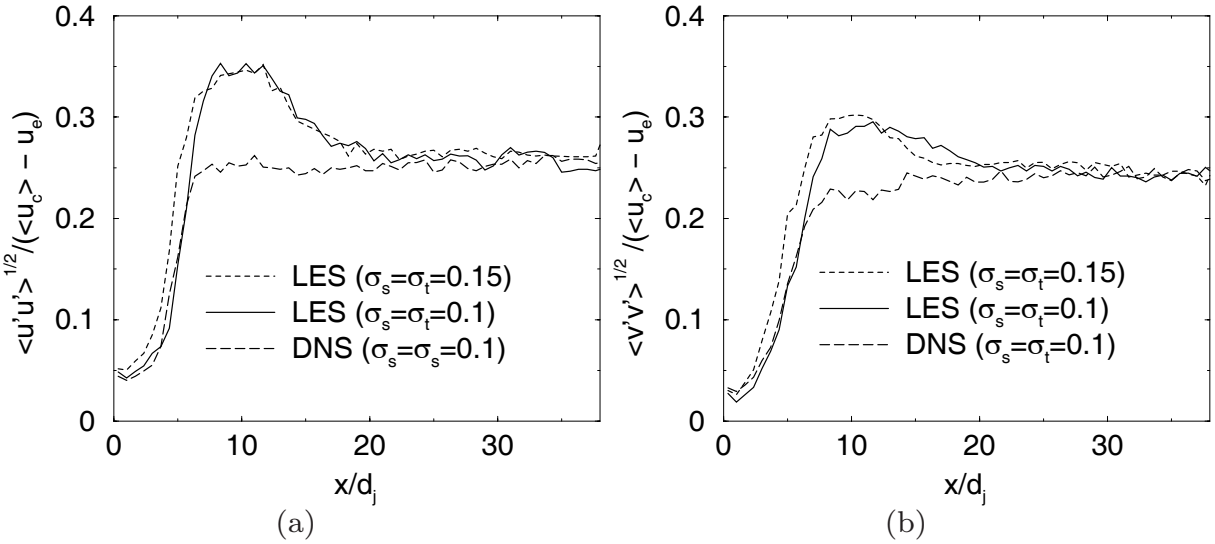

(a) (b)

Figure 4.34: Comparison of the centerline turbulent velocity intensity in (a) axial and (b) radial direction for different inflow-data correlation scales σ and for Re=2000.

breakup at $x/d_j = 6$ is seen with $\sigma = 0.15$, followed by a convergence to the $\sigma = 0.1$- distribution. However, it is also evident that the correlation length σ has no influence on the overshoot.

Effect of the relaxation parameter: ADM introduces different quantities such as the filter function G, cutoff scale κ_{ct}, deconvolution order N_d, and relaxation parameter χ_u. The relaxation parameter is part of the relaxation term, which in fact is a model for $\underline{\underline{\tau}}^{nrp}$ (see Section 2.4) and accounts for the effect of the nonlinear interactions involving scales which cannot be represented on the grid. The relaxation term employs a high-pass filter in spectral space and affects predominantly only the range of scales $\kappa_c < \kappa < N_s$ (as discussed in Chapter 2). The information obtained by the high-pass filtering depends on polyonomial order used in each spectral element N_s. In contrast to global spectral methods, where high N_s values commonly are used (for example $N_s = 32$ to $N_s = 65$ in the LES of turbulent channel flows of Stolz et al. [122]), spectral element methods divide the global geometry in a number of elements N_e and expand the solution as a series of basis functions of low order ($N_s = 8$ in the present LES). ADM applies the filter and relaxation term for each spectral element separately and it is evident that the high-pass information is based on much fewer modes than for global spectral methods. This behavior is also evident from Fig. 4.35, where the relaxation term functions are plotted for $N_s = 8$ and 12. The relaxation

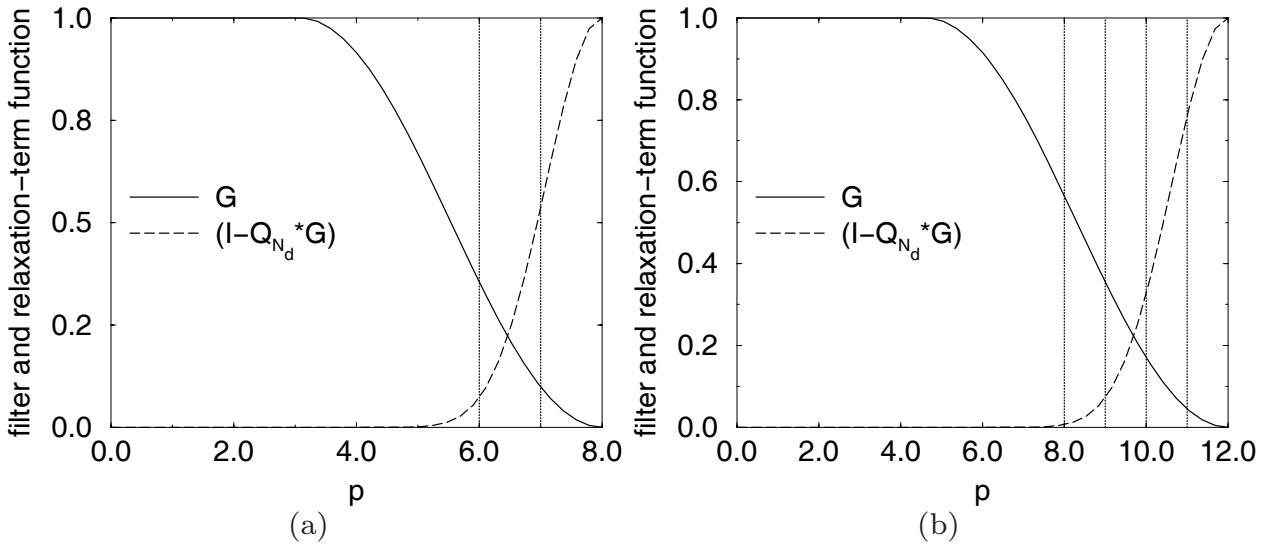

Figure 4.35: Comparison between the filter and the relaxation-term function for (a) $N_s = 8$ and (b) $N_s = 12$.

term acts as a high pass filter. While a relaxation term with $N_s = 8$ includes the information of three modes ($N_s = 6, 7, 8$), the relaxation term with $N_s = 12$ is based on five modes ($N_s = 8, 9, 10, 11, 12$). If fewer modes are involved in the high-pass filtering of the relaxation term, the application of the high-pass filter to spectral elements may affect the inertial range of the spectrum and lead to incorrect results.
A further effect is the modification of the triad interaction of modes by the relaxation term (controlled through χ_u), especially if large amounts of high-frequency information is extracted from the system. Triad interaction is the process by which new modes are generated from the interaction of existing modes (see for example Pope [103]). Extensive extraction of high-frequency information can prevent interaction between the resolved and represented scales possibly leading to an incorrect modelling of the energy transfer to small scales. The comparison of different relaxation parameters of the turbulent intensities along the centerline in axial and radial direction is shown in Fig. 4.36. A larger overshoot of the axial velocity and a further build up of the turbulent intensity in the scale-similarity region is obvious for $\chi_u = 900$. The higher overshoot is surprising, as higher dissipation is expected for higher values of χ_u. The effect can be explained by the insufficient relaxation-term determination due to the smaller number of modes involved, and by the notable modification of the triad interaction between resolved and represented scales. Fig. 4.37 shows instantaneous pictures of the axial velocity for $\chi_u = 100$ (reference case), 500 and 900. While

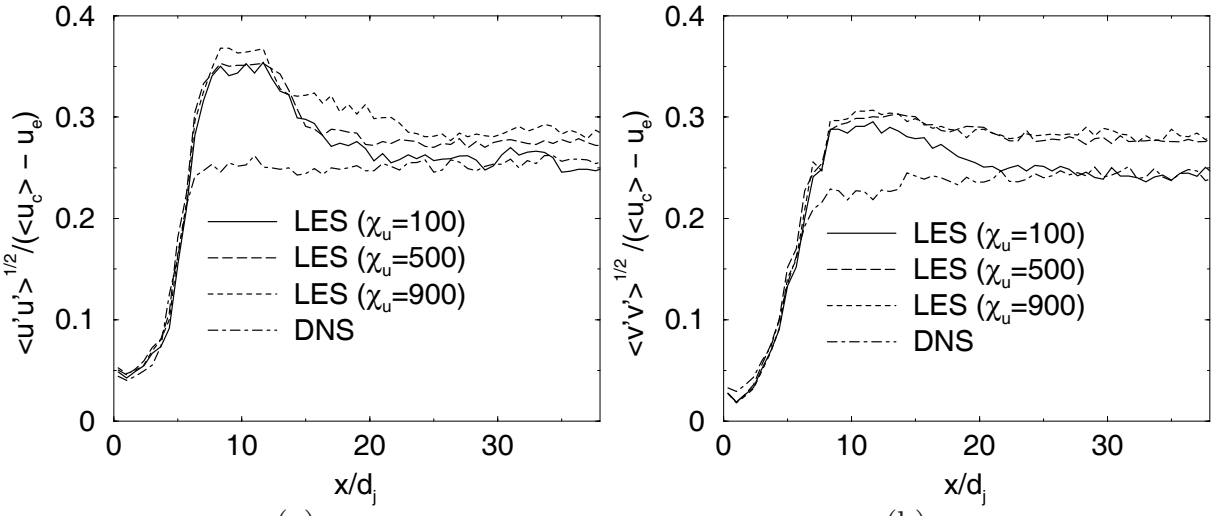

Figure 4.36: Centerline turbulent velocity intensity in (a) axial and (b) radial direction for relaxation parameters of $\chi_u = 100$ (reference), $\chi_u = 500$ and $\chi_u = 900$.

differences can be seen in Fig. 4.36 between $\chi_u = 100$ and 900, almost no difference is evident from the instantaneous velocity fields of Fig. 4.37.

Alternative formulation of the momentum equation: The idea here is to derive the filtered momentum equation in the classical way according to Pope [103] and to model then the residual stress tensor with ADM. This formulation was also used by Bouffanais et al. [17]. The derivation of the alternative formulation starts with the filtered Eq. (2.2) neglecting buoyancy effects

$$\frac{\partial \overline{\underline{u}}}{\partial t} + \overline{\underline{u}(\nabla \cdot \underline{u})} = -\nabla \overline{p}_2 + \frac{1}{Re} \nabla \cdot \overline{\underline{\underline{S}}} \,, \tag{4.15}$$

which can be written as

$$\frac{\partial \overline{\underline{u}}}{\partial t} + \overline{\underline{u}}(\nabla \cdot \overline{\underline{u}}) = -\nabla \overline{p}_2 - \left[\overline{\underline{u}(\nabla \cdot \underline{u})} - \overline{\underline{u}}(\nabla \cdot \overline{\underline{u}}) \right] + \frac{1}{Re} \nabla \cdot \overline{\underline{\underline{S}}} \,. \tag{4.16}$$

The residual shear stress is modelled by ADM as

$$\overline{\underline{u}(\nabla \cdot \underline{u})} - \overline{\underline{u}}(\nabla \cdot \overline{\underline{u}}) = \overline{\underline{u}^\star(\nabla \cdot \underline{u}^\star)} - \overline{\underline{u}^\star}(\nabla \cdot \overline{\underline{u}^\star}) + \chi_u (I - Q_N * G) * \overline{\underline{u}} \,. \tag{4.17}$$

The centerline fluctuations in the axial and radial directions are shown in Fig. 4.38 for the Boyd and the Legendre filter with $\chi_u = 100$. Three observations can be made:

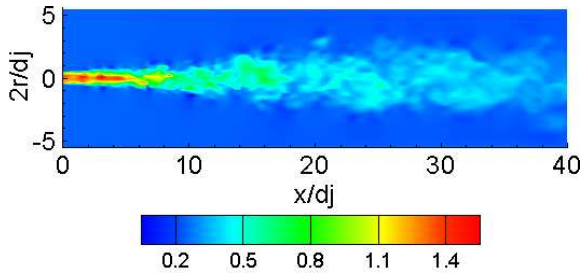

(a) $\chi_u = 100$

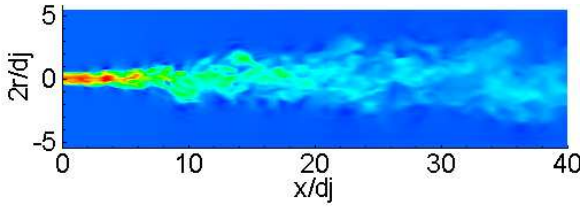

(b) $\chi_u = 500$

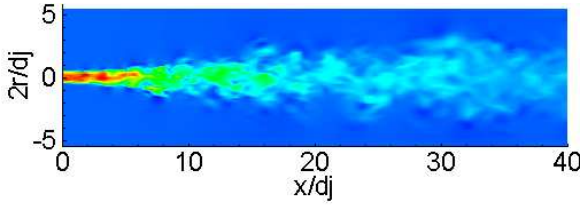

(c) $\chi_u = 900$

Figure 4.37: Instantaneous pictures of the axial velocity field for (a) $\chi_u = 100$, (b) $\chi_u = 500$ and (c) $\chi_u = 900$.

- The alternative formulation avoids the overshoot obtained with the original formulation,
- the alternative formulation results in a higher level of fluctuations in the self-similarity region than the original formulation and the DNS,
- the Boyd filter results in higher fluctuations than the Legendre filter.

Instantaneous axial velocity fields for the alternative formulation are shown in Fig. 4.39.

Summarizing, the Reynolds number, the mean velocity inflow profile, the correlation length of the inflow generator and the relaxation parameter χ_u as well as an alternative formulation of the momentum equation have no effect of the overshoot of the turbulent velocity intensities along the centerline of the LES. Therefore, the underestimated dissipation of the Approximate Deconvolution Model in combination with the spectral element code in the range of $x/d_j < 20$, where the flow is in transition

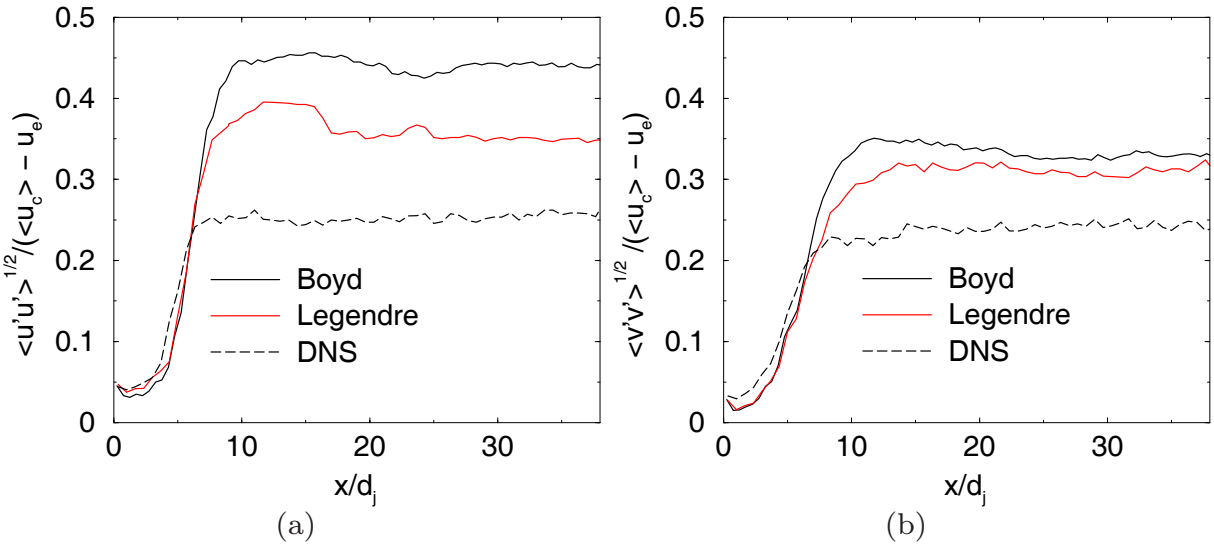

Figure 4.38: Centerline turbulent velocity intensity (a) in axial and b) in radial direction for the alternative formulation using the Boyd and the Legendre filter and $\chi_u = 100$.

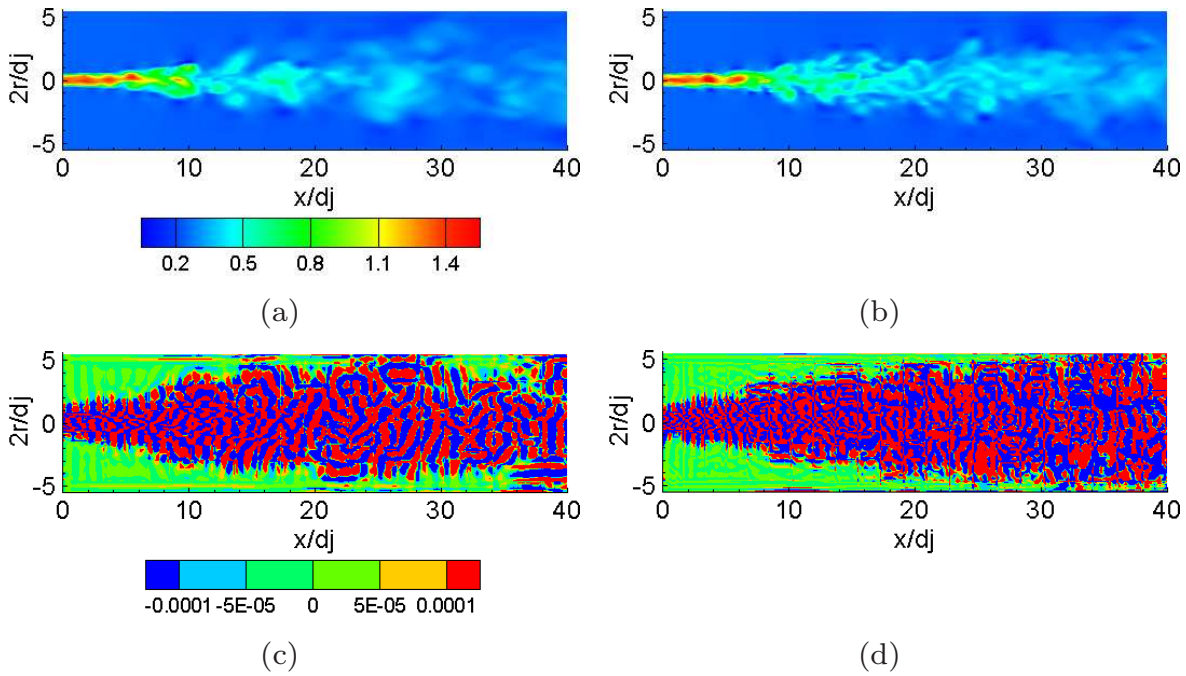

Figure 4.39: Instantaneous axial velocity fields for the alternative formulation with (a) Boyd filter and (b) Legendre filter. Instantaneous relaxation-term field for the alternative formulation with (c) Boyd filter and (d) Legendre filter.

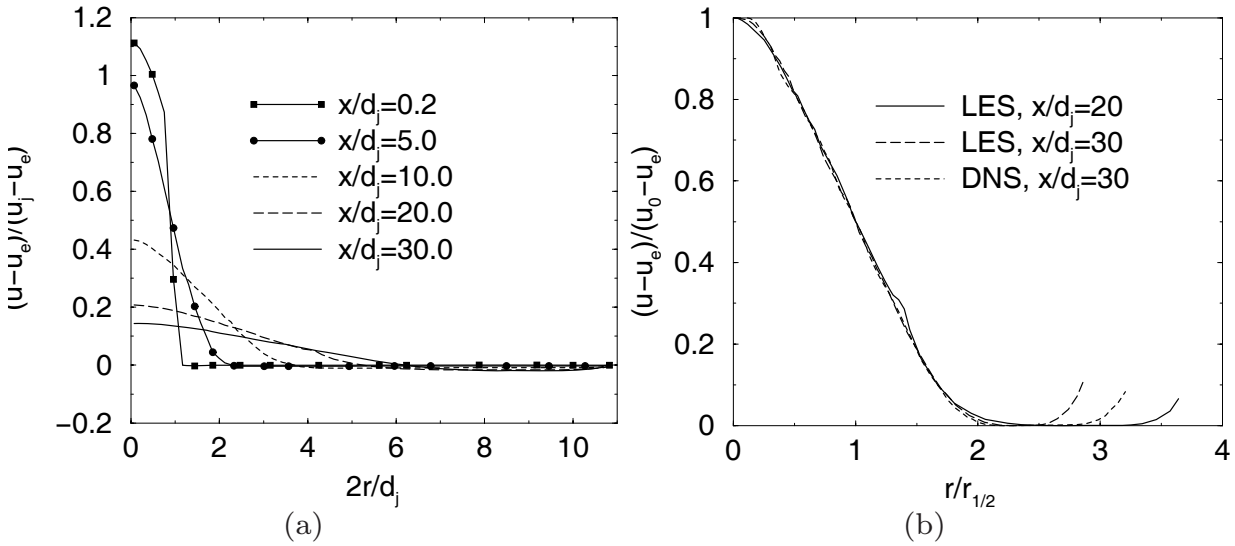

Figure 4.40: Mean axial velocity profiles in radial direction at different streamwise locations.

to a fully developed turbulent flow, could be the reason for the overshoot. Nevertheless, the turbulent intensity for the reference LES is in good agreement with the DNS in the scale similarity region.

Radial Profiles

In this Section, the radial profiles of the reference LES with $\sigma_s = \sigma_t = \sigma = 0.1$ and $\chi_u = 100$ are presented. The radial direction is normalized either with the nozzle diameter d_j or with $r_{1/2}$ for scale-similar quantities. Fig. 4.40 (a) shows the mean axial velocity at different streamwise locations. It is evident that close to the nozzle ($x/d_j = 0.2$) the mean axial velocity profile is similar to the 1/7-law inflow profile (see Fig. 4.32), while further downstream ($x/d_j > 10$), the mean axial velocity profiles become scale similar. In Fig. 4.40 (b), the scale similarity of the mean axial velocity is shown for $x/d_j = 20$ and 30, normalized with $r_{1/2}$, for the radial direction and with $u_0 - u_e$ for the velocity. The normalized mean axial velocity profiles at $x/d_j = 20$ and $x/d_j = 30$ are compared with those from the DNS at $x/d_j = 30$. The velocity u_e used in the non-dimensional representation of Fig. 4.40, is the local co-flow velocity at each section. The mean longitudinal velocities determined using LES agree well with those determined using DNS. The increase of the velocity at locations $r/r_{1/2} > 2.5$ is due to the moving-wall boundary and is different for each simulation because of different velocity half widths $r_{1/2}$ and centerline velocities u_c.
The radial profiles of Reynolds normal and shear stresses are shown in Fig.

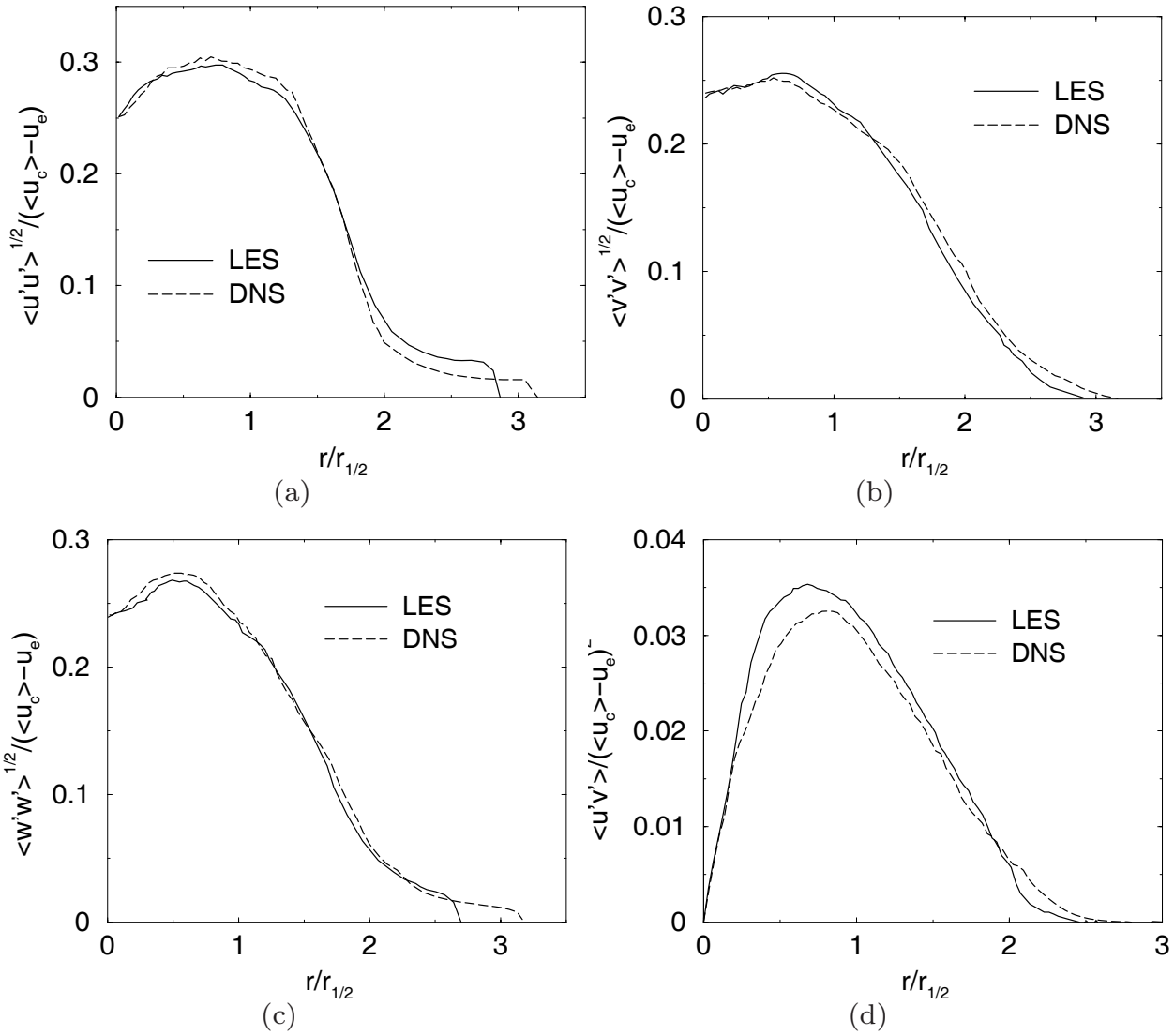

Figure 4.41: Reynolds normal stresses (a) in axial, (b) in radial and (c) in azimuthal direction and (d) the shear stress at $x/d_j = 35$.

4.41. The profiles are in the scale similarity region, where the turbulent intensity along the centerline has a value of 25% and the agreement between the LES and the DNS results is good. In the region of the co-flow, the Reynolds normal stresses reach a magnitude of around $3\% - 5\%$ and decay to zero at the moving-wall boundary.

4.8 Conclusions

An LES of an isothermal, turbulent and confined jet of $Re = 2,000$ is performed with the Approximate Deconvolution Model (ADM) using a spectral element code and the statistical results are compared with DNS

data specially performed for this study. The mean inflow velocity profile is perturbed with correlated fluctuations in time and space, which are generated with an inflow generator according to Klein [68].
Preliminary investigations between the LES and experimental results of Amielh et al. [3] showed some deviations for the turbulent intensities:

- The LES showed an overshoot in the transition region of the flow for the turbulent intensities in the axial and radial direction, whereas further downstream in the scale similarity region the turbulent intensities fall down to the experimental magnitude
- The increase of the turbulent intensities between $x/d_j < 10$ are faster for the LES.

It was not clear whether the deviations have their origin in the partially unknown boundary and initial conditions of the experiment or whether there were problems with the LES implementation. Therefore a DNS with the identical setup as for the LES was performed.
The spatial resolution study of the DNS with $N_s = 8, 10$ and 12 showed that only DNS with $N_s > 12$ lead to stable simulations. The LES, in contrast to the DNS, leads to stable simulations already for $N_s > 6$. Therefore the stabilizing character of ADM is shown.
A priori investigations of the Boyd- and the Legendre filter showed a more accurate filter inversion for the Boyd filter with the consequence that the relaxation term contains only higher mode information. The relaxation term with the Legendre filter shows more intense structures structures, which will be affected during the LES. From this point of view, we would expect that the Boyd filter should be preferred. However, *a posteriori*-investigations show better results for the turbulent intensities along the centerline with the Legendre filter, which is explained by the more dissipative character of the relaxation term. The Legendre filter was used for further LES.
The statistics in the axial direction, especially the axial and radial velocity intensities on the centerline are in good agreement with the DNS results after the transition region ($x/d_j > 20$). In the transition region $x/d_j < 20$ the LES overestimates the intensities by 30%.
The radial distributions, such as mean axial velocity, normal- and shear stresses in the scale similarity region ($x/d_j > 20$) are in very good agreement with the DNS results.
Different Re, mean axial velocity profiles at the inflow, different correlation scales for the inflow generator and relaxation parameter χ_u were investigated in order to explain the LES overshoot in the transition re-

gion. None of these could eliminate the overshoot and the influence of the relaxation parameter was found to be marginal. Therefore, the overshoot results from the combination of ADM with the spectral element code. The filtering is performed in each spectral element in which relatively low polynomial orders are used, with the result that less information about the high wavenumber modes is included in the relaxation term. The consequence is an underestimated dissipation which leads to an overshoot of the turbulent intensity in the transition region. Changing the relaxation parameter χ_u to higher values could not reduce the overshoot. An alternative formulation according to the classical LES with eddy-viscosity models was also investigated. The results show that the overshoot is eliminated but the level of fluctuations of the axial velocity along the centerline remain at a level that is about 25% higher than the DNS.
The centerline fluctuations in the axial direction reduce after the transition region of the jet to the correct level (this, however, is not the case with the alternative formulation). It can be concluded that the combination of the spectral element code and ADM gives good results in the fully developed, scale similarity region. This observation is also supported by the channel LES of Chapter 3 for a fully-developed turbulent channel flow.

Chapter 5

Non-Isothermal Turbulent Jet

Low-Mach number, variable density jets are free of pressure waves and can be realized either by subsonic streams (low velocity in comparison to the speed of sound) at different temperature or with species of different molecular weights. At constant pressure, the fact that density depends on T and species molecular weights as can be seen from the ideal gas law

$$\sum_{i=1}^{N} p_i V = \sum_{i=1}^{N} n_i R_i M_i T = \sum_{i=1}^{N} n_i M_i \rho_i \ , \tag{5.1}$$

where p_i, V, T, n_i, R_i, M_i and ρ_i are the partial pressure, the volume, the number of moles, the specific gas constant, the molcular weight, the temperature and the density, respectively, for species i. In this work, a non-isothermal, turbulent jet is realized only by a temperature difference of a factor of two between the co-flow and the jet for a Reynolds number of $Re = 2,000$.
The Chapter is organized as follows: An introduction to variable density jet behavior is given in Section 5.1, expanded by the literature review in Section 5.2. The variable-density jet setup is presented in Section 5.3 and the DNS presented in Section 5.4 will be used for further comparison with LES results (Section 5.5). Conclusions follow in Section 5.6.

5.1 Introduction to Variable Density Jets

The flow of variable density turbulent jets is identical to the jets described in Section 4.1 with the additional influence of the variable density. Fluid density changes can be brought by mixing fluids of different molecular weight, or by heating them. The density is also affected by high-Mach number flows associated with pressure changes, but such flows are outside the scope of this work.
According to Chen and Rodi [22], variable density turbulent jets can be classified in four categories presented in Fig. 5.1. If buoyancy acts in the direction of the velocity at nozzle, the jet is called a *buoyant jet*. When the bouyancy force acts in the opposite direction, the jet is a *negative buoyant jet*. The region near the nozzle is dominated by momentum forces and it behaves like a non-buoyant jet. An intermediate region follows where the influence of the momentum becomes smaller and smaller. The final region is dominated by buoyancy and behaves like a plume. If the effect of buoyancy is negligible (isothermal, equal species molecular weight, no chemical reactions, low-Mach number), the jet falls under the class of *non-buoyant jets*. The other limiting case, where the buoyancy force completely dominates the flow, is called a *plume*. In a plume, no initial momentum is present and the change in density can be, for example, generated by a heat source. Under atmospheric conditions, all buoyant jets become plumes far away from their origin.

The dynamics of variable density jets is driven by inertial, buoyant, and viscous forces. To characterize the flow, the following parameters are useful. The ratio of inertial and viscous forces is the Reynolds number Re, whereas the ratio of buoyant to viscous forces is the Grashof number Gr defined as

$$Gr = \frac{g(\rho_e - \rho_j)d_j^3}{\rho_j \nu^2} \ , \tag{5.2}$$

where g, ρ_j and ρ_e are the gravitational constant and the jet and co-flow density, respectively. The ratio of inertial to buoyant forces is the Froude number, defined as

$$Fr = \frac{u^2}{g d_j(\rho_c - \rho_j)/\rho_j} \ , \tag{5.3}$$

and is the most important parameter for turbulent buoyant jets.
The analysis of Chen and Rodi [22] shows that two distinct forms of self-similarity are possible. One similarity in the flow regions where buoyancy forces play an important role (i.e. plumes) and another in jet flows with

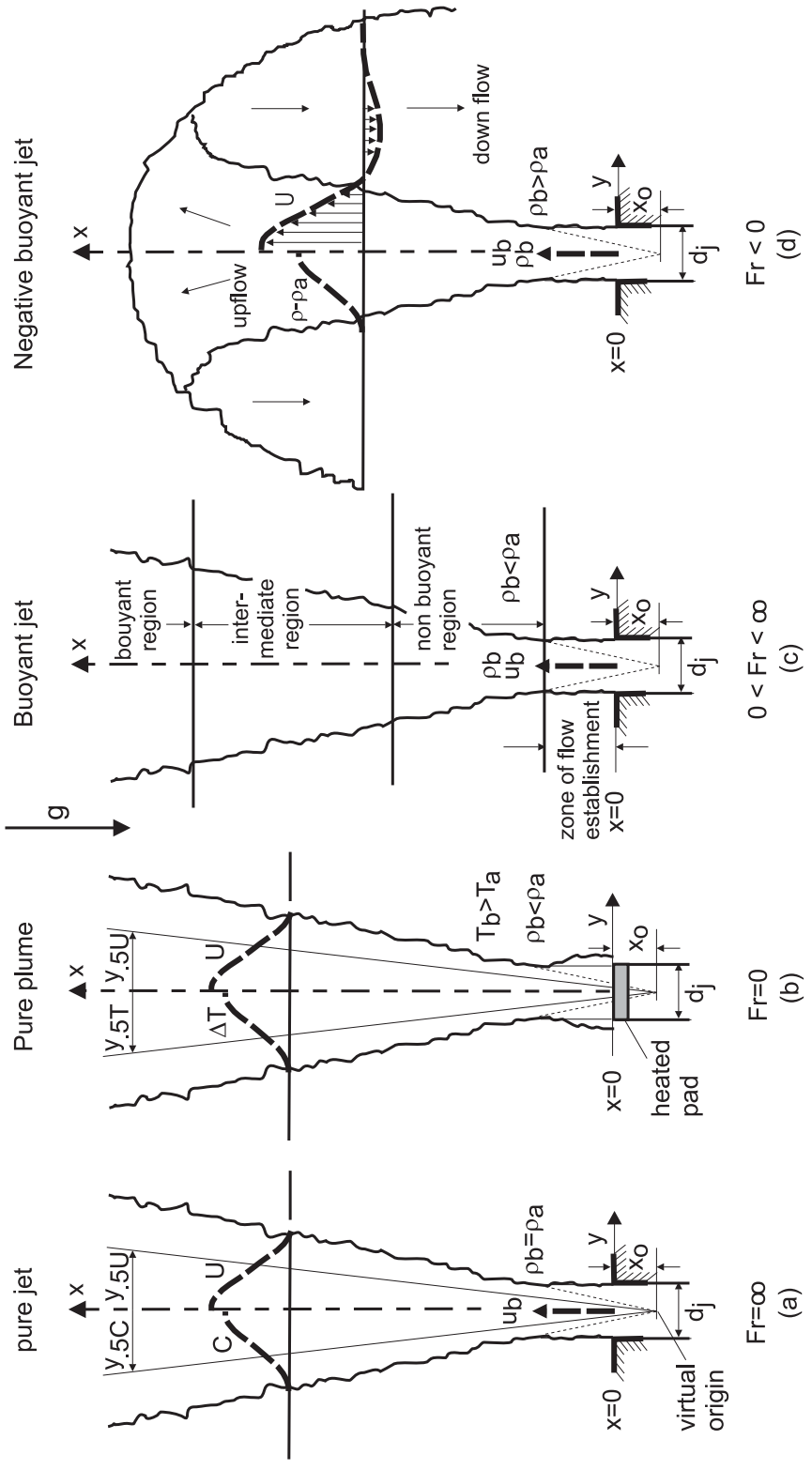

Figure 5.1: Buoyant jets in uniform surroundings according to Chen and Rodi [22]

negligible buoyancy forces. No self-similar behavior is present in the in-

termediate region of a buoyant jet because the flow undergoes a transition from a non-buoyant similarity to a plume similarity. Experimental studies can be found from Antonia and Bilger [5, 8] regarding unheated or slightly heated jets; Gouldin et al. [60] concerning coaxial jets of a propane-air mixture, and Amielh et al [3] and Djeridane et al [37] considering free jets of helium-air and CO_2-air mixtures.

5.2 Literature Review of Variable Density Jets

Variable density jets are realized either by flows of different species of different molecular weight or by different temperatures of the ambient or the co-flow stream and the jet flow. It should be noted that one has to distinguish between variable density jets, which influence the velocity through the equation of state (this is the case of this work) and variable density jets where the density change acts as a passive scalar (where incompressible flow equations are used).
A large number of studies concern variable density jets exists. The most important experimental works about heated jets can be found in the literature by Antonia et al. [8], Venkatamarani [72], Antonia and Bilger [6] and Chevray and Tutu [23]. More recently, a detailed study was performed by Chua et al. [27] to investigate the influence of the initial conditions, but also of the wire probe configuration, on various properties associated with second-order moments. The investigations of Antonia and Bilger [7] and Anselmet et al. [4] focused on the dissipation of temperature fluctuations. Some recent work also concern the study of the scalar concentrations and consequently the influence of density variations on the jet development [102, 118, 95, 114, 99].
Most of the numerical investigations of variable density jets contains passive scalars. The first DNS in three spatial dimensions of the passive-scalar mixing in a turbulent jet was performed by Lubbers et al. [81] investigating the statistics of the passive scalar along the centerline and in radial direction whereas Ribault et al. [77] performed a DNS of a planar jet to study the evolution of the mean and fluctuating passive scalar and its probability density function. A direct computation of a turbulent compressible jet and its associated sound was performed by Freund et al. [47], who also used their results to study the effect of compressibility on passive scalar mixing (Freund et al. [48]. More recently Pantano et al. [96] performed a DNS including chemical reactions in order to study the mixing

of conserved scalars in nonpremixed turbulent combustion.
LES of passive scalars has mostly relied on gradient approximation of the subgrid scalar flux, introducing a turbulent Prandtl number Pr_t. The value of Pr_t is either a specified model parameter as Horiuti [62] has used, or obtained using a dynamic procedure as used by Moin et al. [90]. The dynamic Prandtl number model has been used, for example, by Askelvoll et al. [9] as part of the computation of two coaxial jets with fast combustion. An alternative procedure for obtaining the subgrid scalar flux introduces a tensor eddy diffusivity that is given by modelled streched-vortex dynamics (see Pullin [105]).
No literature about numerical work of heated, variable density jets could be found. Numerical simulation of heated, variable density flows is used for chemical reactions, i.e. combustion. Chemical reactions and combustion is not the topic of this work, however as an addition, LES of turbulent jet flames are reported by Pitsch and Steiner [101], Dai et al. [33] and Kempf et al. [67].

5.3 Non-Isothermal Jet Setup

The non-isothermal turbulent jet is considered in the cylindrical coordinate system shown in Fig. 5.2. The setup is similar to that of the

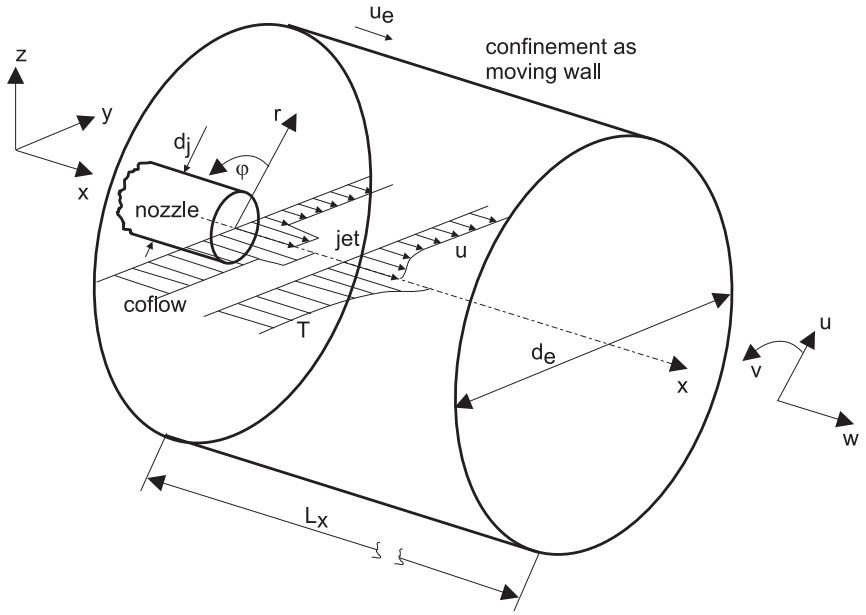

Figure 5.2: Sketch of the setup for the non-isothermal turbulent jet.

isothermal jet (see Section 4.3), except that the co-flow and the jet flow

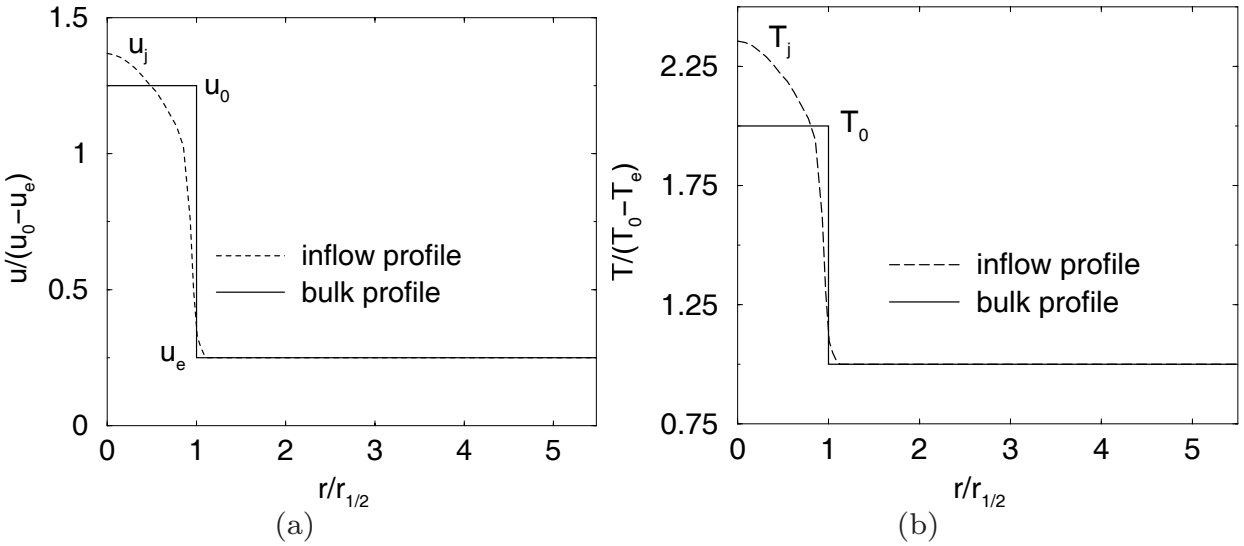

Figure 5.3: The boundary conditions at the inlet for a) the axial velocity and b) the temperature at $x/d_j = 0$.

have different temperatures. The simulations are performed in a cylindrical domain with a length $L_x = 20d_j$ and a diameter of $d_e = 11d_j$. A shorter domain is used for the non-isothermal jet relative to the isothermal jet domain since the centerline statistics become self-similar after $15d_j$, as seen in preliminary calculations. The boundary conditions for the mean axial velocity and temperature at the inlet are shown in Fig. 5.3. The length, time, velocity and temperature scales are defined as d_j, $d_j/(u_0 - u_e)$, $u_0 - u_e$ and $T_0 - T_e$, respectively, and the Reynolds number is defined as

$$Re = \frac{d_j(u_0 - u_e)}{\nu} = 2,000 \ , \tag{5.4}$$

where ν is the kinematic viscosity of the jet stream at the inflow temperature T_0. Locally, the kinematic viscosity increase caused by the increased temperature results in a local reduction of Re and a laminarization of the flow, leading to smoother structures in the velocity field. Figure 5.8 shows a comparison between the isothermal, axial, turbulent velocity of Chapter 4 and the non-isothermal, axial, turbulent velocity of this Chapter. The velocity field with identical inflow velocity conditions looks similar but the laminarization effect of the non-isothermal jet is obvious by the smoother structure of the velocity field. The mean inflow velocity profile is perturbed by correlated perturbations (see Section 4.4). The perturbation amplitude is set equal $0.05(\langle u_c \rangle - u_e)$ with correlation scales of $\sigma_s = \sigma_t = \sigma = 0.1$; $M = 25$ is used for the interpolation from the equidistant mesh of the inflow generator to the

non-equidistant mesh of the domain of Fig. 5.2. The inflow boundary conditions for the mean axial velocity and the temperature (Fig. 5.3) are specified as Dirichlet-boundary conditions, while the mean radial and azimuthal velocities are set equal to zero. The lateral boundaries (confinement as moving walls) are defined as Dirichlet conditions at the radius $r/r_{1/2} = 5.5$. Outflow boundary conditions are set at the outflow ($x/d_j = 20$) and the SE-filter (see Fig. 2.2) is used in all simulations.
The statistics are determined according to Eq. (4.4) - (4.6) and are based on data collected after an initial simulation of 200 time units to wash out the initial condition for 400 time units.

5.4 Direct Numerical Simulation

Most experimental and numerical studies deal with temperature fluctuations instead of the strong temperature variations considered in this work. Temperature fluctuations can then be considered as a passive scalar which do not influence density. However, strong temperature variations between co-flow and jet flow directly affect density and the Reynolds number and, as a consequence, the dynamics of the turbulent flow. The DNS data for the velocity and temperature discussed in this Section will be used for the comparison with further LES.
In the absence of gravitational force, the set of differential equations (Eqs. (2.1) to (2.4)) for the DNS of low-Mach number, non-isothermal, turbulent flows reduces to

$$\rho \frac{DT}{Dt} = \frac{1}{RePr} \nabla^2 T \tag{5.5}$$

$$\nabla \cdot \underline{u} = \frac{1}{T\rho} \left\{ \frac{1}{RePr} \nabla^2 T \right\} \tag{5.6}$$

$$\begin{aligned} \rho \left[\frac{\partial \underline{u}}{\partial t} + (\underline{u} \cdot \nabla) \underline{u} \right] &= \left[\frac{\partial \rho \underline{u}}{\partial t} + \nabla \cdot (\rho \underline{u}\ \underline{u}) \right] \\ &= -\nabla p_2 + \frac{1}{Re} \nabla \cdot \underline{\underline{S}} \end{aligned} \tag{5.7}$$

$$1 = \rho T \ , \tag{5.8}$$

where the equations are based on the assumption of constant thermal diffusivity λ, constant dynamic viscosity μ and constant average heat capacity c_p^a. In the continuity equation, the non-zero divergence of the velocity

field is imposed by the variation of temperature. The velocity excess is $\lambda_e = \frac{u_0 - u_e}{u_e} = 0.25$ and should result in a linear inverse centerline decay of the axial mean velocity according to Antonia and Bilger [5]. The Craya-Curtet number for the isothermal jet is $C_t = 6.8 > 0.9$ (see Section 4.1) and therefore does not lead to strong recirculation zones close to the confining walls (see Section 4.1.1). The simulations are performed in the geometry shown in Fig. 5.2 with a spectral element mesh (Fig. 5.4) containing $2,380$ spectral elements with a timestep of $dt = 0.001 \frac{d_j}{u_0 - u_e}$.

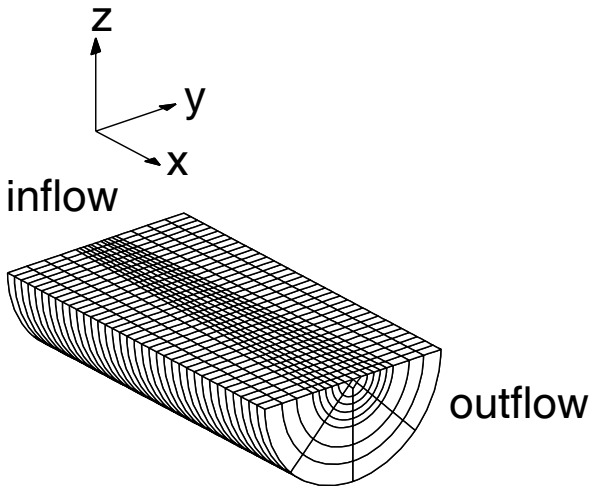

Figure 5.4: Cut through the centerline of the DNS mesh with $2,380$ spectral elements. The mesh contains 35 elements in the axial, 9 elements in radial and 8 elements in azimuthal direction.

5.4.1 Spatial Resolution Study

The influence of the spatial resolution is investigated by varying the polynomial order ($N_s = 6$, 8 and 10) for the mesh of Fig. 5.4. The mesh contains 35 elements in the axial, 9 elements in the radial and 8 elements in azimuthal direction, totaling to $2,380$ elements. In Table 5.4.1 the resolutions of the present DNS are compared with the resolution of the isothermal jet of Chapter 4 and the DNS of the passive scalar turbulent jet of Lubbers et al. [81]. The spatial resolution of the non-isothermal mesh in the axial direction is higher than for the isothermal DNS of the present work as well of the DNS of the turbulent jet with passive scalars of Lubbers et al. [81]. The resolution for $N_s = 10$ in the radial direction is comparable with the isothermal DNS with $N_s = 12$, but lower than DNS of Lubbers et al. [81].
The comparison of the mean axial velocity decay for different N_s is

Sim.	**flow**	Re	Δx	Δr	
DNS	axis. 3D jet	$2,000$	$0.0095d_j$	$0.106d_j$	$N_s = 6$, non-isoT
DNS	axis. 3D jet	$2,000$	$0.0071d_j$	$0.075d_j$	$N_s = 8$, non-isoT
DNS	axis. 3D jet	$2,000$	$0.0057d_j$	$0.060d_j$	$N_s = 10$, non-isoT
DNS	axis. 3D jet	$2,000$	$0.5d_j$	0.026	[81]
DNS	axis. 3D jet	$2,000$	$0.151d_j$	$0.0647d_j$	$N_s = 12$, isothermal

Table 5.1: Spatial resolution comparison between non-isothermal and isothermal DNS of Chapter 4 and Lubbers et al. [81].

presented in Fig. 5.5 (a). The centerline mean axial velocity decays according to the $1/x$-law in the isothermal case; In the non-isothermal case, the decay is faster and is not sensitive to N_s. The turbulent intensities along the centerline in the axial and radial directions (Fig. 5.5 (b) and (c)) reach a value of 25% and 24% for $N_s = 10$, respectively, which is slightly higher than the isothermal turbulent jet, whereas the turbulent velocity intensity along the centerline is only slightly overestimated for $N_s = 6$ and $N_s = 8$ compared to the results for $N_s = 10$. The profiles in the radial direction, normalized by $r_{1/2}$ are presented in Fig. 5.6 at the streamwise location $x/d_j = 15$. Qualitatively, the mean axial velocity, the Reynolds stresses in the axial, radial and azimuthal direction as well as the shear stresses are similar to the stresses of the isothermal jet and show marginal dependence on N_s.

The decay of the mean temperature along the centerline is shown in Fig. 5.7 (a) and also follow the $1/x$-law and the sensitivity on N_s is marginal, whereas a higher sensitivity is seen for temperature turbulent intensity along the centerline (Fig. 5.7 (b)). The intensity for $N_s = 6$ and $N_s = 8$ overestimates the case of $N_s = 10$ by $3 - 4\%$ and an overshoot is seen in the region of $x < 10$. The mean temperature and the turbulent temperature fluctuation at $x/d_j = 15$ in the radial direction are shown in Fig. 5.7 (c) and (d). The shape of the profile for all resolutions agree well and the marginal differences agree with the results in Fig. 5.7 (b).
The qualitative comparison between the axial velocity and the temperature fields for different N_s are shown in Fig. 5.8, showing the marginal sensitivity on the fields of N_s. Fig. 5.8 (g) shows an instantaneous axial velocity field of the isothermal DNS for $N_s = 12$. The laminarization effect of the non-isothermal turbulent jet caused by the increased tem-

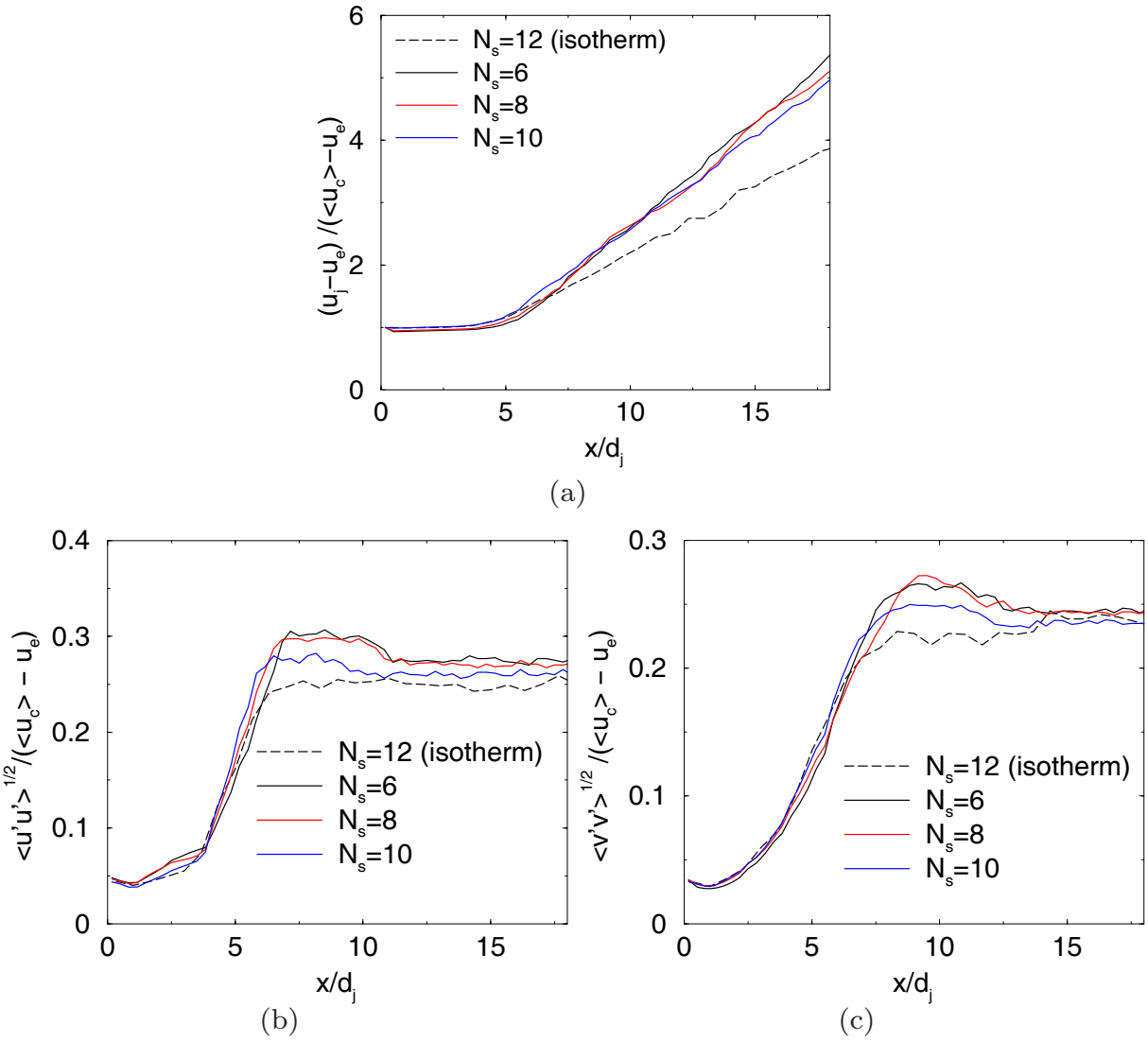

Figure 5.5: (a) mean axial velocity decay, turbulent velocity intensity in (b) axial and (c) radial direction of the present DNS for different N_s compared with the isothermal DNS results of Chapter 4.

perature and therefore the decrease of the density and the Re is shown by smoother turbulent structures.

Overall, the mean axial velocity along the centerline of the non-isothermal jet decays faster than the isothermal jet and the turbulent velocity intensities are slightly higher than the turbulent intensity of the isothermal jet. The DNS results of $N_s = 10$ will be used for further comparison in this Chapter.

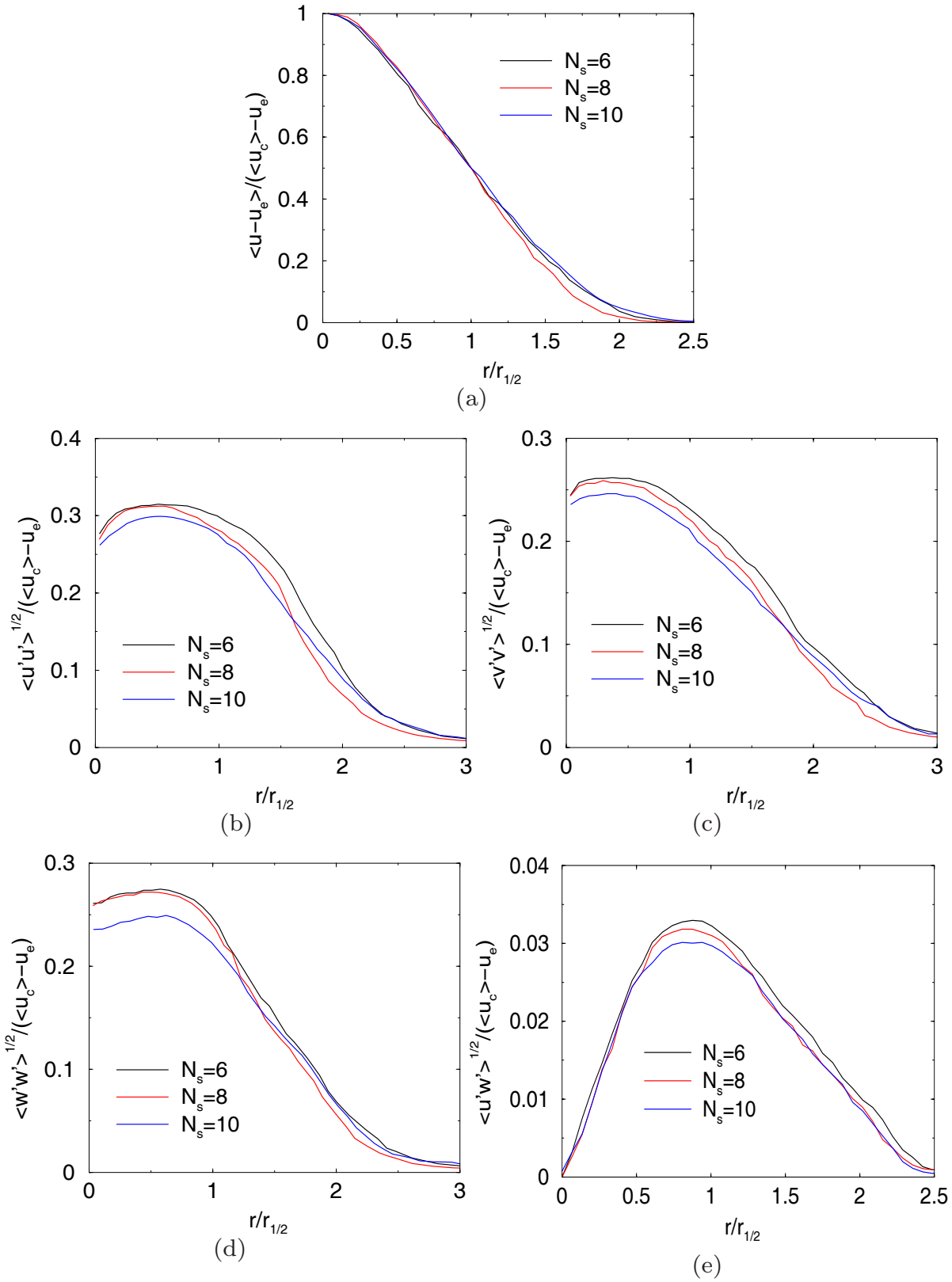

Figure 5.6: Radial velocity profiles at $x/d_j = 15$: (a) axial mean velocity, Reynolds stress in (b) axial, (c) radial and (d) azimuthal direction and (e) the shear stress for different N_s.

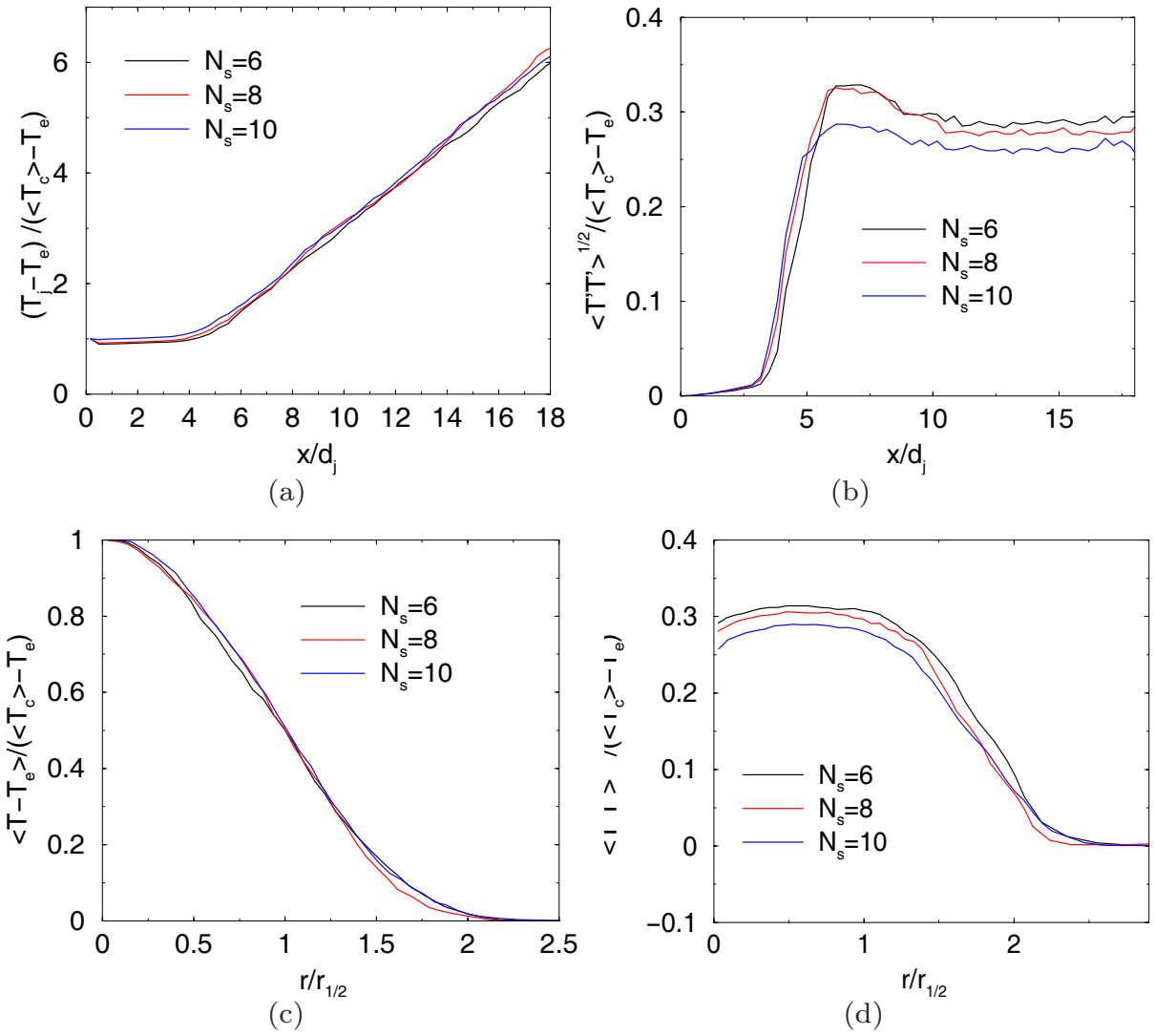

Figure 5.7: Temperature profiles: in axial direction (a) mean temperature decay compared with the mean axial velocity decay of the DNS with $N_s = 8$, (b) temperature intensity at $x/d_j = 15$ (c) mean temperature and (d) temperature intensity.

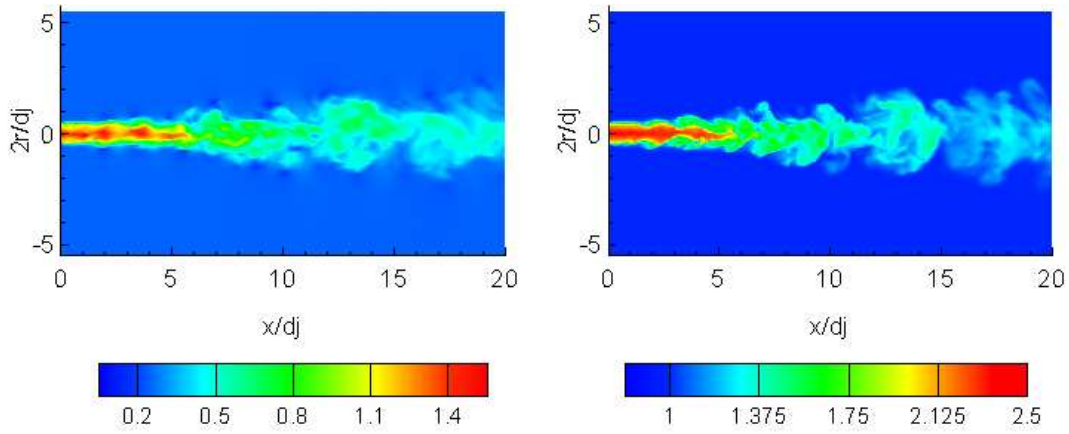

(a) u, $N_s = 6$ (b) T, $N_s = 6$

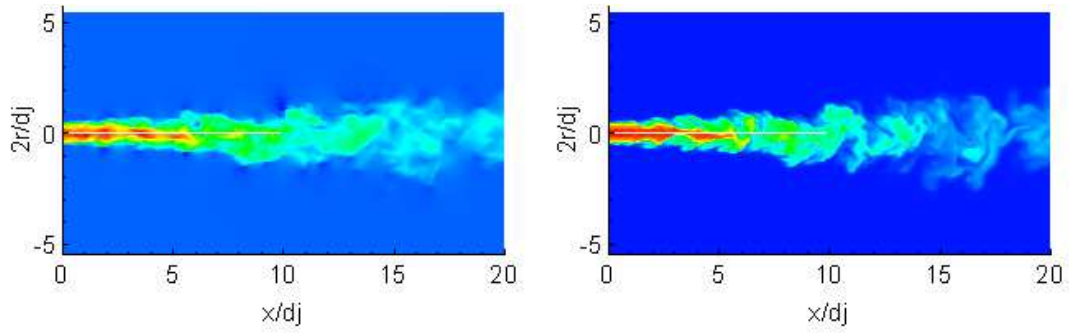

(c) u, $N_s = 8$ (d) T, $N_s = 8$

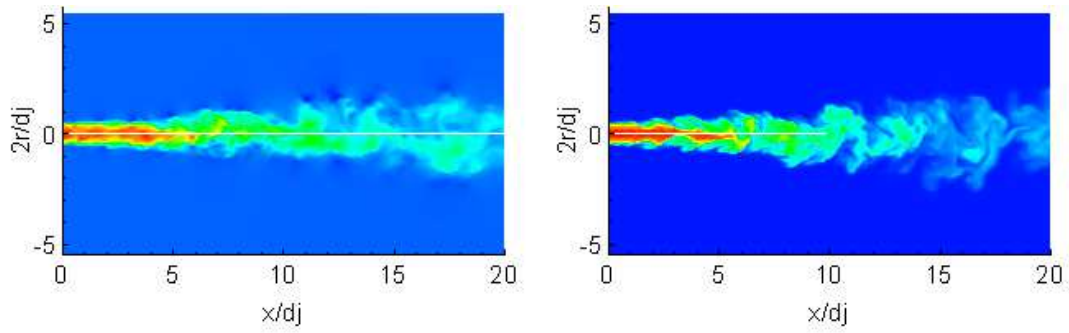

(e) u, $N_s = 10$ (f) T, $N_s = 10$

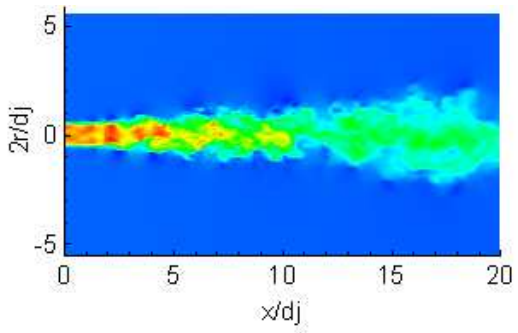

(g) iso: u, $N_s = 12$

Figure 5.8: Qualitative comparison of the instantaneous axial velocity and temperature fields for the spatial resolutions of $N_s = 6$, $N_s = 8$ and $N_s = 10$ in comparison with (g) the axial velocity field of the isothermal turbulent jet (isoT).

5.5 Large Eddy Simulation

The LES of low-Mach number, non-isothermal, turbulent jets using ADM in the spectral element code is based on the following set of equations,

$$\begin{aligned}\overline{\rho}\left[\frac{\partial\widetilde{T}}{\partial t}+\underline{u}^{\star}\cdot\widetilde{(\nabla T^{\star})}\right] &= \frac{1}{RePr}\nabla^2\widetilde{T}- \\ &- \overline{\rho}\chi_T(I-Q_N*G)*\widetilde{T}\ , \end{aligned} \tag{5.9}$$

$$\begin{aligned}\nabla\cdot\widetilde{\underline{u}} &= \frac{1}{\overline{\rho}\widetilde{T}}\left\{\frac{1}{RePr}\nabla^2\cdot\widetilde{T}-\overline{\rho}\chi_T(I-Q_N*G)*\widetilde{T}+\right. \\ &+ \left.\overline{\rho}\Big[\widetilde{\underline{u}}\cdot(\nabla\widetilde{T})-\underline{u}^{\star}\cdot\widetilde{(\nabla T^{\star})}\Big]\right\}\ . \end{aligned} \tag{5.10}$$

$$\begin{aligned}\overline{\rho}\Big[\frac{\partial\widetilde{\underline{u}}}{\partial t}+(\underline{u}^{\star}\cdot\widetilde{\nabla})\underline{u}^{\star})\Big]+\nabla\overline{p}_2 &= \frac{1}{Re}\nabla\cdot\widetilde{\underline{\underline{S}}} \\ &- \overline{\rho}\chi_u(I-Q_N*G)*\widetilde{\underline{u}} \end{aligned} \tag{5.11}$$

with

$$\widetilde{\underline{\underline{S}}}=\nabla\widetilde{\underline{u}}+(\nabla\widetilde{\underline{u}})^T-\frac{2}{3}(\nabla\cdot\widetilde{\underline{u}})\underline{\underline{I}} \tag{5.12}$$

$$1=\overline{\rho}\widetilde{T}\ . \tag{5.13}$$

assuming constant thermal diffusivity λ_∞, constant dynamic viscosity μ_∞, constant average heat capacity $c^a_{p\infty}$ and the absence of buoyancy. The inflow generator with $\sigma_s=\sigma_t=\sigma=0.1$ to perturb the 1/7-law mean inflow velocity and temperature profiles shown in Fig. 5.3 and a timestep of $dt=0.001\frac{d_j}{u_0-u_e}$ are used.
The computational mesh shown in Fig. 5.4, is based on 2,380 spectral elements and used with lower N_s than for the DNS of Section 5.4.

The LES results of the non-isothermal jet are discussed for different spatial resolutions. The relaxation parameters of $\chi_u=\chi_T=300$ are used and N_s is varied according to Table 5.5. The spatial resolutions of the LES for $N_s=6$ and 8 are identical to the spatial resolution of the DNS for the same N_s.

Sim.	**flow**	Re	Δx	Δr	
LES	axis. 3D jet	$2,000$	$0.2260d_j$	$0.1512d_j$	$N_s = 4$
LES	axis. 3D jet	$2,000$	$0.1504d_j$	$0.1006d_j$	$N_s = 6$
LES	axis. 3D jet	$2,000$	$0.1130d_j$	$0.0756d_j$	$N_s = 8$
DNS	axis. 3D jet	$2,000$	$0.0712d_j$	$0.0756d_j$	$N_s = 8$

Table 5.2: Comparison of spatial resolutions of non-isothermal LES for $N_s = 4, 6, 8$ and DNS for $N_s = 8$.

5.5.1 Filtering

Both the Legendre- and the Boyd filter were tested for the non-isothermal turbulent jet LES using the mesh of Fig. 5.4 with $N_s = 8$ and relaxation parameters $\chi_u = \chi_T = 300$. The LES with the Legendre filter becomes unstable after 150 time units caused by temperature peaks, and associated density peaks at the spectral element boundaries finally becoming the simulation unstable. The temperature and density peaks are explained by the operation of the direct-stiffness summation, which has to be performed after filtering with the Legendre filter, and introduce artificial noise to the fields at the elemental boundaries (see Section 2.5.4). On the other hand, the non-isothermal LES with the Boyd filter is numerically stable but overestimates the turbulent intensities along the centerline, similarly to what has observed in the isothermal LES jet results of Chapter 4. The instantaneous temperature fields using the Legendre and the Boyd filter are presented in Fig. 5.9 and the fields show a similar behavior. It should be noted that the fields with the Legendre filter in Fig. 5.9 (b) is after a simulation of $100t_u$ (the LES became unstable after $150t_u$).
The statistics for $150tu$ stable LES are shown for the Boyd and the Legendre filter in Fig. 5.10. The turbulent intensities for the velocity and the temperature show an overshoot in the region of $x/d_j < 15$ for the Legendre and the Boyd filter, but the Legendre filter decreases further downstream to the intensities of the DNS whereas the Boyd filter does not. The same effect was seen for the non-isothermal jet turbulent velocity intensity in Fig. 4.32.

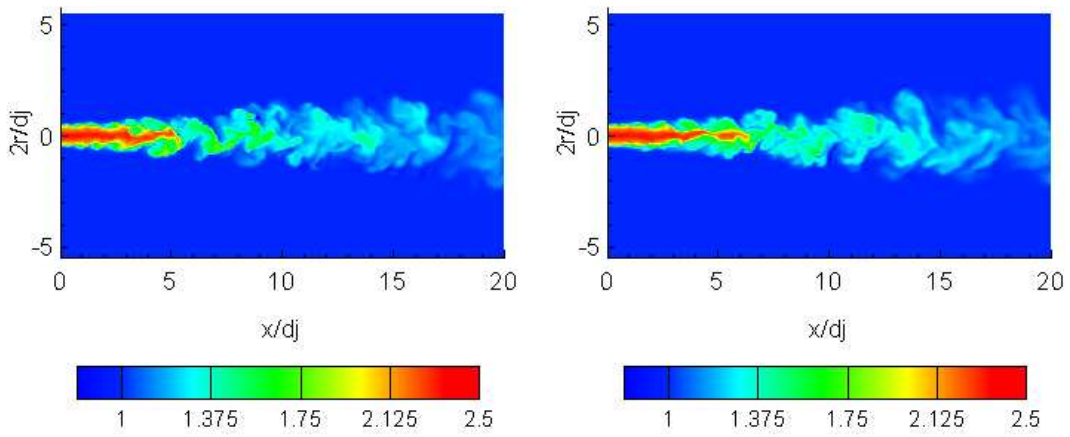

(a) Legendre: T (b) Boyd: T

Figure 5.9: Instantaneous temperature fields of the non-isothermal jet LES using (a) the Legendre filter and (b) the Boyd filter with $N_s = 8$, $\chi_u = \chi_T = 300$ and the mesh of Fig. 5.4.

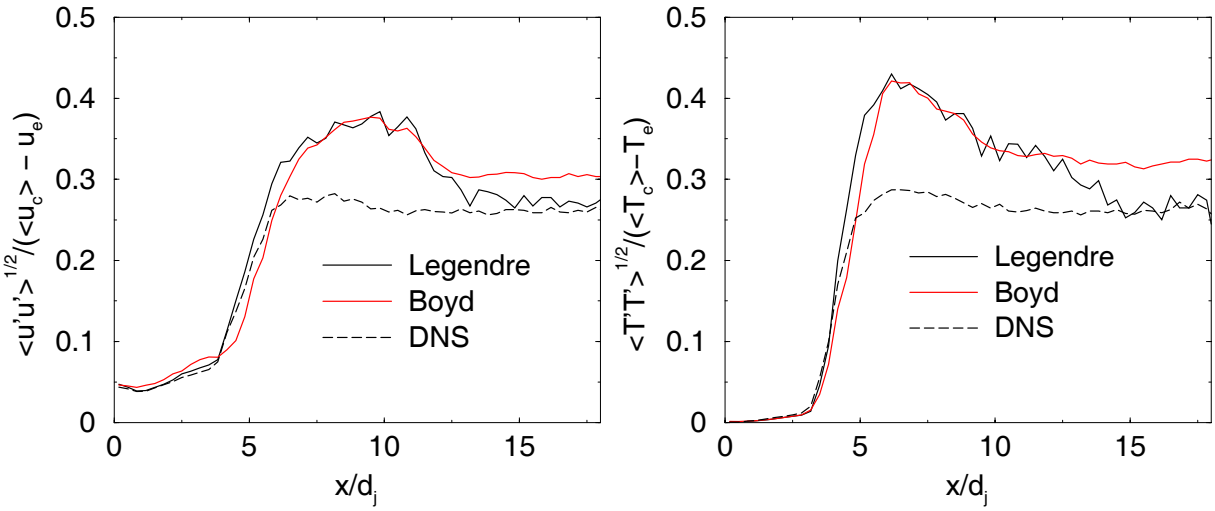

(a) (b)

Figure 5.10: Comparison between the Legendre (for the stable 150 time units) and the Boyd filter for (a) the turbulent velocity intensity in axial direction and (b) the turbulent temperature intensity in comparison with the DNS with $N_s = 10$.

5.5.2 Results and Discussion

For different spatial resolutions instantaneous axial velocity and temperature fields are compared in Fig. 5.11. For $N_s = 4$, a laminar flow is obtained although turbulent initial fields and the inflow generator to perturb the mean axial inflow velocity field are used for all simulations. The laminarization for $N_s = 4$ is explained by the filter function, which acts on the $2nd$ mode during the simulation, filters all high-frequency information by the low-pass filter and modifies the mean velocity profiles. The effect of using $N_s < 6$ was already seen in the turbulent channel flows in Chapter 3 and the negative effect of filtering modes which are smaller than $\kappa < 3$ was obvious. The comparison between the velocity and temperature fields for $N_s = 6$ and $N_s = 8$ shows the expected results that the higher spatial resolution is able to resolve more small structures.

The mean axial velocity decay is faster than the decay of the DNS (Fig. 5.12 (a)). The LES statistics overestimate the DNS velocity between $15\% - 30\%$ and the DNS temperature between $18\% - 29\%$ in the range of $x/d_j > 13$ (Fig. 5.12 (b) and (c)). The overestimation is also present if the LES statistics are compared with the DNS statistics of the same spatial resolution (see Figs. 5.5 (b), (c) and 5.7 (b)). The Boyd filter showed the same behavior for the isothermal case (see Chapter 4). We assume that the lower magnitude of the relaxation term of the Boyd filter leads to the overestimated intensity for the non-isothermal jet.

Figure 5.14 shows the CPU time for the LES in comparison with the CPU time for the DNS of $50,000$ timesteps. The simulations are performed on 64 parallel CPU's of a linux cluster equipped with Intel Xeon processors. The DNS needs for the same spatial resolution marginally less CPU time than the LES.

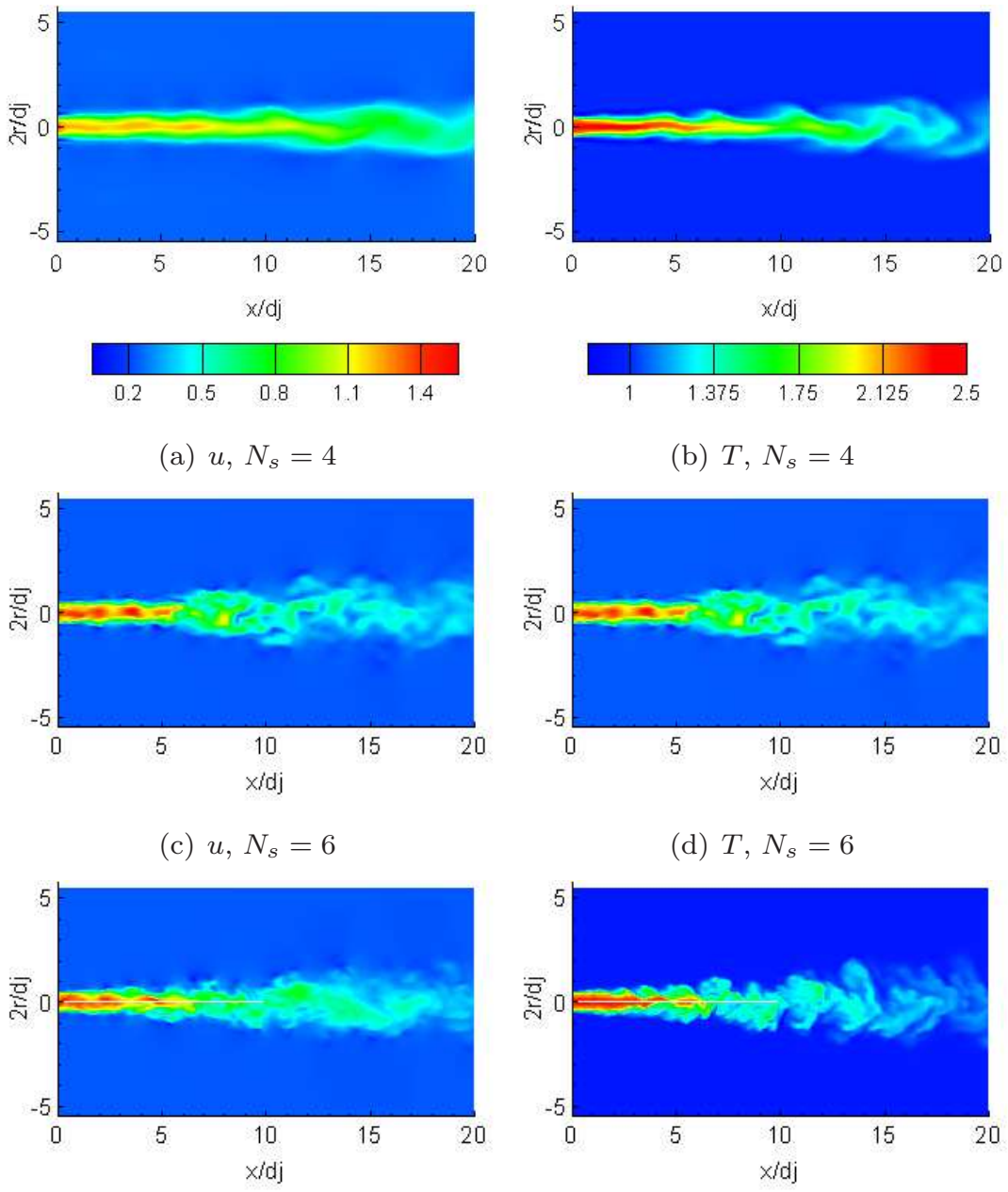

(a) u, $N_s = 4$ (b) T, $N_s = 4$

(c) u, $N_s = 6$ (d) T, $N_s = 6$

(e) u, $N_s = 8$ (f) T, $N_s = 8$

Figure 5.11: Comparison of instantaneous axial velocity and temperature fields for LES and the spatial resolutions of $N_s = 4$, $N_s = 6$ and $N_s = 8$.

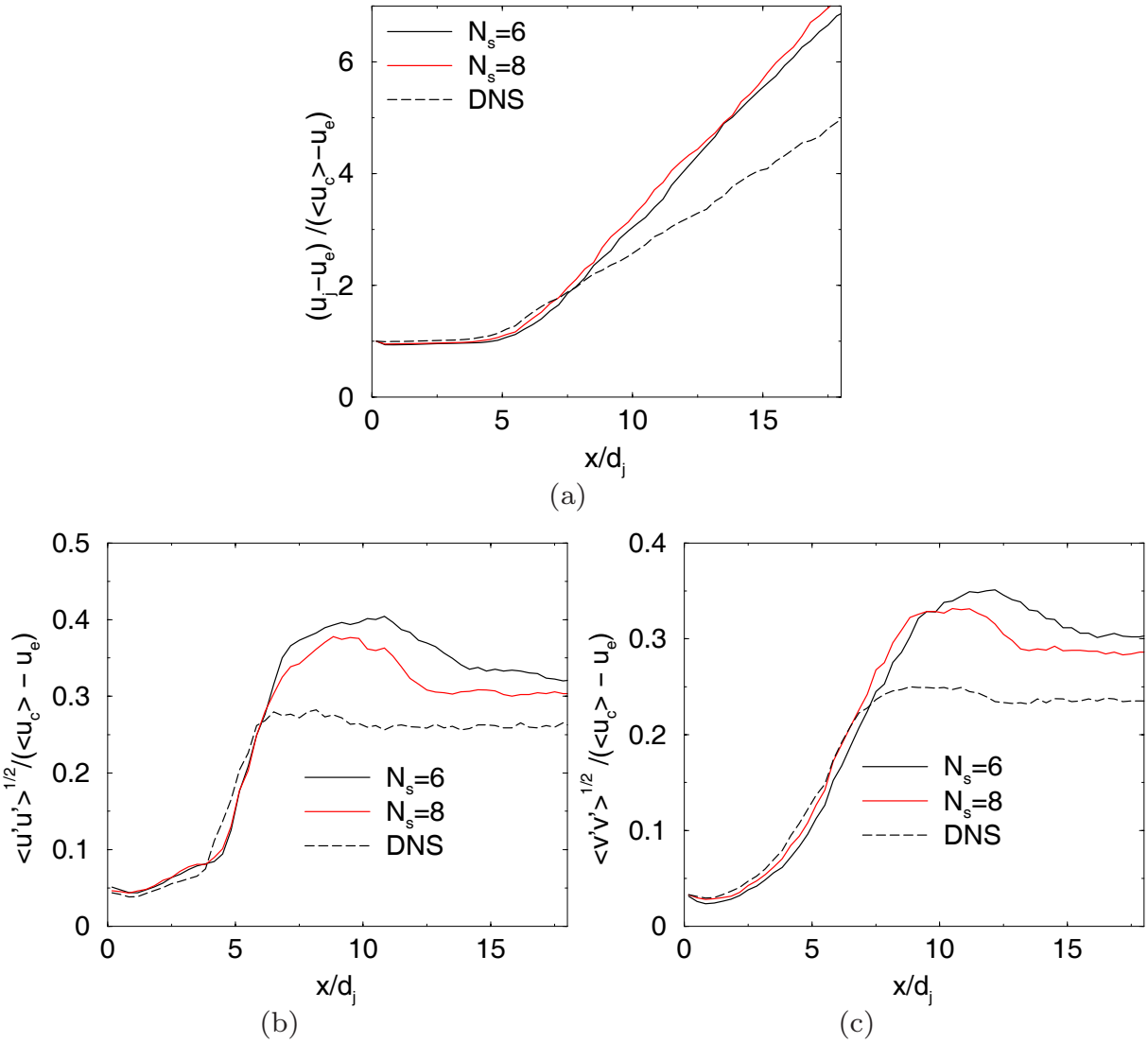

Figure 5.12: (a) mean axial velocity decay, turbulent velocity intensity in (b) axial and (c) radial direction of the present LES for different N_s compared with the DNS-results of Section 5.4.

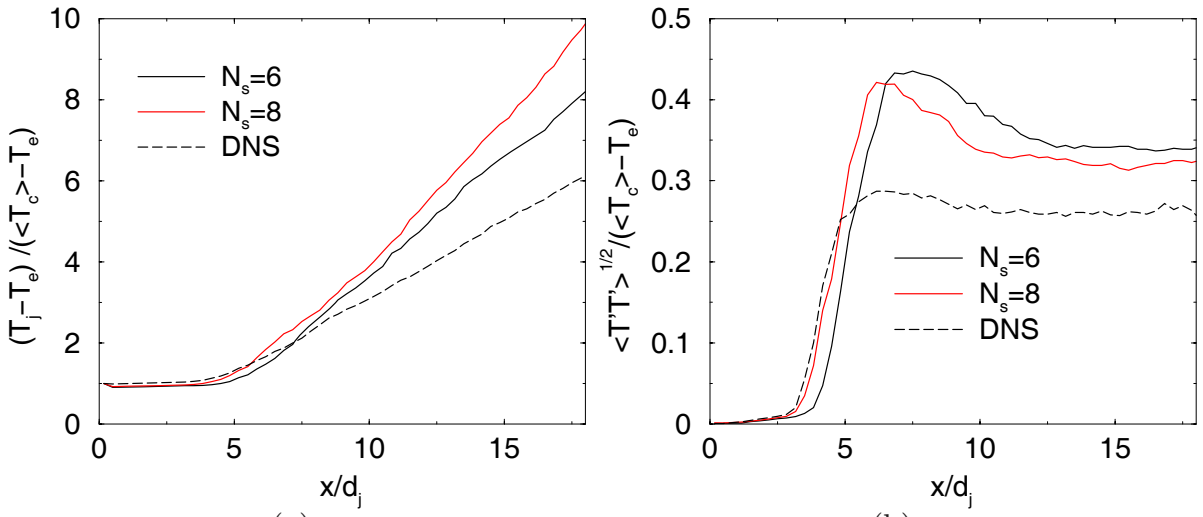

Figure 5.13: Temperature profiles in axial direction (a) mean temperature decay and (b) temperature intensity at $x/d_j = 15$ compared with the DNS of Section 5.4

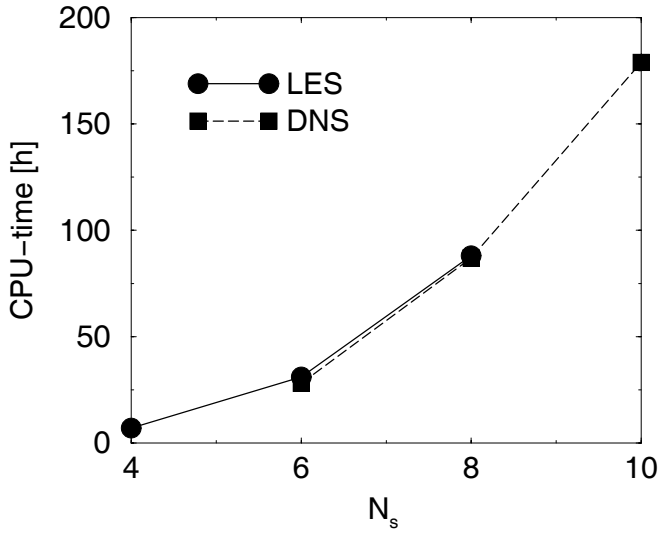

Figure 5.14: CPU-time, based on 64 parallel processors and 50 time-units simulation ($\rightarrow$ 50000 timesteps) for the non-isothermal LES with different resolutions and the corresponding DNS.

5.5.3 Testing the Numerical Implementation

The spatial resolution study showed a strong overestimation of the turbulent velocity and temperature intensity. The intensities of the LES shows higher magnitude for $N_s = 6$ and $N_s = 8$ than the corresponding DNS of Section 5.4. This result is surprising. A LES with a *rectangular filter function* according to Fig. 5.15 is performed to test the implementation, and the relaxation parameters are set to $\chi_u = \chi_T = 0$. The set of Eqs. (5.9) to (5.13) for LES should converge to the set of DNS Eqs. (5.5) to (5.8) with the *rectangular filter function*. The LES with G_r and $N_s = 6$ is compared

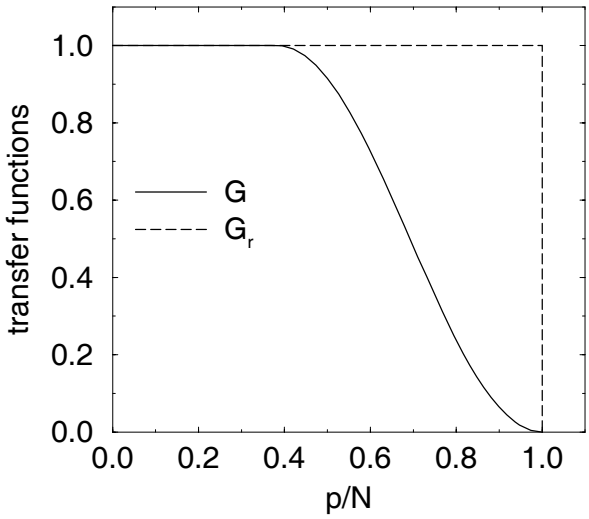

Figure 5.15: The *rectangular filter function* G_r in comparison with the original filter function G.

with the DNS of $N_s = 6$. The mean-axial velocity, and the turbulent velocity- and temperature intensity along the centerline are shown in Fig. 5.16. The congruence of the LES with G_r and the DNS with $N_s = 6$ is obvious and it is therefore concluded that the LES implementation is correct.

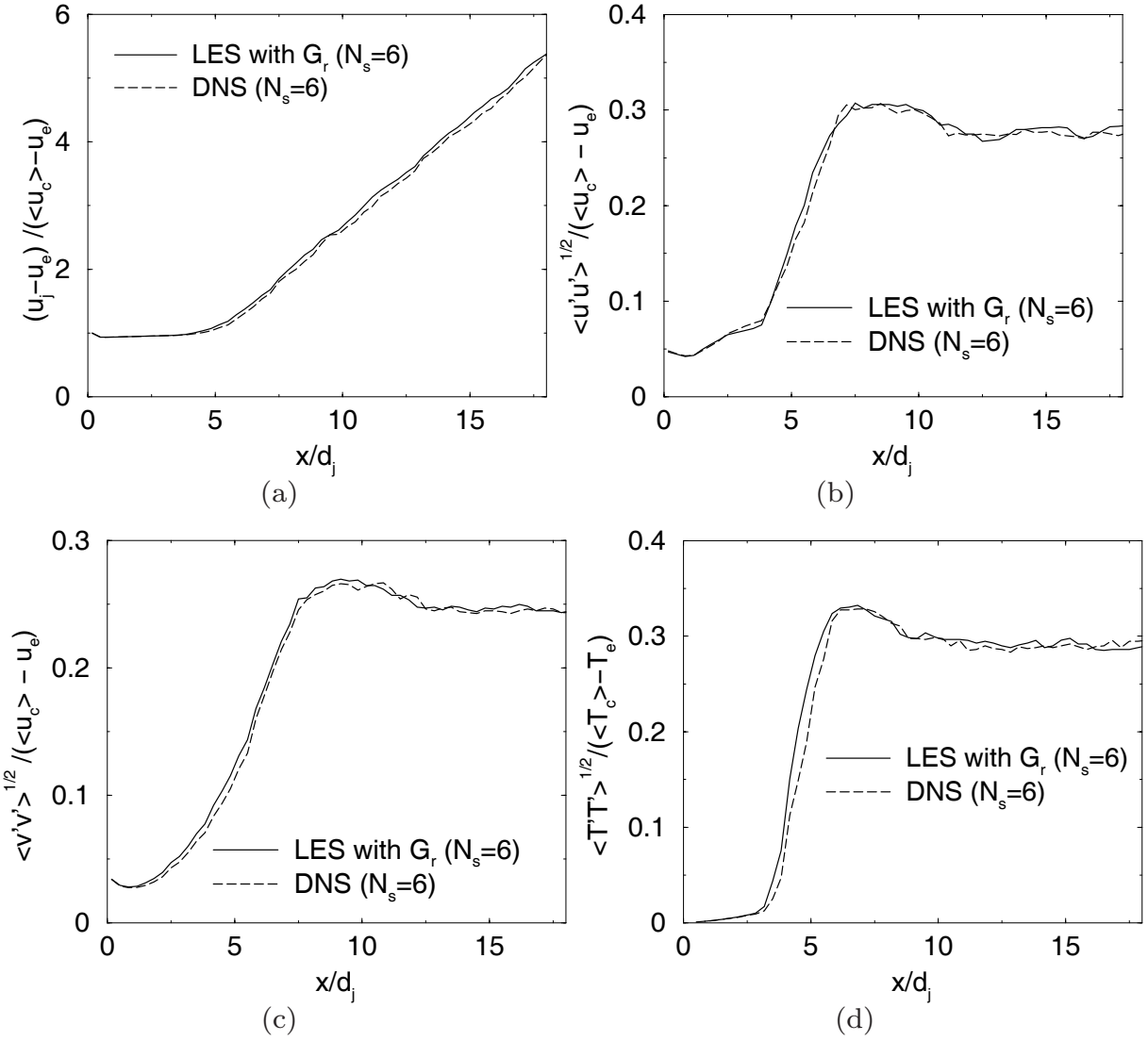

Figure 5.16: (a) mean axial velocity decay, turbulent velocity intensity in (b) axial and (c) radial direction and (d) the turbulent temperature intensity of the LES with G_r for compared with the DNS-results of Section 5.4.

5.6 Conclusions

The LES of the variable density turbulent jet is performed in a domain with a length of $x/d_j = 20$. The shorter domain relative to the isothermal jet was chosen since the turbulent jet becomes scale similar after $x/d_j = 10$.
The Legendre filter which was used for the isothermal jet could not be used for the non-isothermal jet LES. In contrast to the Boyd filter, the Legendre filter modifies the elemental boundaries and must be corrected afterwards with the direct-stiffness summation. This summation generates artificial peaks on the neighboring elemental boundaries. The temperature peaks, coupled with the density through the ideal gas law results in numerical instability. It is evident from the isothermal jet that the Boyd filter, which does not filter the elemental boundaries, overestimates the turbulent intensities along the centerline of the jet. The same conclusion can be drawn for the non-isothermal jet. Although the LES with the Boyd filter are numerically stable, the turbulent intensities are overestimated.
For comparisons a DNS with the same mesh was performed. It was not possible to perform accurate LES with spatial resolutions significantly lower than for the DNS because of numerical instabilities. To check the correct implementation of the model, an LES with a rectancular filter function was used and the centerline statistics of the results were compared with the DNS of the same spatial resolution. The LES with the rectangular filter function was almost identical with those of the DNS. The LES with the Boyd filter overestimates the turbulent intensities (velocity and temperature) of the DNS with the same spatial resolution. We assume that the lower magnitude of the relaxation term of the Boyd filter leads to the overestimated intensity for the non-isothermal jet, especially in the region $x/d_j < 15$.
Overall the comparison of LES results of the non-isothermal jet using the Boyd filter with the DNS results are not satisfactory.

Chapter 6

Conclusions and Outlook

Summary

The subject of the present work are the Large Eddy Simulations (LES) of turbulent channel and jet flows using the Approximate Deconvolution Model (ADM) as a subgrid model. The model was implemented on a spectral element code originally developed for DNS.

The spatial resolution is defined by the number of elements and the maximal polynomial order N_s. ADM was implemented and the relaxation parameter χ was set constant, in contrast to the original formulation of Stolz et al. [122] using a variable relaxation parameter. Two filter types are used: Boyd filter (elemental boundaries are not filtered) and Legendre filter (elemental boundaries are not filtered).
For the validation of the ADM implementation, an incompressible turbulent channel flow LES was performed for $Re_\tau \approx 178$ and $Re_\tau \approx 580$ and the results were compared with the DNS of Moser et al. [91]. The focus of the investigations was the near-wall behavior of the flow, especially the wall law and the friction Reynolds number.
The further validation case was an incompressible isothermal turbulent jet flow with $Re = 2,000$ being a classical case for flows in transition. The flow at the jet exit was perturbed with spatially and temporally correlated fluctuations according to Klein et al. [68]. DNS were performed with an identical setup as for the LES for better comparison of the LES results. The focus of investigation was primarily on scale-similarity behavior of mean and turbulent velocities.
ADM was further used to model the subgrid field of the temperature of a non-isothermal, variable-density jet with $Re = 2,000$. The turbulent

jet flow was no longer incompressible and the focus of investigations also was the scale-similarity behavior of mean and turbulent velocity and temperature. The LES results compared with DNS data obtained during the course of this work.

Observations

The following observations can be made from the comparison between the DNS and the LES of the turbulent channel flow (Chapter 3), the isothermal jet flow (Chapter 4) and the non-isothermal jet flow (Chapter 5).

- Using polynomial orders less than $N_s = 6$ the low-pass filter for explicit LES filtering modifies the mean velocity profile of the turbulent channel flow and leads to overall incorrect results.
- Good agreement is obtained for the wall law, the friction Reynolds number and the Reynolds stresses of LES and DNS results in the turbulent channel flow.
- Two types of filter are used (Boyd and Legendre filter) and tested for the isothermal and non-isothermal turbulent jet. The turbulent intensities in the scale-similarity range are overestimated by 20% while the Legendre filter converges to the DNS intensities.
- The turbulent velocity intensities along the centerline using the Legendre filter (axial and radial velocities) of the isothermal jet are overestimated by the LES in the transition region of the jet ($0 < x/d_j < 15$) whereas further downstream (scale-similarity region) the turbulent intensities agree well with DNS result.
- The investigation of different Reynolds numbers, inflow velocity profiles, correlation lengths of the inflow perturbation, relaxation parameters and an alternative, mathematically identical formulation of the convective term could not eliminate the overshoot of the turbulent intensities in the transition range.
- Only filtering in the Boyd space showed stable simulations for the non-isothermal jet.
- Using the same spatial resolution for LES and DNS for the non-isothermal jet the turbulent intensities for velocity and temperature are highly overestimated by the LES using the numerically stable filtering in the Boyd space.

Conclusions

From these observations, the following conclusions are drawn:

- The combination of the spectral element code and ADM shows very good agreement with the DNS if the flow is not in transition. This was the case for the turbulent channel flow where the wall law for the mean streamwise velocity, the friction Reynolds number and the Reynolds stresses agree well with DNS results and from the non-isothermal jet flow where the centerline fluctuation and the stresses in radial direction in the scale-similarity region also agree well with the DNS results. The situation is less satisfactory in flow regions where transition is present. This was seen in the developing region of the isothermal jet flow, where the turbulent intensities are overestimated by ADM. The reasons are: i) it is a challenge for a subgrid model, which is based on a existing inertial range of the turbulent spectra, to model turbulent flows in transition, in which the inertial range is establishing during transition and ii) in contrast to global spectral methods, where a large number of modes (> 30) are used to describe the solution, the spectral element method, used in this work, uses polynomial orders up to 10 to describe the solution. Therefore the information contained in the represented scales (scales between the cutoff and the maximum polynomial order) is based on less orders than for a global spectral method. Therefore the deconvolved field of ADM could be less accurate than for a global spectral method.

- Two filter types for LES filtering are investigated: i) filtering in the Boyd space where the elemental boundary points are not affected and ii) filtering in the Legendre space where the elemental boundary results are modified and must be corrected after the filtering procedure. We found a coupling between the filter type and the relaxation-term field and saw that the Legendre filter, which creates artificial noise at the elemental boundaries, increases the level of the relaxation-term field. The Legendre filter shows a better agreement between LES and DNS and we assume the origin to be in the increased level of the relaxation term.

- The artificial noise at the elemental boundaries caused by the Legendre filter lead to unstable LES of the non-isothermal jet. The reason is the artificial temperature noise at the elemental boundaries. The temperature noise influences directly the determination of the ve-

locity divergence and reduces the stability of the numerical scheme integration.

Suggestions for Future Work

From the point of view of the present work, future efforts should focus on a deeper understanding of the filtering and the subgrid-term modelling. The Boyd and the Legendre filtering procedures show different effect on the turbulent intensities. It is not clear whether the filtering itself or the influence on the relaxation term is responsible for this behavior. An extensive investigation of the filtering procedures could clarify the issue. Furthermore, the results of using a filtering procedure in physical space instead in the polynomial space used in this work, as used by Stolz et al. [122], would be interesting.
In this work the relaxation parameter of ADM was considered as a constant over the whole domain. A dynamic determination of the relaxation parameter depending on the turbulent field could probably improve the results.

Appendix A

Conservation Equations

In this Chapter the conservation equations for species and energy will be derived for multicomponent, single-phase flows and will then be rewritten in nondimensional form. The motivation to derive all used conservation equations was the fact that it was not possible to find one textbook in which the equations for multi-species flows are derived in deep detail. Furthermore, there are many different forms of the energy equation, depending on the assumptions. The following equations can partially be found in the literature of Landau et al. [73], Pope [103] and Williams [141]. The standard form of momentum and mass conservation are shown and their normalization is performed in this Chapter as well. In the following, the symbol $\check{}$ indicates a dimensional quantity, and this quantity without a mark will be dimensionless.

A.1 Species and Mass Conservation

For the derivation of the species and mass conservation in a multicomponent system it is helpful first to define some useful quantities. The derivation considers the species density $\check{\rho}_i$ which is the mass of species i per unit volume, and the mass fraction $Y_i = \check{\rho}_i/\check{\rho}$, which is the density of species i divided by the total density. Species in a multicomponent system move with different velocities $\underline{\check{u}}_i$. The velocity of species i with respect to a stationary coordinate system is defined as the sum of the bulk velocity (mass averaged velocity) $\underline{\check{u}}$ and the diffusion velocity $\underline{\check{V}}_i$, $\underline{\check{u}}_i = \underline{\check{u}} + \underline{\check{V}}_i$. For a mixture of N species, the mass averaged velocity (bulk velocity) $\underline{\check{u}}$ is

defined as

$$\underline{\check{u}} = \frac{\sum_{i=1}^{N} \check{\rho}_i \underline{\check{u}}_i}{\sum_{i=1}^{N} \check{\rho}_i} \ . \tag{A.1}$$

The diffusion velocity of species i is defined as $\underline{\check{V}}_i = \underline{\check{u}}_i - \underline{\check{u}}$ and describes the motion of the species relative to the local motion of the fluid stream. The mass flux of species i is a vector quantity denoting the mass of species i that passes through a unit area per unit time and is defined as $\underline{\check{m}}_i'' = \check{\rho}_i \underline{\check{u}}_i = \check{\rho} Y_i \underline{\check{u}}_i$. The diffusion flux relative to the stationary coordinate system can be defined as $\underline{\check{j}}_i = \check{\rho}_i \underline{\check{V}}_i$ and must satisfy

$$\sum_{i=1}^{N} \underline{\check{j}}_i = \sum_{i=1}^{N} \check{\rho}_i \underline{\check{V}}_i = 0 \ . \tag{A.2}$$

The continuity of species i in the multicomponent system is derived by considering a control volume $\check{V}_0$ with surface is $\check{A}_0$. The mass of species i in the infinitesimal volume $d\check{V}$ is

$$\check{\rho}_i d\check{V} \tag{A.3}$$

and the change in time within $\check{V}_0$

$$\int_{\check{V}_0} \frac{\partial \check{\rho}_i}{\partial \check{t}} d\check{V} \ . \tag{A.4}$$

The change of mass of species i is caused by the mass flux of species i through $\check{A}_0$

$$\begin{aligned} -\int_{\check{A}_0} (\check{\rho}_i \underline{\check{u}}_i) \cdot d\underline{\check{A}} &= -\int_{\check{A}_0} \left[\check{\rho}_i (\underline{\check{u}} + \underline{\check{V}}_i) \right] \cdot d\underline{\check{A}} \\ &= -\int_{\check{V}_0} \check{\nabla} \cdot \left[\check{\rho}_i (\underline{\check{u}} + \underline{\check{V}}_i) \right] d\check{V} \ , \end{aligned} \tag{A.5}$$

where $d\underline{\check{A}}$ is the normal to the surface $\check{A}_0$. The conservation equation for species i can then be written with Eqs. (A.4) and (A.5) as

$$\int_{\check{V}_0} \frac{\partial \check{\rho}_i}{\partial \check{t}} d\check{V} = \int_{\check{V}_0} -\check{\nabla} \cdot \left[\check{\rho}_i (\underline{\check{u}} + \underline{\check{V}}_i) \right] d\check{V} \tag{A.6}$$

and the integrands of left and right hand-side of Eq. (A.6) have to be identical

$$\frac{\partial \check{\rho}_i}{\partial \check{t}} + \check{\nabla} \cdot (\check{\rho}_i \underline{\check{u}}) = -\check{\nabla} \cdot (\check{\rho}_i \underline{\check{V}}_i) \ . \tag{A.7}$$

The summation of Eq. (A.7) over all N species leads to the mass conservation-equation

$$\frac{\partial \check{\rho}}{\partial \check{t}} + \check{\nabla} \cdot (\check{\rho}\underline{\check{u}}) = -\check{\nabla} \cdot \Big(\underbrace{\sum_{i=1}^{N} \check{\rho}_i \underline{\check{V}}_i}_{=0(A.2)} \Big) = 0 \; . \tag{A.8}$$

Equation (A.7) can be rewritten with respect to $Y_i = \rho_i/\rho$ in a conservative form as

$$\frac{\partial(\check{\rho}Y_i)}{\partial \check{t}} + \check{\nabla} \cdot (\check{\rho}Y_i\underline{\check{u}}) = -\check{\nabla} \cdot (\check{\rho}Y_i\underline{\check{V}}_i) \tag{A.9}$$

The left hand side of Eq. (A.9) can be formed with the identity

$$\nabla \cdot (U\underline{v}) = \underline{v} \cdot (\nabla U) + U(\nabla \cdot \underline{v}) \tag{A.10}$$

(U and $\underline{v}$ denote a scalar and a vector, respectively) to

$$\begin{aligned} \check{\rho}\frac{\partial Y_i}{\partial \check{t}} + Y_i\frac{\partial \check{\rho}}{\partial \check{t}} \quad &+ \quad (\check{\rho}\underline{\check{u}}) \cdot (\check{\nabla}Y_i) + Y_i\Big[\check{\nabla} \cdot (\check{\rho}\underline{\check{u}})\Big] = \\ &= \quad Y_i \underbrace{\Big[\frac{\partial \check{\rho}}{\partial \check{t}} + \check{\nabla} \cdot (\check{\rho}\underline{\check{u}})\Big]}_{=0 \; (A.8)} + \check{\rho}\Big[\frac{\partial Y_i}{\partial \check{t}} + \underline{\check{u}} \cdot (\check{\nabla}Y_i)\Big] \end{aligned} \tag{A.11}$$

and with Eq. (A.9) to the species conservation-equation, written in primitive form

$$\check{\rho}\left[\frac{\partial Y_i}{\partial \check{t}} + \underline{\check{u}} \cdot (\check{\nabla}Y_i)\right] = -\check{\nabla} \cdot (\check{\rho}Y_i\underline{\check{V}}_i) \; . \tag{A.12}$$

Note, the following expression holds for each scalar $\check{f}$ (species i and temperature T), because of the continuity equation Eq. (A.8)

$$\check{\rho}\frac{D\check{f}}{D\check{t}} = \check{\rho}\Big(\frac{\partial \check{f}}{\partial \check{t}} + \underline{\check{u}} \cdot (\check{\nabla}\check{f})\Big) = \frac{\partial \check{\rho}\check{f}}{\partial \check{t}} + \check{\nabla} \cdot (\check{\rho}\check{f}\underline{\check{u}}) \; , \tag{A.13}$$

where the first term on the left hand-side is called the material derivative. The species conservation-equation can then be written in summarized form with Eqs. (A.9), (A.12) and (A.13) as

$$\begin{aligned} \check{\rho}\frac{DY_i}{D\check{t}} \quad &= \quad \frac{\partial(\check{\rho}Y_i)}{\partial \check{t}} + \check{\nabla} \cdot (\check{\rho}Y_i\underline{\check{u}}) \\ &= \quad -\check{\nabla} \cdot (\check{\rho}Y_i\underline{\check{V}}_i) \; . \end{aligned} \tag{A.14}$$

A.1.1 Simplified Species Conservation

The diffusion velocity $\underline{V}_i$ in Eq. (A.14) is unknown and has to be specified. From the kinetic theory of gas (see Williams [141])

$$\begin{aligned}\check{\nabla} X_i &= \sum_{k=1}^{N} \frac{X_i X_k}{\check{D}_{ik}} (\underline{\check{V}}_k - \underline{\check{V}}_i) + \\ &+ (Y_i - X_i) \frac{\check{\nabla}\check{p}}{\check{p}} + \frac{\check{\rho}}{\check{p}} \sum_{k=1}^{N} Y_i Y_k (\underline{\check{f}}_i - \underline{\check{f}}_k) \\ &+ \sum_{i=1}^{N} \frac{X_i X_k}{\check{\rho}\check{D}_{ik}} (\frac{\check{\alpha}_k}{Y_k} - \frac{\check{\alpha}_i}{Y_i}) \frac{\check{\nabla}\check{T}}{\check{T}} \ , \end{aligned} \tag{A.15}$$

where $\check{D}_{ik} = \check{D}_{ki}$ is the binary diffusion coefficient of species i in species k, X_i is the mole fraction of species i, $\underline{\check{f}}_i$ is the body force acting on species i (e.g. gravity, electromagnetic force if species i is charged), and $\check{\alpha}_k$ is the thermal diffusion coefficient of species i. This linear system of N equations must be solve for each component for the species diffusion velocity at each grid point of the computational domain. To avoid high computational costs, simplifications are commonly used. Neglecting pressure diffusion (Dufour effect) and thermal diffusion effects, and further assuming that the diffusion of any species $i = 1, ..., N-1$ is mainly governed by its collisions with an abundant N^{th} species (for example nitrogen), Eq. (A.15) reduces to the well known Fick's law of diffusion

$$\underline{\check{V}}_i^{Fick} = -\check{D}_{i,N_2} \check{\nabla}(ln Y_i) \ . \tag{A.16}$$

If all species equations Eq. (A.14) are added up, the total mass conservation Eq. (A.8) is recovered, if the identity

$$\sum_{i=1}^{N} Y_i \check{V}_i = 0 \tag{A.17}$$

Eq. (A.5) is satisfied. However, if Fick's law is used, the sum over all species of Eq. (A.16) is equal zero only if all diffusion coefficients are equal ($\check{D}_{i,N_2} = \check{D}$). Otherwise, conservation of total mass cannot be satisfied and a correction velocity $\underline{\check{u}}_c$ has to be introduced to guarantee mass conservation. If all the species diffusion coefficients are not equal, the total diffusion velocity $\underline{V}_i$ must then be extended to

$$\underline{\check{V}}_i = \underline{\check{V}}_i^{Fick} + \underline{\check{u}}_c \ , \tag{A.18}$$

where $\underline{\check{u}}_c$ is defined from Eq. (A.17) as

$$\sum_{i=1}^{N} Y_i(\underline{\check{V}}_i^{Fick} + \underline{\check{u}}_c) = \sum_{i=1}^{N} Y_i \underline{\check{V}}_i^{Fick} + \underline{\check{u}}_c \underbrace{\sum_{i=1}^{N} Y_i}_{=0} := 0 \tag{A.19}$$

and

$$\underline{\check{u}}_c := -\sum_{i=1}^{N} Y_i \underline{\check{V}}_i^{Fick} \ . \tag{A.20}$$

Equation (A.14) then becomes

$$\begin{aligned} \check{\rho}\frac{DY_i}{D\check{t}} &= \frac{\partial(\check{\rho}Y_i)}{\partial\check{t}} + \check{\nabla}\cdot(\check{\rho}Y_i\underline{\check{u}}) \\ &= \check{\nabla}\cdot\left[\check{\rho}\check{D}_{i,N_2}(\check{\nabla}Y_i) - \check{\rho}Y_i\underline{\check{u}}_c\right] , \end{aligned} \tag{A.21}$$

where $\underline{\check{u}}_c$ is calculated according to Eq. (A.20).

A.1.2 Nondimensional Mass and Species conservation

Equations (A.8) and (A.21) are nondimensionalized by using reference quantities denoted by the subscript ∞, e.g. farfield or stagnation conditions and a typical length scale $\check{L}_\infty$ of the considered flow. Nondimensional quantities are defined by

$$\begin{aligned} \underline{u} &= \frac{\underline{\check{u}}}{\check{u}_\infty} \\ \underline{x} &= \frac{\underline{\check{x}}}{\check{L}_\infty} \\ \rho &= \frac{\check{\rho}}{\check{\rho}_\infty} \\ D_{i,N_2} &= \frac{\check{D}_{i,N_2}}{\check{D}_{\infty,N_2}} \\ t &= \frac{\check{t}}{\check{L}_\infty/\check{u}_\infty} = \frac{\check{t}\check{u}_\infty}{\check{L}_\infty} \\ \nabla &= \check{\nabla}\check{L}_\infty \ . \end{aligned} \tag{A.22}$$

Nondimensional numbers are defined by

$$Re = \frac{\check{u}_\infty\check{L}_\infty\check{\rho}_\infty}{\check{\mu}_\infty} = \frac{\check{u}_\infty\check{L}_\infty}{\check{\nu}_\infty} \tag{A.23}$$

$$Sc_i = \frac{\check{\mu}_\infty}{\check{\rho}_\infty \check{D}_{\infty N_2}} \tag{A.24}$$

$$\tag{A.25}$$

where Re, Sc_i and $\check{\nu}_\infty$ denotes the Reynolds number, the Schmidt number and the kinematic viscosity, respectively. The combination of the nondimensional quantities and numbers with the mass conservation Eq. (A.8) and the species conservation Eq. (A.21) lead to the nondimensional mass conservation

$$\frac{d\rho}{dt} + \nabla \cdot (\rho \underline{u}) = 0 \tag{A.26}$$

and the nondimensional species conservation

$$\begin{aligned} \rho \frac{DY_i}{Dt} &= \frac{\partial(\rho Y_i)}{\partial t} + \nabla \cdot (\rho Y_i \underline{u}) \\ &= \frac{1}{ReSc_i} \nabla \cdot \Big[\rho D_{i,N_2} (\nabla Y_i) + \check{\rho} Y_i \underline{u}_c \Big] \ . \end{aligned} \tag{A.27}$$

A.2 Momentum Conservation

The reader is refereed to any text book about fluid mechanics for the derivation of the momentum conservation equation . The author especially prefers the book of Landau and Lifschitz [73]. The momentum conservation for a Newtonian fluid, which is a fluid exhibiting a linear relationship between shear stress and rate of deformation, is considered in primitive formulation

$$\check{\rho} \Big[\frac{\partial \check{\underline{u}}}{\partial \check{t}} + (\check{\underline{u}} \cdot \check{\nabla}) \check{\underline{u}} \Big] + \check{\nabla} \check{p} = \check{\nabla} \cdot (\check{\mu} \check{\underline{\underline{S}}}) + \check{\rho} \underline{\check{g}} \ , \tag{A.28}$$

where

$$\check{\underline{\underline{S}}} = \check{\nabla} \underline{\check{u}} + (\check{\nabla} \underline{\check{u}})^T - \frac{2}{3} (\check{\nabla} \cdot \underline{\check{u}}) \underline{\underline{I}} \tag{A.29}$$

and $\check{p}$, $\check{\underline{\underline{S}}}$ and $\check{\mu}$ denote the pressure, the shear stress tensor and the (dynamic) viscosity, respectively. $\underline{\underline{I}}$ is the unit tensor. The gravitational acceleration vector $\underline{\check{g}}$ is directed opposite to the radial unit vector $\underline{e}_g$ in spherical coordinates with the gravity constant $\check{g} = 9.81 \frac{m}{s^2}$ on the earth surface.
The convective term in Eq. (A.28) can be splitted

$$\check{\rho} (\check{\underline{u}} \cdot \check{\nabla}) \check{\underline{u}} = \check{\nabla} \cdot (\check{\rho} \check{\underline{u}} \otimes \check{\underline{u}}) - \check{\underline{u}} \Big(\check{\nabla} \cdot (\check{\rho} \check{\underline{u}}) \Big) \ , \tag{A.30}$$

where $\underline{\check{u}} \otimes \underline{\check{u}}$ is defined the dyadic product (see Bronstein et al. [20]). Equation (A.28) can be rearranged by using Eqs. (A.30) and (A.8) to the compressible momentum equation, written in primitive variables

$$\frac{\partial(\check{\rho}\underline{\check{u}})}{\partial \check{t}} + \check{\nabla} \cdot (\check{\rho}\underline{\check{u}} \otimes \underline{\check{u}}) + \check{\nabla}\check{p} = \check{\nabla} \cdot (\check{\mu}\underline{\underline{\check{S}}}) + \check{\rho}\underline{\check{g}} \; . \tag{A.31}$$

A.2.1 Nondimendional Momentum Conservation

Eqs. (A.28) and (A.31) are nondimensionalized by using Eqs. (A.22), (A.23) and additional reference quantities denoted by the subscript ∞, are defined by

$$\begin{aligned} p &= \frac{\check{p}}{\check{p}_\infty} \\ \mu &= \frac{\check{\mu}}{\check{\mu}_\infty} \\ \underline{g} &= \frac{\underline{\check{g}}}{\check{g}_\infty} \; . \end{aligned} \tag{A.32}$$

Additional nondimensional numbers are defined by

$$Fr = \frac{\check{u}_\infty}{\sqrt{\check{g}\check{L}_\infty}} \tag{A.33}$$

$$Ma = \frac{\check{u}_\infty}{\sqrt{\gamma \frac{\check{p}_\infty}{\check{\rho}_\infty}}} \tag{A.34}$$

$$\hat{Ma} = \frac{\check{u}_\infty}{\sqrt{\frac{\check{p}_\infty}{\check{\rho}_\infty}}} = \sqrt{\gamma} Ma \; , \tag{A.35}$$

where Fr and $\hat{Ma}$ are denoted as Froude number and Mach number and γ is the ratio of the specific heats $\check{c}_p/\check{c}_v$. Using the nondimensional quantities and numbers in combination with Eqs. (A.28) and (A.31) the nondimensional momentum conservation-equations write as

$$\begin{aligned} \rho\Big[\frac{\partial \underline{u}}{\partial t} + (\underline{u} \cdot \nabla)\underline{u}\Big] &= -\frac{1}{\hat{Ma}^2}\nabla p + \frac{1}{Re}\nabla \cdot (\mu \underline{\underline{S}}) + \frac{1}{Fr^2}\rho \underline{e}_g \\ \frac{\partial(\rho \underline{u})}{\partial t} + \nabla \cdot (\rho \underline{u} \otimes \underline{u}) &= -\frac{1}{\hat{Ma}^2}\nabla p + \frac{1}{Re}\nabla \cdot (\mu \underline{\underline{S}}) + \frac{1}{Fr^2}\rho \underline{e}_g \end{aligned} \tag{A.36}$$

with

$$\underline{\underline{S}} = \nabla \underline{u} + (\nabla \underline{u})^T - \frac{2}{3}(\nabla \cdot \underline{u})\underline{\underline{I}} \; . \tag{A.37}$$

A.3 Energy Conservation

In this work only the internal energy-equation is considered, which can be formulate as an energy conservation-equation explicit in temperature. The internal energy equation is derived based on the definition of the total energy, which is the sum of the kinetic, the internal and the potential energy, which in our case will be neglected

$$\check{E}_{tot} = \check{E}_{kin} + \check{E} \ . \tag{A.38}$$

First, equations for $\check{E}_{tot}$ and $\check{E}_{kin}$ are derived and in a second step $\check{E}$ is given by the subtraction of this two.

A.3.1 Total Energy

A control volume $\check{V}_0$ (with surface $\check{A}_0$) is considered for which Eq. (A.38) can be written as

$$\check{E}_{tot} = \int_{\check{V}_0} \check{\rho}\Big(\frac{1}{2} \mid \underline{\check{u}} \mid^2 + \check{e}\Big) d\check{V} \tag{A.39}$$

and its change in time

$$\frac{d\check{E}_{tot}}{d\check{t}} = \int_{\check{V}_0} \frac{d}{d\check{t}} \left[\check{\rho}\Big(\frac{1}{2} \mid \underline{\check{u}} \mid^2 + \check{e}\Big) \right] d\check{V} \ , \tag{A.40}$$

where $\underline{\check{u}}$ and $\check{e}$ are the bulk velocity and is the specific internal energy (concerning mass), respectively. The temporal change of E_{tot} is caused a) through the heat flux $\underline{\check{\dot{q}}}''$ through $\check{A}_0$

$$-\int_{\check{A}_0} \underline{\check{\dot{q}}}'' \cdot d\underline{\check{A}} = -\int_{\check{V}_0} \Big(\check{\nabla} \cdot \underline{\check{\dot{q}}}''\Big) d\check{V} \ , \tag{A.41}$$

b) through the total energy flux through $\check{A}_0$

$$-\int_{\check{A}_0} \left[\check{\rho}\Big(\frac{1}{2} \mid \underline{\check{u}} \mid^2 + \check{e}\Big) \underline{\check{u}} \right] \cdot d\underline{\check{A}} = -\int_{\check{V}_0} \check{\nabla} \cdot \left[\check{\rho}\Big(\frac{1}{2} \mid \underline{\check{u}} \mid^2 + \check{e}\Big) \underline{\check{u}} \right] d\check{V} \tag{A.42}$$

c) through the work caused by surface forces

$$\begin{aligned} \int_{\check{A}_0} \left\{ \Big[-\check{p}\underline{\underline{I}} + (\check{\mu}\underline{\underline{\check{S}}}) \Big] \cdot \underline{\check{u}} \right\} \cdot d\underline{\check{A}} &= \int_{\check{A}_0} \Big[-\check{p}\underline{\check{u}} + (\check{\mu}\underline{\underline{\check{S}}}) \cdot \underline{\check{u}} \Big] \cdot d\check{A} \\ &= \int_{\check{V}_0} \left\{ \check{\nabla} \cdot \Big[-\check{p}\underline{\check{u}} + (\check{\mu}\underline{\underline{\check{S}}}) \cdot \underline{\check{u}} \Big] \right\} d\check{V} \end{aligned} \tag{A.43}$$

and d) through the work done by volumetric forces (gravity, magnetic forces, etc.)

$$\int_{\check{V}_0} \left[\Big(\sum_{i=1}^{N} \check{\rho}_i \underline{\check{f}}_i \Big) \cdot \underline{\check{u}} \right] d\check{V} \ . \tag{A.44}$$

The conservation equation for $\check{E}_{tot}$ can be written as the left-hand side of Eq. (A.40) equal the sum of Eqs. (A.41) to (A.44), where the integrands on the left and the right-hand side has to be identical and leads to

$$\begin{aligned} \check{\rho} \frac{D\check{e}_{tot}}{D\check{t}} = & \quad \frac{\partial(\check{\rho}\check{e}_{tot})}{\partial \check{t}} + \check{\nabla} \cdot (\check{\rho}\check{e}_{tot}\underline{\check{u}}) \\ = & - \check{\nabla} \cdot \underline{\check{\dot{q}}}'' + \\ & + \check{\nabla} \cdot \Big[- \check{p}\underline{\check{u}} + (\check{\mu}\underline{\underline{\check{S}}}) \cdot \underline{\check{u}} \Big] + \\ & + \sum_{i=1}^{N} \Big(\check{\rho}_i \underline{\check{f}}_i \Big) \cdot \underline{\check{u}} \ . \end{aligned} \tag{A.45}$$

A.3.2 Kinetic Energy Conservation Equation

For deriving the kinetic energy conservation Eq. (A.28) is multiplied by $\underline{\check{u}}$

$$\check{\rho} \left\{ \underline{\check{u}} \cdot \frac{\partial \underline{\check{u}}}{\partial \check{t}} \underline{\check{u}} \cdot \Big[(\underline{\check{u}} \cdot \check{\nabla}) \underline{\check{u}} \Big] \right\} = - \underline{\check{u}} \cdot (\check{\nabla} \check{p}) + \underline{\check{u}} \cdot \Big[\check{\nabla} \cdot (\check{\mu} \underline{\underline{\check{S}}}) \Big] \ , \tag{A.46}$$

where the gravity term for the kinetic energy conservation-equation is neglected. Equation (A.46) can be formed to

$$\frac{\partial}{\partial \check{t}} \Big(\frac{1}{2} \check{\rho} \mid \underline{\check{u}} \mid^2 \Big) + \check{\nabla} \cdot \Big(\frac{1}{2} \check{\rho} \mid \underline{\check{u}} \mid^2 \underline{\check{u}} \Big) = - \underline{\check{u}} \cdot (\check{\nabla} \check{p}) + \underline{\check{u}} \cdot (\check{\nabla} \cdot (\check{\mu} \underline{\underline{\check{S}}})) \tag{A.47}$$

and

$$\begin{aligned} \check{\rho} \frac{D\check{e}_{kin}}{D\check{t}} &= \frac{\partial(\check{\rho}\check{e}_{kin})}{\partial \check{t}} \\ &= - \underline{\check{u}} \cdot (\check{\nabla} \check{p}) + \underline{\check{u}} \cdot (\check{\nabla} \cdot (\check{\mu} \underline{\underline{\check{S}}})) \ , \end{aligned} \tag{A.48}$$

which represents the kinetic energy conservation equation.

A.3.3 Internal Energy Conservation Equation

The internal energy conservation equation is derived by subtraction Eq. (A.47) from Eq. (A.45) and using the vector relation $\check{\nabla} \cdot \Big(\underline{\check{u}} \cdot (\check{\mu} \underline{\underline{\check{S}}}) \Big) =$

$\underline{\check{u}} \cdot \left(\check{\nabla} \cdot (\check{\mu}\underline{\underline{\check{S}}})\right) + (\check{\mu}\underline{\underline{\check{S}}}) : \check{\nabla}\underline{\check{u}}$ (see Bronstein et al. [20]), which leads to the internal energy conservation equation

$$\begin{aligned} \check{\rho}\frac{D\check{e}}{D\check{t}} = & \quad \frac{\partial(\check{\rho}\check{e})}{\partial\check{t}} + \check{\nabla} \cdot (\check{\rho}\check{e}\underline{\check{u}}) \\ = & - \check{\nabla} \cdot \underline{\check{\dot{q}}}'' + \\ & + (\check{\mu}\underline{\underline{\check{S}}}) : \check{\nabla}\underline{\check{u}} - \\ & - \check{\nabla} \cdot (\check{p}\underline{\check{u}}) + \underline{\check{u}} \cdot (\check{\nabla}\check{p}) + \\ & + \left(\sum_{i=1}^{N} \check{\rho}_i \underline{\check{f}}_i\right) \cdot \underline{\check{u}} \ , \end{aligned} \tag{A.49}$$

where the operation $(\check{\mu}\underline{\underline{\check{S}}}) : \check{\nabla}\underline{\check{u}}$ is called contracted tensor product (see Bronstein et al. [20]).

A.3.4 Enthalpy Conservation Equation

In this work only open systems ($\check{p} = const$) are considered. For that case Eq. A.49 can be formed to an equation explicit in temperature with the help of the enthalpy. The enthalpy is defined as

$$\check{h} = \check{e} + \frac{\check{p}}{\check{\rho}} \tag{A.50}$$

and can be splitted in the heat of formation $\check{h}^0$ and the sensible enthalpy $\check{h}^s$

$$\check{h} = \check{h}^0 + \check{h}^s = \check{h}^0 + \int_{\check{T}_r}^{\check{T}} \check{c}_p d\check{T} \ , \tag{A.51}$$

where usually $\check{T}_r = 298.15K$, is called reference temperature and used for the definition of $\check{h}^0$. The procedure now is similar to that of deriving the internal energy conservation equation. First an conservation equation for the total enthalpy and then for the heat of formation will be derived. Afterwards first the sensible enthalpy conservation equation will be got by the subtraction according to Eq. (A.51).

Total Enthalpy Conservation Equation

The total enthalpy conservation equation is derived by using Eq. (A.49) and Eq. (A.50), which allows the substitution of $\check{e}$ by $\check{h}$

$$\check{\rho}\frac{D\check{h}}{D\check{t}} = \quad \frac{\partial(\check{\rho}\check{h})}{\partial\check{t}} + \check{\nabla} \cdot (\check{\rho}\check{h}\underline{\check{u}})$$

$$
\begin{aligned}
= \quad & - \quad \check{\nabla} \cdot \underline{\check{\dot{q}}}'' + \\
& + \quad (\check{\mu} \underline{\underline{\check{S}}}) : \check{\nabla} \underline{\check{u}} + \\
& + \quad \frac{D\check{p}}{D\check{t}} \\
& + \quad \Big(\sum_{i=1}^{N} \check{\rho}_i \underline{\check{f}}_i \Big) \cdot \underline{\check{u}}
\end{aligned} \tag{A.52}
$$

Enthalpy of formation Conservation

The heat of formation equation is derived by the multiplication of $\check{h}_i^0$ with Eq. (A.9) and the summation over all species i

$$
\frac{\partial}{\partial \check{t}} \Big(\check{\rho} \sum_{i=1}^{N} \check{h}_i^0 Y_i \Big) + \check{\nabla} \cdot \Big(\check{\rho} \underline{\check{u}} \sum_{i=1}^{N} \check{h}_i^0 Y_i \Big) = - \check{\nabla} \cdot \Big(\check{\rho} \sum_{i=1}^{N} Y_i \check{h}_i^0 \underline{\check{V}}_i \Big) \tag{A.53}
$$

and further with the mass averaged enthalpy for a multicomponent system

$$
\check{h}^0 = \sum_{i=1}^{N} \check{h}_i^0 Y_i \tag{A.54}
$$

to the conservation equation for the heat of formation

$$
\begin{aligned}
\check{\rho} \frac{D\check{h}^0}{D\check{t}} = \quad & \frac{\partial (\check{\rho} \check{h}^0)}{\partial \check{t}} + \check{\nabla} \cdot (\check{\rho} \underline{\check{u}} \check{h}^0) \\
= \quad & - \quad \check{\nabla} \cdot \Big(\check{\rho} \sum_{i=1}^{N} Y_i \check{h}_i^0 \underline{\check{V}}_i \Big) \, .
\end{aligned} \tag{A.55}
$$

Sensible Enthalpy Conservation

According to Eq. (A.51), the sensible enthalpy conservation equation will then be derived by subtracting Eq. (A.55) from Eq. (A.52)

$$
\begin{aligned}
\check{\rho} \frac{D\check{h}^s}{D\check{t}} = \quad & \frac{\partial (\check{\rho} \check{h}^s)}{\partial \check{t}} + \check{\nabla} \cdot \big(\check{\rho} \check{h}^s \underline{\check{u}} \big) \\
= \quad & - \quad \check{\nabla} \cdot \underline{\check{\dot{q}}}'' + \nabla \cdot \Big(\check{\rho} \sum_{i=1}^{N} Y_i \check{h}_i^0 \underline{\check{V}}_i \Big) + \\
& + \quad (\check{\mu} \underline{\underline{\check{S}}}) : \check{\nabla} \underline{\check{u}} + \\
& + \quad \frac{D\check{p}}{D\check{t}} + \Big(\sum_{i=1}^{N} \check{\rho}_i \underline{\check{f}}_i \Big) \cdot \underline{\check{u}} \, .
\end{aligned} \tag{A.56}
$$

A.3.5 Simplified Sensible Enthalpy Conservation

An expression for the heat flux-vector $\check{\underline{q}}''$ in Eq. A.55 will be derived from the gas kinetic theory (see Williams [141]) The heat flux-vector $\underline{\dot{q}_s''}$ in Eq. (A.56) writes then as

$$\check{\underline{q}}'' = -\check{\lambda}\check{\nabla}\check{T} + \check{\rho}\sum_{i=1}^{N}\check{h}_i Y_i \check{\underline{V}}_i + \check{R}\check{T}\sum_{j=1}^{N}\sum_{k=1}^{N}\left(\frac{X_k\check{\alpha}_j}{\check{M}_j\check{D}_{jk}}\right)(\check{\underline{V}}_j - \check{\underline{V}}_k) + \check{\underline{\dot{q}}}_r'' \quad \text{(A.57)}$$

The first term on the right hand side is the heat conduction (Fourier law), and the second term is the enthalpy flux (of all species) flowing relative to the bulk motion of the mixture. The third term describes the thermal diffusion (Sorret effect) and the fourth term is the radiative heat flux.
For the derivation of a simplified conservation equation of the sensible enthalpy the following assumptions are made:

- the work of body forces are neglected: $\sum_{i=1}^{N}\check{\rho}_i\check{\underline{f}}_i = 0$.
- the viscous heating (produced by the diagonal terms of the stress tensor is neglected: $\underline{\underline{S}}$) $(\check{\mu}\check{\underline{\underline{S}}}) : \check{\nabla}\check{\underline{u}} = 0$.
- Soret effect is neglected.
- Sensible enthaply flux flowing relative to the bulk mixture- motion is neglected: $\check{\nabla}\cdot\left(\check{\rho}\sum_{i=1}^{N}Y_i\check{h}_i^s\check{\underline{V}}_i\right) = 0$.
- Radiant heat transfer is neglected: $\check{\dot{q}}_r = 0$.

The assumptions in combination with Eq. (A.56) and Eq. (A.57) leads to a simplified sensible enthalpy conservation equation

$$\begin{aligned}\check{\rho}\frac{D\check{h}^s}{D\check{t}} &= \frac{\partial(\check{\rho}\check{h}^s)}{\partial\check{t}} + \check{\nabla}\cdot\left(\check{\rho}\check{h}^s\check{\underline{u}}\right)\\ &= \check{\nabla}\cdot(\lambda\nabla T) + \frac{D\check{p}}{D\check{t}}\ .\end{aligned} \quad \text{(A.58)}$$

A.3.6 Enthalpy Conservation explicit in Temperature

The enthalpy conservation equation, explicit in temperature will be derived by the substitution of $\check{h}_s$ in Eq. (A.58) by the mass averaged sensible-enthalpy

$$\check{h}^s = \sum_{i=1}^{N} Y_i\check{h}_i^s\ . \quad \text{(A.59)}$$

Further an expression for the material derivativ is needed. Let's start with the definition of the sensible enthalpy

$$\check{h}_i^s = \int_{\check{T}_r}^{\check{T}} \check{c}_{pi} d\check{T} \Rightarrow \frac{d\check{h}_i^s}{d\check{T}} = \check{c}_{pi} \tag{A.60}$$

$$\check{c}_p^a = \sum_{i=1}^{N} Y_i \check{c}_{pi} \tag{A.61}$$

and it follows with Eq. (A.59) for the matieral derivative

$$\check{\rho} \frac{D\check{h}^s}{D\check{t}} = \sum_{i=1}^{N} \check{h}_i^s \check{\rho} \frac{DY_i}{D\check{t}} + \check{\rho}\check{c}_p^a \frac{D\check{T}}{D\check{t}} \ . \tag{A.62}$$

The conservation equation for the enthalpy, explicit in temperature can be written by

$$\begin{aligned} \check{\rho}\check{c}_p^a \frac{D\check{T}}{D\check{t}} &= \check{c}_p^a \Big[\frac{d(\check{\rho}\check{T})}{d\check{t}} + \check{\nabla} \cdot (\check{\rho}\check{T}\underline{\check{u}}) \Big] \\ &= \check{\nabla} \cdot \Big[\check{\lambda} (\check{\nabla}\check{T}) \Big] + \frac{D\check{p}}{D\check{t}} \ . \end{aligned} \tag{A.63}$$

A.3.7 Nondimensional Temperature Conservation

Equation (A.63) is nondimensionalized by using Eqs. (A.22), (A.23) and (A.32) and additional reference quantities denoted by the subscript ∞. Nondimensional quantities are defined by

$$\begin{aligned} T &= \frac{\check{T}}{\check{T}_\infty} \\ \overline{c}_p &= \frac{\check{c}_p^a}{\check{c}_{p\infty}} \\ h_i &= \frac{\check{h}_i}{\check{c}_{p\infty}\check{T}_\infty} \\ \lambda &= \frac{\check{\lambda}}{\check{\lambda}_\infty} \ . \end{aligned} \tag{A.64}$$

As well the the Prandtl number is defined as a nondimensional number by

$$Pr = \frac{\check{c}_{p\infty}\check{\mu}_\infty}{\check{\lambda}_\infty} \ . \tag{A.65}$$

The combination of the nondimensional quantities and numbers with Eq. (A.63) leads to the nondimensional enthalpy conservation equation, explicit in temperature

$$\begin{aligned} \rho c_p^a \frac{DT}{Dt} &= c_p^a \Big[\frac{\partial(\rho T)}{\partial t} + \nabla \cdot (\rho \underline{u} T) \Big] \\ &= \frac{1}{RePr} \nabla \cdot \Big[\lambda (\nabla T) \Big] - \\ &+ \frac{\check{p}_\infty}{\check{T}_\infty \check{\rho}_\infty \check{c}_{p\infty}} \frac{Dp}{Dt} \ . \end{aligned} \tag{A.66}$$

A.4 Equation of State

The equation of state (ideal gas law) for one species i of a gas mixture writes as

$$\check{p}_i \check{V} = \check{n}_i \Re \check{T} \ , \tag{A.67}$$

where $\check{n}_i$ is the mole number of species i and $\Re$ is the universal gas constant with a value of 8.3166 $\frac{J}{molK}$. The goal is to derive an equation of state for a gas mixture. The substitution of $\Re$ in (A.67) with

$$\check{R}_i = \frac{\Re}{\check{M}_i} \tag{A.68}$$

and the summation over all species leads to

$$\sum_{i=1}^{N} \check{p}_i \check{V} = \sum_{i=1}^{N} \check{n}_i \check{R}_i \check{M}_i \check{T} \ , \tag{A.69}$$

which can be written with $\check{m}_i = \check{n}_i \check{M}_i$, Dalton's law $\check{p} = \sum_{i=1}^{N} \check{p}_i$ and the relation

$$\check{R} = \frac{\sum_{i=1}^{N} \check{R}_i \check{m}_i}{\sum_{i=1}^{N} \check{m}_i} = \frac{\sum_{i=1}^{N} \check{R}_i \check{m}_i}{\check{m}} \tag{A.70}$$

to the form

$$\check{p} \check{V} = \sum_{i=1}^{N} m_i R_i T = \check{m} \check{R} \check{T}. \tag{A.71}$$

Equation (A.71) can be rearranged with $\check{\rho} = \check{m}/\check{V}$ to the ideal gas law for a mixture of gas

$$\check{p} = \check{\rho} \check{R} \check{T} \ . \tag{A.72}$$

A.4.1 Nondimensional Equation of State

The equation of state for the gas mixture Eq. (A.72) is nondimensionalized by using Eqs. (A.22), (A.32), (A.64) and the reference molmass denoted by the subscript ∞

$$M = \frac{\check{M}}{\check{M}_\infty} . \tag{A.73}$$

The combination of the nondimensional quantities, the relation

$$\check{R} = \frac{\sum_{i=1}^{N} \check{R}_i \check{m}_i}{\check{m}} = \frac{\Re}{\check{m}} \sum_{i=1}^{N} \frac{\check{m}_i}{\check{M}_i} = \Re \frac{\check{n}}{\check{m}} = \frac{\Re}{\check{M}} \tag{A.74}$$

and Eq. (A.72) leads to the normalized equation of state of a gas mixture

$$\check{p}_\infty p = \rho \check{\rho}_\infty \frac{\Re}{\check{M}} T \check{T}_\infty = \rho \check{\rho}_\infty \frac{\Re}{M \check{M}_\infty} T \check{T}_\infty , \tag{A.75}$$

which can be rewritten with the relation

$$\check{R} = \frac{\sum_{i}^{N} \check{R}_i \check{m}_i}{\check{m}} = \frac{\Re}{\check{m}} \sum_{i=1}^{N} \frac{\check{m}_i}{\check{M}_i} = \Re \frac{\check{n}}{\check{m}} = \frac{\Re}{\check{M}} \tag{A.76}$$

to the form

$$p = \frac{\rho T}{M} \frac{\check{\rho}_\infty \check{R} \check{T}_\infty}{\check{p}_\infty} \tag{A.77}$$

and with $\check{\rho}_\infty \check{R} \check{T}_\infty / \check{p}_\infty = 1$ to

$$p = \frac{\rho T}{M} \tag{A.78}$$

which is the nondimensionalized form of the equation of state for ideal gas.

Appendix B

Low-Mach Number Formulation

In this Chapter the low-Mach number formulation of the equations are derived. The derivation of low-Mach number equations are based on perturbation methods according to Rehm and Baum [107]. The variables are expanded in power of series of $\hat{Ma}$ as for example the pressure

$$p(\underline{x}, t, \hat{Ma}) = p_0(\underline{x}, t) + \hat{Ma}\ p_1(\underline{x}, t) + \hat{Ma}^2 p_2(\underline{x}, t) + O(\hat{Ma}^3)\ , \quad \text{(B.1)}$$

where p_0, p_1 and p_2 are called the leading, first- and second-order pressure, respectively.

B.1 Continuity Equation

Starting from Eq. (B.1) and performing a single asymptotic analysis of the terms ρ and $\rho\underline{u}$ of Eq. (A.26) leads to

$$\begin{aligned}
\rho &= \rho_0 + \hat{Ma}\ \rho_1 + \hat{Ma}^2 \rho_2 + O(\hat{Ma}^3) && \text{(B.2)}\\
\rho\underline{u} &= (\hat{\rho}\underline{u})_0 + \hat{Ma}\ (\rho\underline{u})_1 + \hat{Ma}^2 (\rho\underline{u})_2 + O(\hat{Ma}^3) \\
&= \left[\rho_0 + \hat{Ma}\ \rho_1 + \hat{Ma}^2 \rho_2 + O(\hat{Ma}^3)\right] \cdot \\
&\cdot \quad \left[\underline{u}_0 + \hat{Ma}\ \underline{u}_1 + \hat{Ma}^2 \underline{u}_2 + O(\hat{Ma}^3)\right] \\
&= \rho_0\underline{u}_0 + \hat{Ma}\ (\rho_0\underline{u}_1 + \rho_1\underline{u}_0) + \\
&+ \quad \hat{Ma}^2 (\rho_0\underline{u}_2 + \rho_1\underline{u}_1 + \rho_2\underline{u}_0) + O(\hat{Ma}^3) && \text{(B.3)}
\end{aligned}$$

replace the terms of Eq. (A.26) with Eq. (B.2) and Eq. (B.3) and let $\hat{Ma} \to 0$ then the normalized continuity equation for low-Mach numbers writes

$$\frac{d\rho_0}{dt} + \nabla \cdot (\rho_0 \underline{u}_0) = 0 \tag{B.4}$$

B.2 Momentum Equation

Starting from Eq. (A.36), using Eq. (B.1) and perform a single asymptotic analysis of the terms ρ (Eq. B.2), $\rho\underline{u}$ (Eq. B.3), $\rho\underline{u}\ \underline{u}$, p (Eq. B.1) and $\mu\underline{\underline{S}}$

$$\begin{aligned}
\rho\underline{u}\ \underline{u} &= (\rho\underline{u}\ \underline{u})_0 + \hat{Ma}(\rho\underline{u}\ \underline{u})_1 + \hat{Ma}^2(\rho\underline{u}\ \underline{u})_2 + O(\hat{Ma}^3) \\
&= \rho_0\underline{u}_0\underline{u}_0 + \hat{Ma}\Big[2\rho_0\underline{u}_0\underline{u}_1 + \rho_1\underline{u}_0\underline{u}_0\Big] + \\
&+ \hat{Ma}^2\Big[2\rho_0\underline{u}_0\underline{u}_2 + \rho_0\underline{u}_1\underline{u}_1 + 2\rho_1\underline{u}_0\underline{u}_1 + \rho_2\underline{u}_0\underline{u}_2\Big] + \\
&+ O(\hat{Ma}^3) \qquad\qquad (B.5) \\
\mu\underline{\underline{S}} &= \mu\left[\nabla\underline{u} + (\nabla\underline{u})^T - \frac{2}{3}(\nabla\cdot\underline{u})\underline{\underline{I}}\right] \\
&= \left[\mu_0 + \hat{Ma}\mu_1 + \hat{Ma}^2\mu_2 + O(\hat{Ma}^3)\right] \cdot \\
&\quad \cdot\left[\underline{\underline{S}}_0 + \hat{Ma}\underline{\underline{S}}_1 + \hat{Ma}^2\underline{\underline{S}}_2 + O(\hat{Ma}^3)\right] \\
&= \mu_0\underline{\underline{S}}_0 + \hat{Ma}\Big(\mu_0\underline{\underline{S}}_1 + \mu_1\underline{\underline{S}}_0\Big) + \\
&+ \hat{Ma}^2\Big(\mu_0\underline{\underline{S}}_2 + \mu_1\underline{\underline{S}}_1 + \mu_2\underline{\underline{S}}_0\Big) + O\Big(\hat{Ma}^3\Big) \qquad\qquad (B.6)
\end{aligned}$$

with

$$\underline{\underline{S}}_m = \nabla\underline{u}_m + (\nabla\underline{u}_m)^T - \frac{2}{3}(\nabla\cdot\underline{u}_m)\underline{\underline{I}}\ , \qquad m = 0, 1, 2 \tag{B.7}$$

and replace the terms of Eq. (A.36) with Eqs. (B.1), (B.3),(B.5) and (B.6)

$$\frac{\partial}{\partial t}\left[\rho_0\underline{u}_0 + \hat{Ma}(\rho_0\underline{u}_1 + \rho_1\underline{u}_0) + \hat{Ma}^2(\rho_0\underline{u}_2 + \rho_1\underline{u}_1 + \rho_2\underline{u}_0) + O(\hat{Ma}^3)\right]$$

$$+ \quad \nabla\cdot\left[\rho_0\underline{u}_0\underline{u}_0 + \hat{Ma}\Big[2\rho_0\underline{u}_0\underline{u}_1 + \rho_1\underline{u}_0\underline{u}_0\Big] + \right.$$

$$
\begin{aligned}
&+ \quad \hat{Ma}^2\Big[2\rho_0\underline{u}_0\underline{u}_2 + \rho_0\underline{u}_1\underline{u}_1 + 2\rho_1\underline{u}_0\underline{u}_1 + \rho_2\underline{u}_0\underline{u}_2\Big] + O(\hat{Ma}^3)\Big] \\
&+ \quad \frac{1}{\hat{Ma}^2}\nabla p_0 + \frac{1}{\hat{Ma}}\nabla p_1 + \nabla p_2 + O(\hat{Ma}^3) \\
&= \quad \frac{1}{Re}\nabla\cdot\Bigg[\mu_0\underline{\underline{S}}_0 + \hat{Ma}\Big(\mu_0\underline{\underline{S}}_1 + \mu_1\underline{\underline{S}}_0\Big) + \\
&+ \quad \hat{Ma}^2\Big(\mu_0\underline{\underline{S}}_2 + \mu_1\underline{\underline{S}}_1 + \mu_2\underline{\underline{S}}_0\Big) + O(\hat{Ma}^3)\Bigg] \,. \qquad \text{(B.8)}
\end{aligned}
$$

Let $\hat{Ma} \to 0$, define

$$
\begin{aligned}
\nabla p_0 &:= 0 \qquad \text{(B.9)} \\
\nabla p_1 &:= 0 \qquad \text{(B.10)}
\end{aligned}
$$

and apply them to Eq. (B.8), which leads to the momentum conservation for low-Mach numbers

$$
\begin{aligned}
\rho_0\frac{D\underline{u}_0}{Dt} &= \frac{\partial(\rho_0\underline{u}_0)}{\partial t} + \nabla\cdot(\rho_0\underline{u}_0\underline{u}_0) \\
&= -\nabla p_2 + \frac{1}{Re}\nabla\cdot(\mu_0\underline{\underline{S}}_0) + \frac{1}{Fr^2}\rho\underline{e}_g \,, \qquad \text{(B.11)}
\end{aligned}
$$

where $p_2(\underline{x}, t)$ is called the hydrodynamic pressure and is not to mix up with the thermodynamic pressure $p_0(t)$, which is only a function of time. Note, the assumptions Eq. (B.9) and Eq. (B.10) means, that the thermodynamic pressure p_0 is no longer a function of space and therefore no acoustic waves can be present in the computational domain.

B.3 Species Equation for Non-Reactive Flows

Starting from Eq. (A.27), performing the same procedure, described above leads to the low-Mach number species equation

$$
\begin{aligned}
\rho_0\frac{DY_{i0}}{Dt} &= \frac{\partial(\rho_0 Y_{i0})}{\partial t} + \nabla\cdot(\rho_0 Y_{i0}\underline{u}_0) \\
&= \frac{1}{ReSc_i}\nabla\cdot\Big[\rho_0 D_{i,N_20}(\nabla Y_{i0}) + \rho_0\underline{u}_{c0}\Big] \qquad \text{(B.12)}
\end{aligned}
$$

B.4 Energy Equation for Non-Reactive Flows

Starting from the temperature equation Eq. (A.66), use the same procedure described above and use Eq. (B.9), which leads to the low-Mach number temperature equation

$$\begin{aligned} \rho c_{p0}^{a} \frac{DT}{Dt} &= c_{p0}^{a}\Big[\frac{\partial(\rho_0 T_0)}{\partial t} + \nabla\cdot(\rho_0 \underline{u}_0 T_0)\Big] \\ &= \frac{1}{RePr}\nabla\cdot\Big[\lambda_0(\nabla T_0)\Big] - \\ &+ \frac{p_\infty}{T_\infty \rho_\infty c_{p\infty}}\frac{dp_0}{dt} \end{aligned} \tag{B.13}$$

Curriculum Vitae

1972	born on 4 January in Rüti ZH, Switzerland
1979—1985	Elementary school in Jonschwil
1985—1988	Secondary school in Oberuzwil
1988—1992	Apprenticeship as truck mechanic, AMP Bronschhofen
1989—1992	Berufsmittelschule in St. Gallen
1993—1996	Study of automotive engineering at Engineering School Biel
1996	Diploma in automotive engineering (FH) at Engineering School Biel
1996—2001	Study of mechanical engineering at ETH Zürich
2001	Diploma in mechanical engineering at ETH Zürich
2001—2006	Doctoral student and teaching assistant at the Institute of Energy Technology/LAV at ETH Zürich
25.10.2007	Phd defense

Bibliography

[1] N. Adams. Modeling strategies for Large Eddy Simulation of turbulent flows. *Ercoftac Summer School Thessaloniki (Greece)*, 2004.

[2] N. A. Adams and S. Stolz. Deconvolution methods for subgrid-scale approximation in LES. In B. J. Geurts, editor, *Modern simulation strategies for turbulent flow*. Edwards, R. T. Inc., Philadelphia, 2001.

[3] M. Amielh, T. Djeridane, F. Anselmet, and L. Fulachier. Velocity near field of variable density turbulent jets. *Int. J. Heat Mass Transfer*, 39(No. 10):2149–2164, 1996.

[4] F. Anselmet, H. Djeridi, and L. Fulachier. Join statistics of a passive scalar and its dissipation in turbulent flows. *J. Fluid Mech.*, 280(173-197), 1994.

[5] R. Antonia and R. Bilger. An experimental investigation of an axisymmetric jet in a co-flowing air stream. *J. Fluid Mech.*, 61(4):805–822, 1973.

[6] R. Antonia and R. Bilger. Heated round jet in a co-flowing stream. *AIAA J.*, 14(11):1541–1547, 1976.

[7] R. Antonia, A.J Chambers, and L.W.B. Brown. Relation between structure functions of velocity and temperature in a turbulent jet. *Exp. Fluids*, 1(4):213–219, 1983.

[8] R. Antonia, A. Prabhu, and S. E. Stephenson. Conditionally sampled measurements in a heated turbulent jet. *J. Fluid Mech.*, 72:455–480, 1975.

[9] K. Askelvoll and P. Moin. Large Eddy Simulation of turbulent confined coannular jets. *J. Fluid Mech.*, 315:387–411, 1996.

[10] P.C. Babu and Krishnan M. Upstream entrainment in numerical simualtions of spatially evolving round jets. *Phys. Fluid*, 16(10):3699–3705, 2004.

[11] M. Barchilon and R. Curtet. Some details of the structure of an axisymmetric confined jet with back-flow. *J. Basic Eng.*, 86(4):777–787, 1964.

[12] J. Bardina, J. H. Ferziger, and W. C. Reynolds. Improved subgrid models for Large Eddy Simulation. *AIAA J.*, 80-1357, 1980.

[13] B. J. Boersma, G. Brethouwer, and F. T. M. Nieuwstadt. A numerical investigation on the effect of the inflow conditions on the self-similar region of a round jet. *Phys. Fluids*, 10(4):899–909, 1998.

[14] B.J. Boersma and S.K. Lele. Large Eddy Simulation of compressible turbulent jets. *CTR, Annual research briefs*, 1999:365–377, 1999.

[15] C. Bogey, C. Bailly, and D. Juve. Computation of the sound radiated by a 3-D jet using Large Eddy Simulation. *AIAA J.*, 2000-2009, 2000.

[16] C. Bogey, C. Bailly, and D. Juve. Noise investigation of a high subsonic, moderate reynolds number jet using a compressible Large Eddy Simulation. *Theoret. Comput. Fluid Dynamics*, 16:273–297, 2003.

[17] R. Bouffanais, M.O. Deville, P. Fischer, E. Leriche, and D. Weill. Large Eddy Simulation of the lid-driven cubic cavity flow by the spectral element method. *J. Sci. Comp.*, 2005.

[18] J. B. Boyd. Note: Two comments on filtering (artificial viscosity) for Chebyshev and Legendre spectral and spectral element methods: Preserving boundary conditions and interpretation of the filter as a diffusion. *J. Comput. Phys.*, 143:283–288, 1998.

[19] M. Breuer. *Direkte Numerische Simulation und Large Eddy Simulation turbulenter Strömungen auf Hochleistungsrechnern*. Shaker Verlag, Aachen 2002, 2001.

[20] I. S. Bronstein, K. A. Semendjajew, G. Musiol, and H. Mühlig. Taschenbuch der Mathematik. *Verlag Harry Deutsch Thun und Frankfurt am Main*, 1997.

[21] C. Canuto, M. Y. Hussaini, A. Quateroni, and T. A. Zang. Spectral methods in fluid dynamics. *Springer-Verlag*, 1988.

[22] J.C. Chen and W. Rodi. *Vertical turbulent buoyant jets.* Pergamon Press, Oxford, New York, Toronto, Sydney, Paris, Frankfurt, volume 4 edition, 1980.

[23] R. Chevray and N. K. Tutu. Intermittency and preferential transport of heat in a round jet. *J. Fluid Mech.*, 88(1):133–160, 1978.

[24] D. Choi, Barber T. J., and L. M Chiappetta. Large Eddy Simulation of high-Reynolds number jet flow. *AIAA J.*, 99-16146, 1999.

[25] J. P. Chollet. Spectral closures to derive a subgrid scale modeling forLarge Eddy Simulation. *Lecture Notes in Physics*, 230:161–176, 1985.

[26] J. P. Chollet, P.R. Voke, and L. Kleiser, editors. *Direct and Large Eddy Simulation II, Proc. of the ERCOFTAC Workshop on Direct and Large-Eddy Simulation, Grenoble, France, 16-19 September 1996, ERCOFTAC Series, vol. 5, Direct and Large-Eddy Simulation II.* Kluwer Academic Publishers, Dordrecht, 1997.

[27] L.P Chua. *Measurements in a turbulent circular jet.* PhD thesis, University Newcastle, 1989.

[28] R. A. Clark, J. H. Ferziger, and W. C. Reynolds. Evaluation of subgrid-scale models using an accurately simulated turbulent flow. *J. Fluid Mech.*, 91:1–16, 1979.

[29] G. S. Contantinescu and S. K. Lele. Large Eddy Simulation of a near sonic turbulent jet and its radiated noise. *AIAA J.*, 2001-0376, 2001.

[30] A. W. Cook and J. J. Riley. A subgrid model for equilibrium chemistry in turbulent flows. *Phys. Fluid*, 6:2868–2870, 1994.

[31] A. Craya and R. Curtet. On the spreading of a confined jet. *C. R. Acad. Sci. Paris*, 241(1):621–622, 1955.

[32] R. Curtet. Confined jets and recirculation phenomena with cold air. *C. R. Acad. Sci. Paris*, 2:383–411, 1958.

[33] Y. Dai, T. Kobayashi, and N. Taniguchi. Large Eddy Simulation of plane turbulent jet flow using a new outflow velocity boundary condition. *JSME Int. J. Fluids,Thermal Eng.*, 37:242–253, 1994.

[34] J. Deardorff. A numerical study of three-dimensional turbulent channel flow at large Reynolds numbers. *J. Fluid Mech.*, 41 (2):453–480, 1970.

[35] J. R. DeBonis and J. N. Scott. A Large Eddy Simulation of a turbulent compressible round jet. *AIAA J.*, 2001-2254, 2001.

[36] M.O. Deville, P. F. Fischer, and E. H. Mund. High-order methods for incompressible fluid flow. *Cambridge University Press*, 2002.

[37] T. Djeridane, T. Amielh, F. Anselmet, and L. Fulachier. Velocity turbulence properties in the near-field region of axisymmetric variable density jets. *Phys. Fluid*, 8 (6):1614–1630, 1996.

[38] J. A. Domaradzki and E. M. Saiki. A subgrid-scale model based on the estimation of unresolved scales of turbulence. *Phys. Fluid*, 9:2148–2164, 1997.

[39] J. A. Domaradzki and P. P. Yee. The subgrid-scale estimation model for high Reynolds number turbulence. *Phys. Fluid*, 12(1):193–196, 2000.

[40] J.A. Domaradzki and N.A. Adams. Direct modelling of subgrid scales of turbulence in Large Eddy Simulation. *J. Turb.*, 3:1–19, 2002.

[41] D. R. Dowling and P. E. Dimotakis. Similarity of the concentration field of gas-phase turbulent jets. *J. Fluid Mech.*, 218:109–141, 1990.

[42] F. Ducros, P. Comte, and M. Lesieur. Large Eddy Simulation of transition to turbulence in a boundary layer developing spatially over a flat plate. *J. Fluid Mech.*, 326:1–36, 1996.

[43] C. Ferreira Gago, F. Garnier, and Utheza F. Direct testing of subgrid scale models in Large Eddy Simulation of a non-isothermal turbulent jet. *Int. J. Numer. Meth. Fluids*, 42:999–1026, 2003.

[44] P. Fischer. An overlapping Schwarz method for spectral element solution of the incompressible Navier-Stokes equations. *J. Comp. Phys.*, 133:84–101, 1997.

[45] P. Fischer, L. Ho, and G. E. Karniadakis. Recent advances in parallel spectral element simulation of unsteady, incompressible flows. *Comp. and Struct.*, 30(1-2):217–231, 1988.

[46] P. Fischer and J. Mullen. Filter-based stabilization of spectral element methods. *C. R. Acad. Sci. Paris*, 332, Serie 1:265–270, 2001.

[47] J. Freund, S.K. Lele, and P. Moin. Compressibility effects in a turbulent annular mixing layer. Part 1. Turbulence and growth rate. *J. Fluid Mech.*, 421:229–267, 2000.

[48] J. Freund, S.K. Lele, and P. Moin. Compressibility effects in a turbulent annular mixing layer. Part 2. Mixing of a passive scalar. *J. Fluid Mech.*, 421:269–292, 2000.

[49] B Galperin and S. A. Orszag. *Large Eddy Simulation of Complex Engineering and Geophysical Flows.* Cambridgh University Press, 1993.

[50] L. Gamet and J. L Estivalezes. Application of Large Eddy Simulation and kirchhoff method to jet noise prediction. *AIAA J.*, 36(12):2170–2178, 1998.

[51] W. K George. Self-preservation of turbulent flows and its relation ot initial conditions and coherent structures. In W.K. George and R. Arndt, editors, *Advances in Turbulence.* Hemisphere - Springer, 1987.

[52] M. Germano, U. Piomelli, P. Moin, and W. H. Cabot. A dynamic subgrid-scale eddy viscosity model. *Phys. Fluid*, A3(7):1760–1765, 1991.

[53] B. Geurts. Inverse modeling for Large Eddy Simulation. *Phys. Fluid*, 9 (12):3585–3587, 1997.

[54] B. Geurts. *Elements of Direct and Large Eddy Simulation.* R. T. Edwarts Inc., Philadelphia, 1st edition, 2004.

[55] A. Gharbi, E. Ruffin, F. A. Anselmet, and R. Schiestel. Numerical modelling of variable density turbulent jets. *Int. J. Heat Mass Transfer*, 39(9):1865–1882, 1996.

[56] S. Ghosal, P. Moin, and K. Akselvoll. A dynamic localization model for Large Eddy Simulation of turbulent flows. *J. Fluid Mech.*, 286:229, 1995.

[57] N. Gilbert. *Numerische Simulation der Transition von der laminaren in die turbulente Kanalströmung.* PhD thesis, University of Karlsruhe, 1988.

[58] N. Gilbert and L. Kleiser. Turbulence model testing with the aid of direct numerical simulation results. In In R. Friedrich and editors U. Schumann, editors, *Eighth Symposium on Turbulent Shear Flows*, pages 26–1, Munich, 1991.

[59] D.J. Glaze and S.H. Frankel. Stochastic inlet conditions for Large Eddy Simulation of a fully turbulent jet. *AIAA J.*, 41(6):1064–1073, 2003.

[60] F.C. Gouldin, R.W. Schefer, S.C. Johnson, and W. Kollman. Non reacting turbulent mixing flows. *Prog. Energy Comb. Sci.*, 12:257–303, 1986.

[61] D. C. Haworth and K. Jansen. Large Eddy Simulation on unstructured deforming meshes: toward reciprocating ic engines. *Computers & Fluids*, 29:493–524, 2000.

[62] K. Horiuti. Assessment of two-equation models of turbulent passive scalar diffusionin channel flow. *J. Fluid Mech.*, 238:405–433, 1992.

[63] K. Horiuti. A proper velocity scale for modeling subgrid-scale eddy viscosities in Large Eddy Simulation. *Phys. Fluid*, A5(1):146–157, 1993.

[64] H. H. Hussein, S. P. Capp, and W. K. George. Velocity measurements in a high-Reynolds number, momentum conserving, axisymmetric, turbulent jet. *J. Fluid Mech.*, 258:31–75, 1994.

[65] T. Illiescu and P. Fischer. Large Eddy Simulation of turbulent channel flows by the rational large eddy simulation model. *Phys. Fluid*, 15(10):3036–3047, 2003.

[66] G. E. Karniadakis, M. Israeli, and S. A. Orszag. High-order splitting methods for the incompressible Navier-Stokes equations. *J. Comp. Phys.*, 97:414, 1991.

[67] A. Kempf, M. Klein, and J. Janicka. Efficient generation of initial- and inflow-conditions for transient turbulent flows in arbitrary geometries. 2003.

[68] M. Klein, A. Sadiki, and J. Janicka. A digital filter based generation of inflow data for spatially developing direct numerical or Large Eddy Simulation. *J. Comput. Phys.*, 186:652–665, 2003.

[69] L. Kleiser and U. Schumann. Three-dimensional numerical simulation of laminar-turbulent transition and its control by periodic disturbances. In *In Proceedings of 3rd GAMM Conference on Numerical Methods in Fluid Mechanics*, 1980.

[70] A. N. Kolmogorov. The local structure of turbulence in incompressible viscous fluids for very large Reynolds numbers. *Comptes Renus (Doklady) de l'Acedemie des Sciences de l'URSS*, (4), 1941.

[71] R. H. Kraichnan. The structure of isotropic turbulence at very high Reynolds numbers. *J. Fluid Mech.*, 5:497–543, 1959.

[72] Venkataramani KS., NK. Tutu, and R. Chevray. Probability distributions in a round heated jet. *Phys. Fluid*, 18(11):1413–1420, 1975.

[73] L. D. Landau and E. M. Lifschitz. Lehrbuch der theoretischen Physik. *Akademie Verlag*, Teil 6: Hydrodynamik, 1991.

[74] J. Laufer. The structure of turbulence in fully developed pipe flow. *NACA report*, 1174, 1953.

[75] B. Launder and N. Sandham. *Closure Strategies for Turbulent and Transitional Flows*. Cambridge University Press, 2002.

[76] C. Le Ribault, S. Sarkar, and S. A. Stanley. Large Eddy Simulation of a plane jet. *Phys. Fluids*, 11(10):3069–3083, 1999.

[77] C. Le Ribault, S. Sarkar, and S. A. Stanley. Large Eddy Simulation of evolution of a passive scalar in plane jet. *AIAA J.*, 39(8):1509–1516, 2001.

[78] M. Lesieur and O. Metais. New trends in Large Eddy Simulation of turbulence. *Ann. Rev. Fluid Mech.*, 28, 1996.

[79] D. K. Lilly. A proposed modification of the germano subgrid-scale closure method. *Phys. Fluid*, A4(3):633–635, 1992.

[80] S. Liu, C. Meneveau, and J. Katz. On the properties of similarity subgrid-scale models as deduced from measurements in a turbulent jet. *J. Fluid Mech.*, 275:83, 1994.

[81] C. L. Lubbers, G. Brethouwer, and B. J. Boersma. Simulation of the mixing of a passive scalar in a round turbulent jet. *Fluid Dyn. Res.*, 28:189–208, 2001.

[82] A. S. Lyrintzis and R. R. Mankbadi. Prediction of the far-field jet noise using Kirchhoffs's formulation. *AIAA J.*, 1(2):1–4, 1996.

[83] R. R. Mankabadi, M. E. Hayder, and L. A. Povinelli. Structure of supersonic jet flow and its radiated sound. *AIAA J.*, 32(5):897–906, 1994.

[84] C. Meneveau. Statistics of turbulence subgrid.scale stresses: necessary conditions and experimental tests. *Phys. Fluid*, 6:815, 1994.

[85] C. Meneveau, T. S. Lund, and W. H. Cabot. A lagrangian dynamic subgrid-scale model of turbulence. *J. Fluid Mech.*, 319:353–385, 1996.

[86] O. Metais and M. Lesieur. Spectral Large Eddy Simulation of isotropic and stably stratified turbulence. *J. Fluid Mech.*, 239:157–194, 1992.

[87] J. Mi, D. S. Nobes, and G. J. Nathan. Influence of the jet exit conditions on the passive scalar field of an axisymmetric free jet. *J. Fluid Mech.*, 432:91–125, 2001.

[88] P. Moin and J. Kim. Numerical investigation of turbulent channel flow. *J. Fluid Mech.*, 118:341–377, 1982.

[89] P. Moin, W. C. Reynolds, and J. H. Ferziger. Large Eddy Simulation of incompressible turbulent channel flow. *Technical Report TF-12, Dpt. of Mechanical Engineering, Standford University, Standford, California, 1978*, 1978.

[90] P. Moin, K. Squires, W. Cabot, and S. Lee. A dynamic subgrid-scale model for compressible turbulence and scalar transport. *Phys. Fluid*, 3(11):2746–2757, 1991.

[91] R. D. Moser, J. Kim, and N. N. Mansour. Direct numerical simulation of turbulent channel flow up to $Re_\tau = 590$. *Phys. Fluids*, 11(4):943–945, 1999.

[92] T. Nickels and A. Perry. An experimental and theoretical study of the turbulent coflowing jet. *J. Fluid Mech.*, 309:157–182, 1996.

[93] M. Olsson and L Fuchs. Large Eddy Simulation of the proximal region of a spatially developing circular jet. *Phys. Fluid*, 8(8):2125–2137, 1996.

[94] S. A. Orszag, M. Israeli, and M.O. Deville. Boundary conditions for incompressible flows. *J. Sci. Comp.*, 1:75, 1986.

[95] N. R. Panchapakesan and J. L. Lumley. Turbulence measurements in axisymmetric jets of air and helium. Part 1. Air jet. *J. Fluid Mech.*, 246:197–223, 1993.

[96] C. Pantano. Direct simulation of non-premixed flame extinction in a methane-air jet with reduced chemistry. *J. Fluid Mech.*, 514:231–270, 2004. Article.

[97] R.A. Petersen. The influence of wave dispersion on vortex rings. *J. Fluid Mech.*, 89:469–496, 1978.

[98] C. D. Pierce and P. Moin. A dynamic model for subgrid-scale variance and dissipation rate of a conserved scalar. *Phys. Fluid*, 10(12):3041–3044, 1998.

[99] L. Pietri, M. Amielh, and F. Anselmet. Simultaneous measurements of temperature and velocity fluctuations in a slightly heated jet combining a cold wire and laser doppler anemometry. *Int. J. Heat Fluid Flow*, 21:22–36, 2000.

[100] U. Piomelli and J. Liu. Large Eddy Simulation of rotating channel flows using a localized dynamic model. *Phys. Fluid*, 7(4):839–848, 1995.

[101] H. Pitsch and H. Steiner. Large Eddy Simulation of a turbulent piloted methane/air diffusion flame (Sandia flame d). *Ann. Res. Briefs*, pages 3–18, 1999.

[102] W. M. Pitts. Effects of global density ratio on the centerline mixing behaviour of axisymmetrical turbulent jets. *Exp. Fluids*, 11(2-3):125–134, 1991.

[103] S. B. Pope. Turbulent flows. *Cambridge University Press*, 1st edition, 2000.

[104] M. J. B. M Pourquie. *Large Eddy Simulation of a turbulent jet*. PhD thesis, Delft University Press, 1994.

[105] D. I. Pullin. A vortex-based model for the subgrid flux of a passive scalar. *Phys. Fluid*, 12(9):2311–2319, 2000.

[106] R. M Rais. *Investigations of Diffusion Flame Instability.* PhD thesis, EPFL Lausanne, 2003.

[107] G. R. Rehm and H. R. Baum. The equation of motion for thermally driven flows. *J. Res. National Bureau of Standards*, 83(3):297–308, 1978.

[108] B. Rembold. *Direct and Large Eddy Simulation of Compressible Rectangular Jet Flow, Diss. ETH No. 15081.* PhD thesis, Swiss Federal Institute of Technology (ETH), 2003.

[109] A. Revuelta, C. Martinez-Bazan, L. Sanchez, and A. Linan. Laminar Craya-Curtet jets. *Phys. Fluid*, 15(1):208–211, 2004.

[110] W. Rodi. A new method of analyzing hot-wire signals in highly turbulent flow and its evaluation in a round jet. *DISA Information*, 17, 1975.

[111] R.S. Rogallo and P. Moin. Numerical simulation of turbulent flows. *Ann. Rev. Fluid Mech.*, 16:99–137, 1984.

[112] P. Sagaut. *Large Eddy Simulation of Incompressible Flows.* Scientific Computation Series. Springer-Verlag, 2001.

[113] N. Sandham, N. Adams, and L. Kleiser. The late stages of transition to turbulence in channel flow. *J. Fluid Mech.*, 245:319–348, 1992.

[114] J. C. Sautet and D Stepowski. Single-shot laser mie scattering measurements of the scalar profiles in the near-field of turbulent jets with variable densities. *Exp. Fluids*, 16(6):353–367, 1994.

[115] H. R. Schwarz. *Numerische Mathematik.* B. G. Teubner, Stuttgart, 3th edition, 1993.

[116] K. B. Shah and J. H. Ferziger. A new non-eddy viscosity subgrid-scale model and its application to channel flow. *Annual Research Briefs 1995, Center of Turbulence Research, Stanford University*, pages 73–90, 1995.

[117] J. Smagorinsky. General circulation experiments with the primitive equations: I. The basic equations. *Mon. Weather Rev*, 91:99–164, 1963.

[118] R. M. C. So, J. Y Zhu, and M. V. Otugen. Behaviour of probability-density functions in a binary-gas jet. *Exp. Fluids*, 11(4):227–242, 1991.

[119] S. A. Stanley and S. Sarkar. Influence of nozzle conditions and discrete forcing on turbulent planar jets. *AIAA J.*, 38(9):1615–1623, 2000.

[120] S. Stolz and N. A. Adams. An approximate deconvolution procedure for Large Eddy Simulation. *Phys. Fluids*, 11(7)(No. 7):1699–1701, 1999.

[121] S. Stolz, N. A. Adams, and L. Kleiser. The Approximate Deconvolution Model for Large Eddy Simulations of compressible flows and its application to shock-turbulent-boundary-layer interaction. *Phys. Fluids*, 13(10):2985–3001, 2001.

[122] S. Stolz, N. A. Adams, and L. Kleiser. An Approximate Deconvolution Model for Large Eddy Simulations with application to incompressible wall-bounded flows. *Phys. Fluids*, 13(4):997–1015, 2001.

[123] H. Suto, K. Matsubara, M. Kobayashi, and Y. Kaneko. Large Eddy Simulation of flow and scalar transport in a round jet. *Heat Transfer-Asian Research*, 33(3):175–188, 2004.

[124] H. Tennekes and J. L. Lumley. *A First Course in Turbulence.* MIT press, Cambridge, MA., 1972.

[125] H. H. Thomann. *Strömungslehre 1.* AMIV-Verlag, Zürich, 1996.

[126] M. W. Thring and M. P. Newby. Combustion length of enclosed turbulent jet flames. *Proc. Combust. Inst.*, 4:789, 1953.

[127] A. G. Tomboulides, M. Israeli, and K. Karniadakis. Efficient removal of boundary-divergence errors in time-splitting methods. *J. Sci. Comp.*, 4:291, 1989.

[128] A. G. Tomboulides, J. C. Y. Lee, and S. A. Orszag. Numerical simulation of low Mach number reactive flows. *J. Sci. Comp.*, 12(2):139–167, 1997.

[129] A. Uzun, G. A. Blaisdell, and A. S. Lyrintzis. 3-D Large Eddy Simulation for jet aeroacoustics. *AIAA J.*, 2003-3322, 2003.

[130] A. Uzun, G. A. Blaisdell, and A. S. Lyrintzis. Application of compact schemes to Large Eddy Simulation of turbulent jets. *J. Sci. Comp.*, 21(3):283–319, 2004.

[131] E. R. Van Driest. On turbulent flow near a wall. *J. Aero. Sci.*, 23:1007–1011, 1956.

[132] M. Van Dyke. *An Album of Fluid Motion.* The Parabolic Press, Stanford, California, 1982.

[133] A. Viilu. An experimental determination of the minimum Reynolds number for instability in a free jet. *J. Appl. Mech.*, 29:506, 1962.

[134] P. R. Voke, L. Kleiser, and J. P. Chollet, editors. *Direct and Large Eddy Simulation I, Fluid Mech. and its Appl., vol. 26, Sel. papers of the First ERCOFTAC Workshop on Direct and LES, Guildford, Surrey, U.K., 27-30 March 1994.* Kluwer Academic Publishers, Dordecht, 1994.

[135] P. R. Voke, N. S. Sandham, and L. Kleiser, editors. *Direct and Large Eddy Simulation III, Proc. of the Isaac Newton Institute Symposium/ERCOFTAC Workshop on Direct and Large Eddy Simulation, Cambridge, U.K., 12-14 May 1999, ERCOFTAC Series, vol. 7, Direct and Large Eddy Simulation III.* Kluwer Academic Publishers, Dordrecht, 1999.

[136] A. W. Vreman, B. J Geurts, and J. G. M Kuerten. A priori tests of Large Eddy Simulation of the compressible mixing layer. *J. Eng. Math.*, 29:299, 1995.

[137] B. Vreman. Direct and Large Eddy Simulation of the compressible turbulent mixing layer. *Dissertation University of Twente*, ISBN 90-9008884-9, 1995.

[138] B. Vreman, B. Geurts, and H. Kuerten. On the formulation of the dynamic mixed subgrid-scale model. *Phys. Fluid*, 6(12):4057–4059, 1994.

[139] B. Vreman, B. Geurts, and H. Kuerten. Comparison of numerical schemes in Large Eddy Simulation of the temporal mixing layer. *Int. J. Numer. Meth. Fluids*, 22(4):297–311, 1996.

[140] B. Vreman, B. Geurts, and H. Kuerten. Large Eddy Simulation of the turbulent mixing layer. *J. Fluid Mech.*, 339:357–390, 1997.

[141] F. A. Williams. *Combustion Theory*, volume 2nd edition of . The Benjamin/Cummings Publishing Company, Inc, 1985.

[142] I. Wygnanski and H. Fiedler. Some measurements in the self-preserving jet. *J. Fluid Mech.*, 38(3):577–612, 1969.

[143] A. Yakhot, S. A. Orszag, V. Yakhot, and M. Israeli. Renormalization group formulation of Large Eddy Simulation. *J. Sci. Comp.*, 4(2):139–158, 1989.

[144] V. Yakhot. private communication., 2002.

[145] V. Yakhot and S. A. Orszag. Renormalization group analysis of turbulence I: Basic theory. *J. Sci. Comp.*, 1:3–40, 1986.

[146] Y. Zang, R. L. Street, and J. R. Koseff. A dynamic mixed subgrid-scale model and its application to turbulent recirculating flows. *Phys. Fluid*, 5(12):3186–3196, 1993.

[147] W. Zhao, S. H. Frankel, and L. Mongeau. Large eddy simulations of sound radiation from subsonic turbulent jets. *AIAA J.*, 39(8):1469–1477, 2001.